ATOMISTIC AND EXPERIMENTAL DETERMINATION OF THE STRUCTURAL AND THERMOPHYSICAL PROPERTIES OF THE ACCIDENT TOLERANT FUEL MATERIALS

A Thesis Submitted to the College of

Graduate and Postdoctoral Studies

In Partial Fulfillment of the Requirements

For the Degree of Doctor of Philosophy

In the Department of Mechanical Engineering

University of Saskatchewan

By

Linu Malakkal

Permission to use

In presenting this thesis in partial fulfilment of the requirements for a postgraduate degree from the University of Saskatchewan, I agree that the Libraries of this University may make it freely available for inspection. I further agree that permission for copying of this thesis in any manner, in whole or in part, for the scholarly purpose may be granted by the professors who supervised my thesis work or, in their absence, by the Head of the Department or the Dean of the College in which my thesis work was done. It is understood that any copying or publication or use of this thesis or part thereof for financial gain shall not be allowed without my written permission. It is also understood that due recognition shall be given to me and to the University of Saskatchewan in any scholarly use which may be made of any material in my thesis.

Requests for permission to copy or to make other use of the material in this thesis in whole or part should be addressed to:

Head of the Department of Mechanical Engineering
University of Saskatchewan
57 Campus Drive
Saskatoon, Saskatchewan S7N 5A9 Canada

OR

Dean
College of Graduate and Postdoctoral Studies
University of Saskatchewan
116 Thorvaldson Building, 110 Science Place
Saskatoon, Saskatchewan S7N 5C9 Canada

Abstract

The tragic nuclear accident at the Fukushima-Daiichi power station in Japan brought in to our attention the risk associated with the current design of reactors based on uranium dioxide (UO_2) fuel and zirconium cladding. As an offshoot, the research towards accident tolerant nuclear fuel (ATF) that can withstand the loss of coolant for a long time while improving thermal efficiency has gained momentum. Most desirable thermophysical properties expected of an ATF is high thermal conductivity, the lack of which leads to the poor dissipation and rapid meltdown at the core of the fuel pellet during the loss of coolant.

Several approaches are being considered by researchers across the world to improve the thermal conductivity of nuclear fuels. Apart from the state of art of uranium-based fuels, there is a renewed interest in thorium-based fuels (especially thorium dioxide (ThO_2) and thorium nitride (ThN)) in the quest of ATF. This thesis focuses on evolutionary fuel concepts based on thoria fuels. Unlike UO_2, the information regarding the thermophysical properties of ThO_2 fuels, and the additive materials under the normal operating conditions and the extreme accident conditions are not well known. Therefore, in this thesis, the computational techniques such as density functional theory (DFT) and classical molecular dynamics (MD) are used to determine the thermophysical properties of the thoria fuel, surrogate of thoria CeO_2 and additive materials such as SiC and BeO. One of the significant limitations in the front end of the thoria fuel cycle has the difficulty of fabricating dense pellets by conventional sintering techniques. Hence the processing of thoria fuels by the spark plasma sintering (SPS) was proposed, and the effect of the sintering parameters on the density, microstructure and the thermal conductivity of ThO_2 fuel was established. Finally, using SPS, a novel composite fuel of ThO_2-SiC has been fabricated with the enhanced thermal conductivity.

Acknowledgement

I take this opportunity with immense pleasure to thank God Almighty and all the people who have helped me through the course of my journey towards creating this thesis. First of all, I would like to pay my sincere gratitude to my beloved supervisors Prof. Jerzy Szpunar and Dr. Barbara Szpunar, for allowing me to carry out my dissertation under their esteemed guidance. I also appreciate their unconditional support and valuable comments during the entire course of my PhD journey.

I would also like to thank my advisory committee members: Prof. Carey J. Simonson (Committee chair), Prof. Jim Bugg, Prof. Qiaoqin Yang and Prof. Ranier Dick (Cognate member) for their encouragements, their constructive comments and discussions. Additionally, I appreciate the valuable support from my friends, family, teachers, and the colleagues of the Advanced Materials and Renewable Energy (AMRE) group at the University of Saskatchewan. My sincere thanks to Ravi Kiran Siripurapu, Dr Juan Carlos Zuniga, Dotun Oladimeji, Dr. Ericmoore Jossou, and Jayangini Ranasinghe for their unconditional support during my PhD. I also thank the support provided by Prof. Lukas Bichler and Anil Prasad of the University of British Colombia for their assistance with the fabrication of the fuels. I also remember my previous supervisors Prof. Anil Kumar (IIT Roorkee), and Prof. Sajithbabu C (GEC-Kozhikode) for their guidance and encouragement. Last but not least, I would sincerely recognize the contribution made by Dr. Jijin Raj Ayanath Kuttiyatveetil in helping to improve my writing skills.

Finally, I acknowledge the financial support of the Natural Science and Engineering Research Council of Canada (NSERC), the devolved scholarship and the mechanical engineering departmental scholarships provided by the University of Saskatchewan.

Dedication

I want to dedicate this thesis to my lovely wife, Amrutha Thandan Veettil, for the unconditional support, especially when the tasks many times seemed overwhelming, you have always been my inspiration to be strong and persistent, no matter how significant the obstacles have been.

Also, to my beloved parents, Narendran Malakkal and Lokeswari Malakkal, my siblings Adv. Nandulal Malakkal and Dr. Mridula Thandan Veettil and for my in-laws Viswanathan Thandan Veettil and Santha Kumari K., the reason for all the achievements that I have accomplished. Thanks for your endless love, support and encouragement.

List of publications

The work discussed in this dissertation has been published in the following papers:

L. Malakkal, A. Prasad, E. Jossou, J. Ranasinghe, B. Szpunar, L. Bichler, J. Szpunar; "Thermal conductivity of bulk and porous ThO_2: Atomistic and experimental study"; published in Journal of Alloys and Compounds, Vol.798, pp.507-516 (2019).

L. Malakkal, A. Prasad, D. Oladimeji, E. Jossou, J. Ranasinghe, B. Szpunar, L. Bichler, J. Szpunar; "Atomistic and experimental study on thermal conductivity of bulk and porous cerium dioxide"; published in Nature Scientific Reports, Vol. 9 6326 (2019).

L. Malakkal, B. Szpunar, R. K. Siripurapu, J. A. Szpunar; "Thermal conductivity of bulk and nanowire of cubic-SiC from *ab initio* calculations"; published in Journal of Computational Material Science, Vol.128 pp.249-256 (2017).

L. Malakkal, B. Szpunar, R.K. Siripurapu, J. Zuniga, J.A. Szpunar; "Thermal conductivity of wurtzite and zinc-blende cubic phases of BeO from *ab initio* calculations"; published in Solid-State Sciences Vol. 65 pp.79-87 (2017).

L. Malakkal, A. Prasad, J. Ranasinghe, E. Jossou, D. Oladimeji, B. Szpunar, L. Bichler, J. Szpunar; "The effect of SPS processing parameter on the microstructure and thermal conductivity of ThO_2"; published in Journal of Nuclear Materials (2019).

L. Malakkal, A. Prasad, J. Ranasinghe, M.K.Tummalapalli, E. Jossou, B. Szpunar, L. Bichler, J. Szpunar, "Enhanced thermal conductivity of thorium dioxide-silicon carbide composite fuel pellets fabricated by spark plasma sintering (SPS)", manuscript prepared.

L. Malakkal, B. Szpunar, R.K. Siripurapu, J.C. Zuniga, J.A. Szpunar; "First principle calculation of thermo-mechanical properties of Thoria using Quantum Espresso"; published in International Journal of Computational Material science and Engineering, Vol. 5 1650008 (2016).

Some work of this thesis were also presented at the following conferences.

L. Malakkal, A. Prasad, J. Ranasinghe, E. Jossou, B. Szpunar, L. Bichler, J. Szpunar; "The microstructure and thermal conductivity of spark plasma sintered ThO_2"; presented at 14th international conference on CANDU fuel, Mississauga, Ontario, Canada July 21-24 (2019).

L. Malakkal, B. Szpunar, J. I Ranasinghe, E. Jossou, J. A. Szpunar; "DFT calculation of thermal conductivity and mean free path of ThO_2"; presented at 8th International Conference on simulation methods in nuclear science and engineering Ottawa, Canada, Oct 9-11 (2018).

L. Malakkal, B. Szpunar, J. A. Szpunar; "Comparative study of thermal conductivity of SiC and BeO from *ab initio* calculations"; presented at TMS San Diego USA 2017.

L. Malakkal, B. Szpunar, R. K. Siripurapu, J. C. Zuniga, J. A. Szpunar; "First Principles calculation of thermo-mechanical properties of Thoria using Quantum Espresso"; presented at the 8th international conference on materials for advanced technologies of the materials research society of Singapore, Singapore, 28th June-03rd July 2015.

L. Malakkal, B. Szpunar, R. K. Siripurapu, J. A. Szpunar "Review of thermo-mechanical properties of SiC using first principles method"; presented at the 26th Canadian Material Science international conference held at Saskatoon, 1-3rd June 2014.

L. Malakkal, B. Szpunar, R. K. Siripurapu, J. C. Zuniga, J. A. Szpunar; "An Interface to Quantum ESPRESSO" published as proceedings of 3rd World Congress on Integrated Computational Materials Engineering (ICME 2015) Pennsylvania USA, published by Wiley publications.

Table of contents

Permission to use ..... **i**
Abstract ..... **ii**
Acknowledgement ..... **iii**
Dedication ..... **iv**
List of publications ..... **v**
Table of contents ..... **vii**
List of tables ..... **xiii**
List of figures ..... **xiv**
List of acronyms ..... **xx**
List of symbols ..... **xxiii**
Chapter 1 : Introduction **1**
1.0 Overview **1**
1.1 Significance of nuclear energy **1**
1.2 Nuclear Fission **2**
1.3 Nuclear reactors **2**
1.4 Nuclear fuels and the concept of accident tolerant fuels **4**
1.5 The evolutionary fuel concept **5**
1.5.1 Doped fuel 5
1.5.2 Composite fuel 7
1.6 The revolutionary fuel concept **10**
1.7 Triso-SiC composite fuel **11**
1.8 Thorium based nuclear fuels **11**
1.9 Thesis objectives **12**
1.10 Thesis overview **13**
Chapter 2 : Research Methodology **15**
2.0 Overview **15**
2.1 Computational Methods **15**
2.1.1 Introduction to DFT 15
2.1.2 Born-Oppenheimer approximation 16
2.1.3 Hohenberg-Kohn Theorem 17

2.1.4 Kohn-Sham equations 17
2.1.5 Exchange-correlation functional 19
2.1.6 An introduction to MD simulations 19
2.1.7 Introduction to thermal conductivity calculations 23
2.1.8 Lattice thermal conductivity from Boltzmann transport equation (BTE) 23
2.1.9 Lattice Thermal conductivity from MD simulation 25
2.2 Experimental details of fuel fabrication 26
2.2.1 Powder blending 26
2.2.2 Fabrication by spark plasma sintering 26
2.3 Material characterization techniques 28
2.3.1 X-ray diffraction 28
2.3.2 Scanning electron microscopy/electron backscattered diffraction 29
2.3.3 Density measurement 29
2.3.4 Raman spectroscopy 30
2.3.5 Thermal conductivity measurement by Laser Flash apparatus 31
Chapter 3 : Thermal conductivity of bulk and porous ThO_2; Atomistic and Experimental study 33
3.0 Overview 33
3.1 Abstract 34
3.2 Introduction 34
3.3 Computational and experimental methods 37
3.3.1 Computational details 37
3.3.2 Details of the BTE calculations 37
3.3.3 Details of the EMD calculations for bulk and porous ThO_2 38
3.3.4 Details of the experiments 40
3.4 Results and Discussion 41
3.4.1 Crystal structure and elastic constants from ab-initio calculations 41
3.4.2 Lattice dynamics 43
3.4.3 Three-phonon scattering phase space and Grüneisen parameter of ThO_2 44
3.4.4 Thermal conductivity and mode contribution of bulk ThO_2 45
3.4.5 Thermal conductivity of porous ThO_2 using MD simulations 47
3.4.6 Experimentally measured thermal diffusivity and thermal conductivity of ThO_2 48

3.5 Summary 50

Chapter 4 : Atomistic and experimental study on thermal conductivity of bulk and porous cerium dioxide 52

4.0 Overview 52

4.1 Abstract 53

4.2 Introduction 53

4.3 Methods 55

4.3.1 Computational details 55

4.3.2 Materials and experimental details 59

4.4 Results and Discussion 60

4.4.1 Crystal Structure and elastic constants 60

4.4.2 Lattice dynamics 62

4.4.3 Three-phonon scattering phase space and Grüneisen parameter 63

4.4.4 Theoretical prediction of thermal conductivity and mode contribution. 65

4.4.5 Effect of porosity on the thermal conductivity using MD simulations and experiments. 67

4.4.6 Nanoscale size effect, cross-plane, and in-plane thermal conductivity 70

4.5 Conclusion 73

4.6 Supplementary Informations 75

Chapter 5 : Thermal conductivity of bulk and nanowire of cubic-SiC from *ab initio* calculations 78

5.0 Overview 78

5.1 Abstract 79

5.2 Introduction 79

5.3 Methodology 81

***5.3.1 Calculation of ground states structural and mechanical properties* 81**

***5.3.2 Thermodynamic properties with quasi-harmonic approximation* 82**

(a) Thermal Expansion 82

(b) Heat Capacity 83

***5.3.3 Thermal conductivity* 84**

(a) Slack Model 84

(b) Boltzmann Transport Equation (BTE) 85

5.4 Computational Details **86**
5.5 Results and Discussions. **86**
5.5.1. Structural and mechanical properties 86
5.5.2 Phonon Dispersion and Thermodynamic properties 87
5.5.3 Thermal Properties 88
5.5.4 Lattice Thermal Conductivity 90
5.6 Conclusion **93**
Chapter 6 : Thermal conductivity of wurtzite and zinc blende cubic phases of BeO from ab initio calculations **95**
6.0 Overview **95**
6.1 Abstract **96**
6.2 Introduction **96**
6.3 Methodology **98**
6.4 Computational Details **99**
6.5 Results and Discussions **100**
6.5.1 Ground state structural and mechanical properties 100
6.5.2 Phonon Dispersion 103
6.5.3 Phonon transport properties 106
6.6 Lattice Thermal Conductivity **108**
6.7 Conclusion **111**
Chapter 7 : The effect of SPS processing parameters on the microstructure and thermal conductivity of ThO_2 ..... **112**
7.0 Overview **112**
7.1 Abstract **113**
7.2 Introduction **113**
7.3 Experimental procedure **115**
7.3.1 Starting powder 115
7.3.2 SPS sintering of ThO_2 powder 116
7.3.3 Characterization methods 117
7.4 Results and Discussions **118**
7.4.1 Structural characterization using X-ray Diffraction (XRD) and Raman study 118

7.4.2 Density measurement 119
7.4.3 Microstructural evolution of ThO_2 121
7.4.4 Grain size and inverse pole figure from EBSD study 124
7.4.5 Thermal diffusivity and thermal conductivity 127
7.5 Conclusion 129
7.6 Supplementary Information 130
Chapter 8 : Enhanced thermal conductivity of thorium dioxide-silicon carbide composite fuel pellets fabricated by spark plasma sintering (SPS) 133
8.0 Overview 133
8.1 Abstract 134
8.2 Introduction 134
8.3 Experimental procedure 136
8.3.1 Precursor powder 136
8.4 SPS sintering of ThO_2-SiC composite fuel 136
8.4.1 Powder preparation 136
8.4.2 Sintering 137
8.4.3 Characterization methods 138
8.5 Results and Discussions 139
8.5.1 Structural characterization using X-ray Diffraction 139
8.5.2 Density measurement 140
8.5.3 Microstructure of the composite pellet 140
8.5.4 Thermal conductivity 143
8.6 Conclusion 144
8.7 Supplementary Information 146
Chapter 9 : Conclusion and Future Work 147
9.0 Overview 147
9.1 Conclusion 147
9.1.1 Atomisitc and experimental determination of the thermal conductivity of bulk and porous ThO_2 and surrogate CeO_2 fuels 147
9.1.2 Role of nicrostructure in the thermophysical properties of the additives to thoria fuel 147
9.1.3 Effect of SPS parameters on the densification, microstructure and the thermal conductivity of ThO_2 148

9.1.4 Effect of SiC addiction on the densification, microstructure and the thermal conductivity of ThO_2 149
9.2 Original contribution 149
9.3 Recommendation for future work 150
9.3.1 DFT determination of the thermal conductivity of mixed oxide 150
9.3.2 Irradiation behaviour of the composite pellets 150
9.3.3 Thermal conductivity and the oxidation mechanism of the thorium nitride fuels 150
References 152
APPENDIX A 175
APPENDIX B 176
APPENDIX C 184
APPENDIX D 185
APPENDIX E 194
APPENDIX F 195

List of tables

Table 3.1. Conditions of the thermal conductivity measurements for ThO_2 from literature. 35
Table 3.2. The size dependence of kL of bulk ThO_2 at a temperature of 300 K presented using EMD simulation and the Green-Kubo method. 39
Table 3.3. Lattice parameter (ao) (in Å), bulk modulus (Bo) (in GPa) and stiffness constants (Ci) (in GPa) are given in comparison to previous experimental and theoretical results. 43
Table 4.1. Structural and mechanical properties of CeO_2 compared with previous DFT calculations and the experiment. 61
Table 4.2. The size dependence of kL of bulk CeO_2 at a temperature of 300 K presented using EMD simulation and the Green-Kubo method. 68
Table 5.1. Structural and Mechanical Properties of cubic-SiC at 0 K and 300 K evaluated by QHA with experiments [208]. 87
Table 6.1. Structural properties of w-BeO compared with previous DFT calculations and the experiment [228]. 100
Table 6.2. Mechanical properties (in GPa) of w-BeO compared with previous simulations and experiments. Here USP is ultrasoft pseudopotential and PW is Perdew-Wang method. 101
Table 6.3. Predicted structural parameters and mechanical properties of z-BeO. The obtained results are compared with previous theoretical calculations. Here PZ is Perdew-Zunger method. 102
Table 6.4. Comparison of the Raman active optical mode frequencies (in cm^{-1}) at the Brillouin zone center (Γ point) of w-BeO with the experiment data [250] and previous DFT calculations [240,241] 105
Table 8.1. The density of the composite fuel. Sample A, B, C are ThO_2 with 10 vol% SiC, and sample D carresponds to 15 vol% SiC. 140

List of figures

Fig. 1.1. Shows the anticipated demand for energy and electricity up to the year 2050 [1]..... 1
Fig. 1.2. Generations of nuclear power reactors [3]. 3
Fig. 1.3. Conceptual schematic of microcell UO_2 pellet adapted from ref. [16]. 6
Fig. 2.1. Flowchart of the self-consistent functional (SCF) for ground state SE when the atomic positions of the system are known. 18
Fig. 2.2. Schematic representation of the periodic boundary condition. 21
Fig. 2.3. Schematic representation of MD simulation. 22
Fig. 2.4. Planetary ball mill. 26
Fig. 2.5. (a) SPS equipment-Thermal Technology LLC 10-3 system, (b) Schematic diagram of SPS sintering. 27
Fig. 2.6. (a) XRD equipment BRUKER D8 Discover, (b) Schematic representation of the basic principle of a XRD. 28
Fig. 2.7. (a) SU 6600 Hitachi field emission SEM equipped with an Oxford Instruments Nordlys EBSD detector, (b) Schematic representation of the basic components of a SEM. 29
Fig. 2.8. Mass balance from Torbal. 30
Fig. 2.9. (a) Renishaw Raman microscope, (b) Schematic representation of the basic Raman microscope. 31
Fig. 2.10. (a) Laser flash apparatus from TA instruments (b) Schematic diagram of basic components of laser flash apparatus. 32
Fig. 3.1. Convergence of the k_L with respect to (a) the q-points considered for the second order force constants (by maintaining n=5 and N=18×18×18 for all the cases); (b) the number of grid planes along each axis in reciprocal space for solving the BTE (by considering q= 8×8×8 and n=5 for all the cases). 38
Fig. 3.2. (a) The HFACF for ThO_2 at a temperature of 300 K with a system size of 10×10×10 (blue lines) and 20×20×20 (black lines) unit cells. (b) The HFACF for ThO_2 at a temperature of 300 K (blue line) and 1500 K (red line) with a system size of 10×10×10 unit cells; inset shows the k_L fluctuations with time and the shaded region indicates the time range over which the HCACF integral is averaged to predict the k_L. 39

Fig. 3.3. (a) SEM image of ThO_2 powder (b) SPS sintered ThO_2 (98±0.5% TD) pellets of diameter 12.5 mm × 4 mm thickness. Sintering was done at 1700 ^oC, 50 MPa, and 10 min. 40
Fig. 3.4. Crystal structure of ThO_2 in the conventional cubic unit cell (green and red represent Th and O atoms respectively. 42
Fig. 3.5. (a) Simulated phonon spectra of ThO_2 by the linear response approach with two different q-point meshes, 5×5×5 (black solid line) and 6×6×6 (dashed red line) compared with the experiment done by Clausen K *et al.* [155] (blue dots) and (b) Partial (dotted lines) and total phonon density of states (solid green line). 44
Fig. 3.6. (a) Three-phonon scattering phase space available for ThO_2 (b) mode Grüneisen parameter (γ_{qj}). 45
Fig. 3.7. (a) The temperature dependence of the phonon k_L in ThO_2 using BTE, EMD and experiment compared to previous theoretical [129] and experimental values of k_L. (b) The mode-wise k_L of ThO_2 in comparison with the simulated results for UO_2 by Pang *et al.* [163]..... 46
Fig. 3.8. (a) Simulated k_L of pristine and porous ThO_2 as a function of temperature by considering two different cell size of 10×10×10 (blue line) and 20×20×20 (red line), compared to the experiment. (b) The k_L value in this work is compared with the available MD results (both EMD and NEMD) from literature. It has to be noted that expect for the work by Ghosh *et al.* (95% TD) all other predictions are for (100% TD)..... 48
Fig. 3.9. XRD peaks of ThO_2 powder and pellets sintered at 1700 ℃. 48
Fig. 3.10. EBSD image of pellets sintered at 1600 and 1700 ℃ respectively. 49
Fig. 3.11. (a) The thermal diffusivity of ThO_2 as a function of temperature for specimens sintered at 1600 ^oC and 1700 ^oC. The uncertainty in the data point from the laser flash apparatus is ± 4.5% and the average of three measurement are provided in the graph with the error bar. (b) The thermal conductivity of the specimen with a density of 95% TD and 99% TD (corrected to 100% TD) compared to Bakker *et al.* [4]. 50
Fig. 4.1. Convergence of the k_L with respect to (a) the q-points considered for the second order force constants (by maintaining n=9 and N=18×18×18 for all the cases); (b) the number of neighboring atoms considered for calculating the third order force constant (by keeping q=8×8×8 and N=18×18×18 for all the cases); (c) the number of grid planes along each axis in reciprocal space for solving the BTE (by considering q= 8×8×8 and n=9 for all the cases)..... 57

Fig. 4.2. (a) The HFACF for CeO_2 at a temperature of 300 K with a system size of 10×10×10 and 20×20×20 unit cells. (b) The HFACF for CeO_2 at a temperature of 300 K and 1500 K with a system size of 10×10×10 unit cells; inset shows the k_L fluctuations with time and the shaded region indicates the time range over which the HCACF integral is averaged to predict the k_L..... 58
Fig. 4.3. (a) Scanning electron micrograph of as-received CeO_2 powders from ACROS Organic. (b) Schematic diagram of SPS sintering of CeO_2. 59
Fig. 4.4. Crystal structure of CeO_2 in the conventional cubic unit cell (blue and red represent Ce and O atoms respectively. 60
Fig. 4.5. (a) Phonon spectra of CeO_2 predicted by the linear response approach using q-point of 6×6×6 (red line) and the finite displacement (FD) methods (dotted green line) compared with the experiment done by Clausen K *et al.* [155] (blue dots). (b) Partial (dotted lines) and total phonon density of states (solid black line)..... 62
Fig. 4.6. (a) Three-phonon scattering phase space. (b) Mode Grüneisen parameter (γ_{qj})..... 64
Fig. 4.7. (a) The temperature dependence of the phonon k_L in CeO_2 using BTE and experiment compared to previous theoretical [129] and experimental [170] values of k_L. (b) The mode-wise k_L of CeO_2 in comparison with the simulated results for UO_2 by Pang *et al.* [163]. 66
Fig. 4.8. (a) Simulated and experimental k_L of porous CeO_2 as a function of temperature. (b) Influence of porosity on the k_L of CeO_2, by considering the same porosity on a cell size of 10×10×10 (blue line) and 20×20×20 (red line) unit cells..... 68
Fig. 4.9. The thermal diffusivity of CeO_2 as a function of temperature for specimens sintered at 1000 ^oC and 1100 ^oC. The uncertainty in the data point from the laser flash apparatus is ± 4.5%. 70
Fig. 4.10. Thermal conductivity accumulation as a function of phonon MFP at room temperature. 71
Fig. 4.11. (a). In-plane and cross-plane thermal conductivity of CeO_2. (b) Cross-plane conductivity as a function of temperature..... 72
Fig. 4.12. Phonon dispersion with different q-points from DFPT. 75
Fig. 4.13. The convergence of k_L with number of iterations..... 75
Fig. 4.14. The k_L of CeO_2 at temperature lower than room temperature compared with the value predicted by Khafizov *et al.* [171] at 300 K using molecular dynamics (MD) calculations. 76

Fig. 4.15. Mode Grüneisen coefficient (γ_{qj}) (a) for different q points (b) for different nearest neighbours. 76
Fig. 4.16. XRD peaks of CeO_2 sintered at 1000 ℃ and 1100 ℃. 77
Fig. 5.1. (a) Phonon dispersion curve of the silicon carbide cubic structure. The solid lines show the theoretical prediction and the black dot are the experimental points measured by Serrano *et al.* [217] using IXS. (b) Shows the phonon density of states for SiC. 88
Fig. 5.2. (a) Shows the comparison of C_p from QHA and BTE (using equation (5.13)) with experiment. (b) Comparison of CLTE from our QHA calculation with experiment and previous DFT calculation (c) Entropy of SiC compared with the experiment from Barin [221]. 89
Fig. 5.3. (a) Debye temperature as a function of temperature (b) Grüneisen coefficient as a function of temperature using QHA and BTE. 90
Fig. 5.4. Thermal conductivity of SiC (a) Comparison of BTE with other simulation and experiment [222] (b) Comparison of our work between BTE and Slack (c) inverse fit of k_L as obtained from this work and previous theoretical expression from experiments [208]. 91
Fig. 5.5. Thermal conductivity of SiC nanowires (a) dependence of thermal conductivity on the diameter of nanowires all for [111] orientations (b) dependence of thermal conductivity on orientations of nanowires. 92
Fig. 6.1. (a) Phonon dispersion curve of the w-BeO structure. The solid lines show the theoretical prediction and the black dot are the experimental points measured by Bosak A *et al.* [250] using IXS. (b) Total phonon density of states (PDOS) of BeO. 104
Fig. 6.2. (a) Phonon dispersion curve of the z-BeO structure. The solid lines show the theoretical prediction. (b) Total phonon density of states (PDOS) of z-BeO. 105
Fig. 6.3. (a) Shows the comparison of change of volume as a function of temperature with the experiment by Hazen *et al.* [228]. Inset of Fig. (a) shows the volume thermal expansion by QHA. (b) shows the heat capacity as a function of temperature compared with the experimental values by Victor *et al.* [231]. 106
Fig. 6.4. (a) Shows the volume thermal expansion (α_v) by QHA for z-BeO. (b) Illustrates the heat capacity at constant pressure (C_p) as a function of temperature. 107
Fig. 6.5. (a) Thermal conductivity of w-BeO compared to experiment [78,233,256] (b) The anisotropy in k_L of w-BeO. 109

Fig. 6.6. Lattice thermal conductivity of z-BeO the black line shows the exact solution and the red line illustrates the k_L from RTA. 110
Fig. 7.1. (a) SEM image of the as-received thoria powder (b) SPS sintered ThO_2 (94.6±0.04% TD) pellets of diameter 12.7 mm × 3 mm thickness. The pellet was sintered at a temperature of 1600 ^oC, the pressure of 50 MPa and a hold time of 10 min. 116
Fig. 7.2. (a) Comparison of the X-ray diffraction of the sintered ThO_2 pellets with that of the as-received powder (b) comparison of the Raman spectra of sintered pellets of ThO_2 compared to the powder used for sintering..... 119
Fig. 7.3. The influence of (a) temperature (b) hold time and (c) pressure on the density of the sintered pellets. 120
Fig. 7.4. SEM images for ThO_2 fuel sintered at different temperature keeping sintering pressure as 50 MPa and sintering hold time as 10 min. 122
Fig. 7.5. SEM images for ThO_2 fuel sintered at different sintering time keeping the sintering temperature as 1700 ^oC and appiled pressure as 50 MPa. 123
Fig. 7.6. SEM images for ThO_2 fuel sintered at different sintering pressure keeping the sintering temperature at 1700 ^oC and hold time 10 min. 123
Fig. 7.7. EBSD images for ThO_2 fuel sintered at different temperature a) 1500 ^oC (3 μm) b) 1600 ^oC (3 μm) c) 1700 ^oC (10 μm) d) 1800 ^oC (99 μm). The legend of the color maps is shown as an inset in figure (a), and black color represent the pores in the sample..... 124
Fig. 7.8. EBSD images for ThO_2 fuel sintered at different hold time a) 5 min (7.5 μm) b) 10 min (10 μm) c) 15 min (105 μm). The legend of the color maps is shown as an inset in figure (a),), black color represent the pores in the sample. 125
Fig. 7.9. EBSD images for ThO_2 fuel sintered at different applied pressure a) 30 MPa (5 μm) b) 50 MPa (10 μm) c) 70MPa (26 μm). The legend of the color maps is shown as an inset in figure (a), black color represent the pores in the sample..... 126
Fig. 7.10. Inverse pole figure of ThO_2 a) pellet sintered at 1600 ^oC, 50 MPa and 10 min b) pellet sintered at 1700 ^oC, 50 MPa and 10 min. 127
Fig. 7.11. (a) The thermal diffusivity of ThO_2 as a function of temperature for specimens sintered at 1500 ^oC, 1600 ^oC and 1700 ^oC. The uncertainty in the data point from the laser flash apparatus is ± 4.5%. (b) The thermal conductivity of the samples sintered at 1500 ^oC, 1600 ^oC and 1700 ^oC.

(c) The thermal conductivity for the sample with 95% TD compared with the results of Pillai *et al.* [121], Cozzo *et al.* [126] and the recommended value of Bakker *et al.* [114]. 128
Fig. 7.12**.** XRD images for ThO_2 for fuel sintered (a) at different temperature, keeping pressure and hold time at 50 MPa and 10 min respectively (b) at different pressure, maintaining temperature and hold time at 1700 ^oC and 10 min (c) at different hold time, with temperature and pressure maintained at 1700 ^oC and 50 MPa respectively. 130
Fig. 7.13. Grain size distribution for ThO_2 fuel sintered at different temperature a) 1500 ^oC (3 μm) b) 1600 ^oC (3 μm) c) 1700 ^oC (10 μm) d) 1800 ^oC (99 μm). 131
Fig. 7.14. Grain size distribution for ThO_2 fuel sintered at different hold time a) 5 min (5 μm) b) 10 min (10 μm) c) 15 min (105 μm). 131
Fig. 7.15. Grain size distribution for ThO_2 fuel sintered at different pressure a) 30 MPa (5 μm) b) 50 MPa (10 μm) c) 70 MPa (26 μm). 132
Fig. 8.1. SEM micrograph of (a) ThO_2 powder (b) SiC powder. 136
Fig. 8.2. XRD analysis of the precursors (ThO_2 and SiC) and the ThO_2-15 wt% SiC sintered pellet. 139
Fig. 8.3.(a) SEM micrograph of sample A, (b) SEM micrograph of sample B, (c) SEM micrograph indicating a good interfacial contact in sample A. 141
Fig. 8.4. (a), (b) SEM-EDX micrograph of sample A with the carresponding EDX analysis and distribution maps of the whole elemental composition (c) Th (d) O and (e) Si. 142
Fig. 8.5. Grain size comparison of the ThO_2 pellets with and without the addtion of SiC..... 143
Fig. 8.6. (a) Thermal diffusivity, (b) thermal conductivity values of ThO_2 and ThO_2–SiC composite pellets sintered by SPS. 144
Fig. 8.7**.** XRD images for ThO_2 and ThO_2-SiC composites. 146

List of acronyms

ABWR	Advanced Boiling Water Reactor
ADOPT	Advanced DOped Pellet Technology
Al	Aluminium
Al_2O_3	Aluminum oxide
AP	Advanced Plant
ATF	Accident Tolerant Fuel
B3LYP	Becke 3-parameter, Lee-Yang_Parr
Ba	Barium
BeO	Beryllium oxide
BWR	Boiling Water Reactors
BZ	Brillouin Zone
C	Diamond
CANDU	CAnadian Deuterium Uranium
CASTEP	Cambridge Serial Total Energy Package
CeO_2	Cerium dioxide
CNTs	Carbon Nano Tubes
Cr_2O_3	Chromium oxide
CTE	Coefficient of linear thermal expansion
DFPT	Density Functional Peturbation Theory
DFT	Density functional theory
DOE	Department of Energy
EAM	Embedded Atom Many body
EBSD	Electron Back Scattered Diffraction
EMD	Equillibrium Molecular Dynamics
EOS	Equation Of States
EPR	European Pressurized Reactor
ESBWR	Economic Simplified Boiling Water Reactor
FGR	Fission Gas Release
FP	Fission Product

FR	Fast Reactor
GFR	Gas Cooled Fast Reactor
GGA	Generalized Gradient Approximation
GIF	Generation IV International Forum
GK	Green-Kubo Method
GNP	Graphite Nano Platelet
HCACF	Heat Current AutoCorrelation Function
HTGR	High Tempearture Gas Cooled Reactor
INL	Idaho National Lab
IXS	Inelastic X-ray Scattering
Kr	Krypton
LAMMPS	Large-scale Atomic/Molecular Massively Parallel Simulator
LDA	Linear Denisty Approximation
LFA	Laser Flash Apparatus
LFR	Lead Cooled Fast Reactor
LWR	Light Water Reactor
MD	Molecular Dynamics
MFP	Mean Free Path
Mo	Molybdenum
MSR	Molten Salt Reactor
MWCNT	Multi-Walled Carbon Nano Tubes
NAC	Non-Analytical Contribution
NEMD	Non-Equillibrium Molecular Dynamics
ODS	Oxide Dispersion Strengthened
Pa	Protactinium
PCA	Process Control Agent
PDOS	Phonon Density of States
Pu	Plutonium
PuO_2	Plutonium dioxide
PWR	Pressurized Water Reactors

QE	Quantum Espresso
QHA	Quasi-Harmonic Approximation
Quantum-Espresso	opEn Source Package for Research in Electronic Structure, Simulation, and Optimization
Re	Rhenium
RTA	Relaxation Time Approximation
SCF	Self-Consistent Functional
SCWR	SuperCritical Water-Cooled Reactor
SE	Schrödinger Equation
SEM	Scanning Electron Microscope
SFR	Sodium cooled Fast Reactor
SiC	Silicon carbide
SPS	Spark Plasma Sintering
SWCNT	Single-Walled Carbon Nano Tubes
TD	Theoretical density
Th	Thorium
ThO_2	Thorium dioxide
TRISO	Tri-Structural Isotropic
U	Uranium
UC	Uranium carbide
UN	Uranium mononitride
UO_2	Uranium dioxide
VASP	Vienna Ab-initio Simulation Package
VHTR	Very High Temperature Reactor
W	Tungsten
XRD	X-Ray Diffraction
Zr	Zirconium

List of symbols

${}_0n^1$	Neutron
β^-	Beta decay
Υ	Gamma decay
$\frac{\partial}{\partial t}$	Partial derivative with respect to time
$\hbar$	Modified Plank's constant
i	Imaginary unit
E	Total energy
$\Psi(\boldsymbol{r}, t)$	Wave function
$\widehat{H}$	Hamiltonian Operator
m_e	Mass of an electron
M_I	Mass of a nuclei
Z_I	Charge of a nuclei
R_I	Position of nuclei
r_i	Position of electron
N	Number of electrons/particles
$n(r)$	Electron density
$v_{ext}(\boldsymbol{r})$	External potential
$F[n(\boldsymbol{r})]$	Functional of electron density
$E\,[n(\boldsymbol{r})]$,	Ground state energy
$n_0(\boldsymbol{r})$	Ground state electron density
ϵ_{XC}^{hom}	exchange correlation energy per electron for a uniform electron gas
E_{XC}^{LDA}	Exchange correlation energy from LDA
E_{XC}^{GGA}	Exchange correlation energy from GGA
$\nabla(n(\boldsymbol{r}))$	Gradient of electron density
$\vec{F}_i(t)$	Force acting on a particle i due to the interaction with other atoms at time t
t	Time

m_i	Mass of atom
a_i	Accelaration of atom
$\vec{\nabla}_{r_i} U(\vec{r_i})$	Partial derivative of the potential energy w.r.t atomic coordinates
U	Potentail energy w.r.t atomic coordinates
$r_i(t)$	Coordiante of a particle
$v_i(t)$	Velocity of a particle
δt	Partial derivative of time
λ	Wave length
d	Lattice spacing
Å	Angstrom
θ_B	Braggs angle
M_a	Mass of the sintered specimen in air
M_w	Mass of the sintered specimen in water
ρ_t	Theoretical density of the material
ρ_s	Relative density of the sample
ρ_w	Density of water
V	Volume
MWD/MTU	Megawatt-day per Metric Ton
GWd/tU	Gigawatt-days/metric tonnes of enriched uranium
^oC	Degree Celsius
k_L	Lattice contribution to the thermal conductivity
q	Wave vector
ω	Phonon frequency
C_V	Heat capacity at fixed volume
C_P	Heat capacity at fixed pressure
Ω	Volume of primitive cell
k_B	Boltzmann constant
v_λ	Group velocity of a mode λ
τ_λ	Relaxation time of mode λ

kV	Kilo-volt
W	Watt
L	Thickness of the sample
T	Temperature
K	Kelvin
m	Meter
Ry	Rydberg
eV	Electron volt
MPa	Mega Pascal
GPa	Giga Pascal
nm	Nanometer
THz	Terahertz
S	Entropy
α	Thermal diffusivity
a	Lattice constant
B	Bulk modulus
C_{ij}	Stiffness constant
G	Shear modulus
Y	Youngs modulus
η	Poissons ratio
Z^*	Born effective charges
γ	Grüneisen parameter
P_3	Three phonon phase space
$\theta(T)$	Debye temperature
Q	Energy of pulsed laser beam
S	Suppression function
mm	Millimeter
cm	Centimeter
α_v	Volume thermal expansion
N_A	Avogadro number

ρ_ω	Density of state of phonons
$\hbar\omega$	Energy of phonon
T_m	Melting point
$F_{vib}(V(T),T)$	Vibrational energy
$F(V(T),T)$	Helmontz free energy
$(E(\ V(T),T)$	Electronic energy
$\gamma_p(q)\big\vert_{har}$	Harmonic mode Grüneisen parameter
$k(\omega)$	Bulk spectral conductivity

Chapter 1 : Introduction

1.0 Overview

This chapter focuses on the motivation behind this dissertation. Here the relevance of nuclear energy and brief general review of the concept of accident tolerant fuel (ATF) are discussed. The main goal of this research and the specific objectives of the study are presented in this section. An overview of the content of this thesis is also highlighted.

1.1 Significance of nuclear energy

The supply of a reliable, clean and affordable source of energy, in a sustainable manner, is a fundamental requirement for the modern society. According to the recent scenarios, the world's energy needs are expected to increase by a factor of 1.5–3 times by 2050 [1]. During the same period, electricity production is expected to increase twice, as shown in Fig. 1.1 [1]. The energy sources that will meet the future demand will be determined by the availability of technologies, environmental and health impacts, generating cost, the security of supply, and public acceptance [2]. Among the available energy sources, nuclear energy can potentially provide electricity readily with low carbon dioxide emittance [2] and easily realized the future demands. In 2016, nuclear energy produced over 11% of the world's electricity [1].

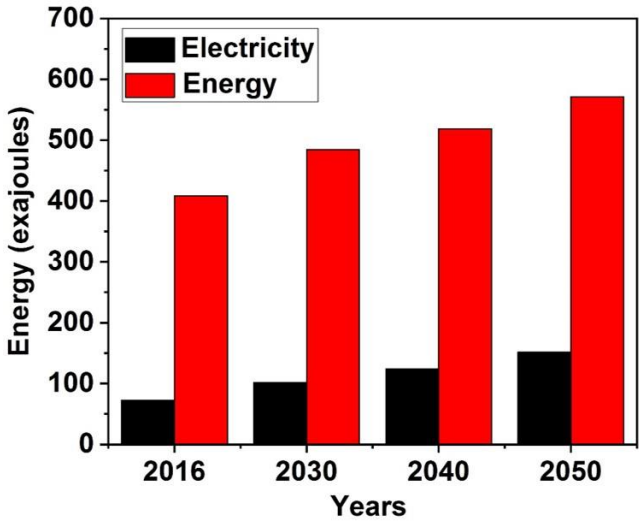

Fig. 1.1. Shows the anticipated demand for energy and electricity up to the year 2050 [1].

Apart from replacing coal and natural gas for electricity production, nuclear energy is playing a role in hydrogen generation, production of radioisotopes, marine propulsion and in providing clean

water for drinking and water for industrial use and irrigation. Therefore, further development of nuclear technology in a sustainable and environmentally conscious manner is crucial.

1.2 Nuclear Fission

Nuclear energy can be obtained from nuclear reactions such as fission or fusion. In the current scenario, the nuclear fission of uranium (U) is the major contributor to nuclear energy. In a fission event, the fissionable nucleus reacts with a neutron ($_0n^1$), becomes temporarily unstable and undergoes fragmentation into fission products. In the case of fissile uranium-235 (U-235), the absorption of neutrons leads to a fission reaction as follows:

$$_{92}U^{235} + {}_0n^1 = {}_{56}Ba^{144} + {}_{36}Kr^{89} + 3({}_0n^1)$$

The U-235 absorbs a neutron and becomes a very unstable U-236, which spontaneously splits into two different atoms most often (barium (Ba) and krypton (Kr)). The three free neutrons collide with other U-235 atoms, further producing three additional free neutrons each, thus sustaining the chain reaction. Thorium 232 (Th-232), another fertile element of increasing importance, transmute into a heavier nuclide U-233 that is fissile. The Th-232 captures a neutron, becomes Th-233 and then undergoes two beta decay to become Pa-233 (Protactinium) and then through another beta decay U-233 is produced as shown below.

$$^{232}Th \xrightarrow{(n,\gamma)} {}^{233}Th \xrightarrow{(\beta^-)} {}^{233}Pa \xrightarrow{(\beta^-)} {}^{233}U$$

1.3 Nuclear reactors

Ever since the beginning of nuclear power production on an industrial scale, nuclear reactor designs have evolved to improve efficiency and safety features. The historical evolution of nuclear reactors is classified into four different generations. Generation I reactors are the early prototypic reactors, first to produce the civilian nuclear power in the mid-20th century. The reactors in the shipping port in the United States and Calder Hall in the United Kingdom are some examples. Generation II reactors are the commercial power reactors incorporating features to increase reactor safety and reduce the risk associated with accidents. The safety features of Generation II reactors were enhanced by the active safety systems which were activated by peoples in the control room. Most of the currently operating nuclear reactors employ generation II technology, and the

examples of generation II nuclear reactor includes the pressured water reactors (PWR), boiling water reactor (BWR), CANDU (Canada Deuterium Uranium). However, the drawback of these Generation II nuclear reactors is that the safety systems cannot be operated if the electric power systems are shut down.

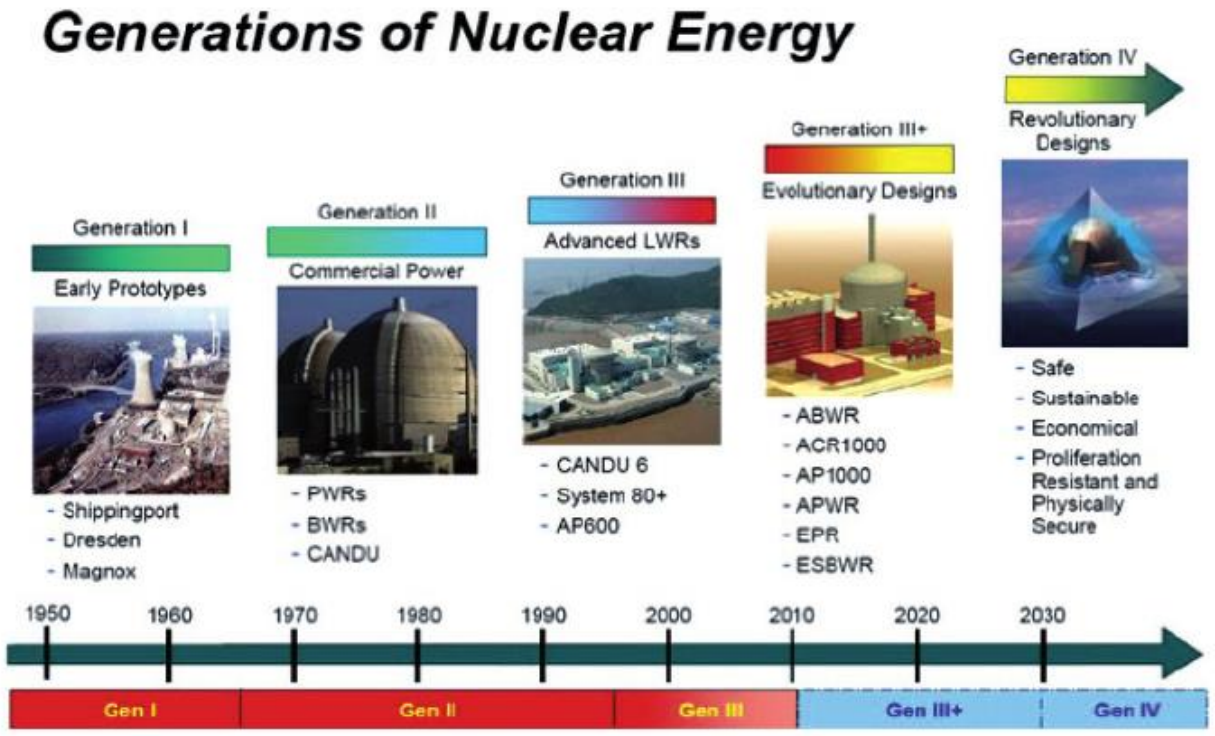

Fig. 1.2. Generations of nuclear power reactors [3].

After the Three Mile Island and the Chernobyl accidents, the generation III or III+ types of the reactors were developed with higher safety levels. Two different approaches were adopted; some designs implement an enhancement of the active safety system used in Generation II nuclear reactors, while the other design implemented an innovative passive safety concept. The passive safety concept requires the minimal need for electricity, mechanical components activation and human intervention because the driving forces to activate the safety features are based on the natural physical principles [3]. French EPR (European pressurized reactor) and the US-Japanese ABWR (Advanced boiling water reactor) were based on the enhanced active safety systems, and US AP (Advanced Plant) 1000 pressurized water reactor and the US-Japanese ESBWR (economic simplified boiling water) were equipped with the passive system [3].

Generation IV reactors are a set of revolutionary reactors that are researched and developed under the Generation IV International Forum (GIF). In the year 2000, 12 countries initiated an international collaboration to identify and select the nuclear technologies for the future that satisfy the main requirements such as a) sustainability, with more effective nuclear fuel exploitation, lower waste production and long-time burden, b) economics c) enhanced safety and d) non-proliferation and physical protection [4]. In 2002, GIF selected six reactor technologies among about hundred concepts reviewed. The selection of these technologies was made based on the criteria of providing clean, safe and cost-effective energy on a sustainable basis. The selected reactors are Gas-cooled Fast Reactor (GFR), Very High Temperature Reactor (VHTR), Sodium-cooled Fast Reactor (SFR), Lead-Cooled Fast Reactor (LFR), molten salt reactor (MSR) and Super-Critical Water-Cooled Reactor (SCWR). Canada has signed to take up research on SCWR because it is an evolution of the current CANDU reactor.

1.4 Nuclear fuels and the concept of accident tolerant fuels

Nuclear fuels are highly complex materials that have undergone constant development over the past four decades [5]. Even though there have been many improvements in the original designs and materials used, the basic concept of uranium dioxide (UO_2) fuel pellets and zirconium cladding has remained the standard for most of the commercial nuclear power plants. The light-water reactors (LWR), the commonly used commercial nuclear power reactor uses UO_2 fuel enriched to approximately 4.0 to 4.95% ^{235}U. However, the Fukushima nuclear mishap has illustrated the risk associated with the current design of reactors based on UO_2 fuel. One of the significant drawbacks of the UO_2 fuel is its low thermal conductivity, which is further degraded due to oxidation and irradiation at high temperature. Therefore, after the Fukushima nuclear disaster in 2011, several countries have started to focus on nuclear reactor fuels with enhanced accident tolerance- ATF [6]. The features of ATF include the following characteristics such as the ability to withstand the loss of coolant in a reactor core for an extended time, higher temperature of operations, reduction of operational and maintenance cost and to the improvement of the nuclear power plant performance.

To achieve accident tolerance, changes are proposed to the fuel pellets and the fuel cladding-two components of the reactor core. In this thesis, the primary focus is on the fuel pellets. Therefore, the discussions will be limited to fuel. The fuel performance under the normal operating conditions and the possible enhanced accident tolerance of a specific ATF can be determined from the

material properties of a given fuel; hence, it is essential to understand the key material properties. The desired material properties are classified into the following categories;

- Thermal properties: higher melting point, higher thermal conductivity, lower specific heat capacity and a lower coefficient of thermal expansion.
- Mechanical properties: lower yield strength, higher toughness, rapid creep rate and high modulus of elasticity.
- Neutronic properties: higher fissile density and higher fission cross-section.
- Chemical properties: lower corrosion and lower fission product release.

Before being assertive on the commercial applications of any of the ATF, it is essential to quantitatively understand if the material properties of the proposed fuel adhere to the constraints established for the use in commercial reactors. Several fuels are currently under considerations for ATFs, ranging from those with slight variations on the current UO_2 technology (the evolutionary fuel concept) and those that are significantly different from the current state of the art (the revolutionary fuel concept). In the following section, each of these fuel concepts is explained in detail.

1.5 The evolutionary fuel concept

In the evolutionary fuel concepts, dopants or additives are used to modify the properties of existing fuels. These fuels can be more easily deployed in a shorter time frame because they use the present state of the art technology, experience and expertise. The evolutionary fuels are broadly classified into two categories; a) doped fuel and b) composite fuel.

1.5.1 Doped fuel

Dopants or additives enhance the critical properties of the existing nuclear fuels, thereby adding its values, reliability and the ability to mitigate the consequences of an accident [7]. Since UO_2 is the most commonly used fuel in the LWR, here we discuss the doped-UO_2 in details. Depending upon the amount of the dopant and the role of the additives, the oxide-doped UO_2 is divided into doped and microcell UO_2 pellet. In the doped-UO_2 pellet, the primary purpose of adding the dopant is to increase the average grain size of the fuel leading to an enhancement in the viscoplastic behaviour and slowing the fission product release [8]. Several researchers have investigated the effect of different dopants such as oxides of chromium [8–11], magnesium [12], niobium [13] and titanium [14] on the microstructure of UO_2. An analysis of the microstructural and mechanical

properties of the unirradiated doped-fuels; chromium oxide (Cr_2O_3) was determined to be most favourable dopant [9]. AREVA developed an improved UO_2 fuel [15] with Cr_2O_3 dopant (amount close to the solubility limit in UO_2), leading to large grain size (50-60 μm) and increased fuel viscoplasticity. Later Westinghouse has developed another dopant fuel of UO_2 called ADOPT (Advanced DOped Pellet Technology) fuel, that contain aluminium oxide (Al_2O_3)-Cr_2O_3 [7]. The addition of Al_2O_3 not only enhances the grain size enlarging the effect of Cr_2O_3 but also helps reduce the amount of Cr_2O_3 while having similar benefits of the pellets with just Cr_2O_3 dopant.

In ceramic microcell UO_2 pellet, the primary role of the dopant is to minimize the fission products (FPs) release in the pellet by providing a microcell structure with oxide additives [16,17]. The microcell consists of UO_2 grains enveloped by thin walls that are continuously connected. Fig. 1.3 shows the conceptual schematic of a microcell UO_2 pellet. The function of the cell walls is to provide multiple chemical traps or a physical barrier against the movement of volatile FPs. The improvement in the retention of FP capability leads to a reduction of the inner surface cladding corrosion caused by FPs as well as the internal pressure of the fuel rod. The cell wall structure is also expected to prevent the massive fragmentation of pellets during a severe accident. The grain size of the ceramic microcell UO_2 fuel is also characterized by large-grain (~100 μm) and cell structure, providing the same beneficial features for the fuel as observed in the previous case of doped UO_2 fuel.

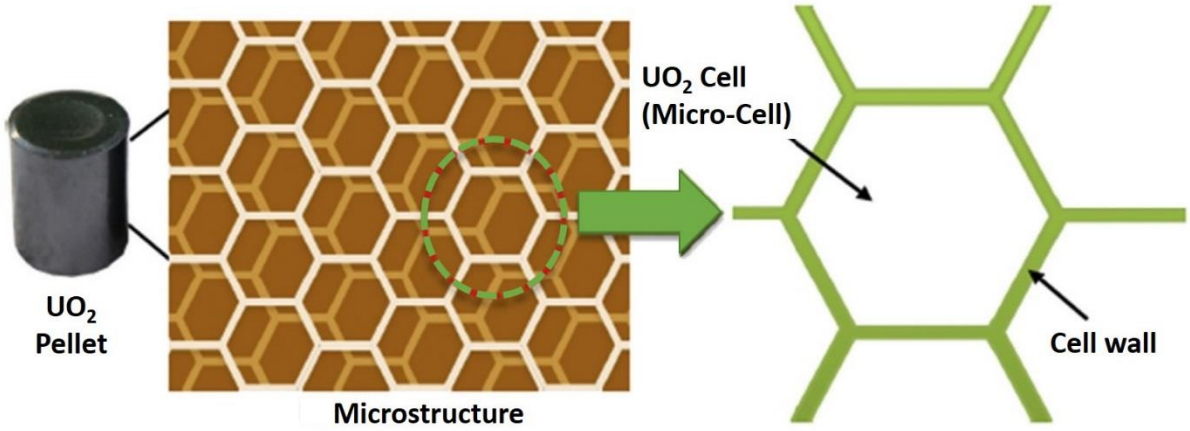

Fig. 1.3. Conceptual schematic of microcell UO_2 pellet adapted from ref. [16].

1.5.2 Composite fuel

A low volume fraction of highly thermally conductive material is added to the fuel to enhance its thermal conductivity. The enhanced thermal conductivity of such fuels enables the lowering of the fuel temperature in normal operating conditions and also increases the safety margins for fuel melting in case of an accident. Depending upon the material added as additive the high thermal conductivity UO_2 fuels are classified into two categories; a) CERMET fuel, b) ceramic additive fuel. As the name suggests, CERMET fuels have a low amount of metals (5 to 10% vol) added as additives-which also provides a physical barrier against the movement of volatile FPs, whereas, in the other case additives are ceramic materials (5 to 10% vol). The amount of additives is limited to 10 vol% because it provides a significant improvement in conductivity in unirradiated samples while not infringing on the enrichment limit of 5%. The first metal-doped fuel that has been used in a commercial reactor was a stainless steel doped UO_2. Haertling and Hanrahan [18] have reviewed UO_2 dispersed in refractory metals, including molybdenum (Mo)–UO_2, tungsten (W)–UO_2 and rhenium (Re)–UO_2 alloys. Among these CERMET fuels, the most widely studied system has been W–UO_2 system and the data are available primarily for W–UO_2 fuel [19,20]. Vatulin *et al.* [21] from Russia have worked extensively on the fabrication of UO_2–Zr and UO_2–Al cermet fuel by the traditional powder metallurgy route, and have been successfully tested in MIR research reactor in Russia.

The potential ceramic materials considered as additive should possess the following properties such as high thermal conductivity, low thermal-neutron absorption cross-section, high melting point and the chemical compatibility with fuel, cladding and coolant. The need to meet these requirements has narrowed the choice of ceramic materials to beryllium oxide (BeO), silicon carbide (SiC) and carbon (in the form of diamond, graphene, carbon nanotubes). Ishimoto *et al.* [22] studied two types of BeO doped UO_2, the continuous type in which BeO is precipitated along the grain boundary, and the dispersed type, were BeO is dispersed randomly. The study revealed that the thermal conductivities of the BeO continuous type were higher than those of the BeO dispersed type, especially at a lower temperature. For example, the thermal conductivity of UO_2 – 1.2 wt% BeO at 1100 K, was higher than that of UO_2 – by 25% for the BeO continuous type and by 10% for BeO dispersed type. Recently, Zhou *et al.* [23] have shown that adding 10 vol% of BeO increased the thermal conductivity by over 40%. Li *et al.* [24] fabricated 10 vol% BeO–UO_2 composites by spark plasma sintering (SPS) technique and showed that the thermal conductivity

of $BeO–UO_2$ increases by 45.3% compared with UO_2 at room temperature. At 1600 °C, the thermal conductivity increment of $BeO–UO_2$ is 60.5%. Such improvement in thermal conductivity, especially at high temperature, will significantly decrease the thermal gradient inside the fuel pellets and reduce the risk of pellet failure. This work also emphasized the advantages of using the SPS technique over conventional sintering techniques. The SPS technique enables to control the chemical reactions between the UO_2 and the second phase, to achieve densification of the powders at significantly lower temperatures and shorter processing time and also to increase the final bonding between the UO_2 and the additive. The cost-benefit analysis of the $BeO–UO_2$ nuclear fuel was investigated by Kim *et al.* [25] showing that the optimum BeO content is about 4.8 wt%. The BeO–doped UO_2 fuels require an increase in ^{235}U enrichment of 0.0073 wt%, to keep the cycle length unchanged. However, the primary concern with beryllium is its toxicity. But, the requirements for safe handling of BeO are similar to those of UO_2. Therefore, the toxicity of BeO is not a limiting factor in the use of this material with UO_2.

Khan *et al.* [26] provided the thermal conductivity of UO_2–SiC fuel as a function of temperature and weight percent of SiC by assuming that the thin coat of SiC that cover UO_2 particles will determine the thermal conductivity of the composite fuel. Their results have indicated that the continuity of the SiC layer is essential for a relatively significant increase in thermal conductivity. Yeo *et al.* [27] fabricated the composite fuels of UO_2–10 vol% SiC composite fuel pellets by oxidative sintering and SPS at a range of temperatures from 1400 to 1600 °C. In this study, SiC in the form of powder particle and whiskers were utilized. The results revealed that the composite pellets sintered by SPS process had smaller grain size, higher density, and enhanced interfacial contact compares to the oxidative sintering. The measurement of thermal conductivity shown that SPS sintered UO_2–SiC composites when compared to UO_2 pellets increased thermal conductivity by 62%, while the oxidative sintered composite pellets had significantly lower thermal conductivity values. Also, it was found that 60% increase of thermal conductivity by 10 vol % SiC addition leads to a nearly 150 °C decrease in the maximum fuel pellet centerline temperature using FRAPCON code developed by PNNL (Pacific Northwest National Laboratory). Yeo *et al*. [28] in another work found that the particle size affected the thermal conductivity of the SPS UO_2-SiC composite. Adding SiC with a larger particle size of (16 μm and 55 μm) reduced the thermal conductivity to a value lower than pure UO_2. A series of irradiation tests have been developed by the Department of Energy (DOE) Fuel Cycle Research and Development to evaluate the

performance of proposed ATF concepts under normal LWR operating conditions. INL placed 6.5% enriched UO_2 with and without additives in the fuel capsules in the test reactors. The first group capsules of UO_2, and UO_2-10 vol % SiC whiskers, fabricated by the University of Florida, were taken out at ~8000 to 10000 MWD/MTU for an initial post-irradiation examination. Visual examination of these capsules did not reveal anything unusual. Capsule neutron radiography was also performed on these capsules. A thermal neutron radiography image did not show any significant cracking in the fuel UO_2-10 vol % SiC whiskers. There does not appear to be any other significant breaches or deformations of the cladding, but more detailed radiographs are to be taken after the rodlets are removed from the capsules.

To increase the thermal conductivity of UO_2 fuel pellets, high density UO_2–5 vol% diamond composite pellets were fabricated by Chen *et al.* [29], using the SPS technique. Diamond particles with nano-size (0.25 μm) and several micro-sizes (3 μm, 12 μm and 25 μm) were mixed with UO_2 powder and sintered using SPS at 1300–1600 ˚C with a hold time of 5 min. The resultant density, chemical reaction, microstructure, thermal conductivity and Young's modulus of the sintered pellets were investigated. The pellets with 3 μm diamond particles had a uniform distribution of particles as well as better thermal and mechanical properties compared to others. An increase in thermal conductivity of up to 41.6%, 38.3% and 34.2% at 100 ˚C, 500 ˚C and 900 ˚C, respectively, were measured in the UO_2–diamond composite pellets as compared to the pure UO_2 fuel pellets. Cartas *et al.* [30] introduced the concept of adding carbon nanotubes (CNTs) into UO_2 for thermal conductivity enhancement using SPS. In this study, 5 and 10 vol% of single-walled (SW) and multi-walled (MW) CNTs were added to pure UO_2. Only one sample with 5 vol% UO_2-SWCNT composite fuel showed a slight increase (2 W/mK at 100 ˚C) in thermal conductivity. In another work, Yao *et al.* [31] sintered UO_2-graphite nanoplatelet (GNP) composite fuel via SPS and reported that the in-plane thermal conductivity nearly tripled by GNP addition. Recently, Ti_3SiC_2 with a continuous network structure was introduced to UO_2 by Li *et al*. [32], to improve the thermal conductivity of UO_2. A dense microstructure with a clean UO_2 -Ti_3SiC_2 interface was obtained using the SPS method. Ti_3SiC_2 exhibited high thermal conductivity at elevated temperature and a coefficient of thermal expansion (CTE) close to UO_2. Therefore, the thermal conductivity of UO_2 -Ti_3SiC_2 was significantly improved compared to that of UO_2, particularly at high temperature.

1.6 The revolutionary fuel concept

Significant changes from the current state of technology are expected in the revolutionary fuel concept. Different types of cladding concepts could be a way forward, for example, the SiC/SiC composite, Oxide dispersion-strengthen (ODS) steel and coated Zr are being investigated to mitigate the steam oxidation observed in traditional Zr-based claddings. The use of these new cladding materials can have reasonably significant reactivity penalties, leading to an increase in the ^{235}U enrichment or a decrease in the nuclear cycle length. To compensate for the reasonably significant reactivity penalties, the fissile density of the pellet has to be increased. The fissile density can be increased either by using the high-density fuel or increasing the ^{235}U enrichment. Even though the fissile density is superior to traditional fuels, none of the high-density fuel materials has good water and steam tolerance as the current UO_2. However, this disadvantage may not disqualify the use of high-density fuels, as the water and steam sensitivity of the fuel has to be evaluated for the combination of cladding and the fuel. Work is also being carried out to increase the water tolerance for high-density fuels, and to make claddings with much higher resistance to leakage. Several high-density fuels such as the nitride fuel, silicide fuel and the carbide fuel are under consideration. Uranium mononitride (UN) has long been considered a potential high density, high-performance fuel candidate for LWR and fast reactor (FR) applications [33]. Apart from the high fissile density and thermal conductivity, the UN also has the advantage of having a melting point of several hundred degrees than the other competing ATF U_3Si_2. However, the deployability of this fuel has been limited due to its resistance to sintering and subsequent difficulty in producing a desirable microstructure, the high costs associated with ^{15}N enrichment, as well as the known proclivity to oxidation and interaction with steam [34]. Efforts are being made to overcome these limitations [35,36]. Like the nitrides, carbide fuels also have higher fissile density and higher thermal conductivity. Conversely, the interest in the uranium carbide (UC) fuel has diminished due to their higher swelling rate under irradiation (roughly twice that of UO_2) [37]. The silicide fuels are being actively researched [38,39] and are a potential ATF. Of the series of compounds in the U-Si phase diagram, only U_3Si_2 is being considered as a potential ATF. Other higher density silicides are rejected due to unacceptable swelling and low melting point. To reduce the swelling of the high density fuels, the concept of two-phase UN-U_3Si_2 [40,41] is being considered. Performance evaluation of high-density fuels, including, silicide fuel, was recently performed in the development of LWR fuels with Enhanced Accident Tolerance [42].

1.7 Triso-SiC composite fuel

Another fuel concept in the LWR is the tri-structural isotropic (TRISO) particle fuel consisting of fissile material bearing kernels, coated with multiple layers of porous or dense SiC and graphite [43]. The TRISO particle fuel is historically developed for high temperature gas-cooled reactors (HTGR). It has shown excellent FP retention capability through the presence of multiple layers of ceramic coating that are chemically stable and mechanically strong at high temperature and very high burnups. The TRISO-SiC fuel concept is being proposed to be adopted to the LWRs [43–46] where the TRISO particle is embedded inside a SiC matrix rather than a graphite matrix to provide dimensional and environmental stability necessary for the LWR operating conditions.

1.8 Thorium based nuclear fuels

Although the majority of the nuclear power plant currently in operation use uranium-based fuels, there has been a focus on using thorium-based fuels in the present or evolutionary reactors [47]. The reason for the renewed interest of the thorium-based fuel has been not only the doubts concerning the long-term availability of the cheap uranium but also its inherent advantages. Thorium is generally estimated to be three to four times more abundant than uranium. ThO_2 does not oxidize, has better thermo-physical properties, has a higher resistance to radiation damage, higher absorption cross-section for thermal neutrons, and a lower fission product release rate, compared to UO_2. Furthermore, ThO_2 is more proliferation-resistant and produces less transuranic elements than uranium-based fuels and aids the incineration of the Pu [48–51]. Considering these advantages, the potential role of the thorium in the so-called ATF, as well as the generation 1V reactors, are investigated. Among the six future reactor concepts that the GIF proposed, the Canadian design SCWR considers the use of solid core thorium [52] and the MSR implement very innovative fuel management approaches with the use of fuel (thorium or uranium) in liquid form [53]. Apart from these two concepts, thorium fuel cycle alternatives were analyzed in proven technologies such as high temperature gas-cooled reactor (HTGR) [54], LWR [55,56] and PWR [57], and also for new technologies such as gas turbine modular helium reactor [58], fixed bed nuclear reactor [59], and accelerator-driven systems [60].

Among the solid core thorium reactors, the most straightforward approach is to substitute uranium fuel bundles with the thorium fuel rods, and several new reactor core configuration has been proposed [55]. However, IAEA (International Atomic Energy Agency) in their report [51] has

identified the challenges that need to be addressed before using ThO_2 based fuel for commercial application. These challenges include the (a) higher sintering temperature (>2000 ˚C) and the requirement of sintering aid (CaO, MgO, Nb_2O_5) for achieving dense pellets, (b) the three-stream process of separation of U, Pu, and Th (c) the database regarding the physical and chemical properties, and the experience of thorium fuel and its fuel cycle is limited compared to UO_2. Efforts are being undertaken to overcome these limitations, for example, "Thor Energy" a private Norwegian technology company has been conducting irradiation testing of the pellets fabricated from the blend of ThO_2 and UO_2 powder and blended ThO_2 and cerium dioxide (CeO_2) pellets [61]. It has to be noted that CeO_2 is a popular surrogate of nuclear fuel. However, the information regarding the thermal properties of CeO_2 is also limited. India's pursuit for thoria based nuclear reactor is another major contributor to the research and development of thoria fuel [62].

1.9 Thesis objectives

From the brief discussion of various ATF, it is evident that the thermal conductivity is one of the most critical physical property considered in the selection of fuel materials. The overarching theme of this thesis is to gain an understanding of the fundamental principle of thermal transport in ATF. In line with this theme number of studies have been undertaken and discussed in the various chapters of this thesis. Computational studies using density functional theory (DFT) and molecular dynamics (MD) were used to determine the fundamental principle of thermal transport in ThO_2 and CeO_2 surrogate fuel. The theoretical predictions enable the selection of material in various applications and also serves as input for the mesoscale methods for improving understanding of the fuel behaviour under accident conditions. Besides, this work also addresses the limitations in the conventional sintering of Thoria fuel by fabricating the fuel using a novel sintering technique. Even though ThO_2 has better thermal conductivity than UO_2, it still falls under the category of low thermal conductivity and hence, we propose to enhance the thermal conductivity of ThO_2 by adding materials with high thermal conductivity. To better understand and solve the outlined problem, the following specific objectives will be pursued.

- To determine the fundamental principles of thermal transport in bulk and porous ThO_2 fuel and the surrogate CeO_2 using atomistic codes within the framework of DFT and MD simulations.

- Using DFT studies, establish the influence of structure on the thermo-mechanical properties and the thermal conductivity of the additive material such as SiC and BeO.
- To analyze the effect of SPS parameters on the densification, microstructure and the thermal conductivity of ThO_2.
- To establish the role of SiC addition on the densification, microstructure and the thermal conductivity of ThO_2.

1.10 Thesis overview

The realization of the objectives, mentioned above, is documented in the following chapters of this manuscript-based thesis. The thesis contains nine chapters. Chapter 1 includes the overview, motivation, various concepts of ATF, review of relevant literature and the objectives of the research. The details of different computational methods, experimental procedure and the characterization technique used are presented in Chapter 2.

In Chapter 3, the atomistic and the experimental determination of the thermal conductivity of the ThO_2 is presented. This chapter has been published in *Journal of Alloys and Compounds*.

In Chapter 4, the atomistic and the experimental determination of the thermal conductivity of the surrogate nuclear fuel CeO_2 is presented. Research findings discussed in this chapter have been published in *Nature Scientific Reports*

Chapter 5 focuses on the determination of the thermophysical properties of cubic-SiC, that is proposed as an additive material in ATF. DFT calculations were used to predict the thermal conductivity of both the bulk and the nano forms of SiC. This work is published in the Journal of *Computational Material Science.*

In Chapter 6, the thermophysical properties of BeO another additive material proposed for ATF is discussed. The anisotropy in thermal conductivity and the effect of structure on the thermal properties of BeO using DFT has been calculated. This work is published in the *Journal of Solid-State Sciences.*

In Chapter 7, the effect of SPS sintering conditions on the density, microstructure and the thermal conductivity of ThO_2 is discussed. Research findings discussed in this chapter have been published in the *Journal of Nuclear Materials.*

In Chapter 8, the enhancement of thermal conductivity in ThO_2 with the addition of SiC has been explored. Research findings presented in this chapter is being prepared to submit to the *Journal of Nuclear Materials.*

Chapter 9 provides the summary, conclusion, the original contribution of the work done and suggestions for further investigation.

Chapter 2 : Research Methodology

2.0 Overview

In this chapter, the techniques used for both the computational and experimental studies are described in detail. Firstly, the computational methods used to evaluate the structural, mechanical and thermal properties of nuclear fuels and additive materials are discussed. Later, the fabrication of ThO_2 and ThO_2-SiC samples using the spark plasma sintering method and the characterisation techniques used for studying the microstructural and thermal properties are provided.

2.1 Computational Methods

In this work, properties of materials are simulated using the density functional theory (DFT) and the molecular dynamics (MD). A summary of the theoretical background of both the techniques is described in the following sections.

2.1.1 Introduction to DFT

The physical and chemical properties of materials depend on the interaction between their electrons and nuclei. The electrons are known to have wave-particle duality as defined by the laws in quantum mechanics. Erwin Schrödinger in 1929 [63] formulated the fundamental equation of physics that describes the quantum mechanical behaviour of matter, Schrödinger equation (SE). The time-dependent SE takes the form:

$$i\hbar\frac{\partial}{\partial t}\,\Psi(\boldsymbol{r},t) = \hat{H}\,\Psi(\boldsymbol{r},\mathrm{t}) \tag{2.1}$$

where i is the imaginary unit, $\hbar$ is the Planck's constant divided by 2π, $\frac{\partial}{\partial t}$ indicates the partial derivative with respect to time, $\Psi(\boldsymbol{r},t)$ is the wave function that describes the quantum system, and $\hat{H}$ is the Hamiltonian operator corresponding to the total energy (E) of the system. If the Hamiltonian operator does not depend on time variable explicitly, the SE can be reduced to the time-independent form, as shown in equation (2.2):

$$\hat{H}\Psi(\boldsymbol{r}) = E\Psi(\boldsymbol{r}) \tag{2.2}$$

The Hamiltonian operator of the system that we are interested in contains the kinetic energies of electrons and nuclei as well as the Coulomb interactions among electrons-electrons, electrons-nuclei and nuclei-nuclei. In this case, the SE can be described by the following equation (2.3).

$$\left[-\sum_i \frac{\hbar^2}{2m_e}\nabla_i^2 - \sum_I \frac{\hbar^2}{2M_I}\nabla_I^2 - \frac{1}{4\pi\epsilon_0}\sum_{i,I}\frac{Z_I\, e^2}{|r_i - R_I|} + \frac{1}{8\pi\epsilon_0}\sum_{i\neq j}\frac{e^2}{|r_i - r_j|}\right.$$

$$\left. + \frac{1}{8\pi\epsilon_0}\sum_{I\neq J}\frac{Z_I Z_J e^2}{|R_I - R_J|}\right]\Psi(\boldsymbol{r},\boldsymbol{R}) = E\Psi(\boldsymbol{r},\boldsymbol{R}) \qquad (2.3)$$

The notation in the equation is as follows: m_e is the mass of electron, and M_I and Z_I are the respective masses and charges of the nuclei. R_I and r_i are the positions of the I^{th} nucleus and i^{th} electron, respectively. The first and second terms of equation (2.3) correspond to the kinetic energy of electrons and nuclei, respectively. The next three terms represent the attractive electrostatic interactions between the electrons-nuclei, repulsive potential energy due to electrons-electrons interaction, and the repulsive potential due to nuclei-nuclei interactions, respectively.

2.1.2 Born-Oppenheimer approximation

In an atom the nuclei are much heavier and move much slower than electrons; therefore, electrons respond much more rapidly to changes in their surroundings than the nuclei. Taking advantage of this fact, the Born-Oppenheimer approximation states that the nuclei can be considered to be spatially fixed. Now, the system can be regarded as to have only moving electrons, under the external field created by fixed positive nuclei. As a consequence of this approximation, the second term in equation (2.3) can be neglected, and the last term reduces to a constant E_{II}. The Hamiltonian in the equation (2.3) reduces to the electronic Hamiltonian given as:

$$\left[-\sum_i \frac{\hbar^2}{2m_e}\nabla_i^2 - \frac{1}{4\pi\epsilon_0}\sum_{i,I}\frac{Z_I\, e^2}{|r_i - R_I|} + \frac{1}{8\pi\epsilon_0}\sum_{i\neq j}\frac{e^2}{|r_i - r_j|} + \mathrm{E_{II}}\right]\Psi(\boldsymbol{r}) = E\Psi(\boldsymbol{r}) \qquad (2.4)$$

where $\Psi(\boldsymbol{r})$ is the electronic wave function.

Despite Born-Oppenheimer approximation, the equation (2.4) is still challenging to solve because the wave function is a function of 3*N* variables; where *N* is the number of electrons in the system. DFT serves as an alternate way to solve SE using electron density ($n(\boldsymbol{r})$), which is a function of only three coordinates.

2.1.3 Hohenberg-Kohn Theorem

The entire field of DFT rests on two fundamental theorems proved by Kohn and Hohenberg [64] and the set of equations derived by Kohn and Sham [65] in the mid-1960s. The first theorem by Kohn and Hohenberg says "*For any system of interacting particles in an external potential* $V(\boldsymbol{r})$*, except for a constant, the total energy is a unique functional* $F[n(\boldsymbol{r})]$ *of the electron density* $n(\boldsymbol{r})$", i.e. the ground state energy E can be expressed as $E[n(\boldsymbol{r})]$, where $n(\boldsymbol{r})$ is the electron density. In the second Hohenberg–Kohn theorem an essential property of the functional is revealed. It says "*The exact ground state energy of the system is the global minimum of this functional and the density that minimizes the functional is the exact ground state density* $n_0(\boldsymbol{r})$". Even though the Hohenberg-Kohn theorem provides a method to solve the SE using the electron density, the theory says nothing about what the functional exactly is and hence, it could not solve the many–body problem.

2.1.4 Kohn-Sham equations

Later in 1965, Kohn-Sham [66] developed a practical approach for solving the SE (2.4). In this method, a fictitious non-interacting system is considered in such a way that its energy is the same as that of the interacting electrons. In this approach, Kohn-Sham constructed and solved a set of SEs, in which each equation includes only a single electron wave function ($\Psi_i(\boldsymbol{r})$) (also known as Kohn-Sham orbitals) as shown in equation (2.5).

$$\left[\frac{\hbar^2}{2m_e}\nabla^2 + V(\boldsymbol{r}) + V_H(\boldsymbol{r}) + V_{XC}(\boldsymbol{r})\right]\Psi_i(\boldsymbol{r}) = \varepsilon_i\Psi_i(\boldsymbol{r}) \tag{2.5}$$

Here ε_i is the energy of the corresponding Kohn–Sham orbital $\Psi_i(\boldsymbol{r})$, potential $V(\boldsymbol{r})$ is the external potential discussed by Hohenberg-Kohn theorem and corresponds to the interactions by fixed-nuclei with electrons due to Born-Oppenheimer approximation. V_H is the Hartree potential that includes the Coulomb repulsion among electrons as defined by equation (2.6).

$$V_H(\boldsymbol{r}) = \frac{e^2}{8\pi\epsilon_0}\int \frac{n(\boldsymbol{r})\, n(\boldsymbol{r}')}{|\boldsymbol{r} - \boldsymbol{r}'|}\, d^3r' \tag{2.6}$$

The last term, $V_{XC}(\boldsymbol{r})$ is called the exchange–correlation functional, which is a correction term that takes into account for all the missing interactions in the fictitious system compared to the real many–body systems and is defined as:

$$V_{XC}(\boldsymbol{r}) = \frac{\delta E_{XC}(\boldsymbol{r})}{\delta n(\boldsymbol{r})} \tag{2.7}$$

Further, the ground state electron density $n(\boldsymbol{r})$ in terms of single electron wave function $\Psi_i(\boldsymbol{r})$ for an N-particle system is defined as;

$$n(\boldsymbol{r}) = \sum_{i}^{N} |\Psi_i(\boldsymbol{r})|^2 \tag{2.8}$$

The accuracy of the practical application of the DFT depends upon knowing the exact $V_{XC}(\boldsymbol{r})$. The exact form of the $V_{XC}(\boldsymbol{r})$ function is still unknown. However, several approximations are currently used to determine the $V_{XC}(\boldsymbol{r})$, as discussed in the next section. Once $V_{XC}(\boldsymbol{r})$ is known, the ground-state electron density and the total energy of the system can be computed in a self-consistent iterative method as depicted in Fig. 2.1.

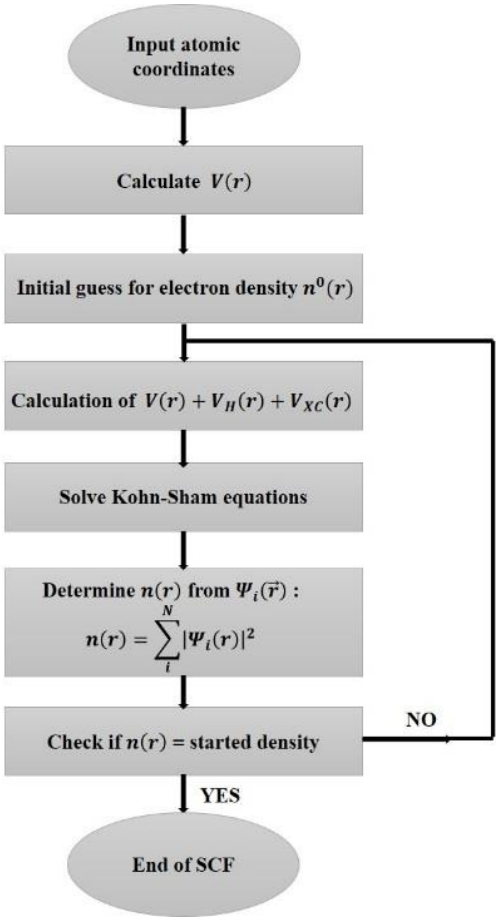

Fig. 2.1. Flowchart of the self-consistent functional (SCF) for ground state SE when the atomic positions of the system are known.

2.1.5 Exchange-correlation functional

The currently available approximations used to determine the exchange-correlation energy include the local density approximation (LDA) [67], generalized gradient approximation (GGA) [68] and hybrid functionals [69]. In LDA, the exchange-correlation energy at a point is determined as a function of the electron density $n(\boldsymbol{r})$ of a homogenous free-electron gas system which can be defined as:

$$E_{XC}^{LDA} = \int n(\boldsymbol{r})\ \epsilon_{XC}^{hom}\big(n(\boldsymbol{r})\big)d\boldsymbol{r} \tag{2.9}$$

where ϵ_{XC}^{hom} is the exchange correlation energy per electron in a uniform electron gas.

In GGA, both $n(\boldsymbol{r})$ and the gradient of the electron density ($\nabla(n(\boldsymbol{r}))$ is used to determine the exchange-correlation energy as shown in equation (2.10).

$$E_{XC}^{GGA} = \int n(\boldsymbol{r})\,\epsilon_{XC}(n(\boldsymbol{r}), |\nabla(n(\boldsymbol{r}))|)d\boldsymbol{r} \tag{2.10}$$

The hybrid functionals which incorporate a portion of the exact exchange from Hartree-Fock theory with the exchange and correlation from other sources have been introduced, and the most commonly used hybrid functional is the Becke, 3-parameter, Lee-Yang-Parr (B3LYP) [70]. In this work, the LDA and GGA pseudopotentials were considered for various materials; the type of pseudopotential used for each element is described in respective chapters. Efficient algorithms are devised to implement the Kohn-Sham equations, and some of the most commonly used DFT codes are the Vienna Ab-initio Simulation Package (VASP) [71], Cambridge Serial Total Energy Package (CASTEP) [72], Quantum-Espresso (opEn Source Package for Research in Electronic Structure, Simulation, and Optimization) [73]. In this thesis, Quantum Espresso (QE) is the code used for all the DFT calculations. To effectively perform the analysis of the results from the QE, we have developed an in-house code, as described in appendix A [74].

2.1.6 An introduction to MD simulations

MD is a modelling and simulation technique that generates the dynamical trajectories of a system of *N* particles, with mass (m_i), by integrating Newton's equation of motion, with suitable initial and boundary conditions, and proper interatomic potentials, while satisfying the thermodynamical constraints. The equations of motion for the *N* particles can be written as

$$\boldsymbol{F}_i(t) = m_i\boldsymbol{a}_i = m_i\ddot{\boldsymbol{r}}_i(t), \qquad i = \{1,2 \dots N\}, \tag{2.11}$$

where $\boldsymbol{F}_i(t)$ is the force acting on a particle *i* due to the interaction with other atoms at time t, m_i and $\boldsymbol{a_i}$ are respectively the mass and acceleration of atom *i*, and $\boldsymbol{r}_i$ is the position vectors. The force $\boldsymbol{F}_i(t)$ acting on the atom can be obtained from the partial derivative of the potential energy $U(\boldsymbol{r}_1, \boldsymbol{r}_2, \boldsymbol{r}_3, \dots, \boldsymbol{r}_N)$ with respect to atomic coordinates, as shown in equation (2.12).

$$\boldsymbol{F}_i(t) = -\boldsymbol{\nabla}_{\boldsymbol{r}_i} U(\boldsymbol{r}_i) \tag{2.12}$$

The success of an MD simulation depends on the accurate description of the interatomic forces by a potential set. In this thesis, a well-tested many-body potential developed for actinide oxides by Cooper *et al.* [75] is used for the simulations. Once the interatomic potential and the initial conditions are known, the equation of motion can be solved numerically. Although several algorithms have been proposed to solve the equation of motion, the Verlet algorithm [76] is still thought to be the most straight forward algorithm, and this algorithm was implemented in the MD code used in this thesis. The Verlet algorithm can be derived by considering the Taylor expansion of the coordinate of a particle $\boldsymbol{r}_i(t)$, one forward ($t+ \delta t$) and backward ($t- \delta t$) in time, which is given as:

$$\boldsymbol{r}_i(t+\delta t) = \boldsymbol{r}_i(t) + \boldsymbol{v}_i(t)\delta t + \frac{1}{2}\boldsymbol{a}_i(t)\delta t^2 \tag{2.13}$$

Similarly,

$$\boldsymbol{r}_i(t-\delta t) = \boldsymbol{r}_i(t) - \boldsymbol{v}_i(t)\delta t + \frac{1}{2}\boldsymbol{a}_i(t)\delta t^2 \tag{2.14}$$

Adding the two expressions gives

$$\boldsymbol{r}_i(t+\delta t) = 2\boldsymbol{r}_i(t) - \boldsymbol{r}_i(t-\delta t) + \boldsymbol{a}_i(t)\delta t^2 \tag{2.15}$$

The equation (2.15) can be used in an MD simulation to predict the changes in positions of the particles. However, the drawback of the Verlet algorithm is that the velocities of the particles are not directly generated. To overcome this difficulty, the velocity Verlet [77] algorithm is used, the derivation approach is similar to the basic Verlet algorithm but explicitly incorporates velocity, as shown in equation (2.16).

$$\boldsymbol{v}(t+\delta t) = \boldsymbol{v}(t) + \frac{\boldsymbol{a}_i(t) + \boldsymbol{a}_i(t+\delta t)}{2}\,\delta t \tag{2.16}$$

Further, the MD simulation is realized by dividing the time into discrete time steps, not more than a few femtoseconds each. In each time step, the forces acting on each atom are computed using a molecular mechanics force field, and the atoms are moved a little bit, to update the position and velocity of each atom. This process is repeated over and over to simulate the evolution of the systems in a given time. The selection of the system size plays a crucial role in simulating the bulk properties of a macroscopic (infinite) system, and the behaviour of a finite system is very different from the infinite system. Irrespective of how large the system size can be considered in MD simulations, the number of particles would be negligible compared to the macroscopic system. Also, the surface effect is predominant in a finite-size system than in the infinite system. The most common solution to overcome the problems of the finite size of the system and to minimize the surface effect is to use the periodic boundary conditions. In this scheme, the particles are enclosed in a simulation box and replicated throughout the space to form an infinite lattice. When a particle enters or moves out of a simulation box, an imaged particle leaves or enters this region, so that the number of particles in a simulation region is always conserved, as illustrated in Fig. 2.2. Since this work considered the prediction of bulk properties, periodic boundary conditions were used for all the MD simulations.

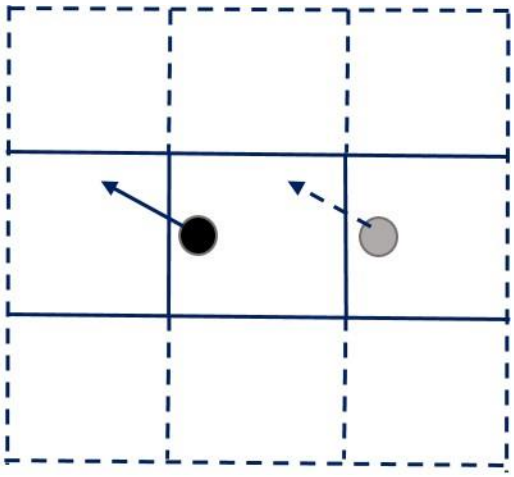

Fig. 2.2. Schematic representation of the periodic boundary condition.

So far, we have discussed the methods to solve the equation of motion and to predict the dynamic trajectories of a system precisely. However, the information about the atomic trajectories needs to be translated into measurable macroscopic properties. The connection between the microscopic simulations and macroscopic properties is made via statistical mechanics, which provides the

mathematical expression that relates the macroscopic properties to the distribution and motion of the atoms of the N-body system. To compute the macroscopic properties, the ensembles of statistical thermodynamics are used.

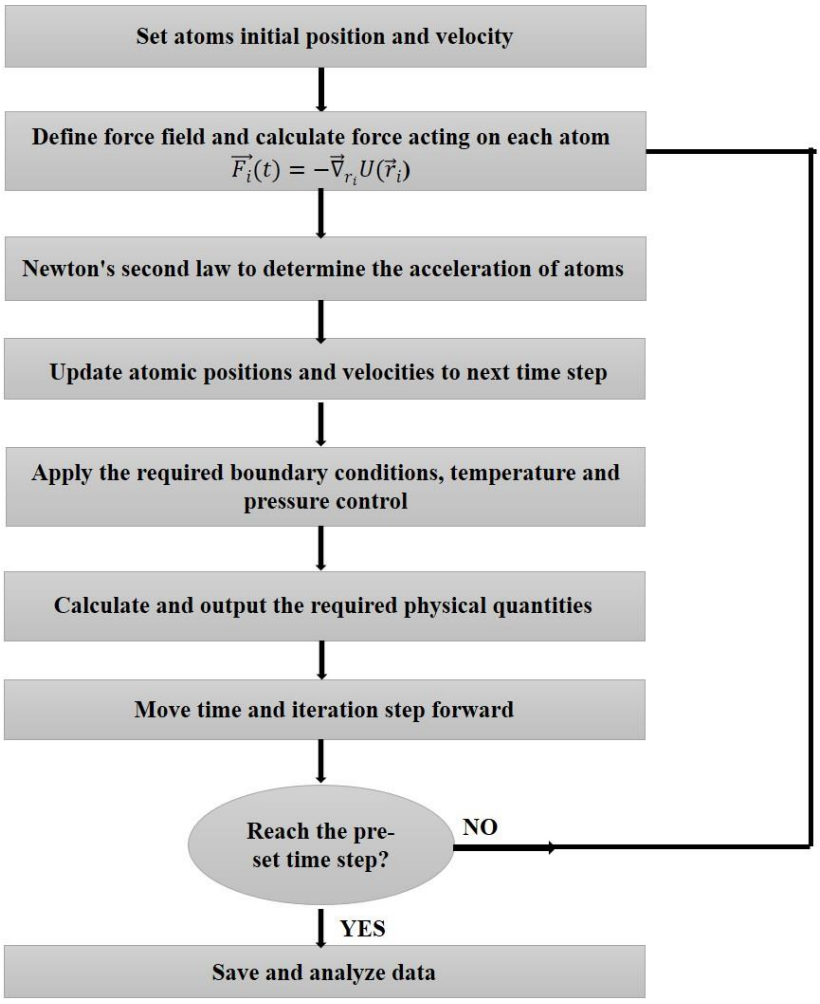

Fig. 2.3. Schematic representation of MD simulation.

In MD simulation, it is implicit that the number of particles (N) and the volume of the simulation box (V) are held constant, and the equation of motion and its numerical implementation are energy (E) conserving. This configuration is a representation of a microstate in the microcanonical ensemble or, commonly known as NVE ensemble. There exist other ensembles that have been used in this thesis, with different characteristics such as the canonical ensemble (NVT), isobaric-isothermal ensemble (NPT) and grand canonical ensemble (μVT) (here T is the constant temperature, P is the fixed pressure and μ is the fixed chemical potential). Ensemble averages give

the bulk properties and based on the ergodic hypothesis one can relate the states of a system sampled over several time steps by MD simulations to the ensemble average. A simplified schematic of the MD simulation is provided in Fig. 2.3.

2.1.7 Introduction to thermal conductivity calculations

The thermal conductivity of ATF is an important material property. Generally, three mechanisms govern the thermal transport in materials: phonons, electrons, and radiation energy. However, in ceramics fuel type, the main contribution to thermal conductivity is by lattice vibrations (phonons) while contributions from electrons and radiation are negligible. Since in this thesis, we were dealing with the ceramic materials the focus was on the lattice contribution to thermal conductivity (k_L). Historically, depending on the mechanisms of phonon scattering, various models have been considered to evaluate the thermal conductivity. The value of k_L for a material can be calculated in different ways that include Slack model [78], Callaway model [79], relaxation time approximation (RTA) [80], and Boltzmann transport equation (BTE) [81]. In this thesis, we calculate k_L using Slack model, BTE and EMD using the Green-Kubo method [82], and the predicted k_L is compared with the experimental data. The methodology to calculate the $k_L$with Slack model has been described in chapter 3 and therefore, is not presented here. Li *et al.* [83] and Carrete *et al.* [84] have recently developed software packages ShengBTE and almaBTE respectively for computing the k_L of bulk crystalline materials based on a full iterative solution to the BTE. We employed the use of ShengBTE and almaBTE to solve the BTE that takes the second and third-order force constants calculated using the ab-initio packages VASP or QE (used here) as the primary inputs. Reference [83] describes the workflow and the methodology for using ShengBTE. In this section, we describe the basic theory used in the prediction of k_L.

2.1.8 Lattice thermal conductivity from Boltzmann transport equation (BTE)

The inputs required to solve the BTE are the second order force constants (harmonic force constant) and third order force constants (anharmonic force constants), which are defined as the second and third derivative of the potential energy (U) with respect to the atomic displacements respectively. The U of the crystal with a unit cell characterized by a vector 'l'and the atomic positions in each unit cell described by the vector 'b', can be expanded in a Taylor series in power of the atomic displacement $u\ (l, b)$ as shown in equation (2.17) [85].

$$U = U_{\mathrm{o}} + \sum_{lb\alpha} \frac{\partial U}{\partial u_\alpha(l,b)} \Big|_0 u_\alpha(lb) + \frac{1}{2} \sum_{lb,l'b'} \sum_{\alpha\beta} \frac{\partial^2 U}{\partial u_\alpha(lb)\partial u_\beta(l'b')} \Big|_0 u_\alpha(lb) u_\beta(l'b') + \frac{1}{3!} \sum_{lb,l'b',l''b''} \sum_{\alpha\beta\gamma} \frac{\partial^3 U}{\partial u_\alpha(lb)\partial u_\beta(l'b')\, \partial u_\gamma(l''b'')} \Big|_0 u_\alpha(lb) u_\beta(l'b')\, u_\gamma(l''b'') \quad (2.17)$$

The second order force constant ($\Phi_{\alpha\beta}(lb, l'b')$) and the third order force constant ($\Phi_{\alpha\beta\gamma}(lb, l'b', l''b''$) are defined as shown in equation (2.18) and (2.19) respectively.

$$\Phi_{\alpha\beta}(lb, l'b') = \frac{\partial^2 U}{\partial u_\alpha(lb)\partial u_\beta(l'b')} \Big|_0 \quad (2.18)$$

$$\Phi_{\alpha\beta\gamma}(lb, l'b', l''b'') = \frac{\partial^3 U}{\partial u_\alpha(lb)\partial u_\beta(l'b')\, \partial u_\gamma(l''b'')} \Big|_0 \quad (2.19)$$

The dynamical matrices for evaluating the phonon density of states is obtained from the second order force constant as follows,

$$D_{\alpha\beta}\left(bb' \Big|_q\right) = \frac{1}{\sqrt{m_b m_{b'}}} \sum_{l'} \Phi_{\alpha\beta}(0b, l'b')\, exp(iq.l') \quad (2.20)$$

where q the wave vector and m is the mass of an atom at a site in the crystal. Further, diagonalizing the dynamical matrix yields the phonon frequencies (ω), which in turn provides the phonon group velocities and heat capacity at a fixed volume (C_v). In this work, the harmonic force constant is calculated using both linear approach (DFPT) [86] and direct approach (Parlinski-Li-Kawazoe method) [87], based on the supercell approach with finite displacement method as implemented in the Phonopy package [88]. From the cubic force constants, the phonon scattering processes are evaluated using Fermi's golden rule, and finally, the $k_L$is calculated using the iterative solutions of the BTE as implemented in ShengBTE. In the approach implemented in ShengBTE, equation (2.21) gives the expression to compute the k_L tensor,

$$k_L^{\alpha\beta} = \frac{1}{N k_B T^2 \Omega} \sum_{\lambda}^{\infty} f_0(\omega_\lambda)[f_0(\omega_\lambda) + 1]\, (\hbar\omega_\lambda)^2 v_\lambda^\alpha v_\lambda^\beta \tau_\lambda \quad (2.21)$$

where Ω is the volume of the primitive cell, α and β are the Cartesian component, x, y, or z. k_B is the Boltzmann constant, ω_λ and v_λ are the angular frequency and group velocity respectively of

mode λ , τ_λ is the relaxation time of mode λ and $f_0(\omega_\lambda)$ is the Bose-Einstein distribution function at equilibrium.

2.1.9 Lattice Thermal conductivity from MD simulation

Generally, there are two approaches used to calculate the k_L using MD: one is the EMD using the Green-Kubo method and the other one is the non-equilibrium molecular dynamics (NEMD) using the Müller-Plathe method [89]. In this thesis, the calculations were carried out using EMD, therefore, the discussion is limited to the Green-Kubo method. The Green-Kubo method is based on the fluctuation-dissipation theorem, which is a statistical physics method used to predict the behavior of a non-equilibrium system by building a quantitative relation between the fluctuations in the thermal equilibrium system and the response of the system to perturbations. The core calculation of this method is the heat current autocorrelation function, details of which can be found in Ref. [90]. And the thermal conductivity is proportional to the integral of the heat current autocorrelation function over time as given in the equation.

$$k_L = \frac{1}{V k_B T^2} \int_0^\infty \frac{\langle \boldsymbol{q}(t).\boldsymbol{q}(0)\rangle}{3} dt \tag{2.22}$$

Where V the volume of the simulation cell, t is time and q is the heat current, defined as

$$\boldsymbol{q} = \frac{d}{dt}\sum_i \boldsymbol{r}_i E_i \tag{2.23}$$

The summation is over 'i' particles in the system, $\boldsymbol{r}$ is the location of a particle and E is its total energy (kinetic and potential). For ease of computation the above equation can be restated as

$$\boldsymbol{q} = \sum_i E_i \boldsymbol{v}_i + \frac{1}{2}\sum_{i,j} (\boldsymbol{F}_{ij}.\boldsymbol{v}_i)\boldsymbol{r}_{ij} \tag{2.24}$$

Where v is the velocity of a particle and $\boldsymbol{r}_{ij}$ and $\boldsymbol{F}_{ij}$ are the distance and force between particles i and j. The first term represents the contributions of convection, and the second term corresponds to the conduction. The $\langle \boldsymbol{q}(t).\boldsymbol{q}(0)\rangle$ is called the heat current autocorrelation function (HCACF). The heat current is a vector that indicated the magnitude and directions of the flow of heat in a system. At equilibrium, the heat current will oscillate, an overtime average to zero. The Green-Kubo approach relates the thermal conductivity to how long it takes for these oscillations to uncorrelated.

2.2 Experimental details of fuel fabrication

2.2.1 Powder blending

For blending of powders for making the composite pellets we used a planetary ball mill (shown in Fig. 2.4), manufactured by Torrey Hills Technologies, LLC U.S.A. Ethanol was used as a process control agent (PCA) to enhance the efficiency of dispersion and blending. The powder was milled for an hour, and the powder-PCA slurry was separated from the jar and ball into a petri dish. Further, the composite powder mixture was dried in a fume-hood. The ball to powder ratio was maintained at 10:1 ratio.

Fig. 2.4. Planetary ball mill.

2.2.2 Fabrication by spark plasma sintering

SPS, also known as plasma-assisted sintering, pulse electric current sintering, and pulse discharge pressure sintering, uses a pulsed direct electric current along with uniaxial pressure [91], with advantages such as lower power consumption, and shorter sintering time [92]. SPS has been proved beneficial for processing a wide variety of materials including ceramics, metals and polymers [93–97]. There are several reports on SPS of alumina [96], SiC [98] and zirconia [99] where SPS was considered superior to other processing techniques. SPS is also used for sintering of nanocrystalline materials [93,100,101], because of the higher heating rate and shorter processing time in SPS, can resist the grain growth [102]. The powder to be sintered by SPS is filled into a graphite die-punch system [103], and the filled die-punch is placed between hydraulic rams. The

die-punch system is heated by the passage of electric current and with the simultaneous application of pressure, the powder particles start to densify. The materials processed under optimal SPS conditions has very high densification rates [93] and the pellets obtained have densities close to the theoretical density [103].

Several mechanisms have been proposed for the high densification rate of SPS [104]. These include the following; the spark theory [105–107], plasma [94,108], Joule heating [109], and electric field enhanced diffusion [105,106]. In the spark theory, the particles are subjected to spark impact pressure, which also heats the surface of the powder particle and facilitates their adhesion. According to the plasma theory, a plasma is formed under the influence of the electric potential, which cleans the surface of the powder particles aiding the sintering process. The principle of Joule heating is also proposed as a reason for high densification observed in SPS for electrically conductive material. However, the major drawback of this theory is that it cannot explain the high densification observed for non-conductive material. According to basic diffusion theories, diffusion is enhanced in the presence of an electric field, thus improving the powder densification. In this work, the specimens were fabricated using the Thermal Technology LLC 10-3 system located at the Kelowna campus of University of British Columbia (shown in Fig. 2.5.).

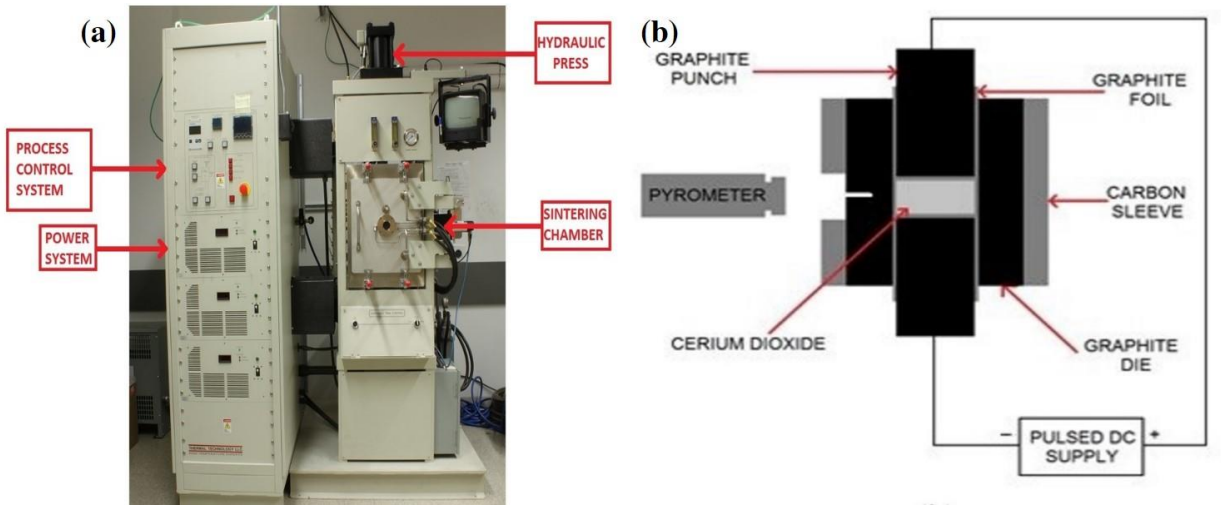

Fig. 2.5. (a) SPS equipment-Thermal Technology LLC 10-3 system, (b) Schematic diagram of SPS sintering.

2.3 Material characterization techniques

2.3.1 X-ray diffraction

X-ray diffraction (XRD) is one of the most powerful non-destructive technique used for the characterization of the crystalline material. XRD can provide information on structures, texture, phase composition, and other structural parameters, such as crystallinity, average grain size in nanomaterials, strain and crystal defect. The XRD is based on the interference of X-rays and the specimen. The X-rays generated by the cathode X-ray tube are filtered to produce monochromatic radiation; the collimated rays are then directed towards the material. Since the wavelength (λ) of X-rays is of the same order of magnitude as the lattice spacing (d) in the samples, the X-rays are diffracted in the material by satisfying the Braggs law, equation (2.25). The diffraction angles of $2\theta_B$ are recorded and used to identify the structure of material.

$$n\lambda = 2d\ sin\theta_B \tag{2.25}$$

In this work, the XRD patterns of the sintered specimens and the powder were obtained using a Bruker D8 Discover XRD with chromium K_α radiation of $\lambda = 2.2898$ Å. The angles of the normal scan were set between 20° to 110° with a step size of 0.01° and a scanning time of 600 sec per step. Fig. 2.6. shows the XRD equipment used in this study, having a Bragg-Brentano geometric arrangement. X'pert high score software has been used for the phase identification and the Nelson-Riley method [110] has been used for lattice parameter measurement.

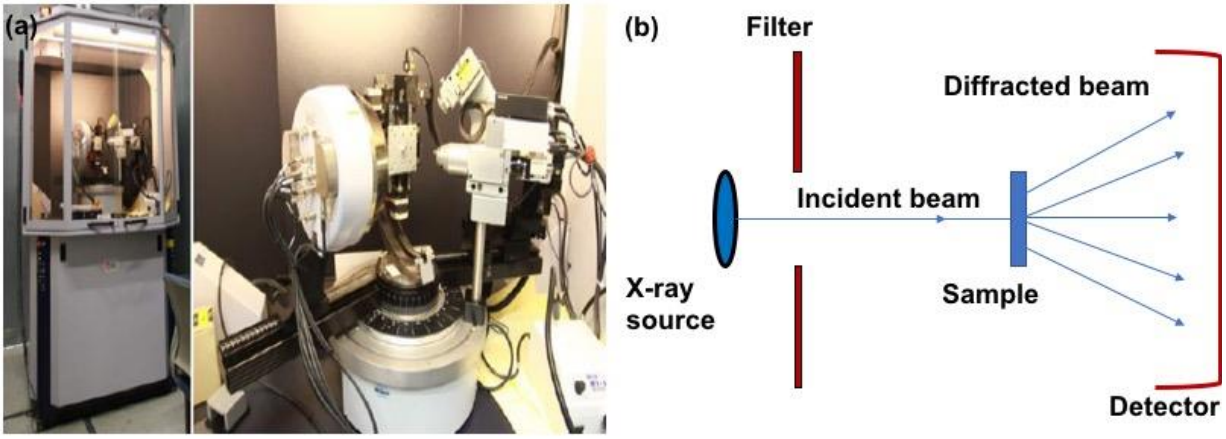

Fig. 2.6. (a) XRD equipment BRUKER D8 Discover, (b) Schematic representation of the basic principle of a XRD.

2.3.2 Scanning electron microscopy/electron backscattered diffraction

The microstructural analysis of the samples was carried out using scanning electron microscopy (SEM). SEM uses a focused beam of electrons to generate a variety of signals from the surface of the specimen. These signals include the secondary electrons (SE), backscattered electrons (BSE), and diffracted backscattered electrons (EBSD), characteristic X-rays (used for elemental analysis), visible light (Cathodoluminescence) and heat. The SE and BSE are used for imaging; SE is used for morphology and topography studies of the samples, whereas, BSE is essential for illustrating the contrasts in compositions in multiphase samples. The EBSD is used to study the texture and grain structure of the materials, and the X-rays are used for elemental analysis. The SEM and the EBSD studies presented in this thesis were carried out by a SU 6600 Hitachi field emission SEM equipped with an Oxford Instruments Nordlys EBSD detector (as shown in Fig. 2.7.). The powders and the polished samples were mounted on aluminum stage using the carbon conductive double-sided tape. The SEM image and the EBSD scans were conducted with an acceleration voltage of 30 kV and a working distance of 9.9 mm. The data was acquired by AZTEC 2.0 data acquisition software in the form of backscattered electrons recorded by the phosphor screen detector, and the post-processing of the obtained scans was done using Channel 5 software by Oxford Instruments.

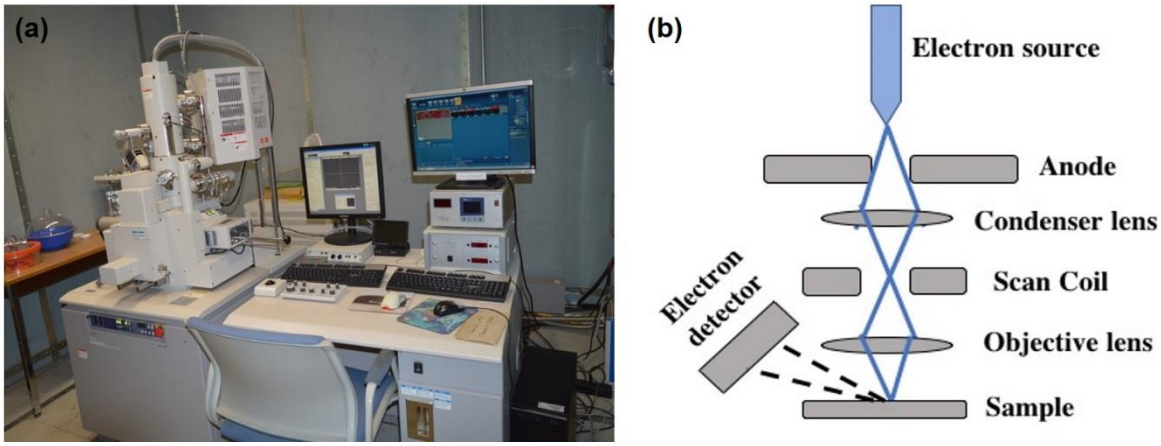

Fig. 2.7. (a) SU 6600 Hitachi field emission SEM equipped with an Oxford Instruments Nordlys EBSD detector, (b) Schematic representation of the basic components of a SEM.

2.3.3 Density measurement

The pellet densities (ρ_s) were measured using the Archimedes principle as follows:

$$\rho_s = \frac{M_a}{(M_a - M_w)} \times \rho_w \tag{2.26}$$

where M_a is the mass of the sample in air; M_w and ρ_w is the weight of the sample in water and density of water respectively.

The relative density of the sintered specimens ρ_s was calculated by using the equation in (2.27), where ρ_t is the theoretical density.

$$\rho_s(\%) = \left(\frac{\rho_s}{\rho_t}\right) \times 100 \tag{2.27}$$

The mass balance used to perform the density measurement is shown in Fig. 2.8. It has to be noted that all the density measurement done in this thesis has been the closed porosity and a minimum of five measurements was taken for each sample, and the average value, was reported.

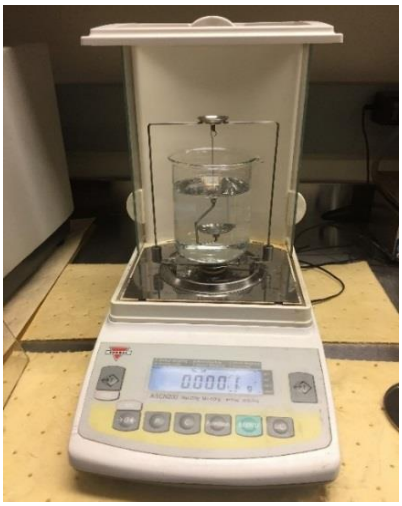

Fig. 2.8. Mass balance from Torbal.

2.3.4 Raman spectroscopy

Raman spectroscopy is based on the principle of inelastic scattering of light. When a particle is irradiated with light of specific frequency, the light is scattered. Some of the scattered photons have the same frequency as that of the incident radiation, and some may contain photon with different frequency. This phenomenon of scattering of light with a frequency change is called the Raman scattering. The frequency change is specific to the molecular vibration and phonon in crystal. Therefore, by analyzing the Raman spectra, it is possible to analyze the composition and

structure of a material. The Raman spectra of the powder and the sintered specimens presented in this thesis were obtained using a Renishaw 2000 Raman Microscope (shown in Fig. 2.9.).

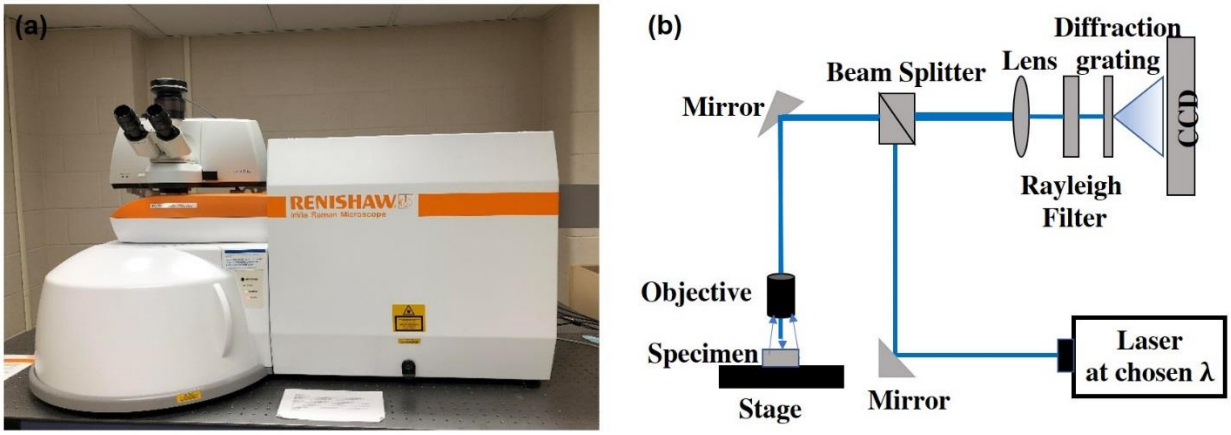

Fig. 2.9. (a) Renishaw Raman microscope, (b) Schematic representation of the basic Raman microscope.

The wavelength of the laser source was 514 nm, and the laser beam was focused with a 100x objective. The scattered light was dispersed with a grating of 1800 lines/mm. The laser power used was 0.01 W. The Renishaw CCD camera collected the scattered laser light. The exposure time was set to 10 seconds, with four accumulation. The samples were analyzed by placing the test specimens on the glass plate without any additional sample preparation.

2.3.5 Thermal conductivity measurement by Laser Flash apparatus

The laser flash method is used to determine the thermal diffusivity (α) and thermal conductivity of the sintered samples. In this method, the specimen to be tested is placed in a furnace with a controlled atmosphere, and the test sample is subjected to a finite impulse of laser energy on the front surface. The heat is then transferred through the sample, causing a transient temperature rise on the rear surface of the specimen.

The temperature rise is recorded with the help of the infra-red (IR) detector placed above the rear surface of the sample and a thermogram which is a plot of rear-face temperature as a function of time is obtained. From the thermogram, the time ($t_{\frac{1}{2}}$) required for the temperature of the rear face to reach half its maximum value is determined. Further, the α of the specimen is given by using the Parkers relations [111], as given in equation (2.28):

$$\alpha = 0.1388 \times \frac{L^2}{t_{\frac{1}{2}}} \tag{2.28}$$

where L is the thickness of the specimen. From the measured α, the thermal conductivity as a function of temperature $(k(T))$ can be evaluated using the relation (2.29):

$$k(T) = \alpha(T) \times \rho(T) \times C_p\,(T) \tag{2.29}$$

where $\rho(T)$ and $C_p(T)$ is the density, and heat capacity at constant pressure as a function of temperature, respectively. The apparatus used for the thermal conductivity measurement was the DLF-1200 from TA-instruments, shown in Fig. 2.10.

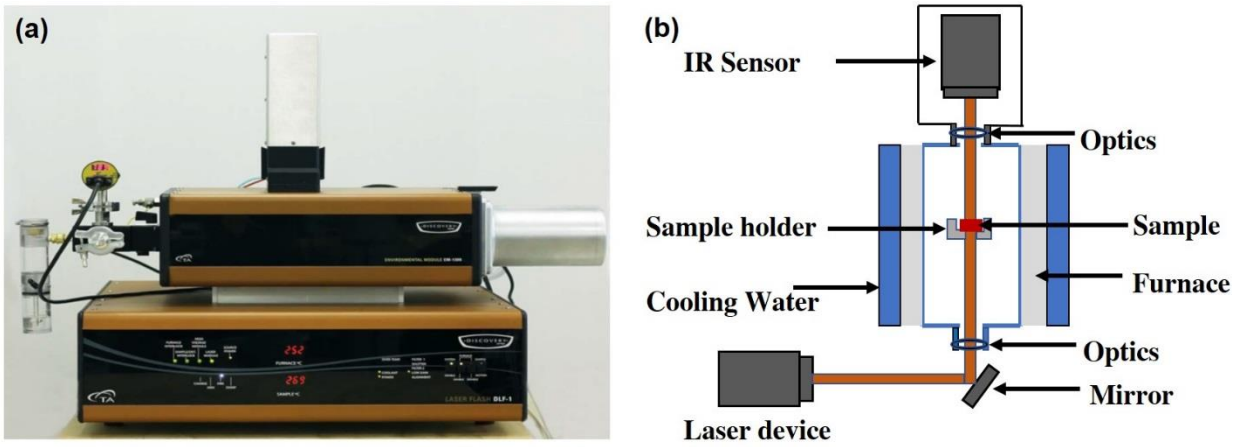

Fig. 2.10. (a) Laser flash apparatus from TA instruments (b) Schematic diagram of basic components of laser flash apparatus.

The measurements were made on cylindrical pellets of diameter 12.7 mm and thickness 2-3 mm. The thickness of the samples was obtained by taking an average of five readings with a standard deviation of 0.01 mm. The samples were prepared by coating the rear and front side with the graphite spray, for better absorption and emissivity of the laser flash. The experiments were performed under the argon atmosphere.

Chapter 3 : Thermal conductivity of bulk and porous ThO_2; Atomistic and Experimental study

3.0 Overview

The thermal conductivity of bulk and porous ThO_2 is determined in this chapter using atomistic and experimental study. The phonon transport properties of ThO_2 were predicted using the *ab initio* calculations unified with the BTE and the EMD simulations using the GK method. An extensive examination of the phonon mode contribution, available three-phonon scattering phase space, and mode Grüneisen parameter were also performed to unveil the underlying mechanism in the thermal transport of ThO_2. The effect of porosity on the thermal conductivity of ThO_2 is also determined by EMD-GK method, and experiments validate the predicted results. Hence, this chapter fulfils a part of the first objective of this thesis of determining the fundamental principles of thermal transport in bulk and porous ThO_2 fuel.

The research findings reported in this chapter have been published as manuscript #1 as follows:

> L. Malakkal, A. Prasad, E. Jossou, J. Ranasinghe, B. Szpunar, L. Bichler, J. Szpunar; "Thermal conductivity of bulk and porous ThO_2: Atomistic and experimental study"; published in Journal of Alloys and Compounds, Vol.798, pp.507-516 (2019). The copyright permission of this manuscript is provided in Appendix B.

The contributions of the PhD candidate are 1) performing DFT and MD calculations, 2) preparing the samples for characterization, 3) performing XRD, SEM, Raman, and EBSD characterizations, 4) measuring of thermal conductivity using Laser flash apparatus, 5) analyzing of the results, 6) writing the manuscript for publication. My supervisors reviewed the manuscript before it was submitted for publication.

The differences between this chapter and the published paper are:

1. The equations to determine the thermal diffusivity and the thermal conductivity using the laser flash apparatus has been removed to avoid repetition, and the equation has been referred to the equation 2.28 and 2.28 in chapter 2.
2. The descriptions of the methodology section have been removed from this chapter to avoid the repetition as this section is covered in chapter 3 of this thesis.
3. The references of the manuscript are listed at the end of this thesis.

Thermal conductivity of Bulk and Porous ThO_2; Atomistic and Experimental study

Linu Malakkal[1], Anil Prasad[2], Ericmoore Jossou[1], Jayangani Ranasinghe[3], Barbara Szpunar[3], Lukas Bichler[2], Jerzy Szpunar[1]

[1]Department of Mechanical Engineering, University of Saskatchewan, Canada

[2]School of Engineering University of British Columbia-Okanagan Kelowna, Canada

[3]Department of Physics and Engineering Physics, University of Saskatchewan, Canada

3.1 Abstract

Thorium dioxide (ThO_2) is proposed to play a vital role in the worlds future energy needs and is considered a better and safer alternative to the currently used nuclear fuel; uranium dioxide (UO_2). Thermo-physical properties of ThO_2 is superior to UO_2, but the fundamental physics governing the thermal transport of ThO_2 is still ambiguous, and the available data for the thermal conductivity (k) of ThO_2 is scattered. Therefore, in this article, a systematic investigation regarding the lattice thermal conductivity (k_L) of the bulk and porous ThO_2 is carried out theoretically and validated with experiments. The phonon transport properties were performed using two different approaches the *ab initio* calculations unified with the Boltzmann transport equation (BTE) and the equilibrium molecular dynamics (EMD) simulations using Green Kubo (GK) method. An extensive examination of the phonon mode contribution, available three-phonon scattering phase space, mode Grüneisen parameter, and mean free path (MFP) distributions were also performed to unveil the underlying physics in the thermal transport of ThO_2. The effect of porosity on the k_L by measurements and molecular dynamics (MD) simulations was explored. The measurements were performed on specimens with different porosity, that were prepared by spark plasma sintering (SPS) using the laser flash (LFA) technique. The results obtained demonstrated that the k_L values predicted by both the BTE and the EMD simulations were in excellent agreement with our experimental measurements. Moreover, the model to simulate the 95% TD using MD simulations also captured the decrease in thermal conductivity with porosity and agreed well with the measured results for 95% TD dense sintered pellets.

3.2 Introduction

Thorium dioxide (ThO_2, also known as thoria) is one of the nuclear fuels considered in Generation *IV* nuclear reactors. ThO_2 has better thermo-physical properties such as higher melting point,

higher thermal conductivity and lower coefficient of thermal expansion, making ThO_2 an attractive alternative to UO_2 [51]. Additionally, ThO_2 exist in nature as Th–232 isotope has higher absorption cross-section for thermal neutrons (7.4 barns) compared to U-238 (2.7 barns). ThO_2 is also relatively inert, does not oxidize, and has higher resistance to radiation damage than UO_2 [51]. The fission product release rate for ThO_2–based fuels is one order of magnitude lower than UO_2. ThO_2 is more proliferation resistant and produces less transuranic elements than uranium-based fuels. Apart from being a nuclear fuel, ThO_2 is also used in other application such as welding electrodes and heat resistant materials [112,113]. Since thermal conductivity (k) is a critical property that governs the heat transport in the reactor core and other applications, it is essential to understand the fundamental physics governing the thermal transport in ThO_2-based materials. Although several experimental and theoretical studies have reported the k_L of ThO_2, the values reported remains ambiguous. The widely accepted correlation for k_L of ThO_2 provided by, Bakker et *al.*[114], $\lambda = (A + BT)^{-1}$(where A= 4.20×10^{-4} mKW^{-1}, B=2.25×10^{-4} mW^{-1} and T is temperature in K for the thermal conductivity of 95 %TD dense ThO_2, is based on the experimental work performed by Murabayashi [115], McElroy *et al*. [116], Koenig [117] and Springer *et al.* [118]. Other researchers [119,120] who used thermal diffusivity measurements have reported k_L of ThO_2 ranging from 10.0 – 16.0 W/mK at 300 K. For example, Pillai and Raj [121] reported values of 11.0 W/mK at 300 K using the steady state axial heat flow apparatus. Other experimental studies by Saoudi *et al.* [122], Yang *et al.* [123], Ghosh *et al.* [124,125] Cozzo *et al.* [126], and Kutty et al. [127] are provided in the table below.

Table 3.1. Conditions of the thermal conductivity measurements for ThO_2 from literature.

Temperature (K)	TD (%)	Thermal conductivity (W/mK)	Authors	Year
300-1700	95.0	8.63 (526 K)	Saoudi *et al.* [122]	2018
300-1500	95.0	8.05 (472 K)	Yang *et al.* [123]	2017
873-1873	95.0	unknown	Ghosh *et al.* [124,125]	2015
500-1500	95.0	8.00 (500 K)	Cozzo *et al.* [126]	2010
400-1780	92.03	10.5 (500 K)	Kutty *et al.* [127]	2008
310-1220	unknown	8.20 (500 K)	Pillai *et al.* [121]	2000

From a theoretical perspective, the predictions of thermal conductivity are mainly limited to the use of Slack method [128] and non-equilibrium molecular dynamic (NEMD) [89] calculations. The Slack model and the potentials of the NEMD simulations rely on the fitting parameters and therefore lacks predictive power, leading to a variation between 12.0 W/mK and 20.0 W/mK in the k_L values of ThO_2 at 300 K. For example, Xiao *et al*. [129], Lu *et al.* [130] and Szpunar *et al.* [131] have simulated the k_L of ThO_2 using the Slack method at 300 K and obtained values of 13.0 W/mK, 12.0 W/mK and 16.0 W/mK respectively. Researchers using molecular dynamics have also calculated k_L of ThO_2. For instance, Ma *et al*. [132] (equilibrium molecular dynamics (EMD)), Behera and Deo [133] (NEMD), Cooper *et al.* [134] (NEMD) and Rahman *et al*. [135] (NEMD) predicting the thermal conductivity at 300 K as respectively 16.5, 22.0, 12.0 and 19.8 W/mK. It is noted that the MD simulations do not account for the quantum mechanical effect and therefore, the k_L values at low temperature are overpredicted. Recently, Liu *et al.* [136] reported on the thermal conductivity of ThO_2 estimated by solving BTE using the second order force constant from displacement method and have predicted k_L at 300 K to be 12.4 W/mK; underpredicted by ~25% in comparison with experimental results. As a result, throughout the literature, the thermal conductivity value of ThO_2 is scattered. To resolve this aberration, we perform an *ab initio* calculation using density functional theory (DFT) [64,65], density functional perturbation theory (DFPT) [86] in synergy with the Boltzmann transport equation (BTE) as implemented in ShengBTE code [83]. The *ab initio* calculations provide us with an insight into the underlying physics of the thermal properties including the phonon phase space, mode Grüneisen parameter, group velocity, phonon mean free path and the mode wise thermal conductivity of ThO_2.

The *ab initio* calculation gives information about the thermal transport of a defect-free single crystal ThO_2 whereas, the experimental samples are polycrystalline and porous having a significant influence on the thermal conductivity of manufactured fuel pellets. The optimum density of a fuel pellet in the reactor core is 95% TD. Hence, it is essential to determine the effect of porosity on k_L of ThO_2 quantitatively. Previously, using MD simulations, Ghosh *et al.* [124,125] and Arima *et al.* [137] predicted the k_L of 95% TD ThO_2 by applying a correction (using Maxwell-Eucken equation) to the calculated values for 100% TD. In addition, Park *et al.* [138] also studied the effect of 0.1%, 1% and 5% oxygen vacancy, 0.1%, 1% and 5% thorium vacancy and uranium

substitutional defect. However, simulations focusing on the effect of the 5% porosity on the k_L of ThO_2 is absent. Therefore, in this work, MD simulations were carried to find the effect of porosity on the k_L of ThO_2 considering two cases with the cell sizes of $10 \times 10 \times 10$ and $20 \times 20 \times 20$. To further validate our theoretical predictions, measurements of thermal conductivity using laser flash apparatus were conducted on samples with varying density prepared by spark plasma sintering (SPS) technique.

3.3 Computational and experimental methods

3.3.1 Computational details

All the first principles calculations were performed using the DFT technique [64,65] as implemented in the open source Quantum ESPRESSO [73] code. The pseudopotential used for both the thorium (Th) and oxygen (O) were norm conserved. The electronic exchange-correlation for O (taken from the pseudopotential library) is based on the generalized gradient approximation (GGA) with the Perdew, Burke, and Ernzerhof functional (PBE)[139]. However, for Th, the pseudopotential generated by Daroca *et al.* [140] using the atomic software of the Quantum ESPRESSO package was used. Geometry optimization evaluates the structural properties at zero Kelvin temperature by minimizing the total energy by varying both cell parameter and atom positions. We obtained the total energy convergence of ThO_2, using an electron wave vector grid and the plane wave energy cutoff of 250 Ry and 8×8×8 respectively. The criteria for the electronic energy convergence and the force convergence was respectively set a value of 10^{-12} eV and 10^{-7} eV/Å.

3.3.2 Details of the BTE calculations

In this work, the harmonic force constant is calculated using linear approach (DFPT) [86]. To obtain the converged phonon properties, the calculations of the harmonic force constant were done using a *q*-point mesh of 6×6×6 (phonon dispersion for different q-points are shown as, (Fig. 3.1.a)). The calculation of the third order force constants was performed on a 4×4×4 supercell, and the force cutoff distance was set to the fifth nearest neighboring atoms (n). The convergence of the k_L with respect to the number of q-points used in the second order force constant, and the number of grid planes (N) along each axis in the reciprocal space for solving the BTE is detailed in Fig. 3.1. The converged k_L values were obtained using a q-point of 6×6×6, number of neighboring atoms as five and the N-grid as 22×22×22. From the cubic force constants, the phonon scattering

processes are evaluated using Fermi's golden rule, and finally, the k_L is calculated using the iterative solutions of the BTE as implemented in ShengBTE [83]. The k_L presented in this work are the fully iterative solution of the Peierls-equation. ThO_2 being a polar material, the non-analytical contribution was considered, and the Born charges and the dielectric constant required to evaluate the non-analytical contribution[141] (nac) were calculated using the DFPT.

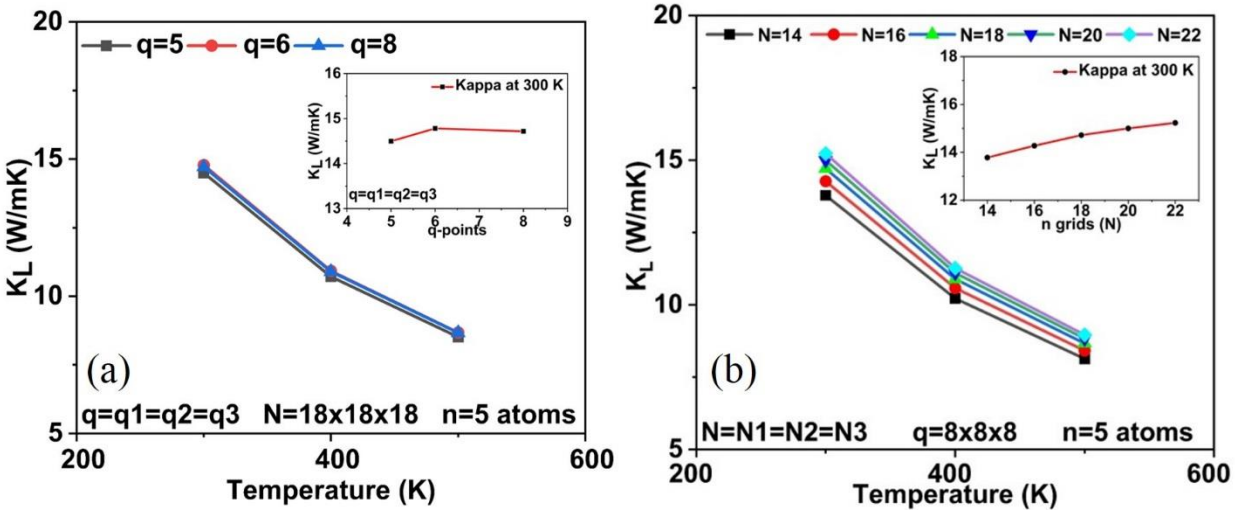

Fig. 3.1. Convergence of the k_L with respect to (a) the q-points considered for the second order force constants (by maintaining n=5 and N=18×18×18 for all the cases); (b) the number of grid planes along each axis in reciprocal space for solving the BTE (by considering q= 8×8×8 and n=5 for all the cases).

3.3.3 Details of the EMD calculations for bulk and porous ThO_2

For MD simulations, we used the EMD techniques together with the Green-Kubo linear response formalism [90] as implemented in LAMMPS (Large-scale Atomic/Molecular Massively Parallel Simulator) MD simulation code [142]. The Green-Kubo formalism uses the heat current autocorrelation function (HCACF) which decay along a direction as described in Ref. [90]. The HCACF at 300 K for a system build on 10×10×10 and 20×20×20 unit cells decayed to zero when the correlation length reaches 20 ps as shown in Fig 3.2. In this work, the k_L of ThO_2 by MD simulations were carried out on systems of size 8×8×8 (6144 atoms), 10×10×10 (12000 atoms), 12×12×12 (20736 atoms) and 20×20×20 (96000 atoms), using the Embedded Atom Many-body (EAM) potentials developed by Cooper *et al*. [75]. Table 3.2 shows a variation of 6% in the k_L values at 300 K when the supercell size is varied from 8×8×8 to 20×20×20. However, at 300 K, the difference in k_L values when the supercell size was varied between 10×10×10 and 20×20×20

is less than 1 %, suggesting that the 10×10×10 system is sufficient enough to represent all the phonon modes available to reproduce the phonon-phonon scattering present in bulk ThO_2 [143]. For investigating the porosity influence on the k_L of ThO_2, two cases with the cell sizes of 10×10×10 and 20× 20×20 were considered.

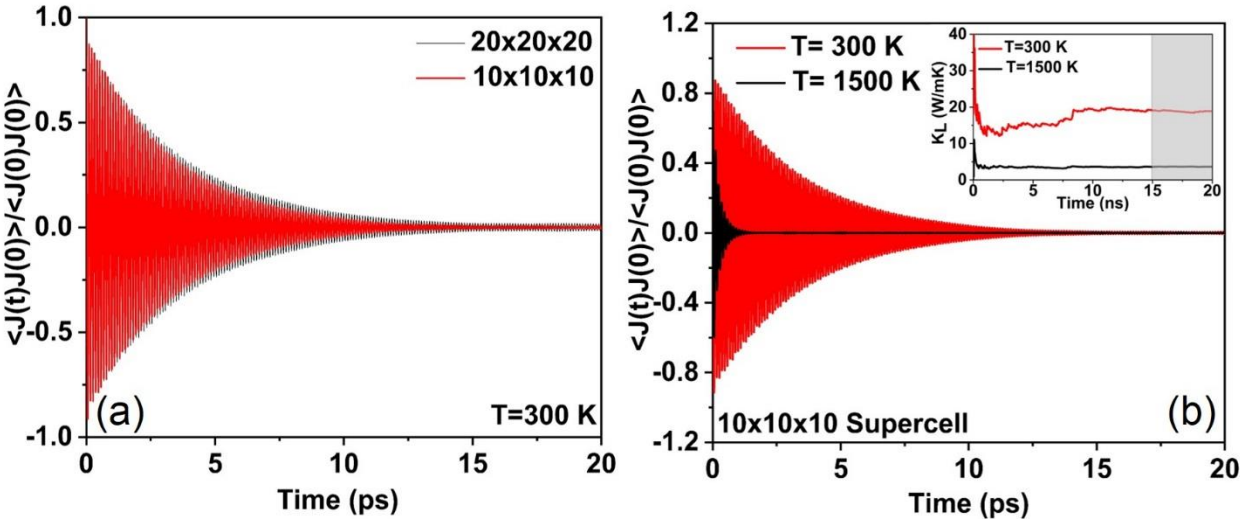

Fig. 3.2. (a) The HFACF for ThO_2 at a temperature of 300 K with a system size of 10×10×10 (blue lines) and 20×20×20 (black lines) unit cells. (b) The HFACF for ThO_2 at a temperature of 300 K (blue line) and 1500 K (red line) with a system size of 10×10×10 unit cells; inset shows the k_L fluctuations with time and the shaded region indicates the time range over which the HCACF integral is averaged to predict the k_L.

In each of the supercells, only one pore was introduced by manually removing 5% of atoms, in such a way that for every thorium atom two oxygen atoms are considered, to maintain the charge neutrality of the system.

Table 3.2. The size dependence of k_L of bulk ThO_2 at a temperature of 300 K presented using EMD simulation and the Green-Kubo method.

Size of the supercell	Number of atoms	Thermal conductivity (W/mk) at 300 K
8×8×8	6144	18.90
10×10×10	12000	17.93
12×12×12	20736	18.35
20×20×20	96000	17.77

To predict the k_L of ThO_2, the Verlet leapfrog algorithm was implemented [76]. Further, the system was first simulated in a constant number of atoms, pressure, and temperature (NPT) ensemble for 6 ns to ensure it reached equilibrium at the desired temperatures, then the ensemble was switched to a constant number of atoms, volume, and temperature (NVT) ensemble and ran for 6 ns. The heat current autocorrelation function (HCACF) were estimated along with an NVE ensemble calculation which generates a 20 ns raw heat current data at every calculation. Finally, the k_L value was computed by averaging the k_L over the time range where the fluctuations were minimal as shown in the inset of Fig. 3.2.b.

3.3.4 Details of the experiments

The commercial ThO_2 powder was supplied by IBILABS, U.S.A. These powders were then characterized by the x-ray diffraction (XRD) and scanning electron microscopy (SEM). The powder XRD (compared well with JCPDS file 042-1462) revealed a single-phase face centered cubic structure with the lattice parameter as 5.60 Å. The SEM micrograph (Fig. 3.3.a) of the commercial powder indicates that the particle has a square shaped morphology and the size has ranged between 1 μm and 6 μm.

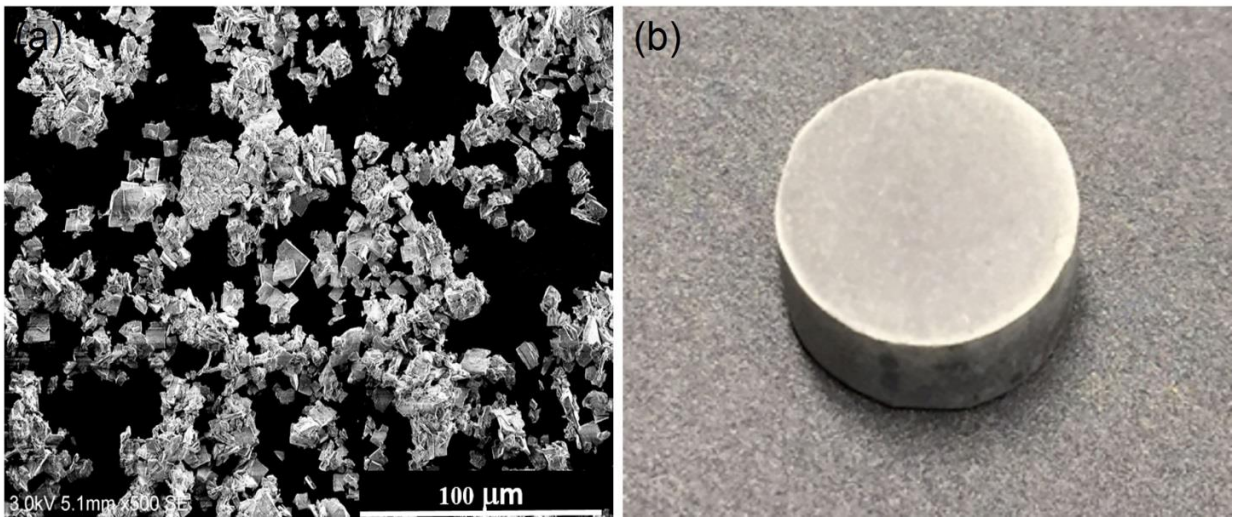

Fig. 3.3. (a) SEM image of ThO_2 powder (b) SPS sintered ThO_2 (98±0.5% TD) pellets of diameter 12.5 mm × 4 mm thickness. Sintering was done at 1700 ^oC, 50 MPa, and 10 min.

The as-received powder was sintered in argon atmosphere using a Thermal technology LLC 10-3 spark plasma sintering system located at UBC (Kelowna, BC). Graphite tooling was used for SPS to fabricate a pellet of 12.7 mm diameter and 4 mm height. Graphoil was used at powder tooling

interface to reduce friction and reaction between powder and tooling. The temperature of the sintering die during the experiment was recorded using an optical pyrometer at a point 4 mm away from the surface of pellet.The two samples considered in this work has been sintered at two different temperature of 1600 ^{o}C and 1700 ^{o}C, while maintaining all other sintering parameters such as sintering pressure, hold time, heating and cooling rate as 50 MPa, 10 min and 100 ^{o}C/min respectively.

After sintering the pellets were ground using 500 grit sandpaper to remove the residual graphite foil. XRD analysis were carried out to identify residual carbon or the formation of carbides or intermetallic during the SPS sintering. The Archimedes' method was used to determine the density of each pellet by immersing the pellets in to the distilled water at room temperature. The sample was polished to mirror finish surface by grinding the pellets with silicon carbide papers up to 4000 grits followed by polishing with 3μm MD mol cloth with 3 μm MD mol suspension and 1 μm MD Nap cloth with 1 μm MD Nap suspension. The polished pellets were subjected for the microstructural and textural studies using SEM, and electron back-scattered diffraction (EBSD) method using a SU 6600 field emission-scanning electron microscopy. The thermal diffusivity and thermal conductivity of the pellets with different density were measured using the laser flash technique. The samples are coated with the graphite spray for better absorption and emissivity of the laser flash. Laser flash technique records the thermal diffusivity (α) of the specimens using the Parkers relations [111] given as shown in equation (2.28). From the measured α, the thermal conductivity as a function of temperature ($k\ (T)$) can be measured using the relation (2.29). The thermal conductivity measurements were made on cylindrical pellets of diameter 12.7 mm and thickness 2-3 mm. The thickness used for the measurement of thermal diffusivity of the samples were an average of five readings with a standard deviation of 0.01 mm.

3.4 Results and Discussion

3.4.1 Crystal structure and elastic constants from ab-initio calculations

ThO_2 has a fluorite structure with three independent atoms per unit cell and belongs to the space group of Fm-3m (225), as shown in Fig 3.4. The equilibrium lattice constants were obtained by minimizing the total energy with respect to the lattice parameter and atomic positions. Table 3.3. presents the calculated lattice constant (a), bulk modulus (B) and stiffness constants (C_{ij}) of ThO_2 in comparison with the values from the previous DFT calculations and the experiment. The PBE

functional predicted the lattice constant within an error less than 0.07% compared with the experimental data reported by Idiri *et al.* [144]. The PBE functional was able to quantify the ground state structural properties accurately compared to other pseudopotentials available in the QE repository [145]. The elastic constants provide the information about the important properties of a material such as stiffness, strength, mechanical stability, hardness, and ductility or brittleness [146]. The single crystal stiffness constants of ThO_2 by using a stress-strain method with the help of our in-house interface qe-nipy-advanced [74]. The mechanical stability of the system can be verified with the following Born's mechanical stability criteria [147] $C_{11} - C_{12} > 0, C_{11} + 2C_{12} > 0, C_{44} > 0$, the predicted stiffness constants have satisfied these conditions, indicating the system is mechanically stable.

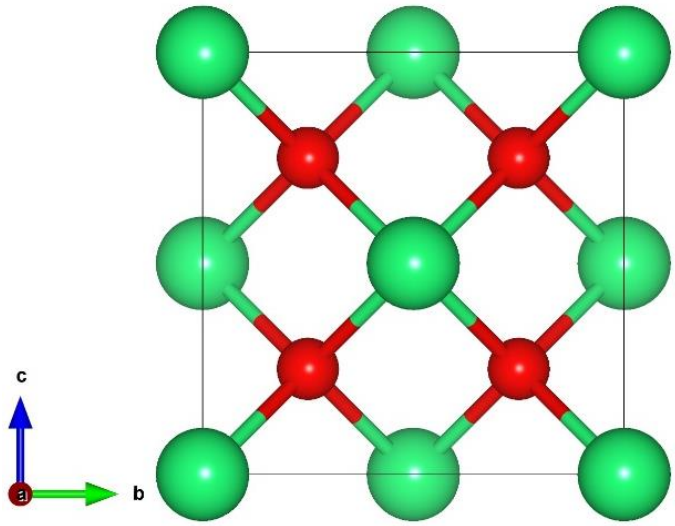

Fig. 3.4. Crystal structure of ThO_2 in the conventional cubic unit cell (green and red represent Th and O atoms respectively.

From the calculated stiffness constants, the polycrystalline bulk modulus, shear modulus (G),Young's modulus (Y) and Poisson's ratio (η) (Table 3.3) were determined using the Voigt-Reuss-Hill approach. From Table 3.3. the bulk modulus values (186 GPa) at zero temperature obtained from PBE method is only ~4% lower than the experimental value of 193 GPa [148] at room temperature. Since this PBE functional pseudopotentials predicted the structural and mechanical properties in excellent agreement with the experimental data, the same PBE functional pseudopotentials were used for the study of phonon properties and the k_L of ThO_2.

Table 3.3. Lattice parameter (a_o) (in Å), bulk modulus (B_o) (in GPa) and stiffness constants (C_{ij}) (in GPa) are given in comparison to previous experimental and theoretical results.

	a_o	B_o	C_{11}	C_{12}	C_{44}	Y	G	η
This work	5.604	186	354	107	75	237	92	0.292
Szpunar *et al.* [149]	5.610	188	352	105	71	222	85	0.30
Lu *et al.* [130]	5.619	190	351	107	74	–	–	0.293
Wang *et al.*[150]	5.62	191	350	111	71	227	87	0.302
Kanchana *et al.*[151]	5.61	198	376	110	68	244	94	0.299
Sevik *et al.*[152]	5.60	216	381	134	106	–	–	–
Idiri *et al.* [153]	5.6	–	–	–	–	–	–	–
Olsen *et al.* [154]	5.598	195	–	–	–	–	–	–
Clausen *et al.* [155]	–	223	377	146	89	–	–	–
Macedo *et al.* [148]	–	193	367	106	79	–	–	–
Phani and Sanyal [156]	–	–	–	–	–	–	–	0.284
Phani and Niyogi [157]	–	–	–	–	–	248	100	–

3.4.2 Lattice dynamics

Theoretical prediction of the lattice dynamics is critical for understanding the thermal properties of crystalline solids at finite temperatures. For instance, from the phonon properties of a material not only predict the thermal conductivity of the materials but also gives insight in to the other thermodynamic properties such as thermal expansion coefficient (α),heat capacity at constant volume (C_v), and entropy (S). Moreover, the fundamental reasons for unique thermal characteristics of a material can be ascertained by analyzing the phonon scattering mechanism through phonon group velocities, and phonon mean free path, relaxation time and phonon scattering phase space [158]. In this work, the phonon dispersion of ThO_2 is evaluated using the DFPT [159] and Fig. 3.5.a shows the calculated phonon dispersion spectra along the Γ-X-Γ-L high symmetry points in the Brillouin zone for two different q-points in comparison with the known experimental data generated by Clausen K *et al*. [155].

Since ThO_2 has three atoms in the primitive unit cell, it has three acoustic mode phonons and six optical phonons. The group theory analysis gives the decomposition of the zone centre modes as

doubly degenerate transverse optical (TO) mode, the triply degenerate Raman active mode and the non-degenerate longitudinal optical (LO) mode. The three-zone center frequencies are 8.42 (8.22), 13.03 (13.98), and 15.93(17.09) THz respectively (shown in brackets are the experimental value from the Ref. [155]). ThO_2 is a polar material and due to polarization effect there is the partial lifting of degeneracy between the LO and TO phonons at the Brillouin zone centre as shown in Fig. 3.5.a. In addition, the Born effective charges, Z^*_{Th} =5.405 (5.37) Z^*_O =2.702 (2.68), agrees well with the values reported (shown in brackets) by Xiao *et al.* [129] The calculated dielectric constant value 4.796 (4.83) was in reasonable agreement with the work done by Lu *et al.* [130]. Fig. 3.5.b, shows the partial and total phonon density of states of ThO_2. Th atoms dominate the frequency vibrations lower than 7.0 THz are dominated by Th ions and the higher frequency vibrations came from the vibrations of O ions. There exist no frequency gap between the optical and acoustic phonons, indicating that three phonon scattering is dominant resulting in relatively lower phonon relaxation time thereby leading to lower k_L.

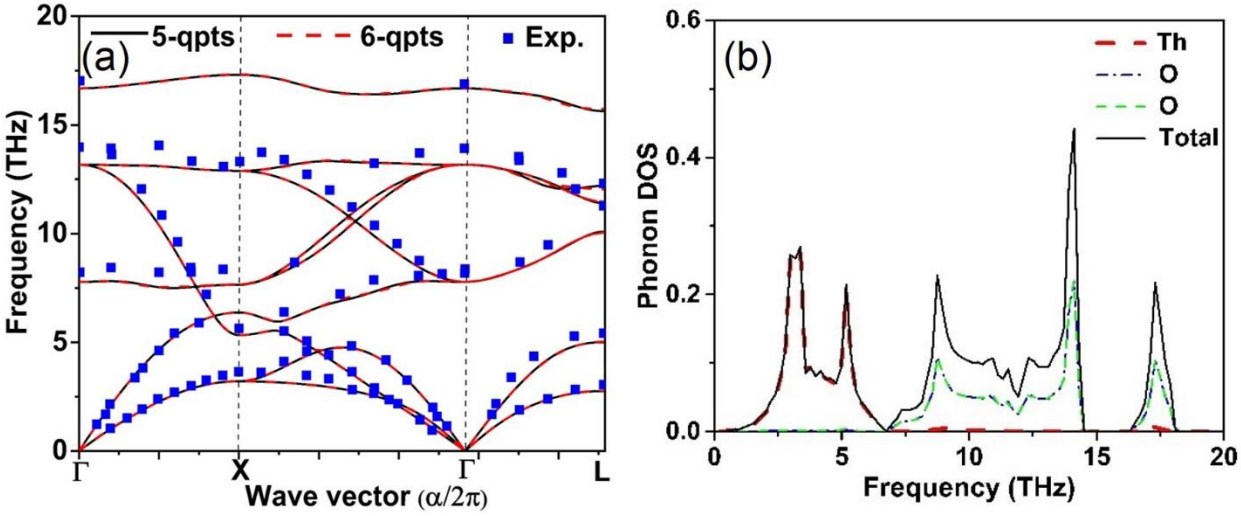

Fig. 3.5. (a) Simulated phonon spectra of ThO_2 by the linear response approach with two different q-point meshes, 5×5×5 (black solid line) and 6×6×6 (dashed red line) compared with the experiment done by Clausen K *et al.* [155] (blue dots) and (b) Partial (dotted lines) and total phonon density of states (solid green line).

3.4.3 Three-phonon scattering phase space and Grüneisen parameter of ThO_2

The number of scattering channels available for a phonon being scattered is quantitatively described by three-phonon scattering phase space (P_3) [160]. The available P_3 gives an insight into the k_L of a material, i.e. larger available P_3, will have more channels for scattering and

subsequently lower k_L. To gain a quantitative understanding of available P_3 on k_L, the total volume in phase space for three-phonon processes (P_3_total) for ThO_2 is compared with our previously reported results such as silicon carbide (420 W/mK at 300 K) [161] a relatively higher k_L material and CeO_2 (16.71 W/mK at 300 K) a material with similar k_L. The P_3_total (in units of 1/rad/ps) predicted along the same Brillioun path is higher for ThO_2 ($4.36x10^{-3}$) than CeO_2 ($4.18x10^{-3}$) and SiC ($1.66x10^{-3}$); clearly indicating that ThO_2 has a larger three phonons scattering phase space, more channels for scattering and hence lower thermal conductivity than SiC and CeO_2.

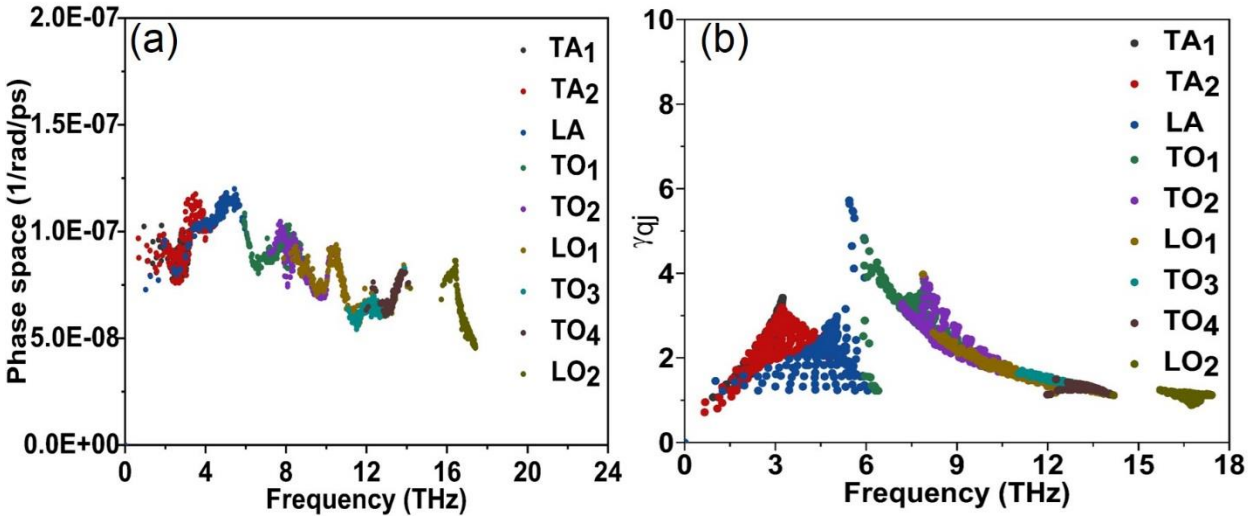

Fig. 3.6. (a) Three-phonon scattering phase space available for ThO_2 (b) mode Grüneisen parameter (γ_{qj}).

Grüneisen parameter (γ) illustrates the anharmonicity in a crystal and determines the strength of each scattering channel and the efficiency of each phonon mode in heat conduction is inversely proportional to the square of Grüneisen parameter, indicating that larger the Grüneisen parameter lower the k_L. According to Fig. 3.6.b, all the mode Grüneisen parameters are positive indicating volume expansion. At 300 K temperature, the average Grüneisen coefficient over the whole frequency range was 2.11 for ThO_2, similar to the average Grüneisen coefficient of the popular surrogate CeO_2. The mode Grüneisen parameter near 7.0 THz (near the TO mode) was higher, indicating that the optical mode scatters the acoustic phonons, thus causing hindrance to heat conduction

3.4.4 Thermal conductivity and mode contribution of bulk ThO_2

Fig. 3.7.a shows the full iterative solution of BTE (black line) for ThO_2 in comparison with our

experimental (red line) and EMD-GK (blue lines) studies. As expected, the k_L of ThO_2 decreases with increasing temperature from 300 K to 1500 K, because the phonon-phonon scattering dominates at high temperatures. The k_L at 300 K is 15.37 W/mK and is in close agreement (~9.5% underpredicted) with the experimental data of 17 W/mK (corrected to 100% TD using the formulation provided in Ref. [162]). Furthermore, the difference in k_L values obtained through our theoretical prediction and the previously reported simulated value of 12.40 W/mK (under prediction by 27%) at 300 K by Liu *et al.* (using BTE) clearly indicate the need for optimizing the parameters considered for the calculations of the second order (from finite difference (FD) method) and the third order force constants. The detailed description of the dependence of k_L on various system parameters is already described in Fig. 3.1. Fig. 3.7.a also shows the k_L value of ThO_2 from 300 K to 1500 K (at an interval of 200 K) predicted by EMD by considering a supercell size of 20×20×20. The values predicted from EMD is also in excellent agreement with the experiments. These accurate theoretical predictions enable us to not only arrive at a rational expression for the porosity correction, but also in the DFT simulations of the mixed oxides.

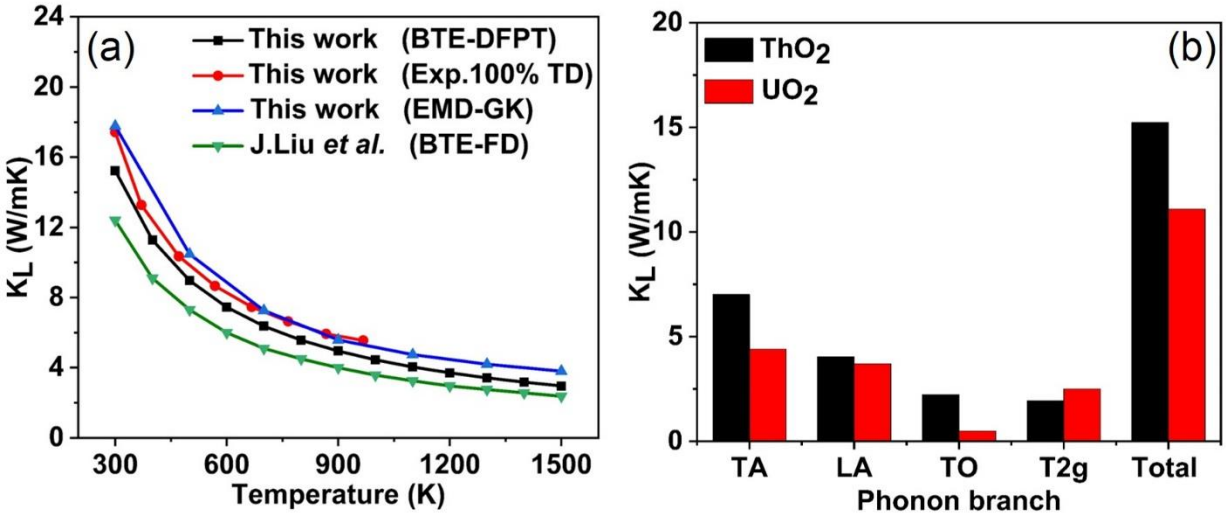

Fig. 3.7. (a) The temperature dependence of the phonon k_L in ThO_2 using BTE, EMD and experiment compared to previous theoretical [129] and experimental values of k_L. (b) The mode-wise k_L of ThO_2 in comparison with the simulated results for UO_2 by Pang *et al.* [163].

Furthermore, the relative contribution of the acoustic and optical phonon modes to the total k_L of ThO_2 was examined Fig. 3.7.b shows the simulated contribution of mode-wise k_L of ThO_2 compared with UO_2 at room temperature previously calculated by Pang *et al.* [163]. In ThO_2 the optical phonons contribute to about 30% of the total k_L compared to the acoustic modes. The

optical contributions at 300 K from the doubly degenerate transverse optical mode (TO), the triply degenerate Raman active mode (T2g) and the non-degenerate longitudinal optical modes are 14.2%, 14.5%, and ~1%, respectively. The theory predicts that like UO_2, ThO_2 will also have strong optical mode contribution to k_L. However, in the case of UO_2, Pang *et al.* [163] have experimentally proved that the contribution of the TO branch to thermal conductivity is, in fact, higher than results from theory. Our theoretical predictions suggest an even more significant contribution of the TO branch towards thermal conductivity of ThO_2, thus warrants an experimental validation.

3.4.5 Thermal conductivity of porous ThO_2 using MD simulations

For the investigation of the effect of pores on the k_L of ThO_2 two different cases were considered. In the first case a supercell of 10×10×10 (12,000 ions) unit cells with a single pore of 2.3 Å radius was simulated. In the second case a supercell 20×20×20 (96,000 ions) unit cells with a single pore of 4.6 Å radius was simulated. In both cases the porosity was maintained at 5%. As a result of periodic boundary condition the separation between the center of pores in the first case and the second case is 54 Å and 108 Å respectively. To model the effect of porosity the distance between the pores should be sufficiently greater than the mean free path of the material for the given temperature. Previously, it was reported that 75% of the total k_L at 300 K is contributed by phonons with a MFP below 79.34 nm, which indicate that the distance between the pores at 300 K should be sufficiently larger to avoid the effect of nanostructuring. Hence it is important that we have a large supercell to demonstrate the effect of porosity.

Fig. 3.8 compares the predicted k_L values of ThO_2 using MD for a pure crystalline ThO_2 (black line, on a supercell of size 20×20×20) and porous ThO_2 modelled on two different supercells of size 10×10×10 (blue line) and 20×20×20 (black line). It is evident from the Fig. 3.8.a, compared to the pure crystalline ThO_2 at 500 K the k_L predicted for a porous ThO_2 on a 10×10×10 supercell has reduced by 42%, whereas the same amount of porosity created on a 20×20×20 supercell decreased the k_L by 18%. The reason for the significant reduction of k_L for the 10×10×10 case can be attributed to the increased phonon scattering on the surface of the pores due to the decreased average distance between the pores, which directly can be compared to the mean free path of the phonons, as shown previously by Nichenko *et al.* Moreover, the experimental measurement done on two specimens with different density as shown in Fig. 3.8.a clearly reveals that EMD

simulations very well predicted the effect of porosity on the k_L of ThO_2. Furthermore, Fig. 3.8.b also compares the available k_L values of ThO_2 in literature using both EMD and NEMD, with the results obtained in this work using both EMD and LFA measurements.

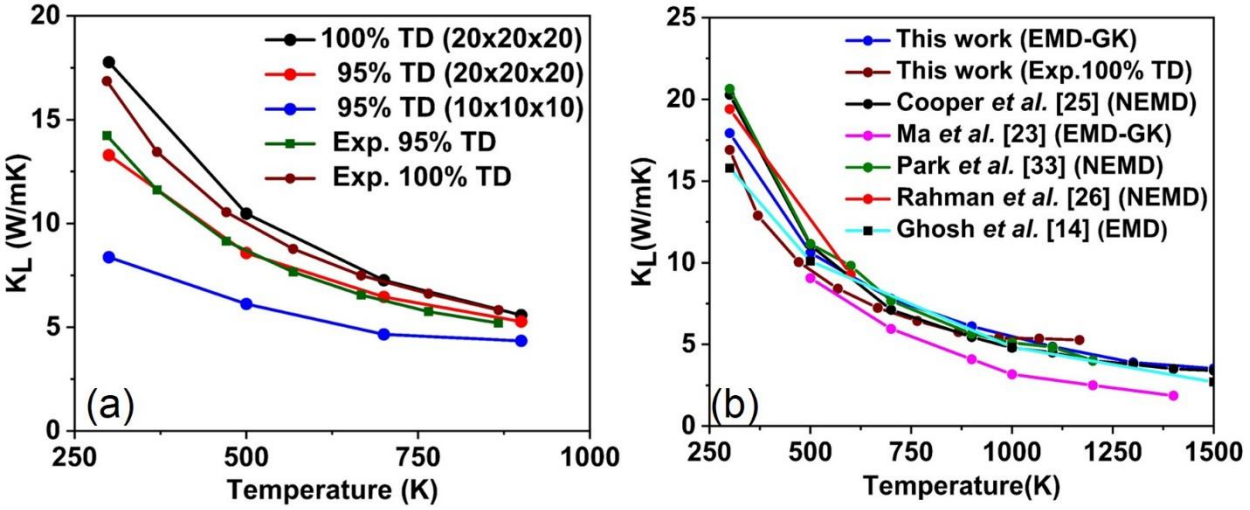

Fig. 3.8. (a) Simulated k_L of pristine and porous ThO_2 as a function of temperature by considering two different cell size of 10×10×10 (blue line) and 20×20×20 (red line), compared to the experiment. (b) The k_L value in this work is compared with the available MD results (both EMD and NEMD) from literature. It has to be noted that expect for the work by Ghosh *et al.* (95% TD) all other predictions are for (100% TD).

3.4.6 Experimentally measured thermal diffusivity and thermal conductivity of ThO_2

To validate the theoretical prediction on the effect of porosity, we carried out experiments on two pellets sintered at 1600 and 1700 ℃, with a relative density of 99% TD and 95% TD (measured using the Archimedes principle) were performed.

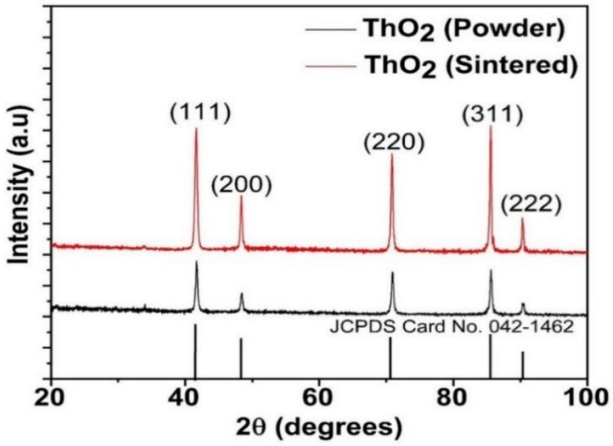

Fig. 3.9. XRD peaks of ThO_2 powder and pellets sintered at 1700 ℃.

These sintered pellets were characterized using XRD for the determination of the phase, and the XRD patterns revealed that the pellet sintered at 1600 ℃ and 1700 ℃ have a face-centred cubic crystal structure as shown in Fig. 3.9. The average grain size of pellets sintered at 1600 ℃ and 1700 ℃ was 3 μm and 10 μm, respectively as shown in Fig.3.10.

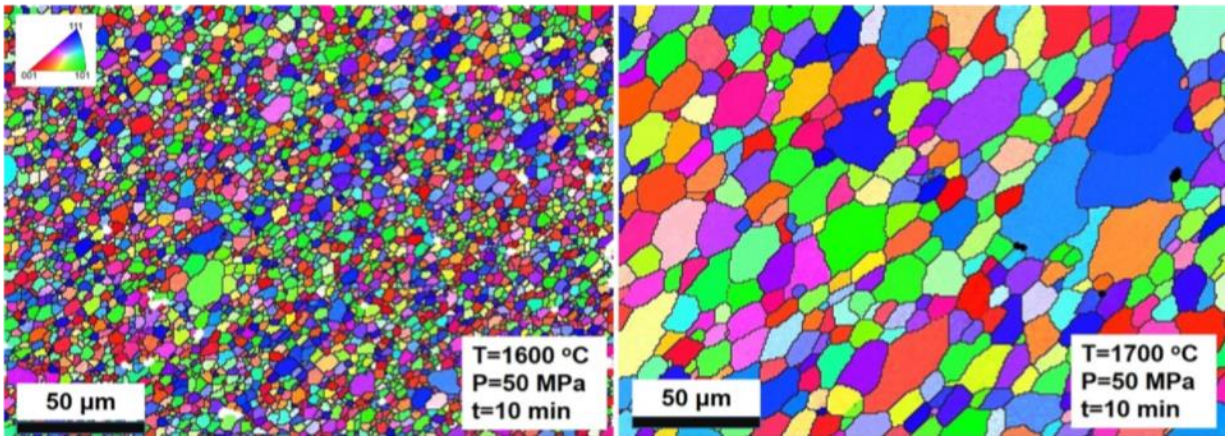

Fig. 3.10. EBSD image of pellets sintered at 1600 and 1700 ℃ respectively.

The result of the thermal diffusivity measurements for ThO_2 obtained with the LFA is presented in Fig. 3.11. The thermal diffusivity values measured for 99% dense pellet are in good agreement with the recently published result by Saoudi *et al.* [122] for a specimen with 98.8% dense pellet. Moreover, the thermal diffusivity of the sample with a density of 99% is less than 10 % at 500 K when compared with the specimen of 95% TD, which clearly indicate the effect of porosity on the thermal diffusivity of ThO_2. Fig. 3.11.b shows the experimental results for the thermal conductivity of the pure ThO_2 for two different density; one is 95% TD, and another sample is corrected to 100% TD. For thermal conductivity, the estimated relative error for the whole temperature range is about 10% by considering the relative uncertainties on the thermal diffusivity (4.5%), specific heat (2%) and density (3%) [122,126]. It is evident from the graph that the pellet with higher density had better thermal conductivity. For instance, the difference in thermal conductivity between two specimens at 500 K was ~14% which agrees with the theoretical predictions by the MD calculation. The variation of density due to the thermal expansion and the Cp was calculated using the equations proposed by Bakker *et al.* [114] for ThO_2. The experimental results for the thermal conductivity of the pure oxides ThO2 for 95% TD are in agreement with that proposed by Bakker *et al.* [114].

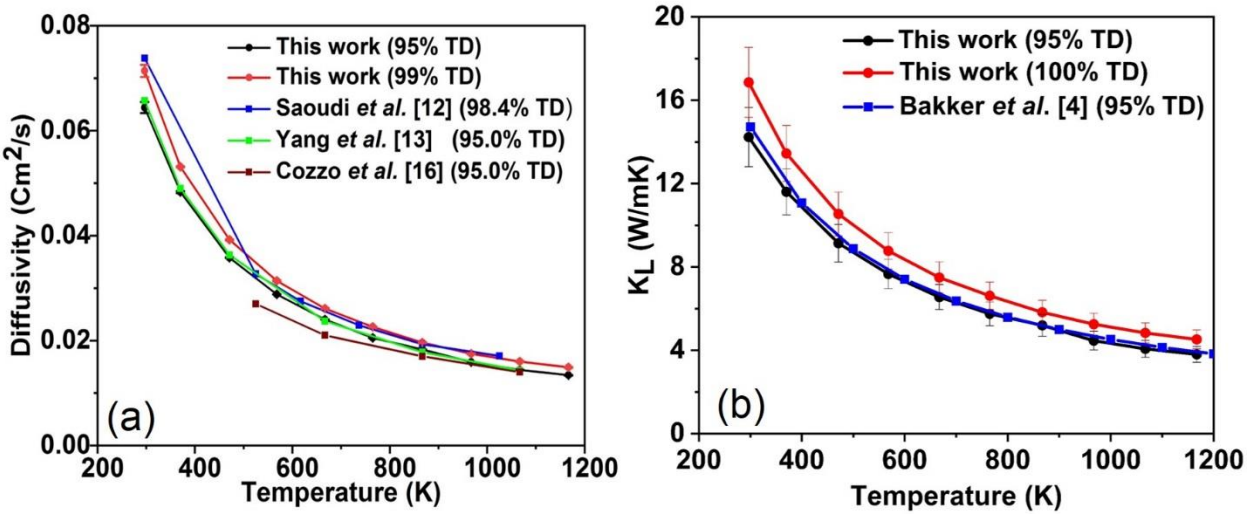

Fig. 3.11. (a) The thermal diffusivity of ThO_2 as a function of temperature for specimens sintered at 1600 ^oC and 1700 ^oC. The uncertainty in the data point from the laser flash apparatus is ± 4.5% and the average of three measurement are provided in the graph with the error bar. (b) The thermal conductivity of the specimen with a density of 95% TD and 99% TD (corrected to 100% TD) compared to Bakker *et al.* [4].

3.5 Summary

We have presented an extensive analysis of the k_L of bulk and porous ThO_2 based on experimental data and theoretical prediction. The combination of the theoretical and experimental approach helps to explain the large discrepancy in the k_L value of ThO_2 reported in the literature. To best of our knowledge the presented theoretical predictions of k_L using BTE is the most accurate prediction of k_L of bulk ThO_2 available so far in terms of its agreement with the experimental results. The recently developed pseudopotential was able to predict the structural and mechanical properties of ThO_2 with better precision than the previously used pseudopotentials. The evaluation of the available three phonon scattering phase space and mode Grüneisen parameter of ThO_2 indicates that the lower k_L of ThO_2 is due to the increase scattering and strong anharmonicity respectively. The investigation of the mode wise contribution clearly suggest that the optical modes plays a significant role in the thermal transport of ThO_2 similar to that observed in UO_2. Additionally, we prepared two ThO_2 pellets of varying density by SPS technique and measured the thermal conductivity of these pellets using laser flash technique. The experimental analysis of the samples reveals the dependence of sintering parameters on the density of the ThO_2 sample and its effect on its measured thermal conductivity. We were able to successfully predict the effect of porosity on thermal conductivity using the classical MD approach and also demonstrate the need

for larger supercell to model porous ThO_2 successfully. In conclusion, the complete analysis of the k_L of ThO_2 using different approaches serves to eliminate the existing ambiguity in the thermal conductivity value of ThO_2.

Chapter 4 : Atomistic and experimental study on thermal conductivity of bulk and porous cerium dioxide

4.0 Overview

This chapter accomplishes the latter part of the first objective of this thesis of determining the fundamental principles of thermal transport in bulk and porous CeO_2. CeO_2 is a popular surrogate material for traditional nuclear fuels, and the k_L value remains ambiguous. DFT simulations unified with the BTE to determine the phonon transport properties of CeO_2. Apart from this, the MD simulations were carried out to understand the effect of porosity on the k_L of CeO_2. The simulations were further validated by measuring the thermal conductivity of CeO_2 pellets prepared by SPS method, using LFA.

The research findings reported in this chapter have been published as manuscript #2 as follows:
L. Malakkal, A. Prasad, D. Oladimeji, E. Jossou, J. Ranasinghe, B. Szpunar, L. Bichler, J. Szpunar; "Atomistic and experimental study on thermal conductivity of bulk and porous cerium dioxide"; published in Nature Scientific Reports, Vol. 9 6326 (2019).

The contributions of the PhD candidate are 1) performing DFT and MD calculations, 2) preparing the samples for characterization, 3) performing XRD and SEM characterizations, 4) measuring of thermal conductivity using Laser flash apparatus, 5) analyzing of the results, 6) writing the manuscript for publication. My supervisors reviewed the manuscript before it was submitted for publication in this journal. The copyright permission of this article is provided in Appendix C

The differences between this chapter and the published paper are:

1. The equations to determine the thermal diffusivity and the thermal conductivity using the laser flash apparatus has been removed to avoid repetition, and the equation has been referred to the equation 2.28 and 2.28 in chapter 2.
2. The equations to determine the ground state structural and mechanical properties of CeO_2 is removed from this chapter to avoid repetition.
3. The descriptions of the methodology section have been removed from this chapter to avoid the repetition as this section is covered in chapter 3 of this thesis.
4. The references of the manuscript are listed at the end of this thesis.

Atomistic and experimental study on thermal conductivity of bulk and porous cerium dioxide

Linu Malakkal[1], Anil Prasad[2], Dotun Oladimeji[3], Ericmoore Jossou[1], Jayangani Ranasinghe[3], Barbara Szpunar[3], Lukas Bichler[2], Jerzy Szpunar[1]

[1]Department of Mechanical Engineering, University of Saskatchewan, Canada

[2]School of Engineering University of British Columbia-Okanagan Kelowna, Canada

[3]Department of Physics and Engineering Physics, University of Saskatchewan, Canada

4.1 Abstract

Cerium dioxide (CeO_2) is a surrogate material for traditional nuclear fuels and an essential material for a wide variety of industrial applications both in its bulk and nanometer length scale. Despite this fact, the underlying physics of thermal conductivity (k_L), a crucial design parameter in industrial applications, has not received enough attention. In this article, a systematic investigation of the phonon transport properties was performed using *ab initio* calculations unified with the Boltzmann transport equation. An extensive examination of the phonon mode contribution, available three-phonon scattering phase space, mode Grüneisen parameter and mean free path (MFP) distributions were also conducted. To further augment theoretical predictions of the k_L, measurements were made on specimens prepared by spark plasma sintering using the laser flash technique. Since the sample porosity plays a vital role in the value of measured k_L, the effect of porosity on k_L by molecular dynamics (MD) simulations were investigated. Finally, we also determined the nanostructuring effect on the thermal properties of CeO_2. Since CeO_2 films find application in various industries, the dependence of thickness on the in-plane and cross-plane k_L for an infinite CeO_2 thin film was also reported.

4.2 Introduction

The lattice thermal conductivity (k_L) depends on the mean free path (MFP), i.e. the distance travelled by the phonons before the occurrence of any scattering events. A detailed quantitative understanding of the mode dependent phonon properties and the bulk MFPs in each material is imperative to exercise control over its thermal management. Furthermore, the thermal transport properties of the bulk and the nanostructured (wires, films, porous, and nanocrystalline material) counterparts of a given material differ significantly due to increased boundary scattering in the latter. Understanding this phenomenon becomes necessary when studying thermal conductivity of

materials such as Cerium dioxide (CeO_2), which finds applications in both bulk and nanostructured form. Bulk CeO_2 is frequently used as a surrogate material in the nuclear industry, as an oxygen storage material in automobile exhaust systems [164], and as an electrolyte in solid oxide fuel cells [165]. Also, nanostructured CeO_2 is used for diverse applications in various industries. For instance, in electronics, the thin films of CeO_2 are among the most prospective buffer layers for high-temperature semiconductor and ferroelectric films deposited on silicon [166,167]. In the nuclear industry, CeO_2 thin film deposits have been proposed for controlling the oxidation of nickel alloys [168], and microspheres of CeO_2 have been synthesized for space nuclear applications [169]. Unfortunately, to date, accurate atomic-scale investigation on the details of mode-wise thermal transport properties and MFP of CeO_2 have not been reported.

Although several studies have reported the k_L of CeO_2, the value remains ambiguous. Experimentally, k_L of CeO_2 has been determined using laser flash technique. Nelson *et al.* [170] and Khafizov *et al.* [171] measured the k_L of 95 % dense CeO_2 pellet and reported respective values of 6.6 W/mK and 17.5 W/mK (correcting for porosity using a modified Loeb expression), at room temperature. The *ab initio* theoretical calculations for the k_L of CeO_2 performed by Xiao *et al.* [129] and the molecular dynamics (MD) study by Khafizov *et al.* [171] predict the k_L as 12 W/mK and 19 W/mK respectively. However, Xiao *et al.* [129] used the analytical Slack model [172], which heavily relied on the fitting parameters that may obscure the underlying physics of heat transfer. Whereas, the MD simulations performed by Khafizov *et al.* [171] could have over-predicted the k_L at lower temperatures as MD simulations do not account for intrinsic scattering at these temperatures. Right through the literature, the value of k_L of CeO_2 at room temperature has varied between (6.6 W/mK and 19 W/mK) and thus exists a disparity. To resolve this aberration, we perform an *ab initio* calculation using density functional theory (DFT) [66], density functional perturbation theory (DFPT) [86] and lattice dynamics in concord with the Boltzmann transport equation (BTE) using ShengBTE [83]. This theoretical approach does not require any assumption on the phonon lifetime to predict the k_L. BTE has been successfully utilized in the investigations of phonon transport properties for many materials [173–178] with high accuracy. In addition to the *ab initio* calculations, MD simulations were carried out to understand the effect of porosity on the k_L of CeO_2. Moreover, using the laser flash experiment technique, the thermal conductivity of porous CeO_2 pellets prepared by spark plasma sintering (SPS) method has also

been reported be a restrictive factor for the heat transfer.

In nanostructured materials, where the phonon MFP is comparable to the grain size, grain boundaries can modulated thermoreflectance technique and an analytical solution of BTE to understand the thermal transport properties of ceria thin films grown by unbalanced magnetron sputtering. The significantly reduced conductivity of these thin films compared to the bulk CeO_2 was attributed to the combined effect of the point defects, grain boundaries, and dislocations. However, their study was not able to shed light on the influence of nanostructuring. For nanoscale applications, the characteristic lengths of the nanostructures can be a limiting factor in the thermal transport. To have a comprehensive understanding of this limiting factor, it is critical to know MFP of CeO_2. It is also important to know what specific length of the nanostructure is going to be significant for CeO_2. Therefore, in this work, the *ab initio* prediction of the MFP, the relaxation time of the phonons, their mode-wise contribution to thermal conductivity, and the effect of nanostructuring on the reduction of thermal conductivity were investigated. These findings will aid the selection of the size and thickness of the nanostructures in tuning the thermal properties. Furthermore, the effect of nanostructuring by studying the cross plane and in-plane thermal conductivity of CeO_2 thin films and the impact of the thickness of the thin films and temperature on the thermal conductivity was also performed. These predicted results not only enable the accurate explanation of the experimental results but also guide further designs and applications.

4.3 Methods

4.3.1 Computational details

All the first principles calculations were performed using the DFT as implemented in the open source Quantum ESPRESSO [73] code. The pseudopotential used were norm conserved, and the electronic exchange-correlation is based on the generalized gradient approximation (GGA) with the Perdew, Burke, and Ernzerhof functional for solids (PBEsol) [139]. Geometry optimization evaluates the structural properties at zero Kelvin temperature by minimizing the total energy by varying both cell parameter and atom positions. We obtained the total energy convergence of CeO_2, using an electron wave vector grid and the plane wave energy cutoff of 950 eV and $8 \times 8 \times 8$ respectively. The criteria for the electronic energy convergence and the force convergence was respectively set a value of 10^{-12} eV and 10^{-7} eV/Å.

In this work, the harmonic force constant is calculated using both linear approach (DFPT) [86] and direct approach (Parlinski-Li-Kawazoe method) [87], based on the supercell approach with finite displacement method as implemented in the Phonopy package [88]. To obtain the converged phonon properties, the calculations of the harmonic force constant were done using a *q*-point mesh of 8 × 8 × 8 (phonon dispersion for different q-points are shown as supplementary information (S.I) S.I.4.1, (Fig. 4.12)) and a 5 × 5 × 5 supercell of the primitive cell containing 375 atoms. The calculation of the third order force constants was performed on a 4 × 4 × 4 supercell, and the force cutoff distance was set to the ninth nearest neighboring atoms. The convergence of the k_L with respect to the number of q points used in the second order force constant, the number of neighboring atoms considered in third order force constant and the number of grid planes along each axis in the reciprocal space for solving the BTE is detailed in Fig. 4.1. From the cubic force constants, the phonon scattering processes are evaluated using Fermi's golden rule, and finally, the k_L is calculated using the iterative solutions of the BTE as implemented in ShengBTE. The k_L presented in this work are the fully iterative solution of the Peierls-equation, and the convergence of $k_L$with the number of iterations starting from the zeroth-order approximation (which is equivalent to operating under RTA) and the k_L at low temperature (< 300 K) are shown in S.I.4.2 (Fig. 4.13) and S.I.4.3 (Fig.4.14) respectively.

For a polar material, the interatomic forces are divided into two additive contributions; the analytic and non-analytic contributions (nac). The analytic contribution accounts for all the forces under the restricted periodic boundary conditions under which the averaged electric field is assumed to be zero. The nonanalytic contribution accounts the additional forces owing to non-zero averaged electric field [141]. The classical Newton's second law of motion for describing the atomic vibrations for a polar solid is as shown in equation (4.1),

$$mj\left(\partial^2 \frac{u_\alpha(t,j;P)}{\partial t^2}\right) = -\left(\frac{\partial E(U)}{\partial u_\alpha(t,j;P)}\right) + eZ_\alpha(j).E. \tag{4.1}$$

where m_j denotes the atomic mass of the j^{th} atom in the primitive unit cell, α (α = *x*, *y*, *z*) is the component of the atomic displacement from its equilibrium position of the j^{th} atom in the P^{th} reference primitive unit cell within a supercell, as detailed in Ref.[141]. The first term on the right-hand side of the equation (4.1) corresponds to the analytical force arising due to the short-range interatomic interactions. The *U* and *E (U)* in the first term represent the whole set of atomic

displacements and the total energy respectively. In the second term, the dot product between the Born effective charge (Z) and the average of the electric field (E) induced by the atomic vibrations accounts for the non-analytic force due to the long-range coulombic interaction. In this work, CeO_2 being a polar material, the non-analytical contribution was considered, and the Born charges and the dielectric constant required to evaluate the non-analytical contribution were calculated using the DFPT. Therefore, the nac contribution needs to be included in the k_L calculation of CeO_2.

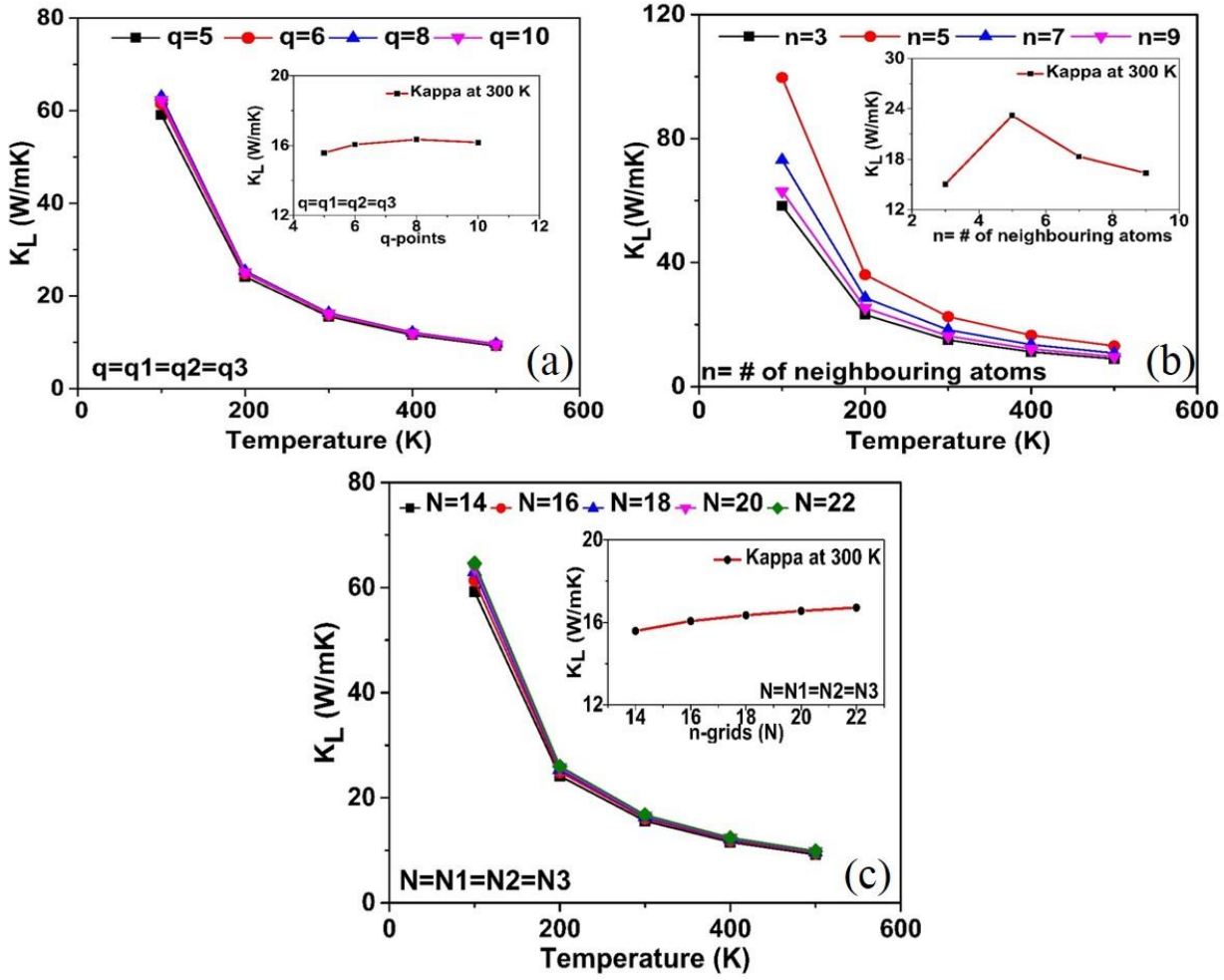

Fig. 4.1. Convergence of the k_L with respect to (a) the q-points considered for the second order force constants (by maintaining n=9 and N=18×18×18 for all the cases); (b) the number of neighboring atoms considered for calculating the third order force constant (by keeping q=8×8×8 and N=18×18×18 for all the cases); (c) the number of grid planes along each axis in reciprocal space for solving the BTE (by considering q= 8×8×8 and n=9 for all the cases).

For MD simulations, we used the equilibrium classical MD techniques together with the Green-Kubo linear response formalism [90] as implemented in LAMMPS (Large-scale

Atomic/Molecular Massively Parallel Simulator) MD simulation code [142]. The Green-Kubo formalism uses the heat current autocorrelation function (HCACF) (shown in Fig. 4.2) which decay along a direction as described in Ref. [90]. To predict the k_L of CeO_2, the Verlet leapfrog algorithm was implemented [76]. Further, the system was first simulated in a constant number of atoms, pressure, and temperature (NPT) ensemble for 4 ns to ensure it reached equilibrium at the desired temperatures, then the ensemble was switched into a constant number of atoms, volume, and temperature (NVT) ensemble and ran for 4 ns. The heat current autocorrelation function (HCACF) were estimated along with an NVE ensemble calculation which generates an 8 ns raw heat current data at every calculation. Finally, the k_L value was computed by averaging the k_L over the time range were the fluctuations were minimal as shown in the inset of Fig. 4.2.b.

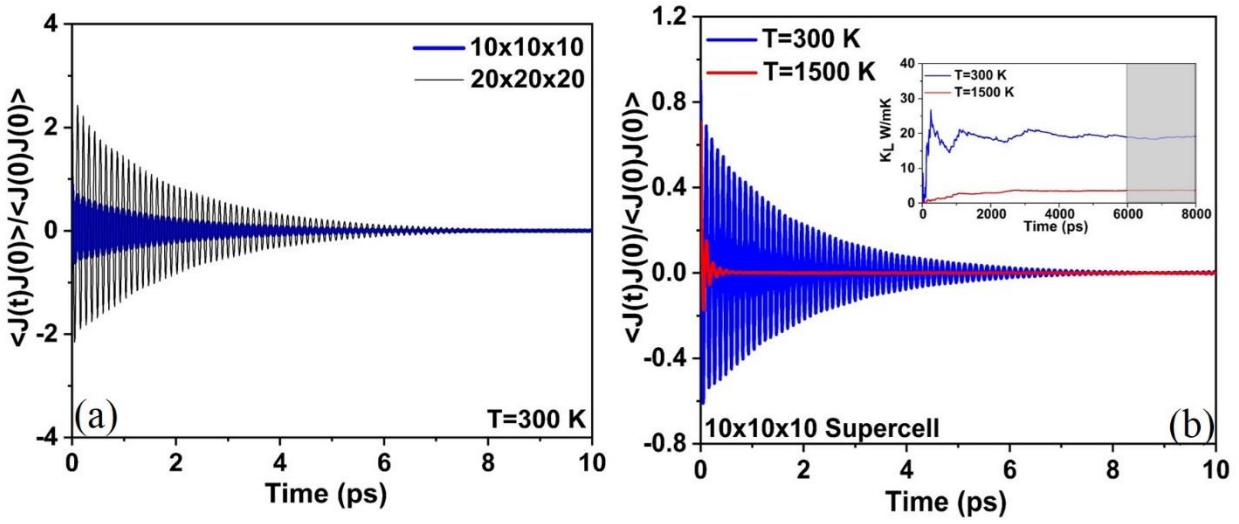

Fig. 4.2. (a) The HFACF for CeO_2 at a temperature of 300 K with a system size of 10×10×10 and 20×20×20 unit cells. (b) The HFACF for CeO_2 at a temperature of 300 K and 1500 K with a system size of 10×10×10 unit cells; inset shows the k_L fluctuations with time and the shaded region indicates the time range over which the HCACF integral is averaged to predict the k_L.

Finally, to study the effect of the nanostructuring and calculate the in-plane and cross-plane thermal conductivity of thin films of CeO_2 we used the open source almaBTE code [84]. Recently, an exact solution to evaluate the BTE in the cross-plane geometries has been obtained. The film conductivity at thickness L as an integral of phonon frequency is given as,

$$k(L) = \int S(\omega, L) k(\omega) d\omega \tag{4.2}$$

Where S is a suppression function that contains the thin film physics and $k(\omega)$ denotes the bulk spectral conductivity. More detailed description of the procedure can be found in the following reference [84,179]. It has to be noted that the almaBTE code uses the second order force constant predicted by the FD method. Hence the k_L values for the nanostructured cases are underpredicted by ~19 % as shown for the bulk CeO_2.

4.3.2 Materials and experimental details

The 99.9% pure CeO_2 powder was obtained from ACROS Organics. The as-received powder was observed under the scanning electron microscope, the micrograph as shown in Fig. 4.3.a revealed that the particles were needle-shaped with dimensions around 20 μm long and 5 μm wide. The as-received powder was sintered using SPS (Thermal Technology LLC 10-3 system) in a graphite die-punch setup as shown in Fig. 4.3.b. The powder die contacts were separated by graphite foils to protect the die from contamination and to reduce friction between the powders and die. A 6 mm hole was drilled from the inner surface of the die, and a pyrometer was focused on this hole to record the temperature of the die. The temperature was controlled by regulating the current passing through the die-punch system, and a Data Acquisition System was used to record displacement, temperature and pressure data.

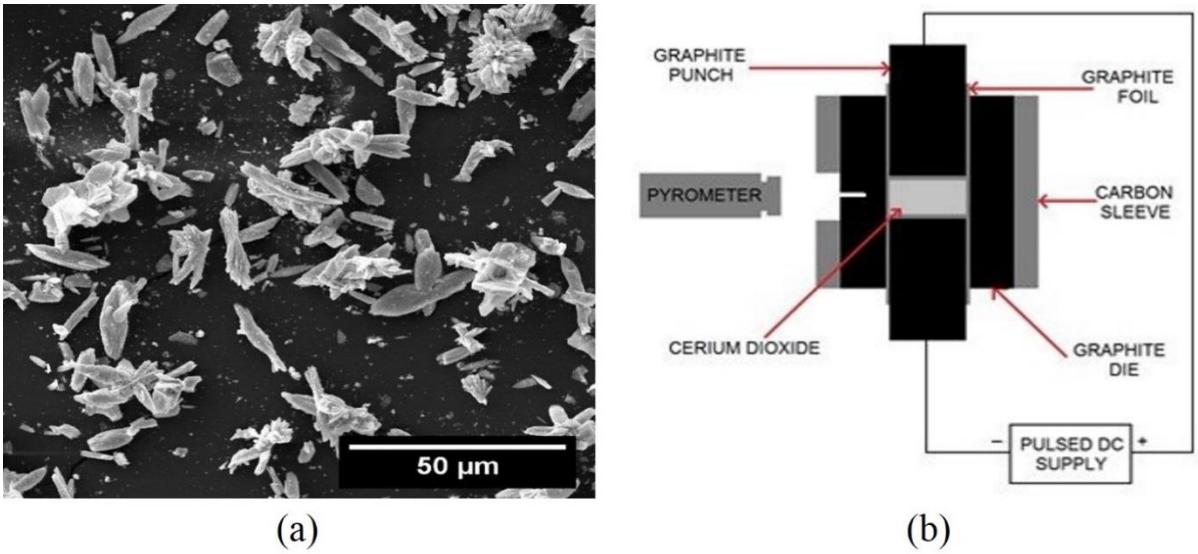

Fig. 4.3. (a) Scanning electron micrograph of as-received CeO_2 powders from ACROS Organic. (b) Schematic diagram of SPS sintering of CeO_2.

The pellets were sintered by varying the sintering parameters such as temperature, pressure and hold time. The sintered pellets were then subjected to X-Ray Diffraction (XRD) using BRUKER D8 with Chromium K-alpha radiation to determine the phase and the presence of any residual carbon during the SPS sintering. The Archimedes' method was used to determine the density of each pellet. Finally, the thermal conductivity was calculated using the laser flash apparatus; Laser flash technique records the thermal diffusivity (α) of the specimens using the Parkers relations [111] given as shown in equation (2.28). From the measured α, the thermal conductivity as a function of temperature ($k\ (T)$) can be measured using the relation (2.29). In this work the Cp changes as a function of temperature was determined by comparing the maximum value of the temperature rise with that of a reference pellet, using the relation $C_p = Q/(dT.m)$, where Q represent the energy of the pulsed laser beam, m mass of the specimen, and dT is the maximum value of the temperature rise. The reference pellet used was a certified stainless steel. However, the density changes as a function of temperature has been kept constant. The thermal conductivity measurements were made on cylindrical pellets of diameter 12.7 mm and thickness 2-3 mm.

4.4 Results and Discussion

4.4.1 Crystal Structure and elastic constants

CeO_2 has a fluorite structure with three independent atoms per unit cell and belongs to the space group of Fm-3m (225), as shown in Fig. 4.4.

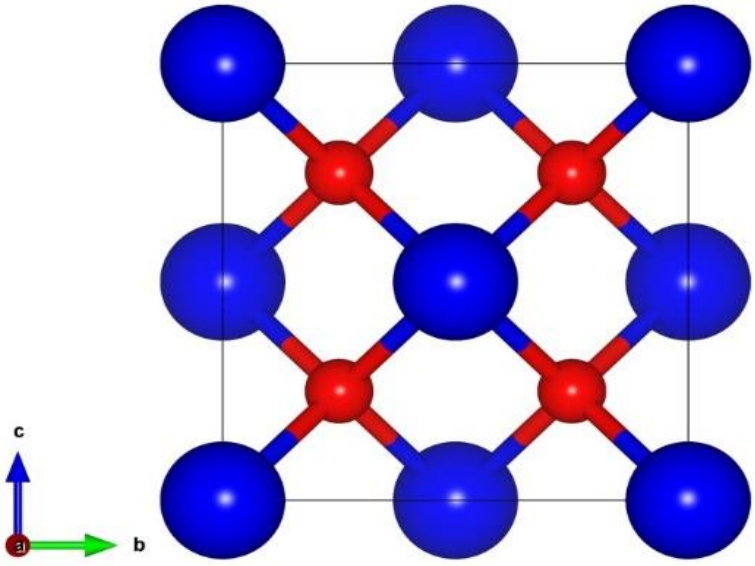

Fig. 4.4. Crystal structure of CeO_2 in the conventional cubic unit cell (blue and red represent Ce and O atoms respectively.

The equilibrium lattice constants were obtained by minimizing the total energy with respect to the lattice parameter and atomic positions. The detailed description of the optimized parameter and the pseudopotential used for the simulation were provided in section 5.3. Table 4.1. presents the calculated lattice constant (a), bulk modulus (B) and stiffness constants (C_{ij}) of CeO_2 in comparison with the values from the previous DFT calculations [180–183] and the experiment [144]. The PBEsol functional predicted the lattice constant within an error less than 0.01% compared with the experimental data reported by Nakajima *et al.* [144] As expected, the new PBEsol functional was able to quantify the ground state structural properties more accurately than previous DFT calculations performed using linear density approximation (LDA) [180], GGA [181], Hartwigsen- Goedecker-Hutter (HGH) [182] and PAW [183] pseudopotentials. The elastic constants are important parameters that provide information on the properties of a material such as stiffness, strength, mechanical stability, hardness, and ductility or brittleness [146]. We evaluated the single crystal stiffness constants of CeO_2 by using a stress-strain method [184,185] with the help of our in-house interface qe-nipy-advanced [74]. The stiffness constants for a mechanically stable cubic structure should satisfy the following Born's mechanical stability criteria [147] $C_{11} - C_{12} > 0, C_{11} + 2C_{12} > 0, C_{44} > 0$. The listed stiffness constants have satisfied these criteria indicating that the system is mechanically stable.

Table 4.1. Structural and mechanical properties of CeO_2 compared with previous DFT calculations and the experiment.

a (Å)	B (GPa)	C_{11} (GPa)	C_{12} (GPa)	C_{44} (GPa)	G (GPa)	Y (GPa)	η	References
5.409	192	355	110	62	82	215	0.313	This work (PBEsol)
5.37	203	371	117	68	-	-	-	LDA [180]
5.45	193	-	-	-	-	-	-	PAW [183]
5.37	210	386	124	73	-	-	-	HGH [182]
5.44	181	347	97	51	74	195	0.218	GGA [181]
5.41	204	403	105	60	-	-	-	Exp. [144]

From the calculated stiffness constants, the polycrystalline bulk modulus, shear modulus, Young's modulus and Poisson's ratio (listed in Table 4.1) were determined using the Voigt-Reuss-Hill

approach [186–188]. From Table 4.1. the bulk modulus values (192 GPa) at zero temperature obtained from PBEsol method is only about 6% lower than the experimental value of 204 GPa [144] at room temperature. Since the calculated structural and mechanical properties are in excellent agreement with the experimental data, the same PBEsol functional pseudopotentials were used for the study of phonon properties and the k_L of CeO_2.

4.4.2 Lattice dynamics

Lattice dynamics is critical for understanding the thermal properties of crystalline solids at finite temperatures. For instance, the phonon densities of states are required to evaluate thermodynamic properties such as thermal expansion coefficient (α), C_V, entropy (S) and k_L. Moreover, the fundamental reasons for unique thermal characteristics of a material can be ascertained by analyzing the phonon scattering mechanism through phonon group velocities, and phonon mean free path, relaxation time and phonon scattering phase space [158]. At present, two approaches the linear-response approach [159] and the direct approach [87,189] are widely used to evaluate the phonon dispersion. In Fig. 4.5.a the calculated phonon dispersion spectra using these two approaches the linear-response approach (QE) and the direct approach (Phonopy) are presented along the Γ-X-Γ-L high symmetry points in the Brillouin zone and compared with the known experimental data.

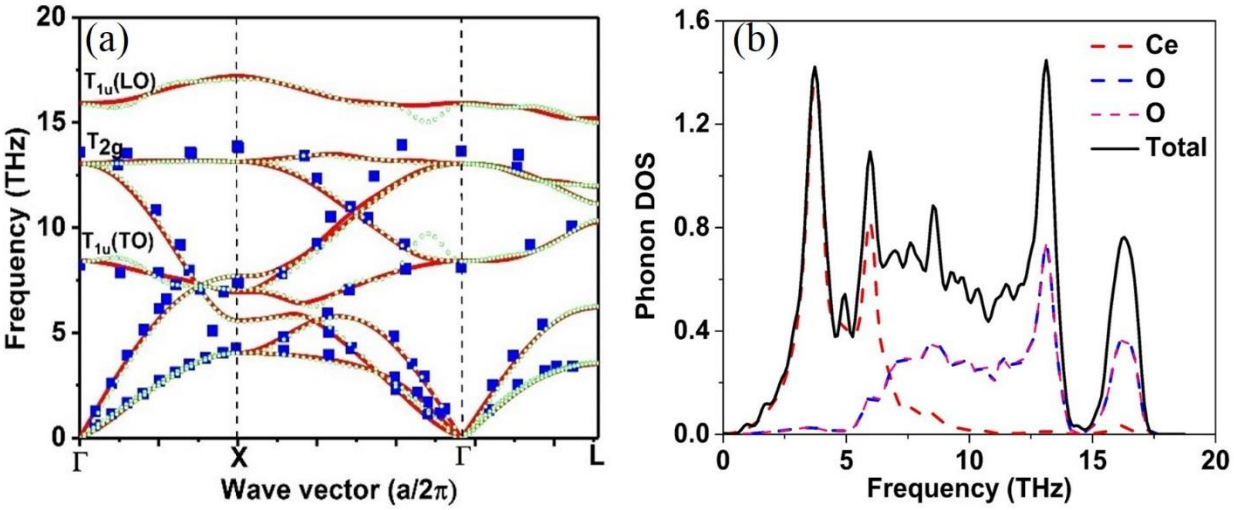

Fig. 4.5. (a) Phonon spectra of CeO_2 predicted by the linear response approach using q-point of 6×6×6 (red line) and the finite displacement (FD) methods (dotted green line) compared with the experiment done by Clausen K *et al.* [155] (blue dots). (b) Partial (dotted lines) and total phonon density of states (solid black line).

The predicted phonon spectra using both the linear-response approach and the finite displacement (FD) methods are in good agreement with the experimental data generated by Clausen K *et al.* [155], for the entire Brillouin zone using inelastic neutron scattering at 293 K. CeO_2 has three (n) atoms per primitive unit cell and thus there are in three dimensions (d = 3) three acoustic mode phonons and d (n-1) = 6 optical phonons. The group theory analysis gives the decomposition of the zone centre modes as doubly degenerate transverse optical (TO) mode, the triply degenerate Raman active mode and the non-degenerate longitudinal optical (LO) mode. The three-zone center frequencies are 8.42 (8.15), 13.03 (13.94), and 15.93(17.84) THz respectively (shown in brackets are the experimental value from the Ref. [190]). The partial lifting of degeneracy between the LO and TO phonons at the Brillouin zone centre is due to the polarization effect, which indicates that the CeO_2 is a polar material as shown in Fig. 4.5.a The Born effective charge for an insulator is a measure of the change in electronic polarization due to ionic displacements. These charges are essential for elucidating the physical understanding of piezoelectric and ferroelectric properties since they describe the coupling between lattice displacements and the electric field. The Born effective charges, Z^*_{Ce} =5.793 (5.746) Z^*_O =2.896 (2.873), agrees well with the values reported (shown in brackets) by Xiao *et al.* [129] The calculated dielectric constant value 7.87 (6.0) is in reasonable agreement the work done by Santha *et al.* [190].

The partial and total phonon density of states is shown in Fig. 4.5.b. The partial density of the state shows that the frequency vibrations lower than 6.0 THz are dominated by the Ce ions and the higher frequency vibrations are mainly contributed by the dynamics of O ions. The phonon dispersion of CeO_2 along Γ-X-Γ-L, high symmetry points in the Brillouin zone does not display frequency gap between optical and acoustic phonons. The absence of frequency gap in case of CeO_2 indicates that three-phonon scattering is dominant resulting in relatively lower phonon relaxation time thereby leading to lower k_L. The accurate prediction of phonon dispersion curve of CeO_2 using both the linear-response approach and direct approach enables reasonable precision in the projection of phonon-assisted properties.

4.4.3 Three-phonon scattering phase space and Grüneisen parameter

Three-phonon scattering phase space (P_3) quantitatively describes the number of scattering channels available for a phonon being scattered [160]. The available P_3 gives an insight into the

k_L of a material i.e. larger available P_3, will have more channels for scattering and subsequently lower k_L. The P_3 is solely determined from a material's phonon spectra and is defined as [158],

$$P_3(q,j) = \frac{1}{3\Omega}(2P_3^{(+)}(qj) + P_3^{(-)}(qj)) \tag{4.3}$$

where q is the momenta of phonons, j is the phonon branches, $\Omega = n_j^3 V_{BZ}^2$ is the normalized factor equal to unrestricted phase space for each type of process. P_3^+ and P_3^- are the absorption and emission processes respectively, defined by,

$$P_3^{\pm}(q,j) = \frac{1}{N_q} \sum_{q_1,q_2,j_1,j_2} \delta(\omega_{qj} \pm \omega_{q_1 j_1} - \omega_{q_2 J_2}) \delta_{q \pm q_1, q+G} \tag{4.4}$$

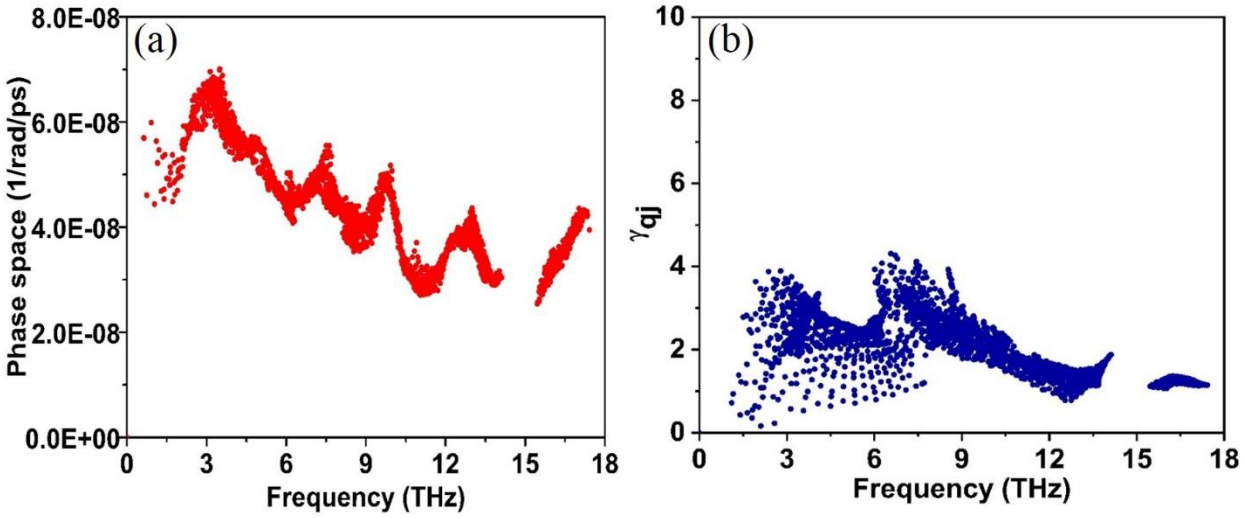

Fig. 4.6. (a) Three-phonon scattering phase space. (b) Mode Grüneisen parameter (γ_{qj}).

where N_q is the total number of q points in the first Brillouin zone. Fig. 4.6.a shows the P_3 of CeO_2 for the acoustic and optical modes. To gain a quantitative understanding of available P_3 on k_L, the total volume in phase space for three phonon processes (P_3*_total*) for CeO_2 is compared with our previously reported results of a relatively higher k_L material such as silicon carbide (420 W/mK at 300 K) [161]. The P_3*_total* (in units of 1/rad/ps) predicted along the same Brillioun path is higher for CeO_2 (4.18×10^{-3}) than SiC (1.66×10^{-3}); clearly indicating that CeO_2 has a larger three phonons scattering phase space, more channels for scattering and hence lower thermal conductivity than SiC. Lindsay and Broido [158] have already established the phase space available for the three-phonon scattering for semiconductors. In this work, the possible P_3 for a lanthanide oxide

was illustrated, and these findings would aid in qualitatively determining the thermal conductivities of new materials with known phonon dispersion.

Grüneisen parameter (γ) illustrates the anharmonicity in a crystal and is defined as the shift in phonon frequency with change in volume. It is an established fact that anharmonicity in an ordered crystal structure determines the strength of each scattering channel and the efficiency of each phonon mode in heat conduction is inversely proportional to square of Grüneisen parameter. To quantitatively examine the anharmonicity of CeO_2, we plot the mode Grüneisen parameters at zero temperature (as shown in Fig. 4.6.b) derived from the third-order anharmonic force constants (shown in equation (4.5)) as implemented in the ShengBTE [83] and is defined as:

$$\gamma_p(q)|_{anh} = -\frac{1}{6\omega_p(q)^2} \sum_{n'l'} \sum_{n"l"} \sum_{\alpha\beta\gamma} \Phi^{\alpha\beta\gamma}_{n^o,n'l',n"l"} \times \left(\frac{e^p_{\alpha_\eta}(q^*) e^p_{\beta\eta'}(q)}{\sqrt{M_\eta M'_\eta}} \right) e^{-iqR'_i} r_{\eta" l" \gamma'} \qquad (4.5)$$

where $\Phi^{\alpha\beta\gamma}_{n^o,n'l',nl}$ *a*re the third-order force constants, *e* is the phonon eigenvectors, *n* denotes the n^{th} primitive cell in the supercell, α is the Cartesian components of *x, y,* or, *z, M_n* refers to the mass of the atomic type *n* in the primitive cell and $r_{\eta l}$ is the position vector of the η^{th} atom in the l^{th} primitive cell. According to Fig. 4.6.b, the sum of all mode Grüneisen parameters are positive indicating volume expansion. At zero temperature, the average Grüneisen coefficient over the whole frequency range was 2.07. The mode Grüneisen parameter near 7 THz (near the TO mode) is higher, indicating that the scattering of acoustic phonons by the optical mode caused hindrance to heat conduction. Changes in mode Grüneisen parameter with different q-points in the second order force constant and the neighboring atoms in the third order force constant is given as S.I in S.I.4.4 (Fig. 4.15).

4.4.4 Theoretical prediction of thermal conductivity and mode contribution.

The full iterative solution of BTE for CeO_2 is shown in Fig. 4.7.a. As expected, the k_L of CeO_2 decreases with increasing temperature because the phonon-phonon scattering dominates the k_L at high temperatures. The k_L at 300 K is 16.71 W/mK. Our predictions were made assuming a defect-free crystal and thus could potentially represent the upper limit of k_L. The previous experimental value of thermal conductivity for CeO_2 appears to be scattered. For example, for ~ 95% dense pellets at 373 K, Jakub *et al.* [191] and Nelson *et al.* [170] reported a value of 9.58 W/mK and 6.2 W/mK, respectively. These scattered values of k_L reported in the literature are generally

justified by pointing to microstructures. This may not be true under all circumstances. In these situations, an accurate theoretical prediction without the usage of fitting parameters can significantly help in arriving at a meaningful physical explanation. The highest reported experimental value for CeO_2 for a ~ 95 % dense pellet at room temperature is by Jakub *et al.* [191] (14.1 W/mK) and our theoretical predictions at 300 K is 16.71 W/mK (red dots) for 100% dense single crystal, are in excellent agreement. Furthermore, the difference in k_L values obtained through our theoretical prediction and the previously reported simulated value of 12 W/mK at 300 K by Xiao *et al.* [129] (using fitting parameters) clearly indicate the apparent disadvantages of using fitting parameters. We also noted that Xiao *et al.* obtained the second order force constant required for their calculation using the finite difference (FD) method. Our k_L predictions using the second order force constant from the FD method (green dot) has also under predicted the value of k_L by 19% in comparison with the k_L predicted using the second order force constant obtained from DFPT method. Moreover, accurate theoretical predictions enable us to arrive at a rational expression for the porosity correction, as there is a multitude of expressions to choose from, depending on the material and temperature range.

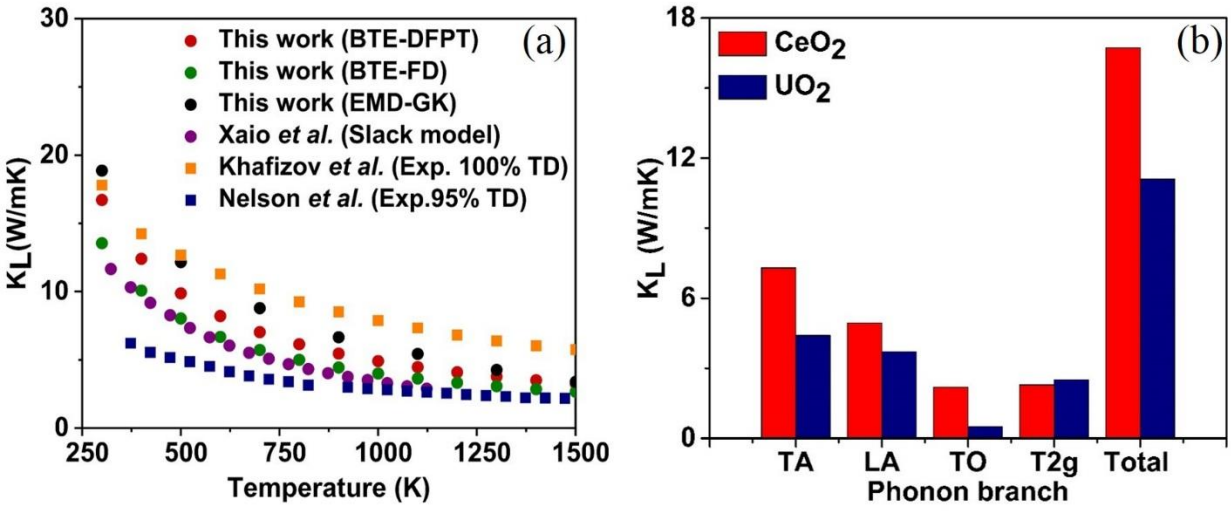

Fig. 4.7. (a) The temperature dependence of the phonon k_L in CeO_2 using BTE and experiment compared to previous theoretical [129] and experimental [170] values of k_L. (b) The mode-wise k_L of CeO_2 in comparison with the simulated results for UO_2 by Pang *et al.* [163].

Furthermore, we probe the relative contribution of the acoustic and optical phonon modes to the total k_L of CeO_2. Typically, for ceramic materials, there is a tendency to neglect the optical contribution owing to their consistently low group velocities and shorter lifetimes [192]. However,

the Uranium dioxide (UO_2) with a reported critical optical mode is an exception [163]. In the wake of this, it would be interesting to know the mode-wise thermal conductivity of the popular nuclear fuel surrogate CeO_2. To best of author's knowledge, the mode-dependent k_L of CeO_2 has not received enough attention. Fig. 4.7.b shows the simulated contribution of mode-wise k_L of CeO_2 compared with UO_2 at room temperature previously calculated by Pang *et al.* [163]. In CeO_2 the optical phonons contribute to about 27% of the total k_L compared to the acoustic modes. The optical contributions at 300 K can be precisely broken down to 13.1%, 13.7%, and ~1% from the doubly degenerate transverse optical mode (TO), the triply degenerate Raman active mode (T2g) and the non-degenerate longitudinal optical mode, respectively. The theory predicts that like UO_2, its surrogate CeO_2 will also have strong optical mode contribution to k_L. However, in the case of UO_2, Pang *et al.* [163] have experimentally proved that the contribution of the TO branch to thermal conductivity is, in fact, higher than the theoretical prediction. Our theoretical predictions suggest an even more significant contribution of the TO branch towards thermal conductivity of CeO_2, and could, therefore, make an experimental validation worthwhile.

4.4.5 Effect of porosity on the thermal conductivity using MD simulations and experiments.

So far in this manuscript, the primary focus was in understanding the underlying physics of thermal transport and determining the k_L of a defect-free single crystal CeO_2 using first principles approach. However, manufacturing a defect-free specimen of CeO_2 with 100% theoretical density (TD) is impracticable, and most importantly k_L of a sample with porosity and defects are expected to be lower than 100% dense CeO_2. Therefore, it is essential to determine the effect of porosity on k_L of CeO_2 quantitatively. Hence, the effect of porosity on the k_L of CeO_2 has been determined using both simulation (MD approach) and experiment. It has to be noted that evaluation of the effect of porosity using first principles is still in genesis, and for that reason, MD simulations were used. Moreover, the theoretical prediction of k_L using both BTE and MD approach complement each other well. The BTE calculates the quantum mechanical scattering rates directly by considering only the lowest order of phonon-phonon interactions and hence become less accurate at very high temperatures where higher order interactions become significant. In contrast, the MD simulations based on classical potential are less reliable at a lower temperature. However, at high temperatures, the phonon-phonon interactions of all orders are duly considered.

In this work, the k_L of CeO_2 by MD simulations were calculated on systems of 8×8×8 (6144 atoms), 10×10×10 (12000 atoms), 12×12 ×12 (20736 atoms) and 20×20×20 (96000 atoms), using the Embedded Atom Many-body (EAM) potentials developed by Cooper *et al.* [75]. Table 4.2 shows that there is no noticeable difference in the k_L of CeO_2 at 300 K with different supercell sizes, suggesting that 8×8×8 system is sufficient enough to represent all the phonon modes available to reproduce the phonon-phonon scattering present in the bulk CeO_2 [143].

Table 4.2. The size dependence of k_L of bulk CeO_2 at a temperature of 300 K presented using EMD simulation and the Green-Kubo method.

Size of the supercell	Number of atoms	Thermal conductivity (W/mk) at 300 K
8×8×8	6144	18.87
10×10×10	12000	18.35
12×12×12	20736	18.35
20×20×20	96000	18.84

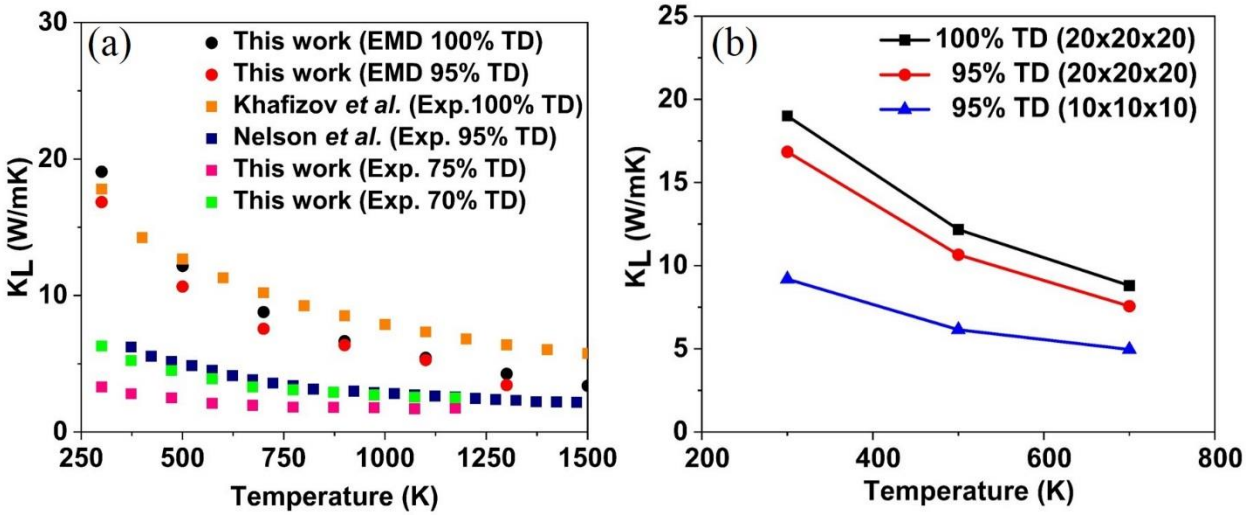

Fig. 4.8. (a) Simulated and experimental k_L of porous CeO_2 as a function of temperature. (b) Influence of porosity on the k_L of CeO_2, by considering the same porosity on a cell size of 10×10×10 (blue line) and 20×20×20 (red line) unit cells

For investigating the porosity influence on the k_L of CeO_2, two cases with the cell sizes of 10×10×10 and 20× 20×20 were considered. In each of the supercells, only one pore was introduced

by manually removing 5% of atoms, in such a way that for every cerium atom two oxygen atoms are considered, to maintain the charge neutrality of the system. The supercell with vacancies are then made to relax keeping the cell volume same, and then MD calculations were carried out to evaluate the thermal conductivity of porous CeO_2 (as explained in section 4.3.1).

Fig. 4.8.a compares the experimental data to the predicted k_L values of CeO_2 using MD for a pure crystalline CeO_2 (black dots) and porous CeO_2 (red dots) modelled on a 20×20×20 supercell. The k_L values predicted for pure crystalline CeO_2 are in reasonable agreement with the experimental data (orange square dots) provided by Khafizov *et al*. [171]. Due to the presence of pores, the k_L of the porous CeO_2 is lower than the pure crystalline CeO_2. However, we noted that k_L values predicted for porous CeO_2 is significantly dependent on the size of supercell considered. Even though the porosity was modelled the same way in both the supercells, the k_L for the case of 10×10×10 is considerably lower than the case of 20×20×20. The Fig. 4.8.b clearly shows that compared to the pure crystalline CeO_2 at 300 K the k_L predicted for a porous CeO_2 on a 10×10×10 supercell has reduced by 52%, whereas the same amount of porosity created on a 20×20×20 supercell decreased the k_L by 12%. The fact that the k_L is significantly lower for the 10x10x10 case and can be explained by the increased phonon scattering on the surface of the pores due to the decreased average distance between the pores, which directly can be compared to the mean free path of the phonons, as shown previously by Nichenko *et al*. [193].

To validate the theoretical predictions and further expand the quantitative understanding of the effect of porosity on thermal conductivity, the experiments were carried out on the specimens prepared by SPS technique. The pellets of CeO_2 with varying densities were made by controlling the sintering parameters such as the sintering temperature, pressure, hold time, and the sintering atmosphere. The more detailed description of the sintering conditions and its effect on density and the microstructure of CeO_2 are given in our previous work [194]. Therefore for brevity, discussions would be limited to the samples on which the thermal conductivity measurements were made. In this work, the experiments were performed on CeO_2 pellets prepared at a sintering temperature of 1000 ^oC and 1100 ^oC by maintaining the pressure and hold time at 50 MPa and 10 min respectively. However, for the benefit of the readers, it is important to note that as the sintering temperature increased (>1500 ^oC), the CeO_2 reduced to Ce_2O_3. Moreover, in our previous work [194], it was observed that at a high sintering temperature (>1100 ^oC) and reductive atmosphere CeO_2 exhibited

a range of stoichiometry and such non-stoichiometric oxide had been susceptible to chemical expansion [195] leading to the disintegration of the sintered pellets. It was for this reason that the experimental determination of thermal conductivity was limited to two samples sintered at 1000 ^{o}C and 1100 ^{o}C.

These sintered pellets were characterized using XRD for the determination of the phase, and the XRD patterns revealed that the pellet sintered at 1000 ^{o}C (green line) and 1100 ^{o}C (pink line) have a face-centred cubic crystal structure (as illustrated in S.1.5 (Fig. 4.16)). The density of CeO_2 was measured using the Archimedes principle, and the density of these pellets sintered at 1000 ^{o}C and 1100 ^{o}C were 70 % and 75 % respectively. As stated earlier in section 4.3.2, the thermal diffusivity can be determined using the Laser flash apparatus and Fig. 4.9 shows the variations of thermal diffusivity of these pellets as a function of temperature. Fig. 4.8.a and 4.9 respectively demonstrate that higher the density of the pellet, higher the thermal diffusivity and thermal conductivity. Moreover, we found that the density of the specimens played a vital role in the measured k_L values (as shown in Fig. 4.8) at lower temperatures (< 1000 ℃), however, at a higher temperature, the difference is less significant.

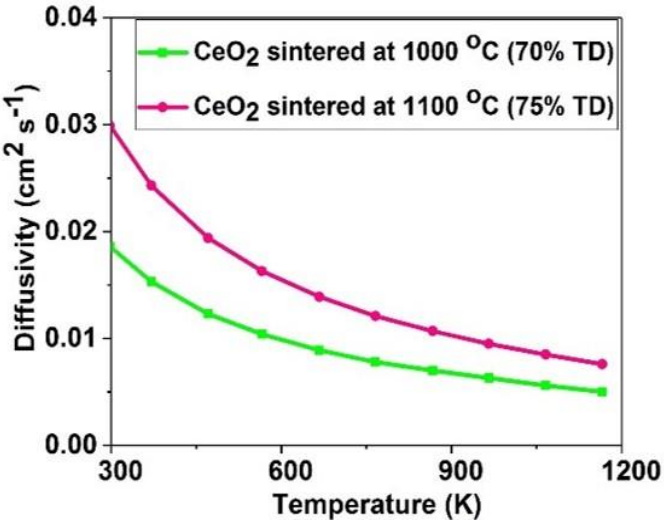

Fig. 4.9. The thermal diffusivity of CeO_2 as a function of temperature for specimens sintered at 1000 ^{o}C and 1100 ^{o}C. The uncertainty in the data point from the laser flash apparatus is ± 4.5%.

4.4.6 Nanoscale size effect, cross-plane, and in-plane thermal conductivity

CeO_2 nanostructures like wires, films, porous and nanocrystalline materials find applications in energy conversion, sensors, and microelectronics where tailoring of thermal transport property is

essential. Moreover, a recent work evinces the capabilities of the ultra-thin CeO_2 for oxygen storage [196]. It is established that the nanostructure surfaces significantly reduce the k_L compared to its bulk counterpart, due to the scattering of the energy carriers. The interplay between the characteristic length and the bulk MFP of the energy carriers is the fundamental physics that determines the dominance of the boundary scattering. The size of the crystalline domain, therefore, acts as limiting length for phonons MFP. Pertaining to this context, a detailed quantitative understanding of the MFP of CeO_2 is certainly advantageous.

In Fig. 4.9 the dependence of normalized cumulative k_L on phonon MFP at 300 K are presented. The normalized k_L increases with the increase in MFP, with significant contributions to the k_L of CeO_2 coming from the phonons with MFP between 1 nm to 100 nm. The contribution of phonons mode to k_L is uneven, and the phonons of MFP below 50 nm constitute 80% of k_L, indicating that curtailing the size below 50 nm can effectively reduce the k_L of CeO_2. Therefore, this grasp of the MFP of CeO_2 will aid the selection of sample size (thickness for thin film, diameter for nanowires and nanoparticles) for diverse technological applications that require a notable deviation from bulk thermal properties.

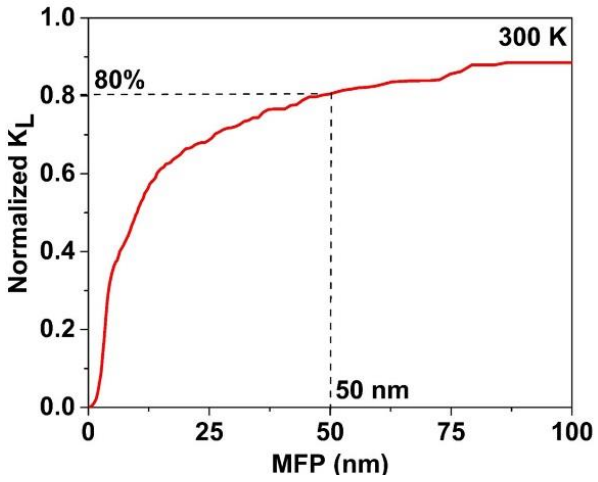

Fig. 4.10. Thermal conductivity accumulation as a function of phonon MFP at room temperature.

To investigate the influence of nanostructuring on k_L of CeO_2, we demonstrate the thickness dependence in the cross-plane and in-plane k_L of CeO_2 along the (001) and (100) planes respectively at 300 K, as shown in Fig. 4.11.a. For these predictions, we utilized almaBTE [84] a solver of the space-time dependent BTE for phonons in the structured material. The effective in-

plane (∥) and cross-plane (⊥) thermal conductivity (k_{eff}) in relaxation time approximation for a film of thickness L are evaluated as:

$$k_{eff}(L) = \sum_{q} S_q(L) C_q \parallel v_q \parallel \Lambda_q \cos^2 \vartheta_q \tag{4.6}$$

where S is, the suppression function that considers the additional phonon scattering instigated by the film boundaries, C_q is the mode contribution to the volumetric heat capacity, v_q the group velocity, Λ_q is the mean free path and ϑ is the angle between the group velocity and transport axis. The sum over q must be interpreted as the combination of a sum of branches and an average over the Brillouin zone. As anticipated, due to the boundary scattering the in-plane and cross-plane k_L of thin films reduced with the reduction in the thickness. If the thickness of CeO_2 is slashed to 10 nm, its cross-plane (in-plane) k_L is only 4.96 (8.50) W/mK at 300 K. To verify the theoretical findings, we compared the results with experiment. It should be noted that theory predicts the k_L for the infinite two-dimensional CeO_2 and therefore, the presence of defects would further scatter the phonons and reduce the k_L of CeO_2 films. Khafizov *et al.* [171] reported k_L of 7.2 W/mK, for a film of long columnar grain size structure with an average column radius of ~ 450 nm and the film thickness of 12 μm.

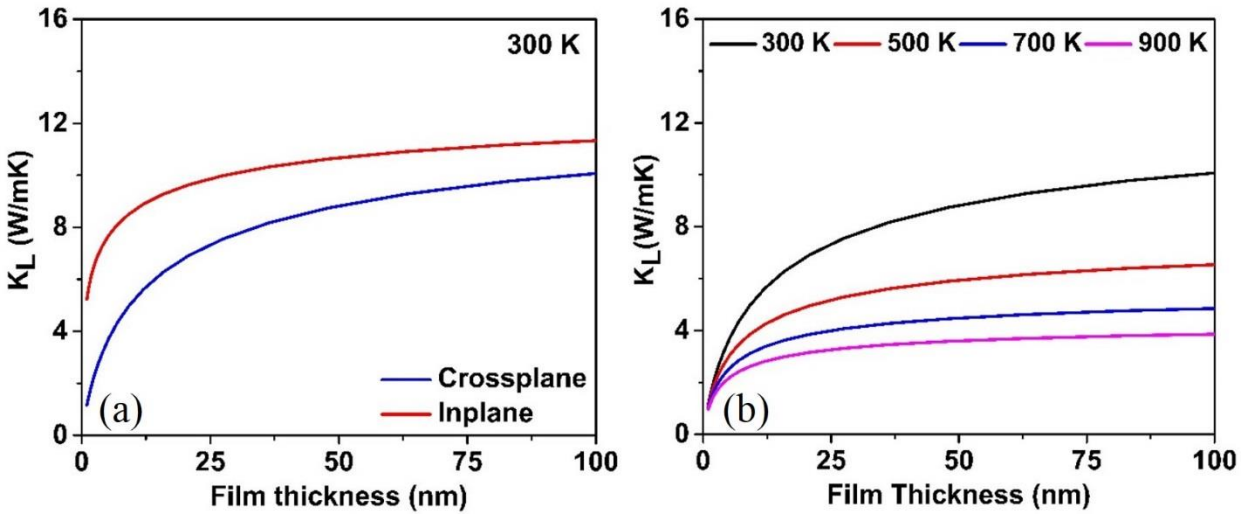

Fig. 4.11. (a). In-plane and cross-plane thermal conductivity of CeO_2. (b) Cross-plane conductivity as a function of temperature.

Here, the thickness of 12 μm exceeds the condition that the characteristic size of CeO_2 must be 50

nm to have a significant reduction in k_L. However, our simulation predicts a k_L of 13.0 W/mK for a thickness of 12 μm. The difference between theory and experiment can be primarily associated with the presence of defects and not to the effect of nanostructuring. Therefore, we can surmise that CeO_2 thin films below ~50 nm with defects can reduce the k_L drastically. Metal oxides generally have large Seebeck coefficient at high temperatures and hence can be considered as candidate materials for advanced thermoelectric.

The coating of CeO_2 on several alloys has improved the oxidation resistance and can be used in high-temperature applications in industries such as automobiles, aerospace and nuclear, where the knowledge of CeO_2 cross-plane thermal conductivity as a function of coating thickness and temperature becomes vital. Therefore, in Fig. 4.11.b we have presented the effect of temperature on the k_L of thin film and have observed that the k_L for thin films reduces considerably with an increase in temperature. The presented theoretical work can equip material scientists with vital information required for designing CeO_2 thin films of optimal thickness that will aid in the design of experiments.

4.5 Conclusion

We have presented an extensive analysis of the k_L of CeO_2 both in its bulk and nanoforms. The theoretical predictions of k_L using first principles unified with BTE not only provides an insight into the underlying physics of k_L of CeO_2 but also helps explain the large discrepancy in the k_L value of CeO_2 reported previously. The structural and mechanical properties of CeO_2 could be predicted with better precision by the recently developed pseudopotential with PBEsol functional than any other previously reported DFT calculations. The phonon dispersions spectra of CeO_2 is evaluated by both direct approach and linear response approach and could describe its polar nature while aptly showing good agreement with the experiment. An investigation of the available three-phonon scattering phase space and mode Grüneisen parameter of CeO_2, reveals that the lower k_L of CeO_2 is primarily due to increased scattering and strong anharmonicity respectively. Along with the theoretical investigation of k_L and its dependence on temperature, we also predict the mode wise contribution to the total k_L of CeO_2. The analysis of mode wise k_L of CeO_2 indicated the notable contribution to the overall thermal conductivity from the optical modes (~30%), akin to UO_2. Additionally, we prepared CeO_2 pellets of varying density by SPS technique and measured the thermal conductivity of these pellets using laser flash technique. The experimental analysis of

the samples reveals the dependence of sintering parameters on the density of the CeO_2 sample and its effect on its measured thermal conductivity. Moreover, we also conducted a theoretical study using the classical MD approach to corroborate the effect of porosity on thermal conductivity. Besides the detailed investigation of the thermal conductivity of CeO_2 in its bulk form, this article also sheds light on the thermal transport property of nanostructured CeO_2. We demonstrate the phonon MFP distribution of CeO_2 is critical in the study of nanostructured materials and devices. The contribution of phonons modes to k_L is uneven, and the phonons of MFP below 65 nm constitute 80 % of k_L, indicating that limiting the size below 65 nm can efficiently reduce the k_L of CeO_2. The in-plane and cross-plane thermal conductivity of CeO_2 thin film as a function of film thickness are also reported. These findings have an impact on heat dissipation in nanoelectronics and photonics, as well as the design of nanostructured thermoelectric materials with reduced thermal conductivity. To conclude, this work serves to moderate the existing ambiguity in the thermal conductivity value of CeO_2 and provides practical information on CeO_2 nanostructuring that will potentially meet the demands of numerous industrial applications.

4.6 Supplementary Informations

S.I.4.1) Phonon dispersion curves of CeO_2 for different qpoints.

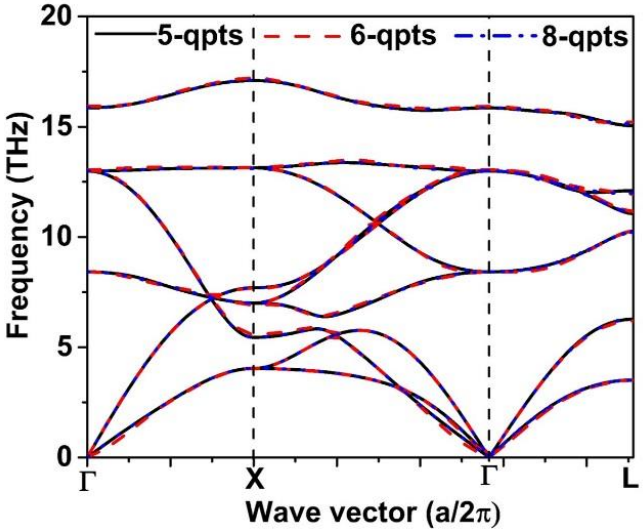

Fig. 4.12. Phonon dispersion with different q-points from DFPT.

S.I.4.2) The convergence of k_L with the number of iterations at 300 K.

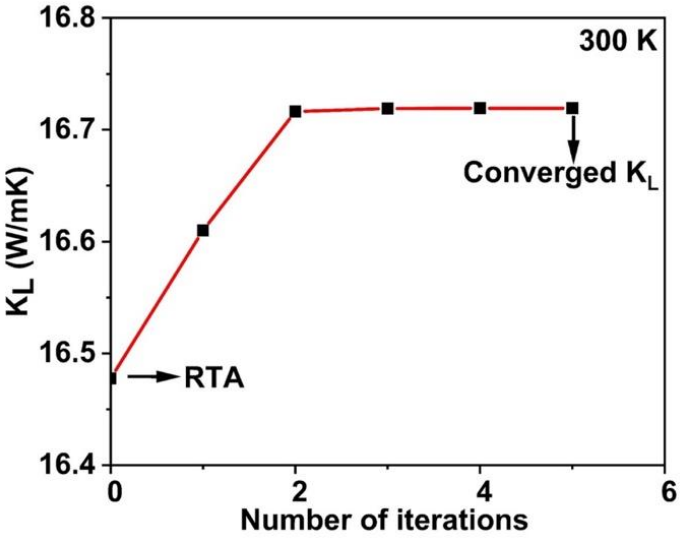

Fig. 4.13. The convergence of k_L with number of iterations.

S.I.4.3) Low temperature k_L of CeO_2.

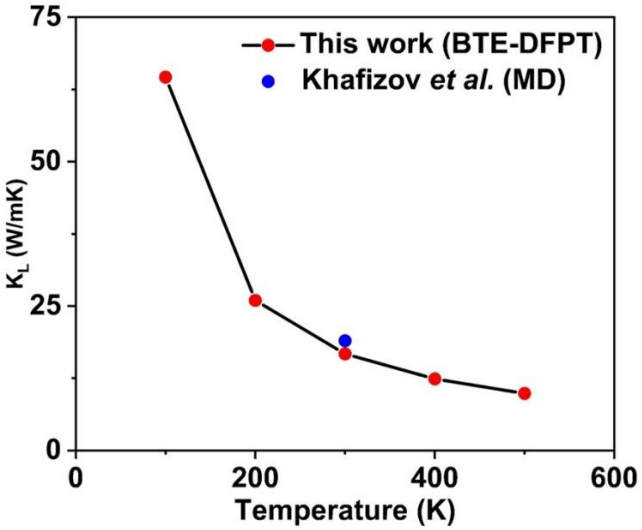

Fig. 4.14. The k_L of CeO_2 at temperature lower than room temperature compared with the value predicted by Khafizov *et al.* [171] at 300 K using molecular dynamics (MD) calculations.

S.I.4.4) Mode Grüneisen coefficient for different cases.

Fig. 4.16.a shows the changes in mode Grüneisen coefficient (γ_{qj}) with different q-points considered while maintaining the other parameters such as the nearest neighbour atoms (n) and the number of grid planes along each axis (N) constant.

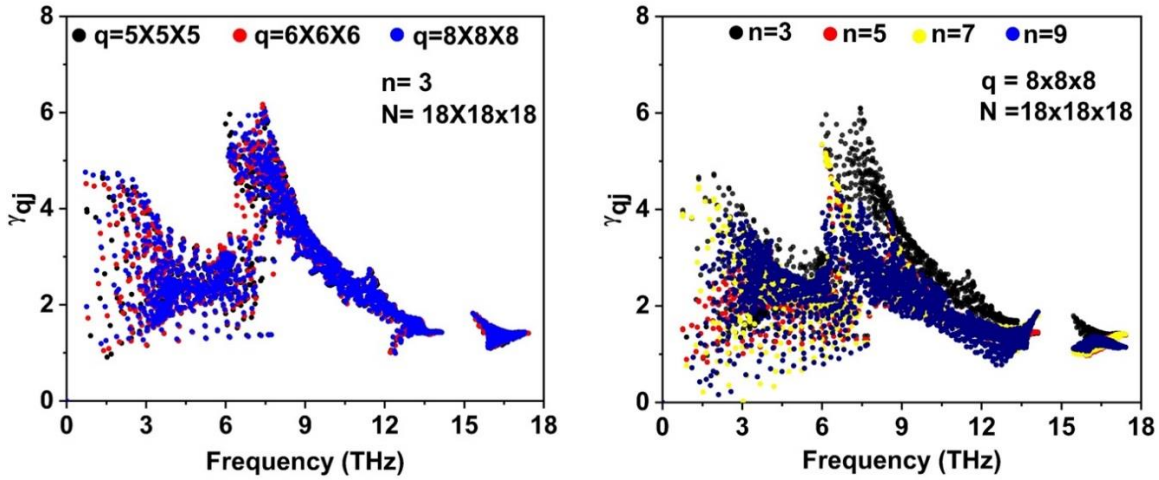

(a) (b)

Fig. 4.15. Mode Grüneisen coefficient (γ_{qj}) (a) for different q points (b) for different nearest neighbours.

Similarly, Fig. 4.16.b depicts the variations in γ_{qj} with different neighbouring atoms considered in the third order force constant calculation keeping the q-points and the N-grid constant. Fig. 4.16.a indicates that the variations in γ_{qj} with respect to different q-points are not significant whereas, the selection of the number of nearest neighbouring atoms in the third order force constant has a considerable effect on the γ_{qj} of CeO_2.

S.I. 4.5) XRD peaks of CeO_2 sintered at 1000 ^oC and 1100 ℃.

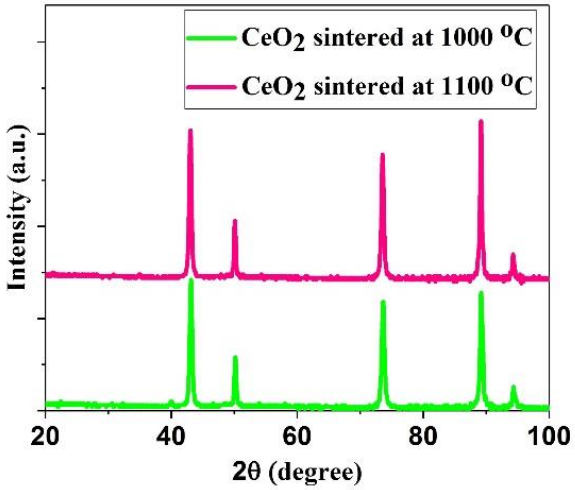

Fig. 4.16. XRD peaks of CeO_2 sintered at 1000 ℃ and 1100 ℃.

Chapter 5 : Thermal conductivity of bulk and nanowire of cubic-SiC from *ab initio* calculations

5.0 Overview

Bulk and nanoforms of SiC are considered as an additive in ceramic composite fuels to enhance the thermal conductivity. Therefore, it is essential to understand the thermal conductivity of SiC in its bulk and nanowire forms- a part of the second objective. This chapter discusses the *abinitio* prediction of the thermal conductivity of bulk and nanowire of cubic-SiC. Besides, we have also determined the structural, elastic, and thermodynamic properties of alpha-SiC using the DFT calculations.

The research findings reported in this chapter have been published as manuscript #3 as follows: Linu Malakkal, Barbara Szpunar, Ravi Kiran Siripurapu, Jerzy A. Szpunar "Thermal conductivity of bulk and nanowire of cubic-SiC from ab initio calculations", *Computational material science* vol. 128, pp. 249-256, 2017. The copyright permission to use this paper is provided in the Appendix D section.

The contributions of the PhD candidate are 1) performing DFT simulations, 2) analyzing of the results; 3) writing the manuscript for publication. My supervisors reviewed the paper before it was submitted for publication in this journal.

The differences between this chapter and the published paper are:

1. The figures have been replotted to maintain the consistency with the figures of other chapters.
2. The references of the manuscript are listed at the end of this thesis.

Thermal conductivity of bulk and nanowire of cubic-SiC from *ab initio* calculations

Linu Malakkal[1], Barbara Szpunar[2], Ravi Kiran Siripurapu[1], Jerzy A. Szpunar[1]

[1]Department of Mechanical Engineering, University of Saskatchewan

[2]Department of Physics and Engineering Physics, University of Saskatchewan

5.1 Abstract

In this work, we predict the structural, elastic, thermal and thermodynamic properties of alpha-silicon carbide (SiC) using the plane-wave pseudopotential approach to density functional theory (DFT) in the local density approximation (LDA). The lattice thermal conductivity of SiC is calculated using the Slack model and Boltzmann transport equation (BTE). We also provide the thermal conductivity of SiC nanowires and the dependence of the thermal conductivity on the diameter and their orientations. The ground state structural and elastic properties show excellent agreement with the experiments. The calculated phonon dispersion curve shows a good agreement with the experimental values measured at room temperature. The thermodynamic properties are studied using quasi-harmonic approximation (QHA), and the predicted properties agree well with the experiment. This study demonstrates the need for including the normal phonon scattering and boundary scattering to evaluate the thermal conductivities at low temperature and is evident from the fact that the thermal conductivity at low temperature predicted by the Slack model is higher compared to the value predicted by the BTE. Our BTE calculation for the bulk SiC agrees well with the known experimental results, and we also provide predictions for the case of SiC in the form of nanowires.

5.2 Introduction

The inherent properties of silicon carbide (SiC) have earned this ceramic material a wide range of industrial applications. The excellent mechanical, thermal, and chemical properties of SiC such as high stiffness, high hardness high mechanical strength at high temperature, high thermal conductivity, and resistance to oxidation made SiC a candidate for various application in nuclear industries [27,197]. After the Fukushima accident, the major focus of nuclear researchers has been the development of accident tolerant fuel (ATF). ATFs with high thermal conductivity can withstand the loss of coolant for a longer period. Currently, various materials with higher thermal conductivity are under consideration for improving the thermal properties of nuclear fuels. The

high thermal conductivity, high melting point, excellent chemical stability, low neutron cross-section and low swelling rate [4] gives SiC a significant advantage in this regard. SiC can, therefore, be used to enhance the thermal conductivity of existing nuclear fuels. Currently, SiC composites [198] are being considered as replacements for existing cladding materials. SiC composite cladding may offer a significant advantage over the zirconium alloys in Gen IV nuclear reactors that often operate at much higher temperatures. Its remarkable properties such as low neutron absorption, excellent corrosion resistance, and strength retention at high temperatures, could enable the development of efficient fuel cladding systems [197]. Also, urania-SiC composite fuel will have significantly improved thermal conductivity, and that will allow lowering the temperature of the fuel and avoiding fast oxidation of Zr alloy and generation of hydrogen. Such fuel/cladding systems with higher thermal conductivity will decrease the temperature in the centerline of fuel pellet and reduce the temperature gradient in the fuel. That will allow reducing thermal stress and will increase the resistance of pellet to cracking and swelling.

The potential applications of SiC composite at high-temperature warrants a more detailed examination of its thermo-mechanical properties. Some research groups have conducted experimental and simulation studies to understand the structural, electronic and thermodynamic properties of SiC [199–208]. However, our knowledge of the thermal conductivity of SiC at higher temperature is minimal. Recent reports that discuss the improvement in the strength of SiC composites by the addition of SiC nanowires is of particular interest because one-dimensional nanostructures used as nanoarchitecture in microelectronics have the potential to improve the thermal conductivity of SiC for nuclear and other applications. SiC nanowires are also of keen interest in mechanical applications [209]; the toughness of the nanocomposites is reported to double by the addition of SiC-nanowire into the SiC whisker-reinforced [210].

In this article, we report the thermal conductivity of bulk and nanowire SiC up to its melting temperature, by solving BTE using *ab initio* calculations. We have used the Sheng-BTE software [83], a solver for phonon contribution to thermal conductivity. Additionally, the phonon contribution to thermal conductivity from BTE are compared with those predicted using the Slack model [172]. The thermo-mechanical properties required as input to the Slack equation are predicted using the first principle code Quantum ESPRESSO (QE) [73]. We employ an interface to QE, qe-nipy-advanced [74], developed in our group. Structural optimization was performed to

evaluate the ground state properties of SiC; QHA is used to compute the properties such as fixed volume heat capacity (C_V), entropy (S), and volume thermal expansion coefficient (α_V) [211]. Further, the Slack equation has been applied to calculate the phonon contribution to thermal conductivity. We have also developed a FORTRAN code that accepts the inputs in a comma-separated format and conveniently generates the phonons contribution to thermal conductivity as a function of temperature, in the same format.

5.3 Methodology

In this section, we briefly describe the methodology used to calculate the thermo-mechanical properties of cubic-SiC. In section 5.3.1, we discuss the calculation of ground-state structural and mechanical properties; in section 5.3.2, we discuss the lattice dynamics and describe the calculation of lattice-assisted properties within QHA. Finally, section 5.3.3 provides the explanation of thermal conductivity calculation with the Slack model method and the BTE.

5.3.1 Calculation of ground states structural and mechanical properties

Geometry optimization evaluates the structural properties at zero Kelvin temperature by minimizing the total energy by varying both cell parameter and atom positions. The ground state structural properties were also assessed using the Birch-Murnaghan equation of state [212]. The elastic constants were calculated using the stress-strain method [184,185]. From the elastic constants, the bulk modulus (B), shear modulus (G), Young's modulus (Y), and Poisson's ratio (η) were determined using the Voigt-Reuss-Hill averaging scheme [186–188]. Because we are analyzing a cubic, polycrystalline structure, therefore the elastic moduli can be evaluated assuming an isotropic aggregate of grains with non-isotropic elastic properties. For a cubic symmetry, there are three independent elastic constants:C_{11}, C_{12}, and C_{44}. The bulk modulus for a cubic structure is the same for the Voigt, Reuss, and Hill averages, as shown in the equation (5.1).

$$B = \frac{1}{3}(C_{11} + 2C_{12}) \tag{5.1}$$

Equation (5.2) gives the shear modulus in the Voigt average:

$$G_V = \frac{C_{11} - C_{12} + 3C_{44}}{5} \tag{5.2}$$

while equation (5.3) gives the Reuss average:

$$G_R = \frac{(5(C_{11} - C_{12})C_{44})}{4C_{44} + 3(C_{11} - C_{12})} \tag{5.3}$$

The arithmetic mean (Hill) $G = (G_V + G_R)/2$ is taken as shear modulus.

The Young's modulus is calculated as:

$$Y = \frac{9BG}{3B + G} \tag{5.4}$$

The Poisson's ratio is calculated as:

$$\eta = \frac{3B - 2G}{2(3B + G)} \tag{5.5}$$

5.3.2 Thermodynamic properties with quasi-harmonic approximation

The phonon density of states is obtained using Density-Functional Perturbation Theory (DFPT) as implemented in QE [73]. With QHA, the vibrational energy (F_{vib}) can be evaluated from phonon at different volume [211]. Described below are the thermodynamic properties derived from phonons using QHA.

(a) Thermal Expansion

The Helmholtz free energy at volume $V(T)$ and temperature T is a sum of the electronic energy $(E(\,V(T), T)$ and vibrational energy $(F_{vib}(V(T), T))$ for a given volume $V(T)$ and temperature (T):

$$F(V(T), T) = E(V(T)) + F_{vib}(V(T), T) \tag{5.6}$$

We can neglect the electronic entropy for insulators. The vibrational Helmholtz free energy is calculated by evaluating the phonon density of states at different volumes and integrating the energy of phonons $(\hbar\omega)$ over the density of states $(\rho(\omega))$ and weighing it by the temperature-dependent Boltzmann factor as described before [129]:

$$F_{ph}(V(T), T) = k_B T \int_{\omega_{min}}^{\omega_{max}} \rho(\omega)\ \ln\left[2\sinh\left(\frac{\hbar\omega}{2k_B T}\right)\right] d\omega \tag{5.7}$$

where k_B is the Boltzmann constant. The equilibrium volume at each temperature was calculated by fitting the free energy to the Birch-Murnaghan equation of state [212]:

$$F(V(T),T) = F_0(T) + \frac{B_0(T)V(T)}{B_0'(T)}\left[\frac{\left(\frac{V_0(T)}{V(T)}\right)^{B_o'(T)}}{B_0'(T)-1} + 1\right] - \frac{B_0(T)V_0(T)}{B_0'(T)-1} \tag{5.8}$$

where $F_0(T)$, $B_0(T)$, and $B_o'(T)$ are the values of the total free energy, bulk modulus and the first derivative of bulk modulus, for the equilibrium primitive unit cell volume $V_0(T)$ respectively at the temperature T. The equilibrium lattice constant for the conventional unit cell was calculated at each temperature from the evaluated conventional unit cell volume (for a face-centered crystal structure four times larger than primitive volume) as:

$$a^c(T) = (V_o^c(T))^{\frac{1}{3}} \tag{5.9}$$

The linear and volumetric thermal expansion coefficients are related and therefore could be calculated from each other at constant pressure (P) as follows:

$$\alpha(T)_p = \frac{1}{L(T)}\left(\frac{\partial L(T)}{\partial T}\right)_p = \frac{1}{3V_o(T)}\left(\frac{\partial V_o(T)}{\partial T}\right)_p \tag{5.10}$$

(b) Heat Capacity

The C_V and S are calculated using equations (5.11) and (5.12) for fixed volume and constant pressure, respectively.

$$C_V(T) = N_A k_B \int_{\omega_{min}}^{\omega_{max}} \frac{\left(\frac{\hbar\omega}{k_B T}\right)^2 e^{\left(\frac{\hbar\omega}{k_B T}\right)}}{[e^{\left(\frac{\hbar\omega}{k_B T}\right)} - 1]^2}\,\rho(\omega)d\omega \tag{5.11}$$

$$S = -k_B \int_0^{\infty} \rho(\omega)\left(ln\left(1 - e^{-\frac{\hbar\omega}{k_B T}}\right) + \frac{\hbar\omega}{k_B T\left(1 - e^{-\frac{\hbar\omega}{k_B T}}\right)}\right)d\omega \tag{5.12}$$

where N_A is Avogadro's number, k_B is the Boltzmann constant and $\rho(\omega)$ is the density of states of phonons (with $\hbar\omega$ energy) per primitive unit cell. Note that C_V remains constant at higher temperatures. The heat capacity at constant pressure C_p is calculated from C_V using equation (5.13) and is compared with available experimental data:

$$C_P = C_V + \alpha_V^2 B(T) V(T) T \tag{5.13}$$

5.3.3 Thermal conductivity

(a) Slack Model

The lattice thermal conductivity (k_L) of SiC is evaluated using the Slack model, according to equation (5.14):

$$k_L = \frac{C\theta(T)^3 M_M V(T)^{\frac{1}{3}}}{\left(n\gamma(T)\right)^2 T} \tag{5.14}$$

Where C is a constant, equal to 3.04×10^4 $Wm^{-2}K^{-1}$ g^{-1} mol and M_M molar mass per primitive cell (40.1 g mol^{-1} for SiC) and $V(T)$ the volume of the primitive cell, but in cubic meters. $\gamma(T)$ is the Grüneisen parameter and $\theta(T)$ is Debye temperature. The Grüneisen parameter is calculated using equation (5.15):

$$\gamma(T) = \frac{3\alpha(T)V_M(T)}{C_V(T)\beta(T)} \tag{5.15}$$

Where $\alpha(T), V_M(T), C_V(T), \beta(T)$ are respectively linear thermal expansion coefficient, molar volume, the fixed volume heat capacity per mole and compressibility. Compressibility is calculated as the inverse of bulk modulus. Equation (5.16) gives Debye temperature (θ in K) within the isotropic approximation (in atomic units: m = ħ = e = 1), where M is the mass, n is the number of atoms per primitive cell (2 for SiC) with its volume $V(T)$ (calculated using $a(T)$ derived above) and $f(\eta(T))$ is the scaling function [211] calculated using equation (5.17):

$$\theta(T) = \frac{\left(6\pi^2 V(T)^{\frac{1}{2}} n\right)^{\frac{1}{3}} f\left(\eta(T)\right)}{k_B(\beta(T)M)^{\frac{1}{2}}} \tag{5.16}$$

where equation (5.5) evaluates the Poisson's ratio ($\eta(T)$) as a function of temperature using the calculated shear and Young moduli:

$$f(\eta\,(T)) = 3^{\frac{1}{3}}\left[2\left(\frac{2(1+\eta\,(T))}{3(1-2\eta\,(T))}\right)^{\frac{3}{2}} + \left(\frac{1+\eta\,(T)}{3(1-\eta(T))}\right)^{\frac{3}{2}}\right]^{-\frac{1}{3}} \tag{5.17}$$

(b) Boltzmann Transport Equation (BTE)

We have used ShengBTE a solver for BTE for phonons to evaluate the lattice thermal conductivity (k_L) by combining first-principles techniques (QE) to obtain interatomic force constants. As used in the QHA, it is the second-order force constant (harmonic approximation), and in BTE, we also include the third-order force constant to take into account the anharmonic effect as well. In the approach implemented in ShengBTE, equation (2.21) gives the expression to compute the lattice thermal conductivity tensor [174]. At high temperatures, the phonon lifetime in crystals is determined by the phonon-phonon scattering. A useful parameter that describes the phonon-phonon scattering is the mode Grüneisen parameter given by equation (4.5). The harmonic mode Grüneisen parameter ($\gamma_p(q)\big|_{har}$) can be obtained by the phonon frequency shift with respect to the volume by equation (5.19), where V_0 is the equilibrium volume.

$$\gamma_p(q)\big|_{har} = -\left(\frac{V_o}{\omega_p(q)}\right)\frac{\partial \omega_p(q)}{\partial V} \tag{5.19}$$

The average Grüneisen parameter with temperature is given by the equation (5.20)

$$\gamma_{Ave} = \frac{1}{C_v}\sum_{p,q}\gamma_p(q)C_{v,p}(q) \tag{5.20}$$

Were $C_{v,p}(q)$ is the mode heat capacity and

$$C_v = \sum_{p,q} k_B\left[\frac{\hbar\omega_p(q)}{k_BT}\right]^2\left(\frac{e^{\frac{\left(\hbar\omega_p(q)\right)}{k_BT}}}{\left(e^{\frac{\hbar\omega_p(q)}{k_BT}}-1\right)^2}\right) \tag{5.21}$$

Sheng BTE also provides the thermal conductivity of nanowires. As mentioned in the introduction, SiC nanowires are of substantial practical interest. To calculate the k_L of nanowires, ShengBTE obtains numerical solutions to the linearized *ab-initio* Peierls-Boltzmann phonon transport equation (PBTE) [213]. The detailed description of the assumptions made to calculate the k_L of the nanowire is described in detail elsewhere [214]. However, for the benefit of the reader, we discuss the key approach in calculating the thermal conductivity of nanowires. For the nanowires that are thick enough to include some unit cells in the transverse direction the phonon dispersion of the bulk material can be used whereas in the direction perpendicular to the nanowire, the phonon

lifetime becomes space-dependent due to the break in the translational symmetry. This additional space-dependent term in the BTE makes the solution computationally demanding. Therefore, Li *et al.* [83] developed an alternative approach in which the focus is in the longer direction, and removes the other two spatial degrees of freedom partially by using the cross-sectional averages. The boundary conditions to solve BTE has a specularity parameter to account for a fraction of incident phonon scattered specularly, but in this case, the phonon scattering is assumed as completely random (i.e. diffusive boundary conditions). Therefore, we obtain the solution of BTE in nanowires for the diffusive boundary conditions. Ref. [215] provides a detailed description of physics and workflow to solve BTE.

5.4 Computational Details

Calculations were performed using DFPT implemented in the Quantum ESPRESSO code. The pseudopotentials used were norm conserved, and the electronic exchange-correlation is described by local density approximation (LDA) with Perdew-Zunger parametrization. The geometry was optimized with the stress components less than 0.01 GPa. We obtained the total energy convergence using a Monkhorst-Pack sampling of 8×8×8 and the plane wave's cut-off energy of 150 Ry. The dynamical matrices for phonon density of states were calculated on a mesh of 5×5×5 q-points in the irreducible Brillouin zone. QHA is used to investigate the thermodynamic properties. The thermal conductivity of SiC is predicted using a Slack model and BTE. A mesh of 5×5×5 q-points was used to calculate the second-order interatomic force constants (IFCs) needed to compute the thermal conductivity of SiC. A supercell of 4×4×4 was used to obtain the third-order IFCs. The force cut-off distance was set such that the interaction range is up to the third nearest neighbors. The BTE was then solved to obtain the thermal conductivity of bulk and nanowire of SiC.

5.5 Results and Discussions.

5.5.1. Structural and mechanical properties

Table 5.1 shows the comparison of the calculated ground state structural and mechanical properties of cubic SiC with values obtained from the experiment [208]. The computed structural and mechanical properties of SiC within QHA at a temperature of 300 K, are also provided. The calculated lattice constant at 300 K agrees very well with experiment [208]. The single crystal stiffness constants of SiC calculated by using a stress-strain method with the help of the QE_nipy-

advanced interface [184,185] also shows good agreement with the experiment. From the calculated stiffness constants, the polycrystalline properties such as bulk modulus, shear modulus, Young's modulus and Poisson's ratio are calculated using the Voigt-Reuss-Hill approach as described in Section 5.3.1. The calculated bulk modulus by EOS and elastic constants are 223 GPa and 221 GPa, respectively and are in agreement with the experimental value of 224 GPa [208].

Table 5.1. Structural and Mechanical Properties of cubic-SiC at 0 K and 300 K evaluated by QHA with experiments [208].

Properties	LDA (0 K)	LDA (300 K)	Experiment [208]
Lattice Parameter (Å)	4.3437	4.3558	4.36
C_{11} (GPa)	397	388	390
C_{12} (GPa)	136	131	142
C_{44} (GPa)	275	267	256
Bulk Modulus (B) (GPa)	223	216	224
Shear Modulus (G) (GPa)	203.9	199	192
Young Modulus (Y) (GPa)	468.8	457	448
Poisson ratio (η)	0.1496	0.1481	0.168

The melting temperatures of the solids can be obtained from the C_{11} elastic constant using an empirical relationship between T_m and C_{11}: $T_m = 553 + 5.91\ C_{11}$ with units of K for T_m and GPa for C_{11} [216]. The estimated melting point of SiC (2900 K) is only 7% lesser than the experimental value obtained (3100 K). The structural and elastic properties of SiC predicted by the using LDA pseudopotential are also close to the experimental values. Since the agreement of calculated and experimental properties was exquisite, we have used the same LDA pseudopotential for the study of phonon dispersion and thermodynamic properties of SiC.

5.5.2 Phonon Dispersion and Thermodynamic properties

The phonon dispersion relations of SiC at its equilibrium volume along the high symmetric Γ-X-Γ-L directions are shown in Fig. 5.1.a. SiC has two (n) atoms in its primitive unit cell and therefore has six phonon modes in the dispersion relations. There are three dimensions$(d = 3)$, and thus three acoustic modes and $d\ (n - 1) =$ three optical modes. The calculated acoustic and optical modes are in excellent agreement with the experiment done by Serrano *et al.* [217] at room

temperature using inelastic x-ray scattering (IXS) with the synchrotron radiation source. The Born effective charges (Z^*) of SiC using the LDA functional (Z^*_{Si} = 2.71 and Z^*_C= -2.71) compares well with the experimental values of (Z^*_{Si} = 2.69 and Z^*_C = -2.69) [218]. The dielectric constant of SiC from our calculation is 6.88 and are in agreement with the experimental value of 6.52 [219].

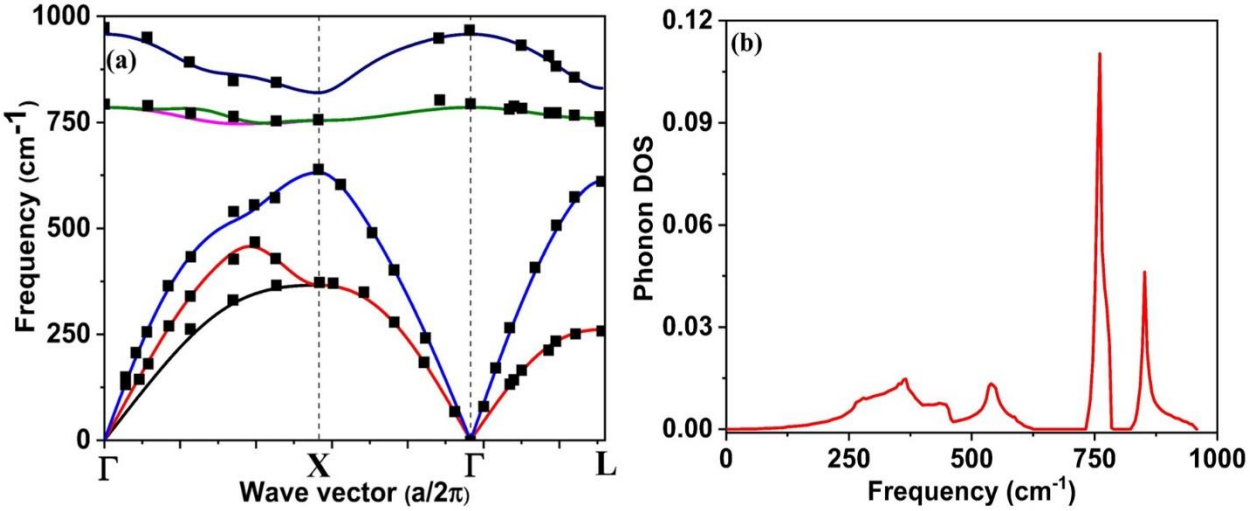

Fig. 5.1. (a) Phonon dispersion curve of the silicon carbide cubic structure. The solid lines show the theoretical prediction and the black dot are the experimental points measured by Serrano *et al.* [217] using IXS. (b) Shows the phonon density of states for SiC.

The density of state plot in Fig. 5.1.b indicates that the phonon states are densely populated in the region around 750-800 cm^{-1}. Similar behavior is shown by aluminum nitride another zinc blende structure [220]. The sharp peak in PDOS of SiC is due to the flat transverse optical branch. The accurate phonon dispersion relations allow us to predict the thermodynamic properties such as heat capacity at the fixed volume, entropy, and coefficient of linear thermal expansion correctly.

5.5.3 Thermal Properties

Section 5.3.2 and 5.3.3 describes calculating the thermodynamic properties using QHA and BTE, respectively. At relatively low temperatures and up to near to the Debye temperature of the material, the DFPT combined with QHA is a powerful method to predict the lattice assisted properties. Fig. 5.2.a clearly shows that the C_p derived by equation (5.13) by both approaches are nearly the same and agrees well with experiment [221]. The coefficient of thermal expansion (CLTE) is an important design parameter for high-temperature structural applications. Fig. 5.2.b shows the CLTE of SiC as a function of temperature in comparison with the experimental data by

Taylor *et al.* [222] and a simulation work by Karch *et al.* [202]. Comparison of the results shows that the current CLTE and previously evaluated values [201] are in good agreement at a lower temperature below 600 K but less than the known experimental data by Taylor. However, our calculation agrees better with the experiments at high temperature compared to the previous DFT calculations. The entropy (calculated using equation (5.12) and shown in Fig. 5.2.c values are also in good agreement with the available experimental data from Barin [221].

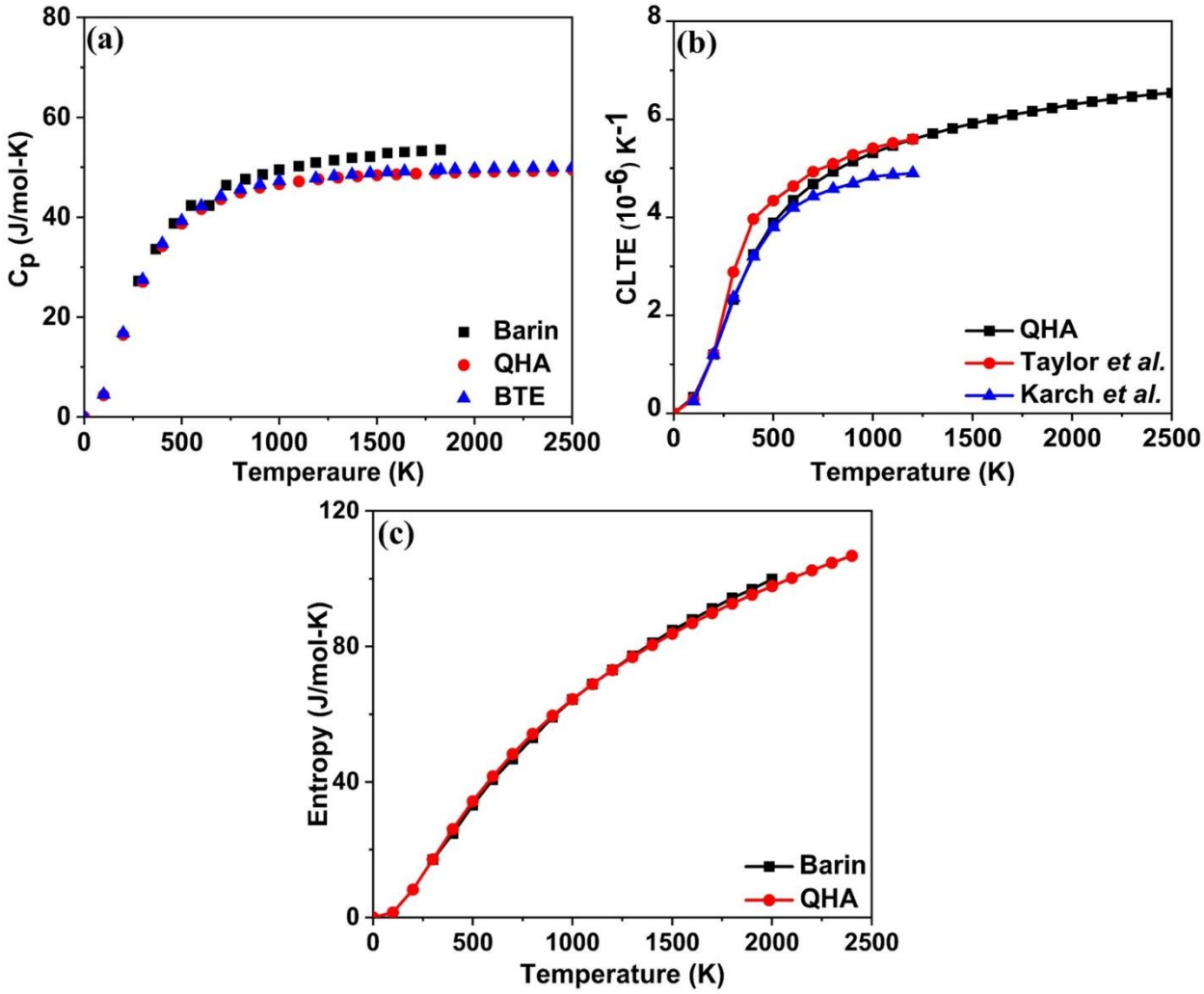

Fig. 5.2. (a) Shows the comparison of C_p from QHA and BTE (using equation (5.13)) with experiment. (b) Comparison of CLTE from our QHA calculation with experiment and previous DFT calculation (c) Entropy of SiC compared with the experiment from Barin [221].

Debye temperature of SiC as a function of temperature is shown in Fig. 5.3.a. The experimental value of Debye temperature of cubic SiC is 1200 K at room temperature, and the value predicted

by this calculation is 1180 K. The Grüneisen coefficient (γ) is an important parameter that any model of thermal conductivity needs to consider. This parameter is the measure of anharmonicity of material. As shown in Fig. 5.3.b, we calculated the γ as a function of temperature using both the QHA and BTE. The γ values from QHA and BTE vary between 0.92-0.97 and between 0.78-0.79 respectively for a temperature range between 1200-2500 K. At high temperatures, the deviation of the γ value is small, and hence, in the case of SiC, we can neglect the anharmonicity at high temperature.

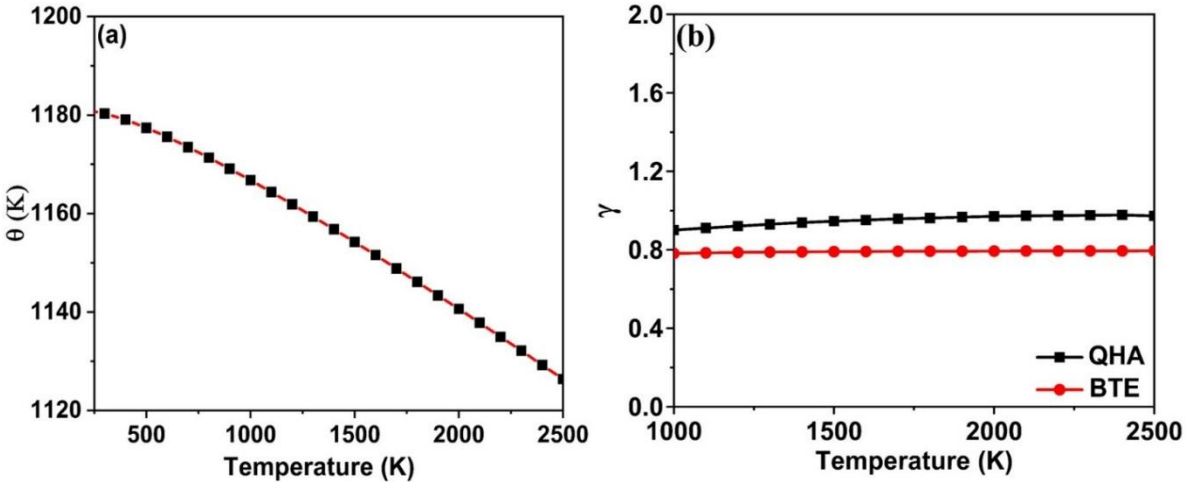

Fig. 5.3. (a) Debye temperature as a function of temperature (b) Grüneisen coefficient as a function of temperature using QHA and BTE.

5.5.4 Lattice Thermal Conductivity

Fig. 5.4.a shows that the k_L predicted by BTE is in good agreement with the experiment done by Taylor *et al.* [222]. The previous theoretical work by Spargavina [223] that uses experimental data's to solve BTE and a fully *abinitio* calculation at low temperature by Lindsay *et al.* [224] serves as validation to our k_L results at high temperature. In Fig. 5.4.b we compare SiC thermal conductivity calculated using both Slack model and BTE. At relatively low temperatures below the Debye temperature (1200 K) the Slack method predicts higher k_L compared to that observed from BTE calculation and the experiment. The high value of k_L at low temperature is because Slack method does not consider the boundary scattering and quasi-momentum conserving (normal process), which is dominant at low temperatures. The Slack model predictions are better at a relatively high temperature near to the Debye temperature where the non-quasi-momentum conserving three-phonons scattering (umklapp process) is dominant. We get the right prediction

for overall temperature range using BTE because it takes into account the boundary scattering, normal process, and the umklapp process. We have extrapolated our calculation up to the melting point temperature because as shown in Fig. 5.3.b Grüneisen coefficient does not vary at high temperatures. Therefore, we can conclude that the high-temperature k_L provided here is complementary data in the design of accident tolerant nuclear fuels.

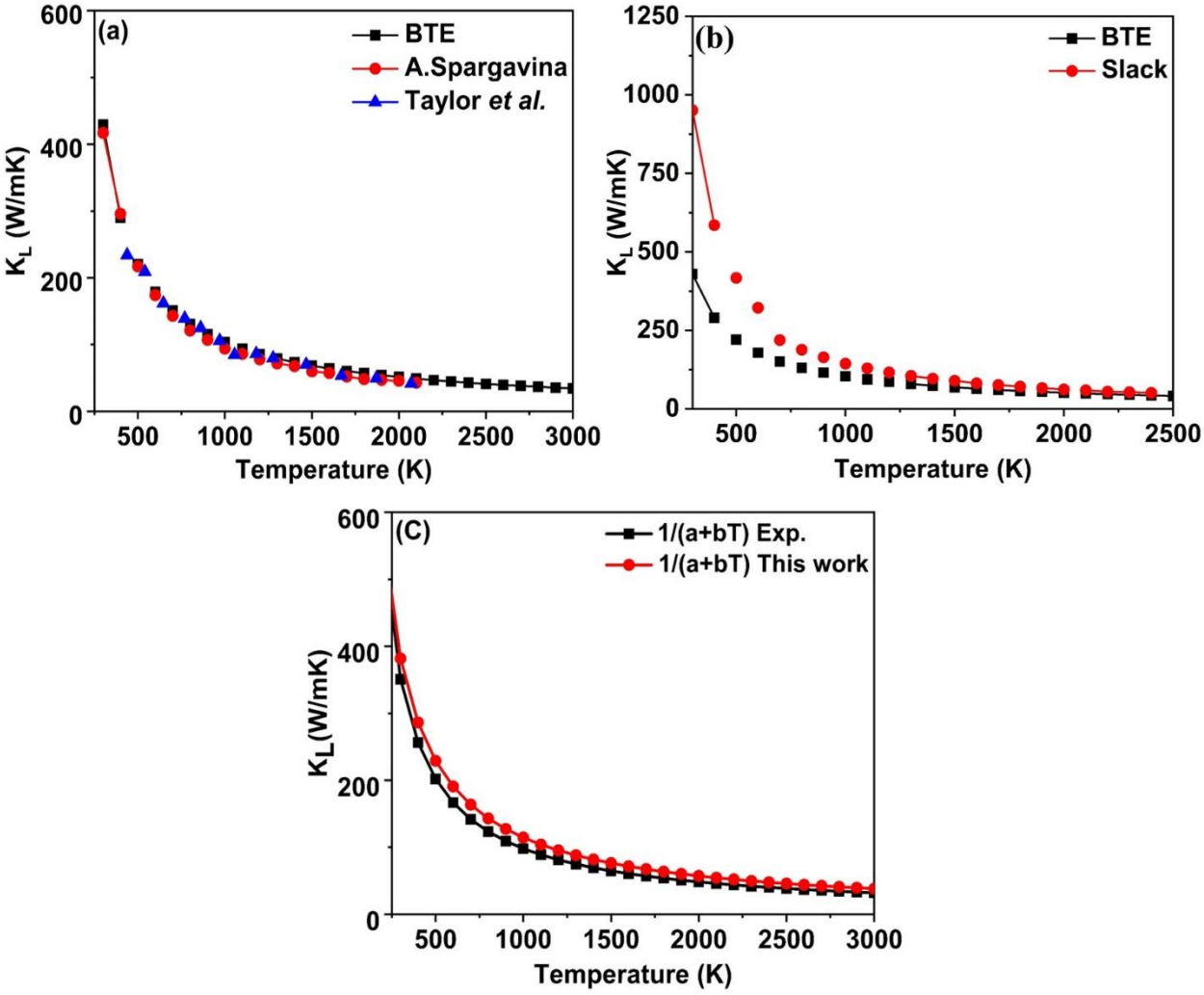

Fig. 5.4. Thermal conductivity of SiC (a) Comparison of BTE with other simulation and experiment [222] (b) Comparison of our work between BTE and Slack (c) inverse fit of k_L as obtained from this work and previous theoretical expression from experiments [208].

Theoretically, the k_L of SiC is expressed as a function of $[a + bT]^{-1}$ with constants a and b. In Fig. 5.4.c, we plot k_L obtained from the theoretical expression of $k_L = [7.66 \times 10^{-12} + 8.73 \times 10^{-6}\, T]^{-1}$ from the simulated values of k_L using BTE and compare with the previously derived

inverse fit calculated from an experimental single crystal SiC data above 300 K [208] ($k_L = [-0.0003 + 1.05 \times 10^{-5}\, T]^{-1}$). The inverse fit from the simulated value and the experiments compare well; however, the previously reported expression uses a non-physical negative value for a parameter associated with phonon scattering on defects. The high-temperature conductivity is also known as a minimal thermal conductivity can be evaluated from inverse fit or using Young's modulus (equation. 5.4) and Clark's model [225] from the equation: $k_{\min} = 0.87\, k_B\, N_A^{\frac{2}{3}}\, M^{-\frac{2}{3}}\, m^{\frac{2}{3}}\, Y^{\frac{1}{2}}\, \rho^{\frac{1}{6}}$ where ρ is the density, M refers to the molar mass, m is the total number of atoms per formula, N_A is the Avogadro's constant, k_B is the Boltzmann's constant. This calculated value of 3.01 W/mK compares well with the previously reported value of 3 W/mK [225]. However, this value is one order of magnitude smaller than that predicted by simulation and the inverse correlation between the previous experimental data. Therefore, we recommend further experiments to verify the minimal thermal conductivity of SiC.

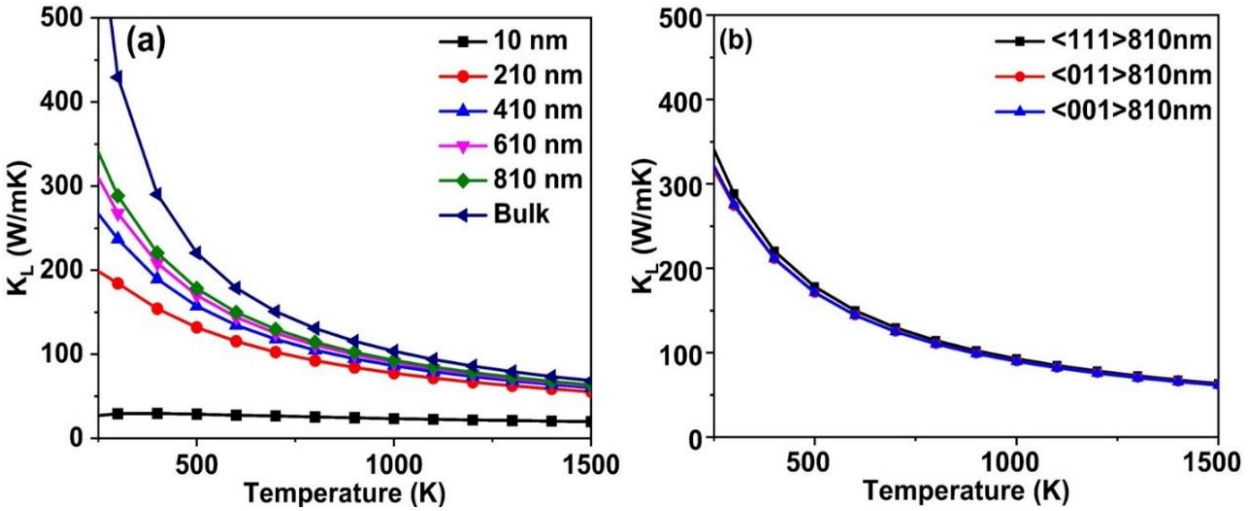

Fig. 5.5. Thermal conductivity of SiC nanowires (a) dependence of thermal conductivity on the diameter of nanowires all for [111] orientations (b) dependence of thermal conductivity on orientations of nanowires.

The nanostructures of some high k_L materials like silicon and diamond are previously reported [226,227], and it would be interesting to know how the thermal conductivity of SiC nanowires depends on the size and the orientation of the nanowire. Therefore, in this study, we investigated cylindrical NWs with diameters above 10 nm in the temperature range of 300-1000 K, in the [111],

[001], [011] crystallographic orientations. Our results for SiC nanowires indicate that k_L is significantly reduced compared to its bulk value (Fig. 5.5.a).

For instance, at 200 nm, the k_L is reduced to 57% compared to the bulk value, whereas in the case of Si nanowire, the reduction was reported as 43% [214]. The significant decrease of k_L of SiC nanowire indicates that the boundary scattering effect k_L considerably more in SiC than in Si. The lower thermal conductivity of nanowires compared to bulk materials are attributed to the following facts; decrease in the mean free paths of the phonons due to surface scattering of a large fraction of surface atoms, the modifications in the phonon group velocity and scattering mechanism due to the change in phonon spectrum in one-dimensional structure.

The increase in phonon-phonon interaction due to the reduction of size also cause an increase in the thermal resistance, thereby reducing k_L [226,227]. Fig. 5.5.b shows the calculated k_L of SiC nanowires for three different orientations [111], [110] and [111]. The result shows that k_L is 10% higher in the [111] direction compared to the [110] and [001] direction. This indicates that the [111] is of importance for SiC nanowires in high-temperature applications. This variation in the thermal conductivity of nanowire on its orientation attributes to the anisotropic phonon dispersion [226]. Our calculation is awaiting the experimental validation. However, the quantitative understanding of the size and orientation dependence of thermal conductivity could provide design and fabrication criteria for making nanoscale devices and for other structural applications.

5.6 Conclusion

In conclusion, the thermal conductivity of SiC cubic phase, in bulk and nanowire form, using *ab initio* approach has been calculated. The existing experimental results for bulk SiC cubic phase compares well with these estimated values. The CLTE calculated using QHA is in excellent agreement with the experiments and are considerably more accurate than the previous DFT calculations. The calculation of thermal conductivity by two different approaches (Slack versus BTE) clearly indicates that the normal process and the boundary scattering are significant effects at the temperatures below 1200 K. New theoretical correlation for thermal conductivity of SiC is derived. The thermal conductivity of SiC nanowires displayed a dependence on diameter and crystal orientation. Although previous studies are describing the synthesis and mechanical properties of nanowires, this study contributes towards a better understanding of the thermal

conductivity of SiC nanowires. Furthermore, the work presented in this article may be used to guide experimental work on any future investigations of thermal conductivity of nanowires.

Chapter 6 : Thermal conductivity of wurtzite and zinc blende cubic phases of BeO from ab initio calculations

6.0 Overview

This chapter covers the latter part of the second objective of the thesis in finding the influence of structure on the thermo-mechanical properties and the thermal conductivity of the additive material BeO using DFT. Beryllium oxide is another candidate material considered as an additive in nuclear fuel to enhance the thermal conductivity. BeO is found in its wurtzite structure, and the thermal conductivity is expected to be anisotropic. Therefore, it is important to determine the extent of anisotropy in BeO. Hence, in this chapter, the directional dependence of the thermal conductivity of w-BeO is explored. Also, this chapter sheds light into the structural, mechanical, thermal and thermodynamic properties of Beryllium oxide (BeO) in the zinc blende (ZB) and wurtzite (WZ).

The research findings reported in this chapter have been published as manuscript #4 as follows:
L. Malakkal, B. Szpunar, R.K. Siripurapu, J. Zuniga, J.A. Szpunar; "Thermal conductivity of wurtzite and zinc-blende cubic phases of BeO from *ab initio* calculations"; published in Solid-State Sciences Vol. 65 pp.79-87 (2017). The copyright permission to use this paper is provided in Appendix E

The contributions of the PhD candidate are 1) performing DFT simulations, 2) analyzing of the results; 3) writing the manuscript for publication. My supervisors reviewed the paper before it was submitted for publication in this journal.

The differences between this chapter and the published paper are:

1. The equations that describe the calculations of thermodynamics properties with QHA has been removed from this chapter to avoid repetition. These equations can be found in chapter 5 of the thesis.
2. The figures have been replotted to maintain the consistency with the figures of other chapters.
3. The references of the manuscript are listed at the end of this thesis.
4. The description of lattice thermal conductivity is removed as this portion is explained in section 2.1.8

Thermal conductivity of wurtzite and zinc blende cubic phases of BeO from *ab initio* calculations

Linu Malakkal[1], Barbara Szpunar[2], Ravi Kiran Siripurapu[1], Juan Carlos Zuniga[3], Jerzy A. Szpunar[1]

[1]Department of Mechanical Engineering, University of Saskatchewan,

[2]Department of Physics and Engineering Physics, University of Saskatchewan,

[3]Information and Communications Technology, Research Computing, University of Saskatchewan.

6.1 Abstract

The structural, mechanical, thermal and thermodynamic properties of Beryllium oxide (BeO) in the zinc blende (ZB) and wurtzite (WZ) form have been calculated using the density functional theory (DFT) in the general gradient approximation (GGA). The ground state structural and elastic properties of w-BeO are calculated using the new GGA ultrasoft pseudopotentials for solids (PBEsol); the simulated results have shown excellent agreement with the experiments. The thermodynamic properties are studied using quasi-harmonic approximation (QHA), and the predicted properties agree well with the experiment for the WZ phase. Both the Boltzmann transport equation (BTE) and Slack model were used to calculate the lattice thermal conductivity of wurtzite BeO (w-BeO). Furthermore, the thermal conductivity along the crystallographic 'a' and 'c' axis is investigated using BTE. Our calculation of w-BeO agrees well with the available experimental measurements. Apart from these studies on w-BeO, we have also compared the mechanical, structural and phonon dispersions of z-BeO with previously reported theoretical studies. Additionally, we report the volume thermal expansion and the heat capacity at a constant pressure of z-BeO for the first time and the bulk thermal conductivity of zinc blende BeO (z-BeO) using BTE.

6.2 Introduction

BeO owes its uniqueness to its excellent mechanical, thermal and chemical properties compared to other alkali metals in this series. The wide range industrial usage of this ceramic material is due to its high stiffness, hardness, mechanical strength, thermal conductivity and resistance to oxidation. In the nuclear industry, BeO finds application as a moderator and as an additive in the recently proposed accident tolerant nuclear fuel [4]. The composite fuel (UO_2-BeO) [23] is

expected to have significantly improved thermal conductivity allowing for the lowering of fuel temperature by avoiding fast oxidation of Zr alloy cladding and generation of hydrogen. Such composite fuels with higher thermal conductivity enhance heat dissipation hence decreasing the temperature in the centerline of fuel pellet and reducing the temperature gradient. The faster heat dissipation also reduces the thermal stress, preventing the cracking and increasing the longevity of the pellet. Additionally, BeO also finds application in developing semiconductor devices, in rocket engines and as a filler in thermal interfaces.

BeO crystallizes in the wurtzite (WZ), cubic zinc blende (ZB) and tetragonal structures. The structural [228], mechanical [228], optical [229], electronic [230], thermodynamics [231] and thermal conductivity [78, 231–233] of the most stable wurtzite BeO (w-BeO) form has been studied by various groups. However, it is noted that no sufficient investigations have been conducted to understand the properties of w-BeO at high-temperatures. The room temperature w-BeO transforms into zinc-blende BeO (z-BeO) structure at 91 GPa. Theoretical calculations of the ZB-phase are limited to the structural, elastic, electronic and phonon properties [234]. Apart from the thermal conductivity prediction at low temperature by Li *et al.* [235], no other reports are available describing the thermal properties in literature. The results presented in this article is focusing on the thermal properties and thermal conductivities of ZB phase, despite the lack of experimental validation.

Among the phases of BeO, the wurtzite form is perhaps the most studied. In general, computational methods using DFT are widely used to predict the properties of the materials with good accuracy. Previous first principles calculations [236–238] investigated the structural, electronic and mechanical properties of w-BeO. Munima *et al.* [239] presented a detailed description of the phonon dispersion relations of w-BeO using first principles. Urszula [240], Luo *et al.* [241] and Song *et al.* [242] studied the thermodynamic properties using quasi-harmonic approximation (QHA) [211]. All the previous calculations used local density approximation (LDA) and generalized gradient approximation (GGA-Perdew Burke Ernzerhof (PBE)) [240] as the exchange-correlation function. The DFT calculation using LDA tend to over-bind and underestimate the lattice parameter, and the GGA-PBE functional had the opposite effect. To overcome the limitation of the LDA and GGA-PBE methods in the previous study, we employ the GGA- PBEsol functional developed for the solid phase (PBEsol) [139].

Moreover, all earlier attempts to describe the thermal conductivity of w-BeO using simulations [235,243] were limited to lower temperatures. We also noted that the calculated thermal conductivity of w-BeO using Slack model was four times smaller than the measured value at room temperature [33]. The lack of thermal conductivity data at high-temperature, the scattered experimental thermal conductivity values, and possible applications of w-BeO in this range of temperature warrants a more detailed examination of thermal conductivity of w-BeO. We have used the Sheng-BTE software [83], to calculate phonon contribution to thermal conductivity and is compared with the predicted lattice thermal conductivity using the Slack model [172]. The main aim of the present study is to describe the thermal conductivity and thermodynamic properties of w-BeO and z-BeO at temperatures up to 1500 K by solving BTE and QHA using *ab initio* calculations. The directional dependence of thermal conductivity is also analyzed for w-BeO.

6.3 Methodology

For wurtzite symmetry, the specific elastic constants are C_{11}, C_{12}, C_{13}, C_{33}, C_{44}, and C_{66}. Among the six-stiffness constant only the first five are independent whereas C_{66} is the average difference of C_{11} and C_{12}. The bulk modulus for the Reuss (B_R), Voigt (B_V), and Hill (B_H) average is shown in equation (6.1), (6.2) and (6.3) respectively.

$$B_R = \frac{C_{33}(C_{11} + C_{12}) - (2C_{13}^2)}{C_{11} + C_{12} - 4C_{13} + 2C_{33}} \tag{6.1}$$

$$B_V = \frac{2}{9}\,(\,C_{11} + C_{12} + 2C_{13} + 0.5\mathrm{C}_{33}) \tag{6.2}$$

$$B_H = \frac{(B_R + B_V)}{2} \tag{6.3}$$

Equations (6.4), (6.5) and (6.6) gives the shear modulus for the wurtzite structure in the Reuss (G_{R}), Voigt (G_V), and Hill (G_H) approximations.

$$G_{\mathrm{R}} = \frac{2.5\big((\mathrm{C}_{11} + C_{12})C_{33} - 2C_{12}^2\big)(C_{55}\mathrm{C}_{66})}{\{3B_V C_{55}C_{66} + [(\mathrm{C}_{11} + C_{12})C_{33} - 2C_{12}^2](C_{55} + C_{66})\}} \tag{6.4}$$

$$G_V = \left(\frac{1}{30}\right)(C_{11} + C_{12} + 2C_{33} - 4C_{13} + 12C_{44} + 12C_{66}) \tag{6.5}$$

$$G_H = \left(\frac{1}{2}\right)(G_R + G_V) \tag{6.6}$$

Further, the Young's modulus (Y) and the Poisson ratio (η) are calculated using equation (5.4) and (5.5), respectively.

The equilibrium lattice constant for the conventional unit cell was calculated at each temperature from the evaluated conventional unit cell volume as shown in equation (6.7). Iwanaga *et al.* [244] showed that 'c/a' ratio variation as a function of temperature is small and therefore, an assumption that 'c/a' ratio remains constant is made to derive the equation (6.7).

$$a^c(T) = \left(\frac{V_o^c(T)}{\left(\frac{c}{a}\right) * sin60}\right)^{\frac{1}{3}} \tag{6.7}$$

The expression to calculate the volumetric thermal expansion coefficient (α_V) at constant pressure (P) is given by equation (6.8).

$$\alpha_V(T)_p = \frac{1}{V_o(T)}\left(\frac{\partial V_o(T)}{\partial T}\right)_p \tag{6.8}$$

6.4 Computational Details

First-principles QE code which implements QHA within DFPT [86] and a plane-wave-pseudopotential framework have been used to calculate structural, mechanical, lattice dynamics and thermodynamic properties of BeO. The exchange-correlation functional GGA was treated in PBEsol (new pseudopotentials functional for solids) [139] parametrization. Vanderbilt-type ultrasoft pseudopotentials [245] provided by QE database were used for both Be and O atoms. The total energy convergence of the w-BeO and z-BeO structures were obtained using a kinetic energy cutoff of 75 Ry and the Brillouin zone integration over a Monkhorst-Pack of 8×8×5 mesh and 8×8×8 mesh respectively. Since we used the ultrasoft pseudopotentials [245], we need an augmented charge around the ion core. Hence the kinetic energy cutoff of plane wave's basis describing charge density was taken twelve times the energy cutoff of the used wave functions. The dynamical matrices for phonon density of states of w-BeO and z-BeO were calculated on a mesh of 6×6×4 and 6×6×6 q-points in the irreducible Brillouin zone respectively. The QHA [211] is used to investigate the thermodynamic properties [17]. We estimated k_L of w-BeO and z-BeO

using the ShengBTE code [83], and we considered a supercell of 4×4×4 to calculate the third-order interatomic force constants (IFCs) for w-BeO and a supercell of 5×5×5 for z-BeO solving BTE. The force cutoff distance was set such that the interaction range is up to the five nearest neighbors for w-BeO and three nearest neighbors for z-BeO. A mesh of 6×6×4 q-points and 6×6×6 q-points was used to calculate the second-order IFCs needed to compute the k_L of w-BeO and z-BeO respectively.

6.5 Results and Discussions

6.5.1 Ground state structural and mechanical properties

The w-BeO has two formula units per unit cell and belongs to the space group of P63mc (186). The ground state (0 K) property of a wurtzite structure is obtained by minimizing the total energy with respect to the lattice parameters ('a' and 'c/a') and internal parameter u. Table 6.1. lists the calculated lattice parameters with the values from the previous DFT calculations and the experiment. The predicted lattice parameter along the a axis and the c/a ratio at room temperature (2.712 Å,1.623 Å) shows excellent agreement with the experimental data (2.698 Å,1.622 Å) reported by Hazen *et al.* [228]. We also noticed that the new PBEsol ultra-soft pseudopotentials computed the lattice parameters more accurately than previously reported literature values using projected augmented wave (PAW) method with LDA correlation (PAW-LDA) [241], GGA correlation (PAW-GGA) [242], and Perdew-Burke-Ernzerhof (PBE) method (PBE-GGA) [240]. In fact, our own calculation of structural parameters of w-BeO using PAW compared less favorably to the values obtained from PBEsol (this work). Note that previously reported results of calculations are at 0 K while the experimental data are at room temperature (~300 K).

Table 6.1. Structural properties of w-BeO compared with previous DFT calculations and the experiment [228].

Lattice Parameters	This work (PBEsol) (0 K)	Other calc. (PAW-LDA) (0 K) [241]	Other calc. (PAW-GGA) (0 K) [242]	Other calc. (PBE) (0 K) [240]	Exp. (300 K) [228]
a (Å)	2.6985	2.665	2.712	2.706	2.698
c (Å)	4.3812	4.329	4.404	4.392	4.376
u	0.378	0.378	0.3778	0.378	0.378
c/a	1.623	1.624	1.624	1.624	1.622

The elastic constant is an important parameter that provides information on various properties of a material such as stiffness, strength, mechanical stability, hardness, and ductility or brittleness of materials [146]. In this work, we calculated the single-crystal stiffness constants of w-BeO by using a stress-strain method [184,185] with the help of the qe-nipy-advanced [74] interface. Table 4.2. lists the calculated stiffness constants and compares them with the previous calculations [239,246] and experiments [228,247,248].

Table 6.2. Mechanical properties (in GPa) of w-BeO compared with previous simulations and experiments. Here USP is ultrasoft pseudopotential and PW is Perdew-Wang method.

Properties	This work (PBEsol) (0 K)	This work (PBEsol) (300 K)	Other calc. (USP-GGA) (0 K) [246]	Other calc. (USP-PW-91) (0 K) [239]	Exp. (300 K) [247]	Exp. (300 K) [248]	Exp. (300 K) [228]
B	215.6	207.5	204	206.8	244	224	212±3
C_{11}	414	393	439.1	424.7	470	461	
C_{12}	162	157	105	125.3	168	126.5	
C_{13}	77	75	72	75.8	119	88.5	
C_{33}	498.6	469	463	474.2	494	491.6	
C_{44}	142.5	135	142	159.4	153	147.7	
C_{66}	125.7	118	167	149.7	152	167.0	
G	158	149			159	165	
Y	382	361			393	397	
η	.207	.209				.249	

The elastic constants for a mechanically stable hexagonal structure should satisfy the following Born's mechanical stability criteria [147] $C_{11} > C_{12}, 2C_{13}^2 < C_{33}(C_{11} + C_{12}), C_{44} > 0, C_{66} > 0$. The listed elastic constants have satisfied all of these criteria, indicating that the system is mechanically stable. From the calculated elastic constants, the polycrystalline bulk modulus (B), shear modulus (G), Young's modulus (Y) and Poisson's ratio (η) are determined using the Voigt-Reuss-Hill approach as described in section 6.3. Alternatively, the bulk modulus can also be calculated by Birch-Murnaghan [212] equation of states (EOS). The bulk modulus values at 0 K

from the EOS and elastic constants are 215.6 GPa and 218 GPa, respectively and are in excellent agreement with the experimental value of 212 ± 3 GPa [228] at 300 K.

The z-BeO belongs to a space group of F-43m (space group No: 216) with Be and O atoms located at the positions (0, 0, 0) and (1/4, 1/4, 1/4) respectively. The calculated lattice parameter (a), bulk modulus (B), elastic constants (C_{11}, C_{12}, and C_{44}) and the first derivative of bulk modulus (B') for the z-BeO are listed in Table 6.3. Although experimental values have not been reported in the literature for the z-BeO till date, our structural and mechanical properties are in good agreement with the previous theoretical works [234,249]. Furthermore, previously unreported values for shear modulus (G), Young modulus (Y) and the Poisson ratio (η) of z-BeO are reported here for the first time.

Table 6.3. Predicted structural parameters and mechanical properties of z-BeO. The obtained results are compared with previous theoretical calculations. Here PZ is Perdew-Zunger method.

Properties	This work (PBEsol) (0 K)	This work (PBEsol) (300 K)	GGA (PBE) [234] (0 K)	LDA(PZ) [249] (0 K)
a (Å)	3.8067	3.8257	3.80	3.7264
B (GPa)	215	206	206	228
C_{11} *(GPa)*	342	326	342	
C_{12} *(GPa)*	155	146	139	
C_{44} *(GPa)*	224	212	217	
B_o'	3.73	-	3.65	
G (GPa)	151	150		
Y (GPa)	365	363		
η	0.207	0.206		

The Born mechanical stability requirement of the cubic crystal lead to following restrictions on the elastic constants: $C_{11} > 0, C_{44} > 0, C_{11} - C_{12} > 0$, and $C_{11} + 2C_{12} > 0$. Our calculated elastic constants are shown in Table 6.3. satisfies these conditions ensuring that the z-BeO is mechanically stable. Using QHA, we also include adiabatic elastic constants of z-BeO evaluated at temperature

300 K. Accurate determination of stiffness constants is critical to ensure accuracy in prediction of the lattice dynamics of materials. The stiffness constant of w-BeO and z-BeO predicted using PBEsol ultrasoft pseudopotential are in reasonable agreement with previous experiments and theoretical calculations. Hence, we have used PBEsol pseudopotential for the study of phonon dispersion and thermodynamic properties of BeO.

6.5.2 Phonon Dispersion

The characteristic phonon vibrational spectra of any material are considered as its unique fingerprint. The frequency of vibration is the measure of the bond stiffness. Therefore, knowledge of phonon dispersion in the entire Brillouin zone ($\Gamma - K - M - \Gamma - A - L - M - K - H - A$ for wurtzite structure) is vital for further investigation of properties such as phonon-assisted photoemission, thermodynamic properties, thermal expansion, and thermal conductivity. Moreover, phonon spectra can also influence the behavior of electron carriers through electron-phonon interaction. Therefore, the understanding of the phonon dispersion of material is a necessity. BeO has four (n) atoms in its primitive unit cell and therefore has twelve phonon modes in the dispersion relations. There are three dimensions$(d = 3)$, and thus three acoustic modes and $d\ (n - 1) = nine$ optical modes. Group theory predicts six Raman active lattice phonons, near the center of the BZ: which includes a branch with phonon polarization in the uniaxial direction (A_1), a doubly degenerate branch with phonon polarization in the plane perpendicular to the uniaxial direction(E_1), and two doubly degenerate (E_2) branches. The A_1 and E_1 phonons are also infrared active while E_2 is only Raman active [239]. We also calculated the phonon density of states that includes all the phonons over the entire Brillouin zone needed to estimate the phonon-assisted properties.

Fig. 6.1.a shows the phonon dispersion relations of BeO at its equilibrium volume along the high symmetric $\Gamma - K - M - \Gamma$ directions. The calculated acoustic and optical modes are in good agreement with the experiment done by Bosak A, *et al.* [250] at room temperature using inelastic x-ray scattering with synchrotron radiation source. Table 6.4. shows the comparison of the calculated Raman active optical phonon modes at the Brillouin zone center (Γ point) using the new PBEsol ultrasoft pseudopotential with the previous DFT calculations [240,241] that were made using GGA-PBE and LDA. The comparison clearly indicates that apart from the slightly underestimated (<5%) optical mode E_2 (1) all other optical modes are in excellent agreement with

the experiment. We also observed that PBEsol ultrasoft pseudopotential captured the optical modes better than the previous DFT calculations. The Born effective charges (Z^*) tensor of BeO in the basal plane and the direction perpendicular to basal plane (c direction) for the PBEsol ultrasoft pseudopotential is Z^*_{Be} = (1.79, 1.85) and Z^*_O= (-1.79, -1.85) which are in close agreement with the experimental values of $|Z^*|$ = 1.85; [251]. The components of dielectric tensor in the basal plane is 3.108 and 3.17 in the c direction, which is comparable with experiment values of 2.95 and 2.99 in the basal plane and in c direction, respectively [229].

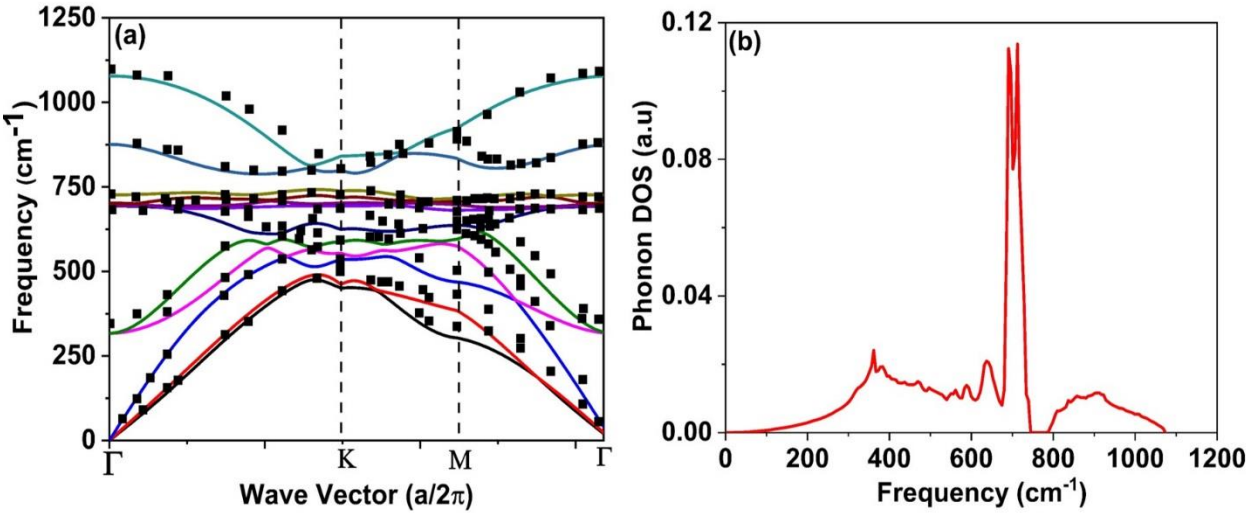

Fig. 6.1. (a) Phonon dispersion curve of the w-BeO structure. The solid lines show the theoretical prediction and the black dot are the experimental points measured by Bosak A *et al.* [250] using IXS. (b) Total phonon density of states (PDOS) of BeO.

The total phonon density of states (PDOS) plot in Fig. 6.1.b clearly shows that the phonon states are densely populated in the region around 680-730 cm^{-1}. The sharp peak in PDOS of BeO is due to the flat transverse optical branch. The gap in the phonon density of the state is a characteristic feature of w-BeO compared to the continuous phonon density of states of the other alkaline earth oxides (CaO, MgO, and SrO) [252]. The phonon dispersion relations of z-BeO at its equilibrium volume along the high symmetric $\Gamma - X - \Gamma - L$ directions and the phonon density of states (PDOS) are shown in Fig.6.2. The z-BeO has two atoms and therefore has six phonon modes in the dispersion relations.

Out of the six modes, three are acoustic modes and three are optical modes. To the best of our knowledge, there are no experimental data available to validate our results. However, we observed

that our zone center frequencies of longitudinal optical (LO) and transverse optical (TO) modes to be 32.2 and 21.6 THz are in agreement with 31.8 and 20.5 THz, respectively with the theoretical work done by Duman *et al.* [234]. We also observed a pronounced maximum in the PDOS similar to the work of Duman *et al.* and this pronounced peak is attributed to the reduced amount of dispersion of TO branch compared to the LO branch, and the minimum gap in the PDOS we observed is 2 THz compared to 2.4 THz of Duman *et al.*

Table 6.4. Comparison of the Raman active optical mode frequencies (in cm^{-1}) at the Brillouin zone center (Γ point) of w-BeO with the experiment data [250] and previous DFT calculations [240,241]

Mode	US-GGA, PBE [241]	US-LDA, PZ [241]	US-GGA Vanderbilt [240]	Exp. [250]	PBEsol (This Work)
$E_2(1)$	329.71	329.89	336.9	337.3	321.6
$A_1(TO)$	658.89	717.79	650.4	678	689.1
$E_2(2)$	658.75	720.6	656.4	683	701
$E_1(TO)$	699.5	757.35	697.5	722.7	732.9
$A_1(LO)$	1092.42	1092.42	1127.1	1080.6	1082.2
$E_1(LO)$	1061.79	1104.62	1152.4	1095.6	1082.2

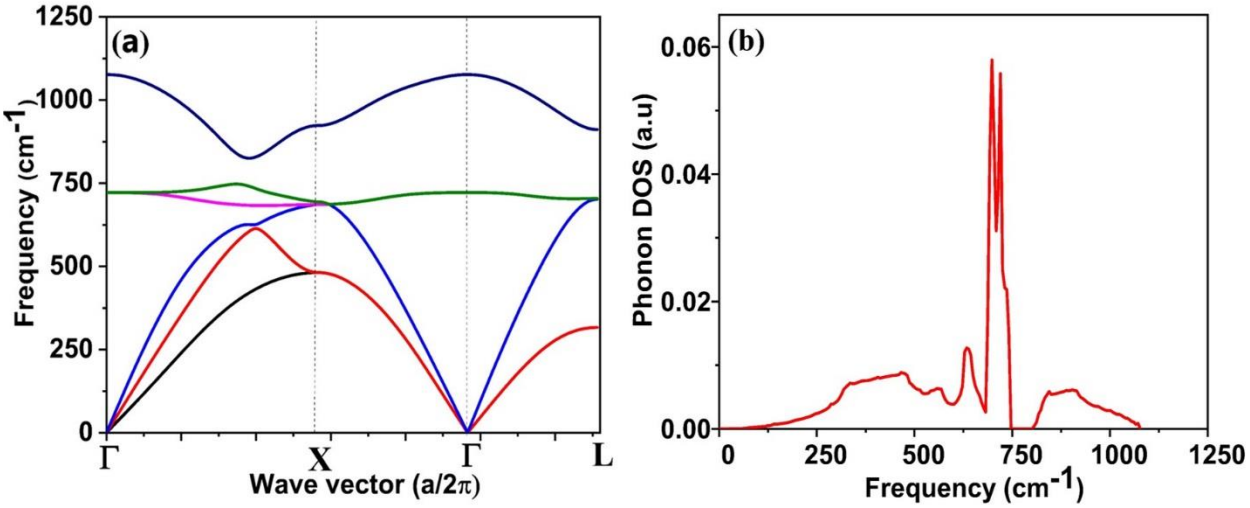

Fig. 6.2. (a) Phonon dispersion curve of the z-BeO structure. The solid lines show the theoretical prediction. (b) Total phonon density of states (PDOS) of z-BeO.

Compared to the w-BeO, the Born effective charges (Z*) of the z-BeO is isotropic owing to its cubic structure. Moreover, charges on Be and O differ only by sign due to its charge neutrality. The $Z^*$of the z-BeO using the PBEsol ultrasoft pseudopotential is 1.79 and is in excellent agreement with the available theoretical calculation of 1.81. The dielectric constant of BeO from our calculation is 3.14 and is in agreement with the theoretical value of 3.09 from Duman *et al.* The accurate phonon dispersion relations, of w-BeO with experiment and the z-BeO with the previous theoretical work has given us the confidence to calculate the phonon-assisted properties such as heat capacity at the fixed volume (C_V) and volume thermal expansion (α_V).

6.5.3 Phonon transport properties

Section 5.3.2 describes the calculation of the thermodynamic properties using QHA. At relatively low temperatures near the Debye temperature of the material, the DFPT combined with QHA is a powerful method to predict the lattice assisted properties. The volume thermal expansion, a significant design parameter for high-temperature structural applications, is computed. Fig. 6.3.a shows the volume as a function of the temperature of w-BeO in comparison with the experimental data by Hazen *et al.* [228].

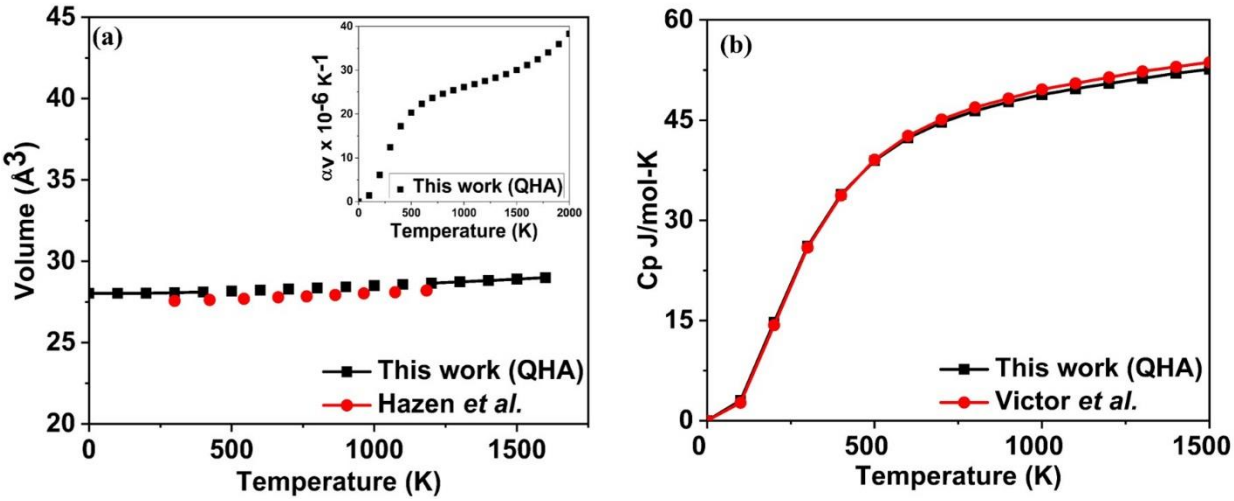

Fig. 6.3. (a) Shows the comparison of change of volume as a function of temperature with the experiment by Hazen *et al.* [228]. Inset of Fig. (a) shows the volume thermal expansion by QHA. (b) shows the heat capacity as a function of temperature compared with the experimental values by Victor *et al.* [231].

Comparison of the results shows that the volume of w-BeO is in good agreement with the experiment with an error of less than 2%. The calculated average value of volume thermal expansion (α_V) between 300 K to 1200 K is 2.26 x 10^{-5} K^{-1} and is comparable to the experimental value of the α_v of 2.66 x 10^{-5} K^{-1} [228]. The new PBEsol ultrasoft pseudopotential has underestimated the α_V compared to the value obtained from the previous DFT calculation using GGA (PBE) potential (3.04 x 10^{-5} K^{-1}) [253]. Since w-BeO has a hexagonal structure, the thermal expansion coefficient normal to the c direction ($\alpha_{\perp}$)and parallel to the c direction ($\alpha_{||}$) is different (i.e. material is anisotropic). However, Iwanaga *et al.* [244] have shown that the anisotropy in thermal expansion is small ($\alpha_{\perp}/\alpha_{||}$ =1.11). The available experimental thermal expansion coefficient ($\alpha_{\perp}/\alpha_{||}$) at temperature 300 K and 700 K are 5.99/5.35 and 8.62/7.79, respectively [254]. As the anisotropic variation for w-BeO is small, we assumed that the coefficient of linear thermal expansion (CLTE) is isotropic to evaluate the Grunesein parameter and the thermal conductivity by using Slack model.

At a temperature, greater than 1500 K the α_V calculated (shown in the inset of Fig. 6.3.a) using the PBEsol pseudopotential displayed a non-linear behavior. However, experimentally it was demonstrated by Anderson [255] that the α_V should increase linearly with temperature.

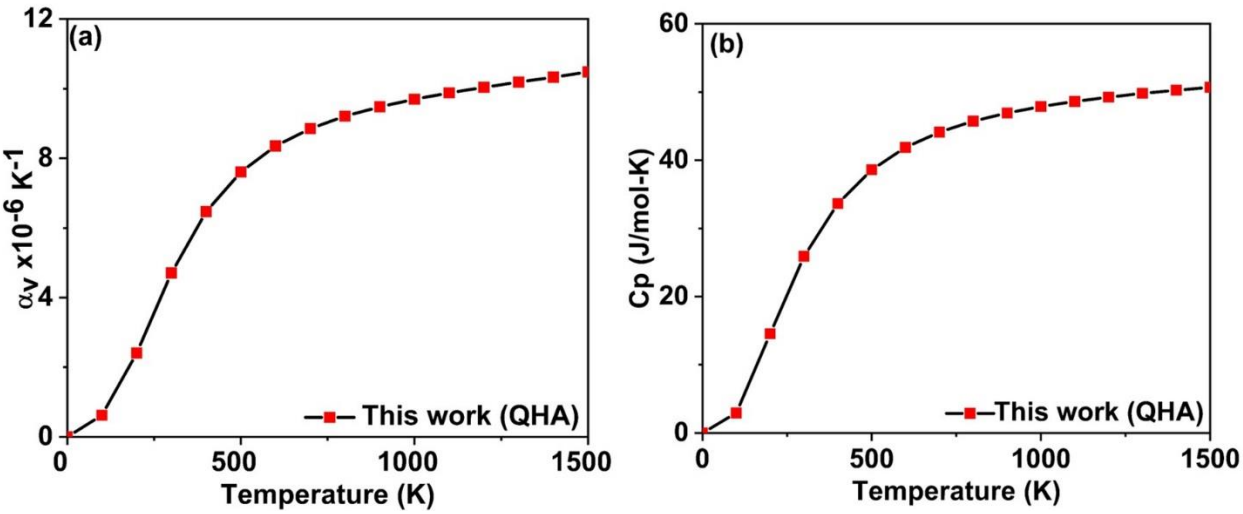

Fig. 6.4. (a) Shows the volume thermal expansion (α_v) by QHA for z-BeO. (b) Illustrates the heat capacity at constant pressure (C_p) as a function of temperature.

Fig. 6.3.b clearly indicates that the C_P derived by equation 5.13 agrees well with the experiment [231] up to 1500 K. However, at a temperature above 1500 K, the calculated C_p values deviated

from the experimental results. This perhaps indicates the failure of QHA at temperatures above Debye temperature, and the need to consider the anharmonic effects due to phonon-phonon interaction for the w-BeO structure. The experimental value of the Debye temperature of w-BeO is 1280 K at room temperature and the value predicted by this calculation is 1220 K. In Fig. 6.4. a, We illustrate the α_V and C_P as a function of temperature for the z-BeO. Unfortunately, we do not have any previous experimental and theoretical values for comparison. Hence, these data can serve as a reference for the experimentalists.

6.6 Lattice Thermal Conductivity

For the realization of the practical applications mentioned in the introduction, it is essential to have a better understanding of the k_L of w-BeO at high temperature. The available experimental data are scattered, and the previous simulations by Li *et al.* [235] and Yu *et al*. [243] are limited to a lower temperature (<500 K). As explained earlier, the anharmonicity becomes necessary at a temperature greater than 1500 K, a factor which has limited the calculation of k_L of BeO at temperatures higher than 1500 K using Slack method and BTE. In Fig. 6.5.a the k_L predicted by BTE and Slack method are compared with the experiment done by Takahashi *et al.* [233], Slack *et al.* [78], and Francle *et al.* [256]. The k_L predicted by BTE at the lower temperature are in excellent agreement with the experiment, however, at a higher temperature, the k_L values are greater than the available experimental values and represent the upper limit of k_L. The difference in theoretical and experimental k_L can be attributed to the porosity of the tested samples, the impurities, and the sintering technique used. The Slack model predictions are better at a relatively high temperature near to the Debye temperature, where the non-quasi-momentum conserving three-phonons scattering (Umklapp process) is dominant.

The previous theoretical attempt to find k_L by Slack [128] estimated a value of 90 W/mK at 300 K, which is four times lower than the experimental value of 370 W/mK. The scrutiny of the results indicates that the discrepancy in predicted k_L of w-BeO arose from incorrect Grüneisen coefficient (γ). It is known that low thermal conductivity in crystalline structure occurs from strong anharmonicity in bonding. γ, the measure of anharmonicity of a structure [175] also indicates the relationship between phonon frequency and crystal volume changes. To resolve this divergence of k_L in BeO we calculated the γ from our thermal expansion data and compared this value with the value previously reported by Slack [128]. The Slack value of γ =1.38 was calculated based on the

overestimated linear thermal expansion data [257] and was almost twice as high as any other wurtzite structure (CaO, ZnO, GaN, AlN, and SiC). Therefore the thermal conductivity calculated previously [33] (indicated in Fig. 6.5.a by pink square) was lower by a factor of four. Our prediction of γ values of 0.83 calculated from the predicted thermal expansion is closer to values obtained with materials having a wurtzite structure (0.7).

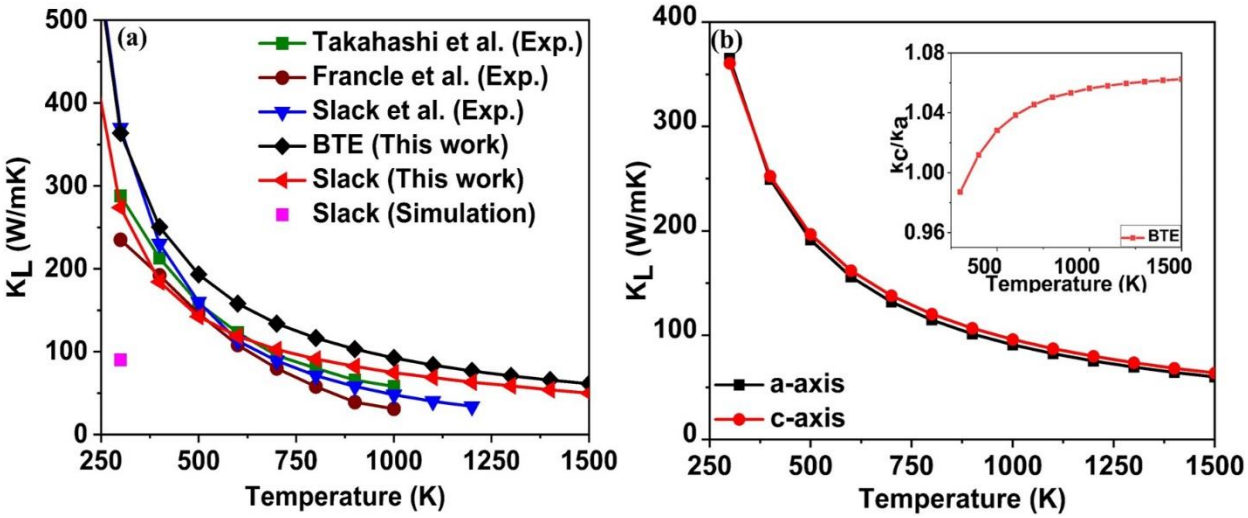

Fig. 6.5. (a) Thermal conductivity of w-BeO compared to experiment [78,233,256] (b) The anisotropy in k_L of w-BeO.

By using the calculated thermal expansion data from our work (Fig. 6.2.a), the Slack method predicted k_L at 300 K has a value of 250 W/mK. Although this new value is much better than the previously reported value of 90 W/mK [128], it is still lower than both the experimental and simulated BTE values (370 W/mK). This underestimation of k_L can be explained by considering the effect of inaccurate estimation of γ in the Slack equation. k_L is inversely proportional to the square of γ, which in turn is directly proportional to the thermal expansion coefficient α_V and therefore any small variation in γ can have drastic effects on k_L. Analytically, the $k_L$can be expressed as a function of $[a+bT]^{-1}$ with constants a and b, and we provide here the fitted values of a and b for possible future applications. The value of constants 'a' and 'b' for w-BeO calculated from the more accurate k_L obtained by solving BTE are 6.81 x 10^{-12} and 1.0 x 10^{-5}, respectively.

In the case of the wurtzite phase, k_L is slightly anisotropic since the out of the plane k_L not equal to the inplane k_L. However, the k_L calculated along a and b axes are the same. Fig. 6.5.b shows the anisotropy in the k_L value of w-BeO and the inset of Fig. 6.5.b shows the k_c/k_a changes as a

function of temperature. The average ratio k_c/k_a (where k_c is k_L along 'c' axes, and k_a is k_L in 'a' axes) over the temperature range of 500 K to 1000 K is 1.045. This small anisotropy in k_L of w-BeO is in agreement with the experimental k_L results reported in [78]. A similar low value of anisotropy is also noted in the experimentally observed values for thermal expansion of w-BeO [254].

As mentioned earlier, the article also discusses the k_L for ZB phase of BeO. Fig. 6.6 shows the calculated k_L as a function of temperature for z-BeO and compares the k_L from relaxation time approximation (RTA). Even though RTA incorrectly treats the normal phonon-phonon scattering process (N-scattering) as resistive, it is generally considered as a good approximation for various materials. However, in the case of z-BeO, the difference between the RTA and the exact solution is 25% at lower temperatures such as 300 K, suggesting that RTA may not be a good approximation for z-BeO in these temperature ranges. The big difference between the full solution and RTA in materials with high k_L (such as BeO) is due to the higher contribution of low-frequency acoustic phonons, which typically contribute more to N-scattering than the non-quasi-momentum conserving three-phonons scattering (U-scattering). The full BTE solution corrects for this inaccuracy of RTA in systems with a larger k_L.

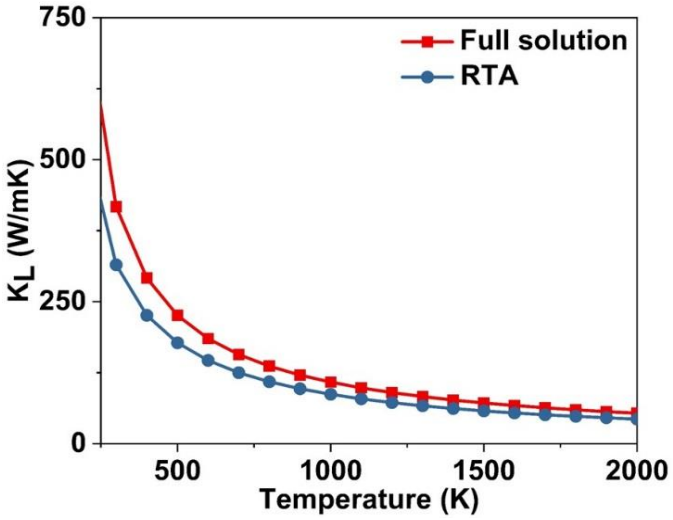

Fig. 6.6. Lattice thermal conductivity of z-BeO the black line shows the exact solution and the red line illustrates the k_L from RTA.

Comparison of k_L for WZ and ZB phases of BeO clearly indicates that z-BeO has a greater k_L than the w-BeO. The k_L values at a temperature of 300 K for z-BeO and w-BeO are 417 W/mK and 370 W/mK respectively. Though the greater value for z-BeO is consistent with the results of W.Li and N.Mingo [235], our theoretical prediction at 300 K is lower (417 W/mK compared to 475 W/mK). We are unable to generate a satisfactory explanation for this aberration, based on our limited knowledge of the parameters used by W. Li and N. Mingo, this finding may eventually be required to be validated experimentally.

6.7 Conclusion

In conclusion, the structural, mechanical, phonons, phonon-assisted thermal properties and thermal conductivity of BeO in the WZ and ZB phase using *ab initio* approach has been calculated. The existing experimental results for w-BeO compares well with the calculated values. We also predicted the anisotropic variation k_c/k_a ratio as a function of temperature and found the anisotropy to be small, which is in agreement with the experimental results. We also demonstrated that the structural, mechanical and phonon dispersion of w-BeO are well captured by PBEsol. Other properties such as the α_v of w-BeO calculated using QHA is slightly underestimated compared to the experiments and are considerably more accurate than the overestimated previous DFT calculations. We have also shown that this difference in α_v has affected γ, which influence the k_L with the Slack model. Moreover, we have observed that the z-BeO is a better thermal conductor than the WZ phase, which may find interesting applications, especially in areas involving thermal management. The higher thermal conductivity of z-BeO and its difference with the previous theoretical value warrants a future experimental investigation.

Chapter 7 : The effect of SPS processing parameters on the microstructure and thermal conductivity of ThO_2

7.0 Overview

One of the main problems with the thorium fuel cycle is the requirement of high sintering temperature and the need for sintering aids to produce a high density ThO_2 fuel pellets using conventional sintering techniques. Therefore, the third objective of this work has been to overcome the limitations of the non-conventional sintering technique by analyzing the effect of SPS processing parameters on the densification, microstructure, and the thermal conductivity of ThO_2. Thus, this chapter realizes the third objective of the thesis.

The research findings reported in this chapter have been published as manuscript #5 as follows:
L. Malakkal, A. Prasad, J. Ranasinghe, E. Jossou, D. Oladimeji, B. Szpunar, L. Bichler, J. Szpunar; "The effect of SPS processing parameter on the microstructure and thermal conductivity of ThO_2"; published in Journal of Nuclear Materials Vol.527, 151811 (2019). The copyright permission to use this paper is provided in Appendix E.

The contributions of the PhD candidate are 1) Preparing and performing the samples for characterization such as XRD, SEM, Raman, and EBSD 2) measuring of thermal conductivity using Laser flash apparatus, 3) analyzing of the results, 4) writing the manuscript for publication. My supervisors reviewed the manuscript before it was submitted for publication in this journal.

The differences between the content of this chapter and the published paper are:

1. The equations to determine the thermal diffusivity and the thermal conductivity using the laser flash apparatus has been removed to avoid repetition, and the reader is referred to the equation 2.28 and 2.28 in chapter 2.
2. The references of the manuscript are listed at the end of this thesis.

The effect of SPS processing parameters on the microstructure and thermal conductivity of ThO_2

Linu Malakkal[1], Anil Prasad[2], Jayangani Ranasinghe[3], Ericmoore Jossou[1], Dotun Oladimeji[3], Barbara Szpunar[3], Lukas Bichler[2], Jerzy Szpunar[1]

[1]Department of Mechanical Engineering, University of Saskatchewan, Canada

[2]School of Engineering University of British Columbia-Okanagan Kelowna, Canada

[3]Department of Physics and Engineering Physics, University of Saskatchewan, Canada

7.1 Abstract

Thorium dioxide (ThO_2), is a nuclear fuel that is expected to play a vital role in the Generation *IV* nuclear reactors. One of the challenges to implementation of thoria for the fuel cycle has been the difficulty in fabricating dense pellets via conventional sintering techniques. In this study, the non-conventional sintering of thoria using spark plasma sintering (SPS) was explored. A systematic investigation into the influence of processing parameters on the densification, microstructure, grain size and thermal conductivity of ThO_2 is presented. The range of sintering temperature, pressure, and hold time has been systematically varied between 1500–1800 ^oC, 50–70 MPa and 5–15 m, respectively. The results revealed that without the help of any sintering aid, pellets with a relative density of 95% theoretical density (TD) were fabricated at a sintering temperature of 1600 ^oC, sintering pressure of 50 MPa and a hold time of 10 min. Furthermore, the characterization of these specimens clearly indicates that by carefully selecting the processing parameters, the density, microstructure, grain size and the thermal conductivity of ThO_2 can be suitably controlled. This study shows that the use of the SPS technique can potentially solve one of the primary concerns in the front end of the thoria fuel cycle.

7.2 Introduction

Thorium dioxide (ThO_2) is proposed to play an essential role in the nuclear power industry and is considered a better and safer alternative to the currently used nuclear fuel – Uranium dioxide (UO_2) [50,51]. There has been a renewed interest in ThO_2 fuel because of its many inherent advantages. ThO_2 has better thermo-physical properties, such as a higher melting point, higher thermal conductivity and a lower coefficient of thermal expansion [51]. ThO_2 is also relatively inert and does not oxidize and has a higher resistance to radiation damage than UO_2 [51]. The fission product release rate for ThO_2–based fuels is one order of magnitude lower than in the case of UO_2 [51].

Moreover, ThO_2 is more proliferation-resistant and produces less transuranic elements than uranium-based fuels [51]. In addition, the stock of civil plutonium could be significantly decreased by using mixed thorium plutonium oxide fuel in light water nuclear reactor [47,61,134]. Thorium is also suited for other reactor types such as the Chinese HTR-10 [258], heavy water CANDU configuration [52], India's advanced heavy water reactor (AHWR) [49], molten fluoride salt design and helium-cooled TRISO-fueled systems [47]. Even though there are several advantages, there are also challenges both in the initial and the final stages of the thorium fuel cycle. The main problems to be addressed in the back end of the thorium fuel cycle is the high gamma radiation associated with daughter product ^{232}U and the inability of ThO_2 to dissolve in nitric acid. This issue of handling the irradiated and spent fuel can be resolved by developing better reprocessing and fabrication techniques [51]. Whereas, the main difficulty in the front end of the thorium fuel cycle is associated with the production of dense ThO_2 pellets by conventional sintering techniques. Since the melting point of ThO_2 is (3378 ± 17 ^oC [259]) is higher than the UO_2 (2847 ± 30 ^oC [260]), it is essential to have a very high sintering temperature (>2000 ^oC) [51] and sintering time to fabricate a dense pellet of ThO_2 via conventional sintering techniques.

In the literature, sufficient details regarding the conventional sintering of ThO_2 are available. For example, Curtis and Johnson [261] have shown that cold pressing and isostatic pressing of ThO_2, could produce pellets of density 73% theoretical density (TD) and 86% TD, respectively, by maintaining a sintering temperature of 1800 ^oC and a dwell time of 8 hrs. They also explored the effect of additives on sintering of ThO_2 and discovered that adding CaO and CaF_2 increased the density of ThO_2 to 97% TD at 1800 ^oC. Another study [262], clearly indicates that addition of suitable additives such as MgO, N_2O_5 resulted in lowering the sintering temperature to as low as 1150 ^oC, but the additives often resulted in the creation of point defects due to the difference in the valency of the cations. Kang *et al.* [263] produced pellets of ThO_2 and $(Th,U)O_2$ with a density ranging from 94 to 98% TD using wet-milled powder sintering at 1700 ^oC. Shiratori *et al.* [264] ball-milled thoria powder derived from the oxalate process for 24 hrs and prepared high density (98% TD) ThO_2 pellets at a low temperature of 1550 ^oC. All these studies showed that although significant progress has been made in conventional sintering of ThO_2, sintering by the traditional methods still has the limitations such as very long processing time, elaborate sample preparation and high sintering temperature.

In the case of UO_2, many researchers have pursued sintering by non-conventional methods, such as inductive hot pressing [265], microwave sintering [266], pressure less induction heating [267], flash sintering [268] and spark plasma sintering (SPS) [269]. Among these techniques, SPS has become a popular sintering method for consolidation of powders, and Ge *et al.* [269] has studied in details the effect of SPS process parameters on the densification, microstructure, grain size and thermal conductivity of UO_2. The feasibility of SPS for the production of commercial-grade fuel pellet has been explored by Timothy *et al.* [270] but warranted the need for further improvements in the die-design configurations and tooling materials for large-scale production. Several studies [271,272] have been carried out to overcome these limitations. For example, Papynov *et al.* [271] explored the use of the non-standard molybdenum die instead of standard graphite die for the production of highly dense UO_2 pellets of the required quality. Besides, researchers such as Muta *et al.* [273,274], Scott *et al.* [275], Saoudi *et al.* [122] and Balice *et al.* [276] have fabricated the mixed oxides pellets via SPS route. The studies related to the use of non-conventional techniques in the fabrication of ThO_2 pellets are limited to the work done by Tyrpekl *et al.* [277] who illustrated that the sintering onset temperature could be lowered by using nanocrystalline ThO_2 powder. The final densities of the pellets Tyrpekl produced using nanocrystalline powder were above 95% TD, whereas the pellet made from commercial powder had a density of only 85%. However, the work on SPS sintering of the commercial ThO_2 by Tyrpekl was limited only to a sintering condition of 1600 ^oC, 70 MPa with a holding time of 10 min. Therefore, in this work, we carried out a systematic study to determine the influence of processing parameter on the density, microstructure, grain size and thermal conductivity on ThO_2 sintered from a non-nanocrystalline powder by considering a broad range of sintering temperatures, pressures and hold time.

7.3 Experimental procedure

7.3.1 Starting powder

IBILABS, U.S.A. supplied the commercial ThO_2 powder with a purity of 99.8%. The powder was characterized by the x-ray diffraction (XRD) and scanning electron microscopy (SEM). The powder XRD (compared well with JCPDS file 042-1462) revealed a single-phase face-centered cubic structure with the lattice parameter of 5.60 Å. Apart from the peaks corresponding to that of ThO_2, a small peak at 34° was also observed in the XRD plots, and this can be attributed to the thallium oxide, an impurity present in the as-received powder. The SEM micrograph of the

commercial powder (Fig. 7.1.a) indicates that the thoria particles had a square-shaped morphology, and the size ranged between 1 μm – 6 μm.

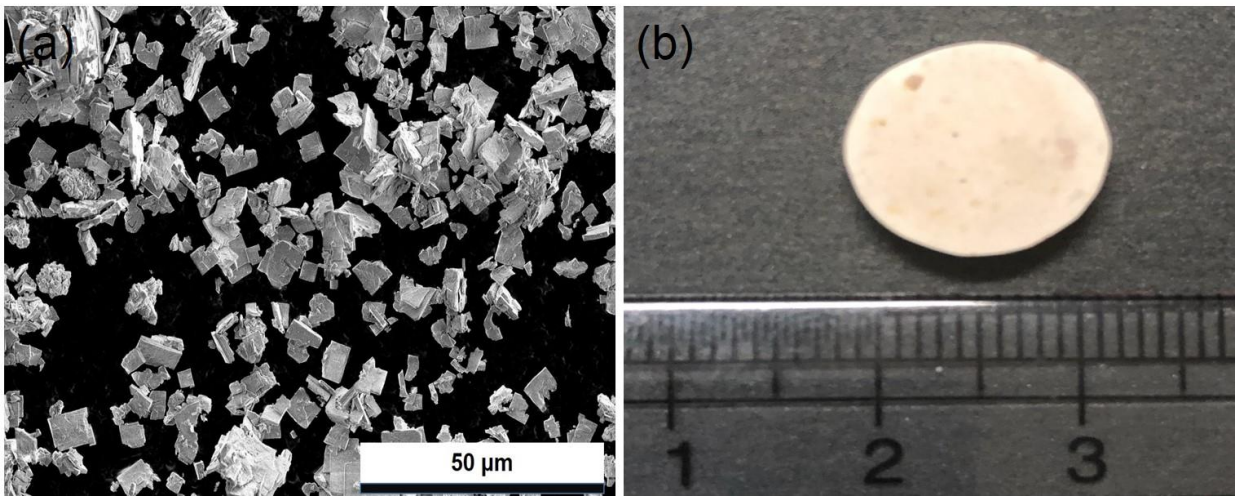

Fig. 7.1. (a) SEM image of the as-received thoria powder (b) SPS sintered ThO_2 (94.6±0.04% TD) pellets of diameter 12.7 mm × 3 mm thickness. The pellet was sintered at a temperature of 1600 ^oC, the pressure of 50 MPa and a hold time of 10 min.

7.3.2 SPS sintering of ThO_2 powder

The as-received ThO_2 powder was sintered in an argon atmosphere using a Thermal Technology LLC 10-3 Spark Plasma Sintering (SPS) system located at the University of British Columbia (Kelowna, BC). The starting powder was loaded into a graphite die of internal diameter 12.7 mm. A thin grafoil (0.125 mm) was used at the graphite tooling – powder interfaces to prevent friction and reaction between ThO_2 and the graphite tooling. A filled die was placed inside the SPS chamber with a carbon sleeve around it. The carbon sleeve was used to reduce radiation heat loss at high temperatures. The sintering temperature during the experiment was monitored using an optical pyrometer. The *in-situ* applied uniaxial pressure, temperature, chamber pressure, current and voltage were continually recorded as a function of time by a data acquisition unit. The sintering process was controlled by a Eurotherm controller, which was programmed using iTools software.

For each sintering experiment, the temperature was ramped from room temperature to 600 ^oC at a heating rate of 30 ^oC/min. The pressure was maintained at 5 MPa, and the system was allowed to reach equilibrium at 600 ^oC for 15 s. After that, the heating rate was increased to 100 °C/min, and the die was heated to the desired maximum sintering temperature, which ranged from 1500 °C to 1800 °C. Furthermore, the pressure was ramped to the desired sintering pressure, which ranged

between 30 – 70 MPa. The pressure ramp rate was coupled to the heating rate to reach the peak temperature and pressure at the same time. Three different hold times at sintering temperature were considered: 5 min, 10 min and 15 min. After sintering at the desired temperature was completed, a constant cooling rate of 200 ^{o}C/min and pressure ramp down rate of 20 MPa/min was used for all experiments. After cooling, the die was removed from the chamber, and the pellet was ejected from the graphite tooling.

7.3.3 Characterization methods

The sintered pellets were ground flat using 500-grit sandpaper, which also helped to remove the residual graphite foil. The polished specimens were characterized using techniques such as X-ray Diffraction (XRD), Raman spectroscopy, Scanning Electron Microscopy (SEM), Electron Back Scattered Diffraction (EBSD) and Laser Flash Apparatus (LFA). The XRD patterns were recorded using Bruker D8 Discover with chromium K_{α} radiation at room temperature. The 2θ angle was scanned from 20^{o} to 110^{o} with a step size of 0.01^{o} and a scanning time of 600 sec per step. The X'pert High Score Plus software was used to fit the peak profile. Renishaw 2000 Raman microscope was used to obtain Raman spectra. The laser source had a wavelength of 514 nm. The scattered light was dispersed with a grating of 1800 $\frac{1}{mm}$and was collected by the Renishaw CCD camera. An objective lens of 100x was used, and the exposure time was set to 10 seconds with 4 accumulation.

The Archimedes' method (Torbal density measurement kit) was used to determine the density of each pellet by immersing the pellets into a distilled water at room temperature. Five readings were recorded for each specimen, and the average and standard error were calculated. The samples were subsequently polished to a mirror finish by grinding the pellets with silicon carbide (SiC) papers starting with a grain size of 46 μm and gradually bringing down to 5 μm. After polishing with the SiC paper, the samples were polished using 3 μm MD mol cloth with 3 μm MD mol suspension, and 1 μm MD nap cloth with 1 μm MD nap suspension. The microstructural and textural studies using SEM and EBSD on the polished specimens was carried out with a SU 6600 field emission-scanning electron microscope.

Thermal diffusivity measurements of samples were carried out using the LFA (TA instruments-DLF-1/EM-1300). This instrument used a high-power laser pulse (450 μs pulse width) from a

solid-state Nd: glass laser pulse source to illuminate the front face of the sample, while the resulting temperature rise was recorded on the rear face of the sample with liquid-nitrogen cooled InSb infrared detector. The samples used in this study were disc-shaped and measured ~12.7 mm in diameter and had the thickness in the range of 2 mm to 3 mm. The sample thickness was determined by averaging 5 values measured using a calibrated micrometer. The standard deviation of the average thickness was less than 0.02 mm. The samples were coated with a graphite spray for better absorption and emissivity of the laser flash. The measurements were conducted in an argon atmosphere starting from room temperature to 900 K. By measuring the time taken for the temperature rise in the rear face, the thermal diffusivity (α) of the specimens was determined using the Parkers relation [111] as expressed in equation (2.28). From the measured α, the thermal conductivity as a function of temperature ($k\ (T)$) was calculated using equation (2.29). The variation of density due to the thermal expansion and the C_p was calculated using the model derived for thermal linear expansion data by Bakker *et al.* [114] for ThO_2.

7.4 Results and Discussions

7.4.1 Structural characterization using X-ray Diffraction (XRD) and Raman study

Fig. 7.2.a compares the XRD patterns of the as-received ThO_2 powder and the pellets of ThO_2 sintered at 1600 ^oC. The XRD peaks of the powder and sintered pellet matched with the joint committee on powder diffraction standards (JCPDS) file NO: 042-1462, indicating a cubic crystal structure with a lattice parameter of 5.60 Å. It is also evident from the diffractogram that no reaction product or intermetallic compounds were formed during the SPS process. For brevity, the XRD analysis of all other samples considered in this work is provided in the supplementary information (S.I) as S.I.7.1 Fig. 7.12. The Raman analysis further confirmed the observations made by XRD. Fig. 7.2.b shows the Raman spectra of the powder and the sintered pellet of ThO_2. Both the spectra are similar and are dominated by the strong band at 466 cm^{-1} corresponding's to the well-known Raman features for the spectrum of a fluorite structure. The T_{2g} mode corresponds to the stretching motion of the eight oxygen atoms around each Th atom. The behavior of this mode in ThO_2 is similar to what has been observed in the literature [122].

The other peaks at 934 cm^{-1} and 1134 cm^{-1} in the spectrum correspond to the $2\omega_R$ (the Raman frequency at the center of the Brillouin zone frequency) and $2\omega_{LO}$ as observed by Ishigame *et al.* [278]. The peak between the $2\omega_R$ and $2\omega_{LO}$ at 1030 cm^{-1} and 1055 cm^{-1} can be attributed to the

overtone of optical phonon M_5' at the zone boundary M (M and L are the symmetry point in the Brillouin zone).

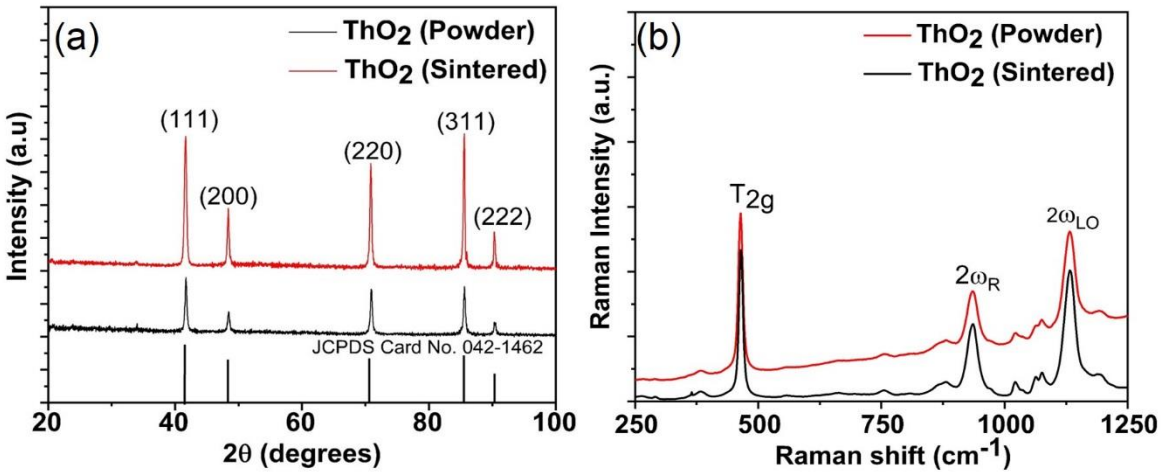

Fig. 7.2. (a) Comparison of the X-ray diffraction of the sintered ThO_2 pellets with that of the as-received powder (b) comparison of the Raman spectra of sintered pellets of ThO_2 compared to the powder used for sintering.

Moreover, the peak at 754 cm^{-1} is considered to arise from combinations $M_5' + M_3'$ and $2L_3$, and the band at 381 cm^{-1} ($M_1 + M_5$) and 876 cm^{-1} ($L_1 + L_3$) is ascribed to the frequency summation of the optical modes at the zone boundary L and M respectively [278]. The notations representing different phonons of ThO_2 are similar to the work done by Ishigame *et al.* [278]. The XRD and Raman analyses indicate that SPS can be effectively used to produce ThO_2 pellet (Fig. 7.2.b) with equal purity of that of the starting material in short times, using an as-received powder without the formation of any reaction products. However, for the samples sintered at high temperature (>1700 ^oC), a slight gradient of color from white to grey has been observed indicating a reduced oxygen stoichiometry, similarly as reported for ThO_2 [277,279–281] and ZrO_2 [282].

7.4.2 Density measurement

The density of fuel plays an important role in the performance of nuclear fuel. The nuclear fuel pellet with a desired density is not only expected to accommodate the fission gas release but also to avoid the possible in-reactor shrinkage that can occur with a low-density fuel [283]. As mentioned in the introduction section, one of the primary objectives of this work was to lower the sintering temperature and time, while achieving the desired density of 95% TD of Thoria. The effect of various sintering parameters on the density of the fuel pellets is presented in Fig. 7.3.

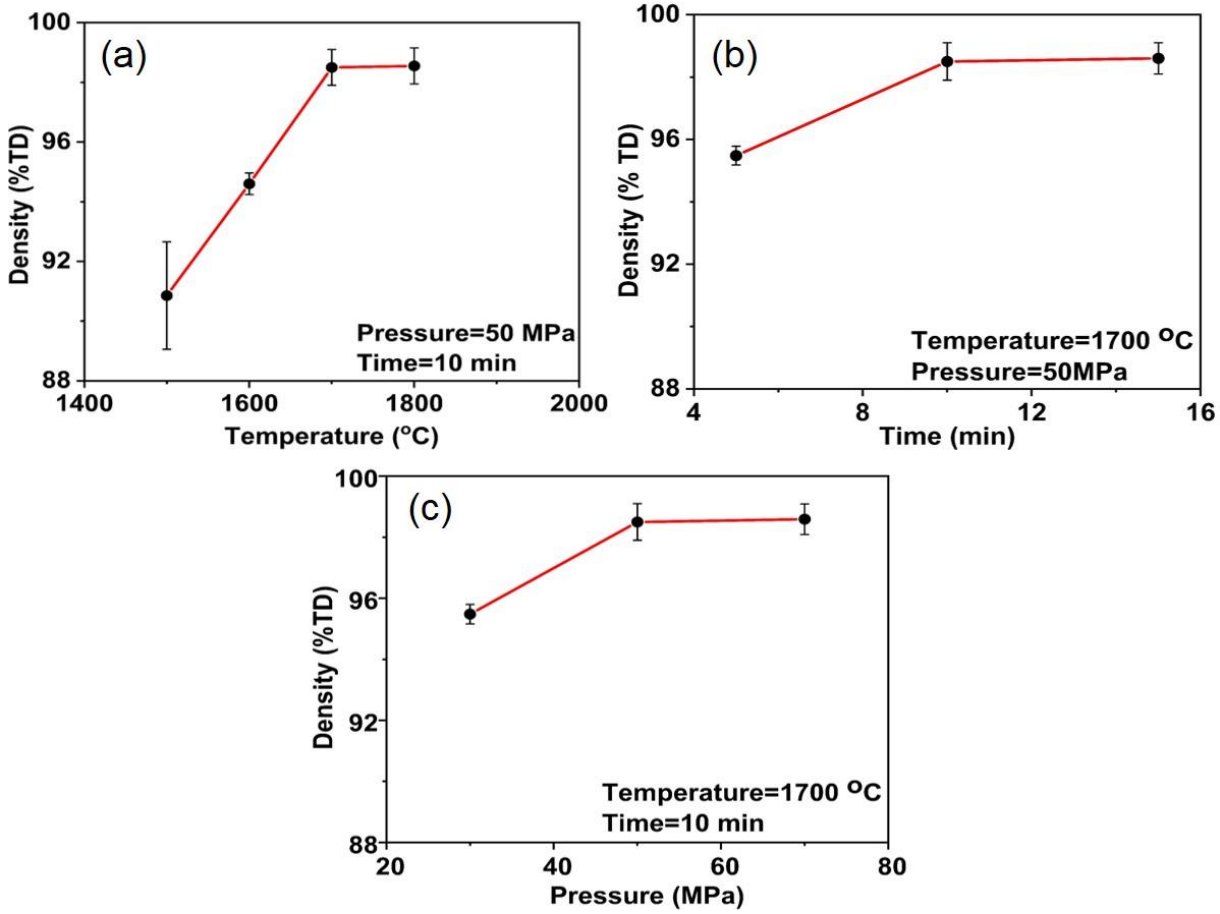

Fig. 7.3. The influence of (a) temperature (b) hold time and (c) pressure on the density of the sintered pellets.

Fig. 7.3.a illustrates the pellet density as a function of sintering temperature. The sintering temperature was varied between 1500 ^{o}C to 1800 ^{o}C (at 100 ^{o}C increments) keeping all other sintering conditions constant. The results reveal that the choice of sintering temperature had a significant effect on the final density of the pellet. Increasing the sintering temperature from 1500 to 1700 ^{o}C resulted in average density increase from 90.9% TD to 98.5% TD. Increasing the sintering temperature further to 1800 ^{o}C did not result in an appreciable increase in density, indicating that the maximum compaction of ThO_2 occurred at a temperature of 1700 ^{o}C. To better understand the effect of the hold time on the final density, pellets were sintered at a different dwell times of 5, 10 and 15 min keeping the sintering temperature and pressure at 1700 ^{o}C and 50 MPa, respectively. The density of the pellet increased from 96.5 to 98.6% TD with the change of hold time from 5 min to 10 min. However, further increasing the hold time to 15 min did not show any

significant influence on the density of the samples, demonstrating that a hold time of 5 min is sufficient to get a pellet of ThO_2 with the desired density.

Finally, the effect of sintering pressure on the density of the sintered pellet was investigated by changing the pressure from 30 MPa to 50 MPa and finally to 70 MPa, keeping all other sintering parameters constant (1700 ^oC and 10 min). Fig. 7.3.c indicates that at a temperature of 1700 ^oC, maintaining a pressure of 30 MPa for 10 min was sufficient to obtain the desired density (95.5% TD). The maximum density of 98.6% TD was obtained at 50 MPa and increasing the pressure to 70 MPa did not have any effect on the density of the pellets. From all these cases, the pellets sintered using the following conditions; a) 1600 ^oC – 50MPa -10 min (94.5% TD), b) 1700 ^oC – 30MPa -10 min (95.5% TD) and c) 1700 ^oC – 50MPa – 5 min (95.4% TD) have produced ThO_2 pellets with the desired density. All these measurements of density indicate that SPS is capable of producing high density pellet of ThO_2 from the commercial powder at a temperature as low as 1600 ^oC, while the sintering pressure and time were maintained at 50 MPa and 10 min, respectively. In contrast to the work done by Tyrpekl, where the maximum density of ThO_2 pellets from the commercial powder was only 85% TD, we have fabricated pellets of ThO_2 with higher density (95% TD) using SPS.

7.4.3 Microstructural evolution of ThO_2

Microstructural analysis of ThO_2 pellets was carried out to study the effect of sintering parameters on the development of the microstructure and the evolution of porosity in the fuel matrix. From the SEM micrographs, inferences can be made about the onset of essential phenomena such as the neck formation, inter and intragranular pore formation and coalescence, and grain growth. Fig. 7.4 shows the evolution of microstructure of a sintered ThO_2 pellet at the various sintering temperature. The SEM micrograph at 1500 ^oC indicates the beginning of the neck formation, which marks the initial stage of sintering. The micrograph at 1600 ^oC reveals the densification as well as the creation of separate pore structure, marking the onset of the intermediate step of sintering. At 1700 ^oC, almost no porosity was visible due to pore shrinkage and closure. Additionally, grains have started to grow.

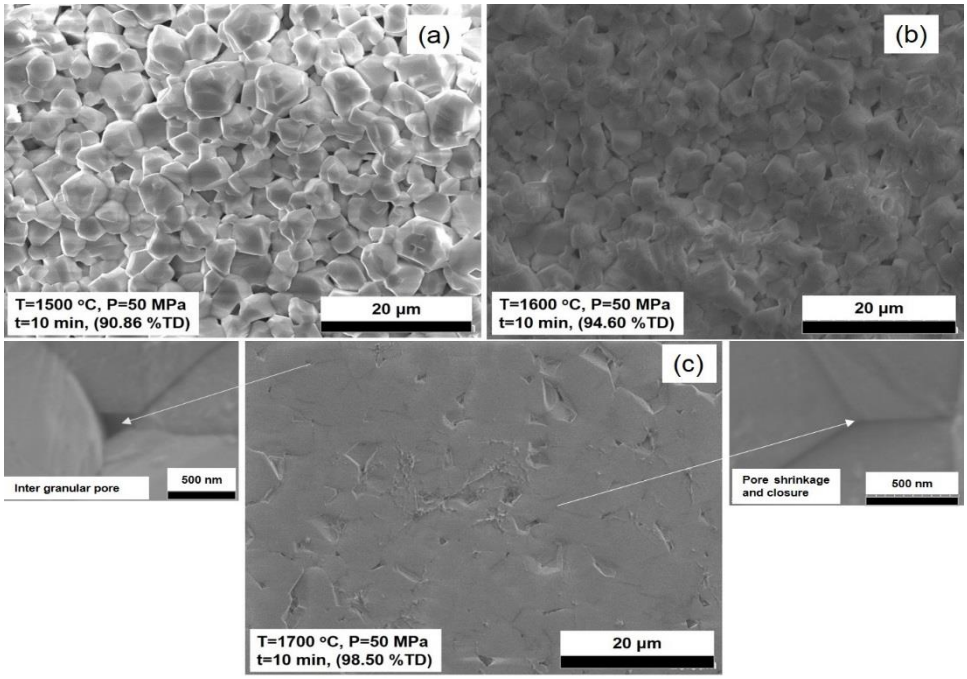

Fig. 7.4. SEM images for ThO_2 fuel sintered at different temperature keeping sintering pressure as 50 MPa and sintering hold time as 10 min.

The effect of sintering hold time on the microstructure evolution considering three different hold times (5, 10 and 15 min) while keeping the sintering temperature and sintering pressure at 1700 ^oC and 50 MPa, respectively, is illustrated in Fig. 7.5. At a hold time of 5 min, the microstructure has already attained a uniform structure with some intergranular pores. Comparing with the particle size of the as-received powder, the grains of the pellets sintered for 5 min has begun to grow (7 µm). As the hold time increased from 5 min to 10 min, the intergranular pores have disappeared, and with a further increase of hold time to 15 min, there was a significant grain growth. Finally, Fig. 7.6 shows the apparent effect of applied pressure on the microstructure of ThO_2. Starting from an applied pressure of 30 MPa, the porosity has decreased, and grain size has increased in each case.

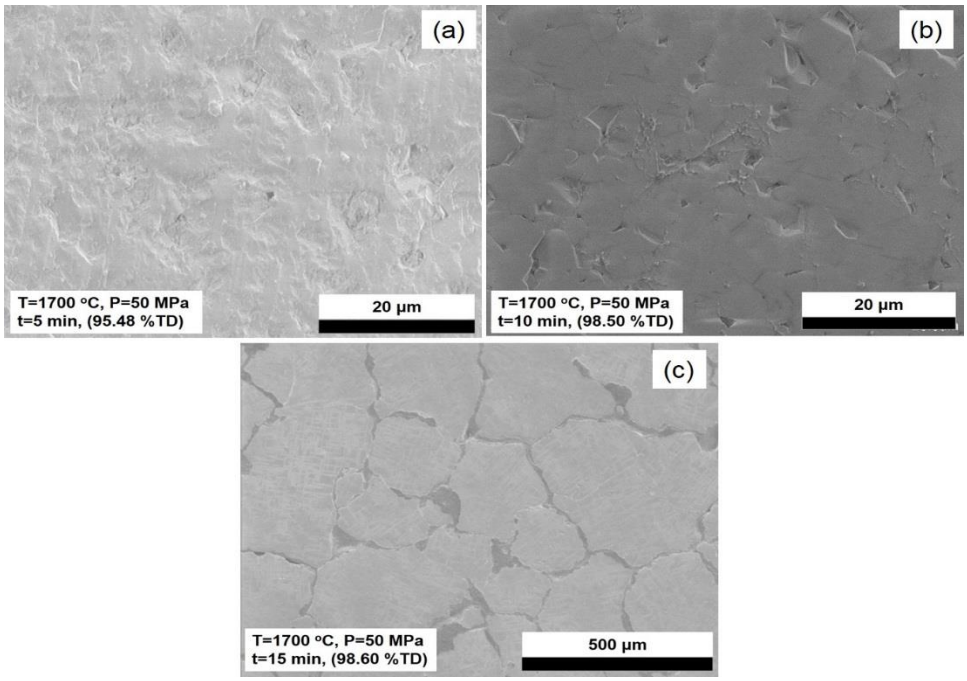

Fig. 7.5. SEM images for ThO_2 fuel sintered at different sintering time keeping the sintering temperature as 1700 ^oC and appiled pressure as 50 MPa.

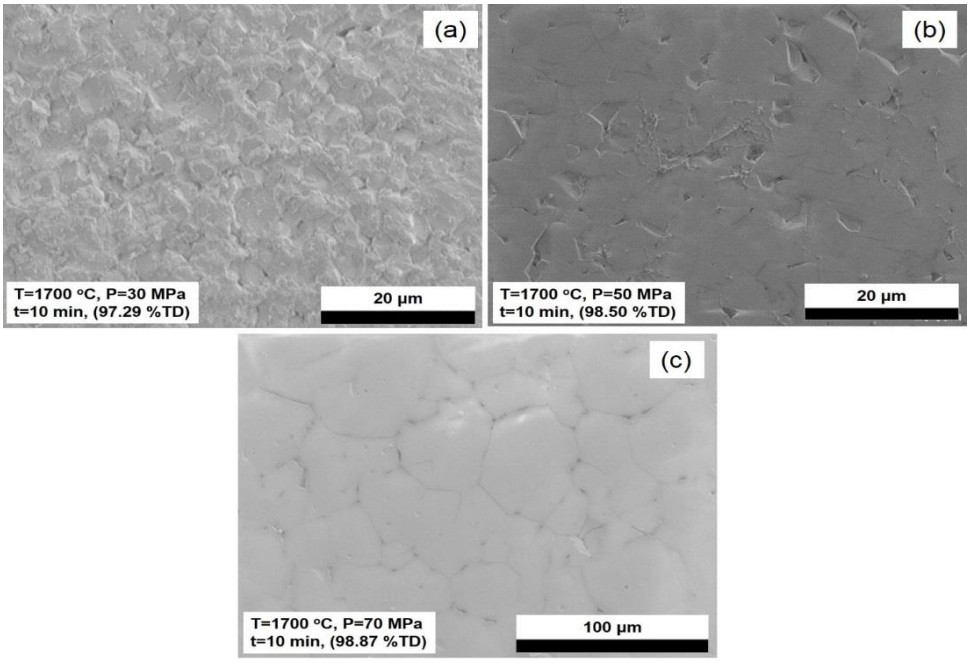

Fig. 7.6. SEM images for ThO_2 fuel sintered at different sintering pressure keeping the sintering temperature at 1700 ^oC and hold time 10 min.

7.4.4 Grain size and inverse pole figure from EBSD study

In the case of UO_2, Turnbull [284] has shown that the grain size of the fuel pellet plays a significant role in the fission gas release and swelling. Among the pellets of UO_2 with a grain size of 7 μm and 40 μm, the pellet with the grain size of 40 μm has shown to have a significant reduction in both fission gas release and swelling. The grain size also influences the creep; for instance, when the stress is lower than the threshold stress, the creep rate is inversely proportional to the square of grain size [285]. Since the grain size plays a vital role in the performance of the fuel, it is imperative to have control over the grain size of the fuel pellets. In the present work, characterization of the pellets with EBSD allowed for the acquisition of orientation maps which visually and quantitatively show the grain size of the sintered pellets. Orientation maps can also give information regarding the microstructural evolution from powder to a sintered structure, the porosity and the preferred orientation of the grains. The orientation maps for the SPS ThO_2 as a function of sintering temperature from 1500 to 1800 °C with an applied pressure of 50 MPa and hold time of 10 min are shown in Fig. 7.7.

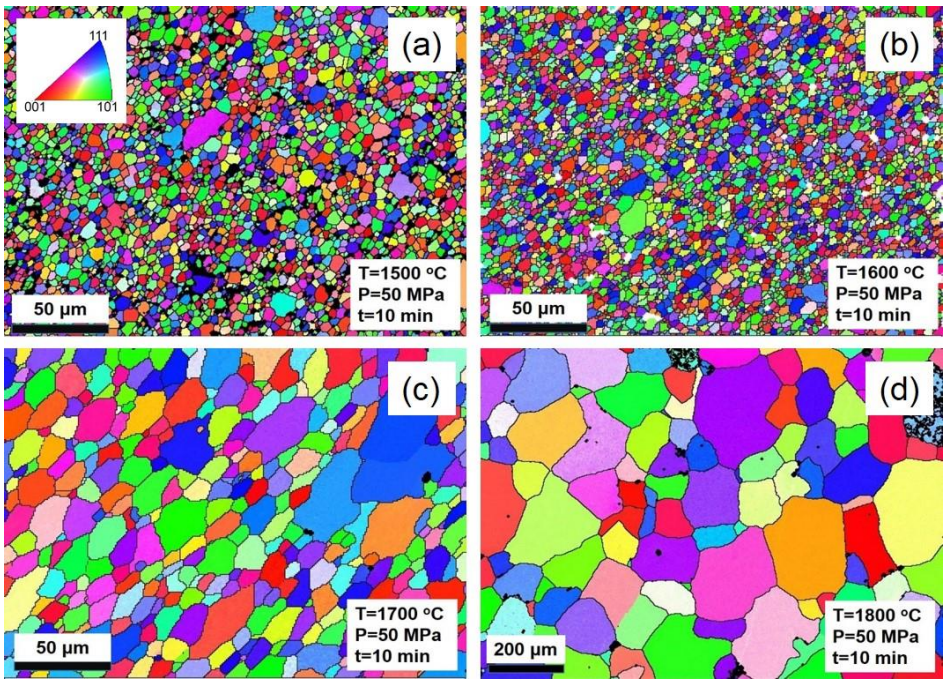

Fig. 7.7. EBSD images for ThO_2 fuel sintered at different temperature a) 1500 °C (3 μm) b) 1600 °C (3 μm) c) 1700 °C (10 μm) d) 1800 °C (99 μm). The legend of the color maps is shown as an inset in figure (a), and black color represent the pores in the sample.

In these IPF maps, the different colors correspond to the crystallographic orientation of each grain in such a way that the vector normal to different crystallographic planes of the grains is parallel to the normal direction (ND) of the specimen. For instance, the blue color grains correspond to <111>//ND, the green color grains correspond to <110>//ND, and the red color grains have <100>//ND orientation.

The correlation between the sintering temperature and the density is evident from the orientation maps. The EBSD orientation map also reveals that the quantity of intergranular pores was significantly higher at 1500 ºC than in the case at 1600 ºC. The average grain size for both the pellets sintered at 1500 ºC and 1600 ºC remained at 3 µm, indicating that the onset of grain growth required a temperature higher than 1600 ºC. As the temperature increased to 1700 ºC, the grains started to grow and had an average grain size of 10 µm. A further rise in temperature to 1800 ºC has caused a significant increase in the size of the grain with an average size of 99 µm.

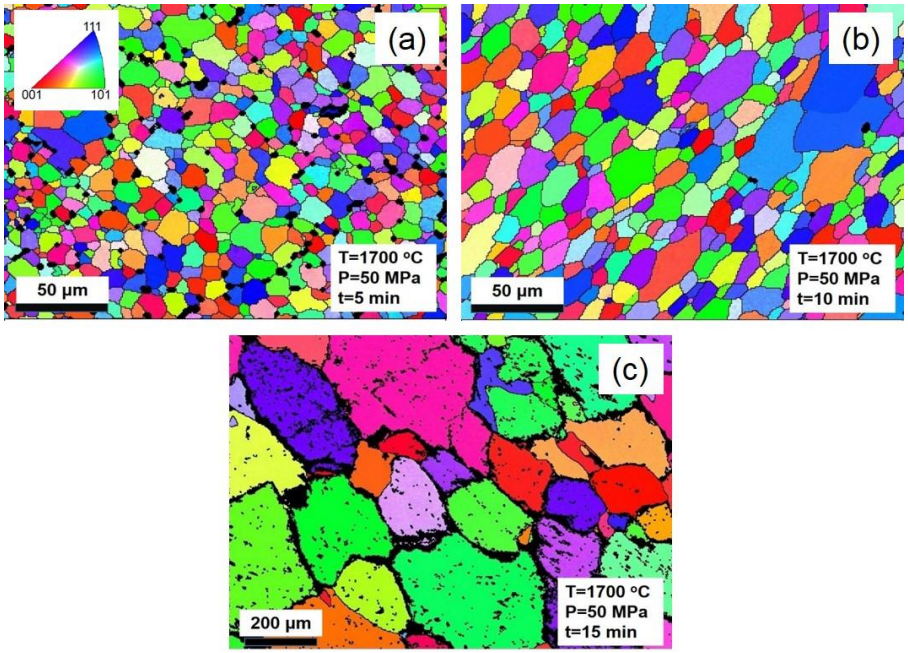

Fig. 7.8. EBSD images for ThO_2 fuel sintered at different hold time a) 5 min (7.5 µm) b) 10 min (10 µm) c) 15 min (105 µm). The legend of the color maps is shown as an inset in figure (a),), black color represent the pores in the sample.

Fig. 7.8 shows the orientation maps for SPS ThO_2 produced at different hold time. The orientation map indicated that maintaining the sintering dwell time of 5 min, 10 min and 15 min has led to a grain size of 7.5 µm, 10 µm, and 105 µm, respectively. Also, a significant number of intergranular

pores when the hold time was kept at 5 min was observed. In the case where the hold time was maintained at 15 min, cracks were formed along the grain boundaries, as was seen by visual inspection. The formation of intergranular cracks due to grain growth has been investigated by Paggi *et al.* [286] and have attributed this phenomenon to the Hall-Petch effect.

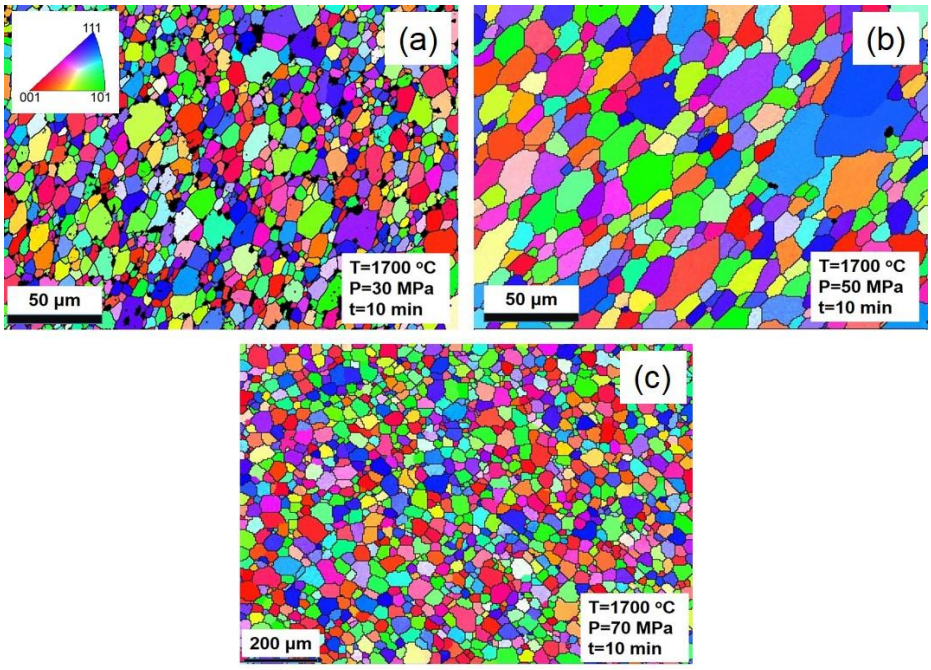

Fig. 7.9. EBSD images for ThO_2 fuel sintered at different applied pressure a) 30 MPa (5 µm) b) 50 MPa (10 µm) c) 70MPa (26 µm). The legend of the color maps is shown as an inset in figure (a), black color represent the pores in the sample.

The orientation maps for the SPS ThO_2 processed at varying pressures are shown in Fig. 7.9. The effect of applied pressure on the microstructure and grain size is apparent. The grain size has increased from 5.5 µm to 10 µm and 26 µm when the applied pressure was changed from 30 MPa to 70 MPa at an interval of 20 MPa. It has to be kindly noted, for brevity, the grain size distribution for each pellet is provided as S.I. from S.I.7.2-S.I.7.4.

On the micro-texture analysis of the specimens, Fig. 7.10 presents the comparison of the inverse pole figures (IPF) triangle of two samples sintered at 1600 ^{o}C and 1700 ^{o}C. The majority of the grains were oriented near <111>//ND fiber texture with a minor spread near <011>//ND during the sintering process at 1600 ^{o}C. Similarly, at 1700 ^{o}C, the grains were oriented near <233>//ND. This behaviour could be attributed to the increased sintering temperature.

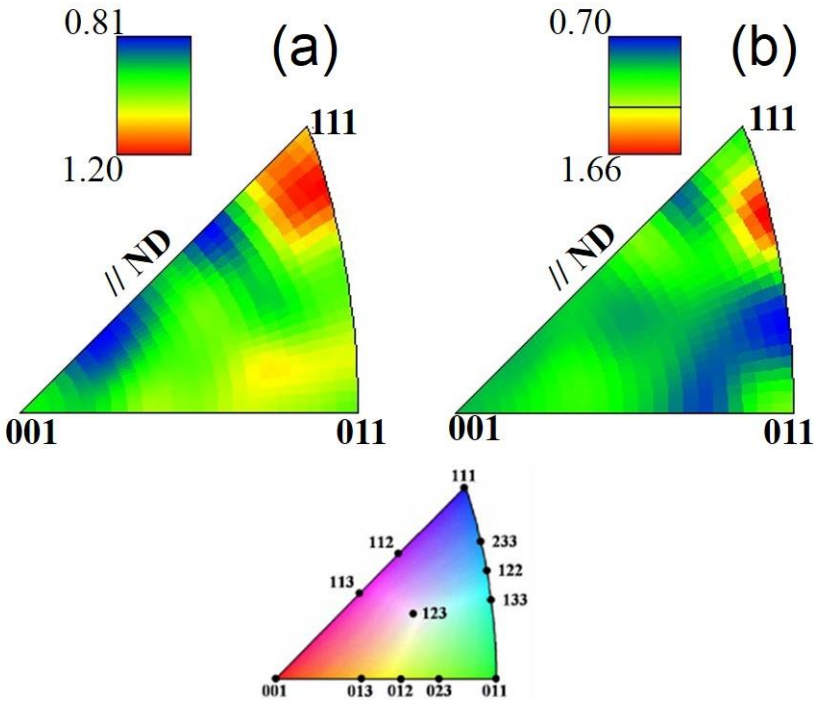

Fig. 7.10. Inverse pole figure of ThO_2 a) pellet sintered at 1600 ^oC, 50 MPa and 10 min b) pellet sintered at 1700 ^oC, 50 MPa and 10 min.

7.4.5 Thermal diffusivity and thermal conductivity

Fig. 7.11 shows the results of thermal diffusivity and the thermal conductivity measurement on ThO_2 sintered at different sintering conditions by SPS. The analysis was conducted three times at each temperature, and an average value was plotted. The measurements were performed on three different samples sintered at 1500 ^oC, 1600 ^oC and 1700 ^oC and the densities of these samples are measured to be ~91% TD, ~95% TD and ~99% TD, respectively. The pellets sintered at 1500 ^oC had the lowest thermal diffusivity value of 0.046 cm^2/s at 100 ℃, while the sample sintered at 1700 ^oC showed a diffusivity of 0.053 cm^2/s, an increase of 13%. With the rise in test temperature, the difference between the thermal diffusivity tends to decrease. Using the thermal diffusivity values, the thermal conductivity values were calculated and are presented in Fig. 7.11.b. The variation of density due to the thermal expansion and the C_p was calculated using the equations proposed by Bakker *et al.* [114] for ThO_2.

The thermal conductivity measurements indicate that the samples sintered at high temperature had a higher thermal conductivity. The reason for this was the improved microstructure, including the density and the grain size.

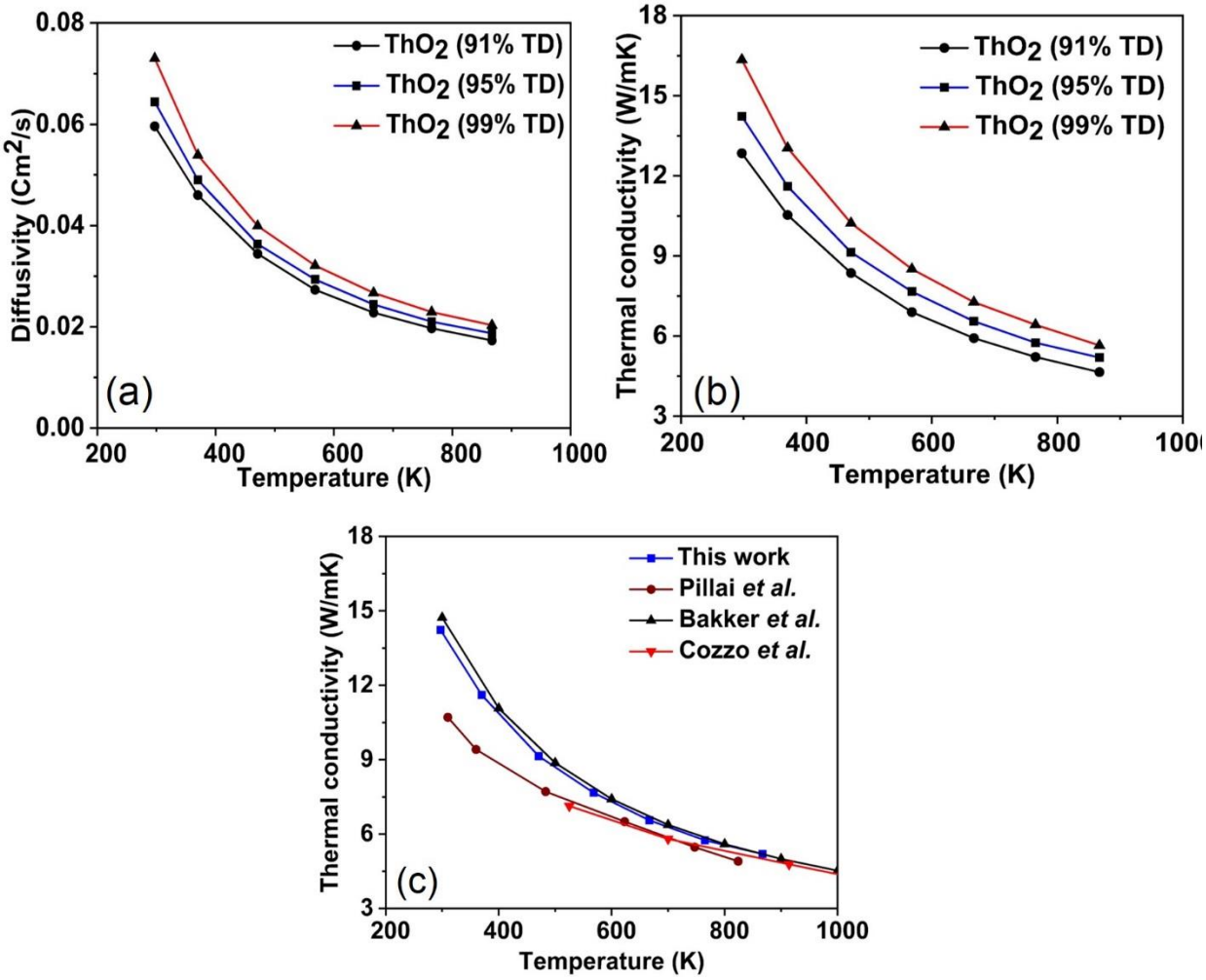

Fig. 7.11. (a) The thermal diffusivity of ThO_2 as a function of temperature for specimens sintered at 1500 ^oC, 1600 ^oC and 1700 ^oC. The uncertainty in the data point from the laser flash apparatus is ± 4.5%. (b) The thermal conductivity of the samples sintered at 1500 ^oC, 1600 ^oC and 1700 ^oC. (c) The thermal conductivity for the sample with 95% TD compared with the results of Pillai *et al.* [121], Cozzo *et al.* [126] and the recommended value of Bakker *et al.* [114].

Fig. 7.11(c) shows the thermal conductivity of our sample with 95% TD compared with the results of Pillai *et al*. [121], Cozzo *et al.* [126] and the recommended value of Bakker *et al.* [114]. Our results are in excellent agreement with the recommended values of Bakker, whereas, the data of Pillai and Cozzo are lower. For thermal conductivity using laser flash apparatus, the estimated relative error for the whole temperature range is about 10% by considering the relative uncertainties on the thermal diffusivity (4.5%), specific heat (2%) and density (3%) [122,126,287].

7.5 Conclusion

This study shows that by using SPS, it is possible to fabricate high density ThO_2 pellets at a low sintering temperature in a short time, without the addition of any sintering aid such as MgO and N_2O_5. A detailed analysis of the influence of sintering parameters on the densification of the ThO_2 pellets has been presented. The ThO_2 pellet with the desired density of 95 %TD can be obtained at a temperature as low as 1600 ℃, thus can potentially overcome one of the major issues in the front end of the fuel cycle provided the problems with the industrial scalability of the SPS techniques are solved. Also, we have shown that by varying the sintering temperature, sintering pressure, and sintering time, it is possible to tune the microstructural characteristics of ThO_2 fuel. EBSD studies quantitatively showed that higher sintering temperatures, pressure and hold time results in larger grain size. By optimizing the processing parameters, the grain size of the sintered pellets could be varied between 3 μm to 105 μm. The orientation maps demonstrated that some <111> texturing was observed in the pellet sintered at 1600 ^{o}C. The thermal diffusivity and thermal conductivity measurement reveal their dependence on the density of the samples. The understanding of the influence of the sintering parameters on the density, intergranular pores, grain size and thermal conductivity enables to tailor the sintering parameter to fabricate a highly customized fuel with desired properties.

7.6 Supplementary Information

S.I.7.1 XRD Analysis of the samples

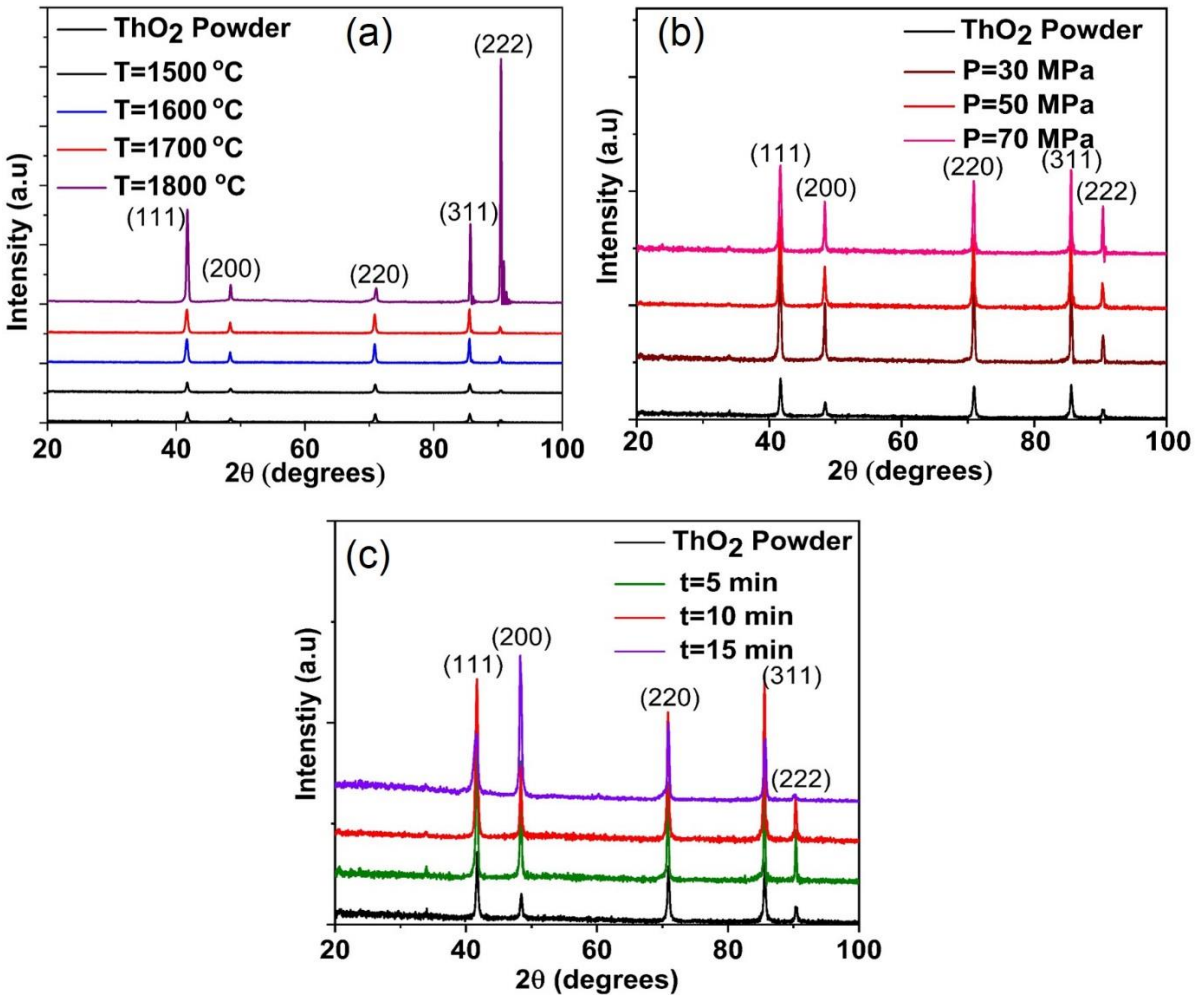

Fig. 7.12**.** XRD images for ThO_2 for fuel sintered (a) at different temperature, keeping pressure and hold time at 50 MPa and 10 min respectively (b) at different pressure, maintaining temperature and hold time at 1700 ^{o}C and 10 min (c) at different hold time, with temperature and pressure maintained at 1700 ^{o}C and 50 MPa respectively.

S.I.7.2 Grain size distribution

1. Effect of sintering temperature on the grain size of the specimen.

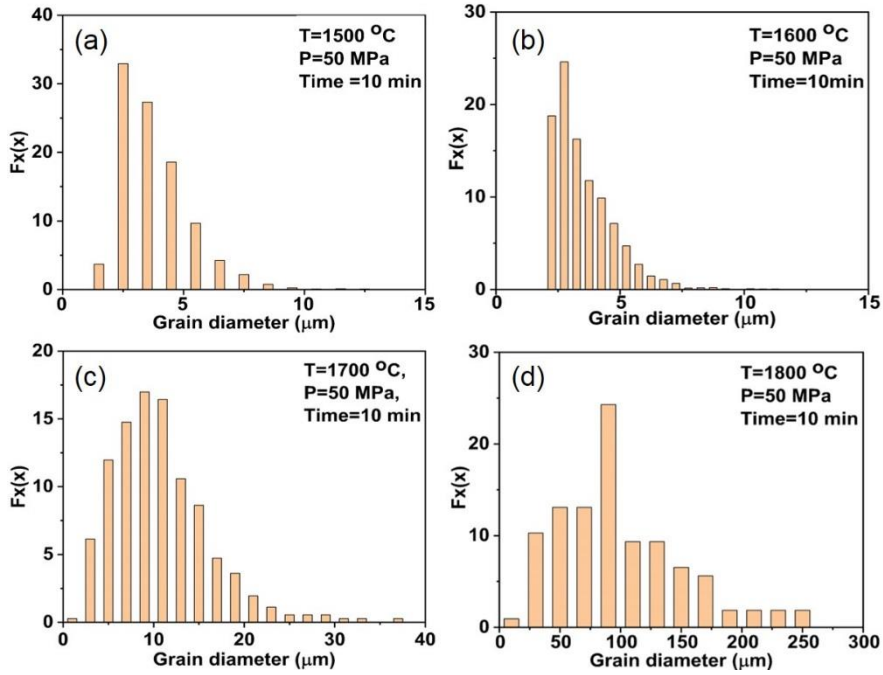

Fig. 7.13. Grain size distribution for ThO_2 fuel sintered at different temperature a) 1500 °C (3 μm) b) 1600 °C (3 μm) c) 1700 °C (10 μm) d) 1800 °C (99 μm).

2. Effect of sintering hold time on the grain size of the specimen

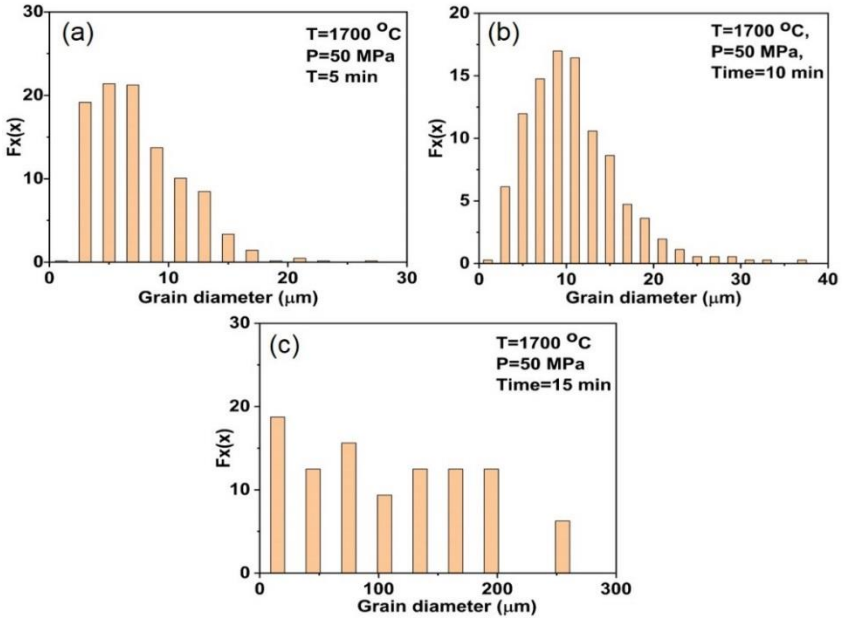

Fig. 7.14. Grain size distribution for ThO_2 fuel sintered at different hold time a) 5 min (5 μm) b) 10 min (10 μm) c) 15 min (105 μm).

3. Effect of sintering applied pressure on the grain size of the specimen.

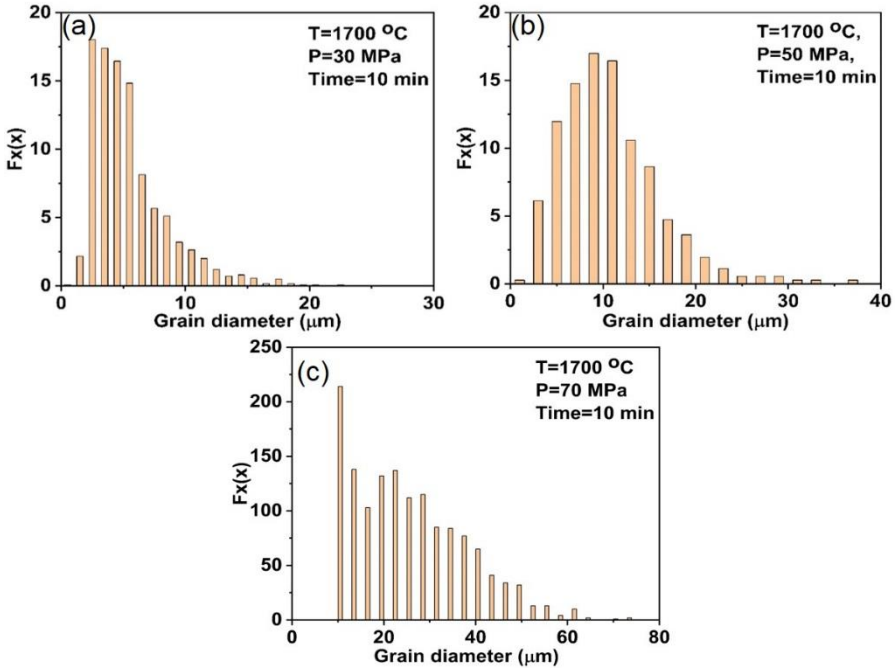

Fig. 7.15. Grain size distribution for ThO_2 fuel sintered at different pressure a) 30 MPa (5 μm) b) 50 MPa (10 μm) c) 70 MPa (26 μm).

Chapter 8 : Enhanced thermal conductivity of thorium dioxide-silicon carbide composite fuel pellets fabricated by spark plasma sintering (SPS)

8.0 Overview

So far, the thermal conductivity of the ThO_2, surrogate CeO_2 and the additives such as SiC and BeO have been individually investigated. We have also studied the effect of SPS processing parameter the densification, microstructure and the thermal conductivity of ThO_2. The final objective of this work has been to establish the role of SiC addition on the densification, microstructure and the thermal conductivity of ThO_2. This chapter describes in detail the effect of the addition of SiC in ThO_2 on the densification, microstructure, and the thermal conductivity of ThO_2-SiC composite fuels fabricated by SPS sintering process.

The research findings reported in this chapter are prepared as manuscript #6 as follows:

L. Malakkal, A. Prasad, J. Ranasinghe, M.K. Tummalapalli, E. Jossou, B. Szpunar, L. Bichler, J. Szpunar, "Enhanced thermal conductivity of thorium dioxide-silicon carbide composite fuel pellets fabricated by spark plasma sintering (SPS)", manuscript prepared.

The contributions of the PhD candidate are 1) performing DFT and MD calculations, 2) preparing the samples for characterization, 3) performing XRD, SEM, and EBSD characterizations, 4) measuring of thermal conductivity using Laser flash apparatus, 5) analyzing of the results, 6) writing the manuscript for publication. My supervisors reviewed the manuscript before it was submitted for publication in this journal.

The differences between the content of this chapter and the submitted paper are:

1. The equations used to determine the thermal diffusivity and the thermal conductivity using the laser flash apparatus has been removed to avoid repetition. They are presented as equations 2.28 and 2.28 in chapter 2.
2. The references of the manuscript are listed at the end of the thesis.

Enhanced thermal conductivity of spark plasma sintered thorium dioxide-silicon carbide composite fuel pellets

Linu Malakkal[1], Anil Prasad[2], Jayangani Ranasinghe[3], Murali Krishna Tummalapalli, Ericmoore Jossou[1], Lukas Bichler[2], Jerzy Szpunar[1]

[1]Department of Mechanical Engineering, University of Saskatchewan, Canada

[2]School of Engineering University of British Columbia-Okanagan Kelowna, Canada

[3]Department of Physics and Engineering Physics, University of Saskatchewan, Canada

8.1 Abstract

ThO_2-SiC composite fuel pellets were fabricated via the SPS method, to investigate the role of addition of SiC in enhancing the thermal conductivity of ThO_2 fuel. SiC particles with an average grain size of one micrometre in 10 and 15 vol% were used to manufacture the composite pellets. The changes in the densification, microstructure and the thermal conductivity of the composites were explored by comparing with pure ThO_2 pellets. The structural and microstructural characterization of the composite pellets has revealed that SPS could achieve pellets without the formation of any reaction products or intermetallics. The density measurement by the Archimedes principles and the grain size from the EBSD analysis have indicated that the composites have higher densities and smaller grain size than the pellets without SiC addition. Finally, thermal conductivity measurements as a function of temperature have revealed that SPS sintered ThO_2–SiC composites showed an increase of up to 56% in thermal conductivity compared to ThO_2 pellets.

8.2 Introduction

In the pursuit of a sustainable, renewable, and clean source of energy, the energy from the nuclear fission reaction is an attractive alternative to the power generated from fossil fuels. However, compared to other sources of renewable energy, the primary deterrent to the promotion of nuclear power has been the occurrence of tragic accidents such as in Chernobyl and Fukushima. After the Fukushima nuclear mishap, much focus has been given in developing new fuel-cladding concepts under the name of accident tolerant fuels (ATF) [5]. The ATFs are expected to have higher thermal conductivity making these fuels more resistant to meltdown during the loss of coolant accident (LOCA). The ceramic nuclear fuels in current use such as UO_2 and ThO_2 have lower thermal conductivity, thereby causing a higher radial thermal gradient in the fuel pellet, which could cause

the core of the pellet to melt. Two broad methods are being proposed to solve the problems of the lower thermal conductivity of the conventionally used ceramic fuels. They are the modification of the fuel geometry (modification from the solid cylinder to hollow cylinder) [288–290] and the enhancement of the thermal conductivity by the addition of materials with high thermal conductivity such as SiC [26–28,291], BeO [22,23,25,292,293], diamond [29], and Mo [294].

Recently, various researchers have investigated the effect of the addition of high thermal conductivity materials in the enhancement of thermal conductivity of UO_2. For example, Yeo *et al.* [27] fabricated the composite fuels of UO_2–10 vol% SiC composite fuel pellets by oxidative sintering and SPS at a range of temperatures from 1400 to 1600 °C. In this study, the measurement of thermal conductivity revealed that SPS sintered UO_2–SiC composites compared to UO_2 pellets showed an increase of up to 62% in thermal conductivity. Zhou *et al.* [23] and Li *et al.* [24] have respectively demonstrated that adding 10 vol% of BeO increased the thermal conductivity by over 40% and 45.3% compared to UO_2 at room temperature. Chen *et al.* [29], using the SPS technique have made high density UO_2–5 vol% diamond composite pellets and found an increase in thermal conductivity of up to 41.6%, 38.3% and 34.2% at 100 ℃, 500 ℃ and 900 ℃, respectively, compared to the pure UO_2 fuel pellets. Cartas *et al.* [30] introduced the concept of adding carbon nanotubes (CNTs) into UO_2 for thermal conductivity enhancement using SPS. In another work, Yao *et al.* [31] sintered UO_2-graphite nanoplatelet (GNP) composite fuel via SPS and reported that the in-plane thermal conductivity nearly tripled by GNP addition.

Apart from UO_2 and its composites, the role of ThO_2 in the ATF, as well as the generation 1V reactors, are also investigated [51]. Among the six future reactor concepts that the GIF proposed, the Canadian design SCWR considers the use of solid core thorium [52] and the MSR use the fuel (thorium or uranium) in liquid form [53]. Apart from these two concepts, thorium fuel cycle alternatives were analyzed in proven technologies such as high temperature gas-cooled reactor (HTGR) [54], LWR [55,56] and PWR [57], and also for new technologies such as gas turbine modular helium reactor [58], fixed bed nuclear reactor [59], and accelerator-driven systems [60].

Even though there are several advantages in considering ThO_2 fuels, its lower thermal conductivity is still a concern. Therefore, in this study, we have tried to enhance the thermal conductivity of ThO_2 fuel by adding SiC as an additive. Towards this goal, we have fabricated ThO_2-SiC

composite fuels. Apart from thermal conductivty, the effect of SiC addition in the densification, microstructural, and the grain size of ThO_2 is also explored.

8.3 Experimental procedure

8.3.1 Precursor powder

The ThO_2 powder used in this study was supplied by IBILABS, U.S.A. (purity of 99.8%). The powder XRD of ThO_2 revealed a single-phase face-centered cubic structure was having the lattice parameter of 5.60 Å. An additional peak corresponding to Thallium oxide, an impurity declared by the manufacturer was observed at a diffraction angle of 34°. Observation of powder via scanning electron microscopy (SEM) showed that the particle has a square-shaped morphology (Fig. 8.1.a) and the particle size ranged between 1-6 μm. Alfa Aesar Inc. supplied the SiC powder used in the study with a purity greater than 99.8% and an average particle size of 1 μm. The XRD analysis of the SiC powder revealed a single-phase face-centered cubic structure (β phase) with a lattice parameter of 4.42 Å. The SEM micrograph of the SiC powder showed the particle had a sharp-edged faceted morphology as shown in Fig. 8.1.b.

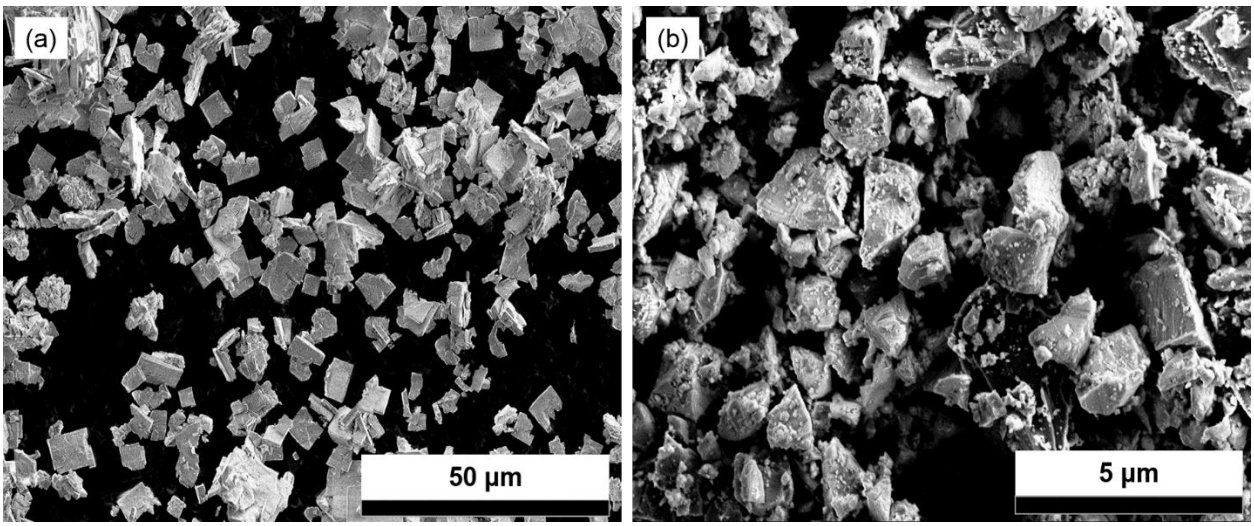

Fig. 8.1. SEM micrograph of (a) ThO_2 powder (b) SiC powder.

8.4 SPS sintering of ThO_2-SiC composite fuel

8.4.1 Powder preparation

Two powder batches were prepared; ThO_2 with 3.25 wt% SiC (~10 vol %) and ThO_2 with 5wt% (~15 vol%) SiC. A 30 g of composite powder blend of two batches were prepared using a planetary

ball mill. The powders were transferred to a stainless steel jar with a 10 mm diameter stainless steel balls, by maintaining the powder to ball ratio of 10:1. Ethanol was used as a process control agent (PCA) to enhance the efficiency of dispersion and blending. The powder was milled for an hour, and the powder-PCA slurry was separated from the jar and ball into a petri dish. The composite powder mixture was then dried in a fume-hood.

8.4.2 Sintering

The dried composite powders were sintered in an argon atmosphere using a Thermal technology LLC 10-3 Spark Plasma Sintering (SPS) system located at University of British Columbia (Kelowna, BC). The starting powder was loaded into the graphite die of internal diameter 12.7 mm. A thin graphite foil (0.125 mm) was used at tooling powder interfaces to prevent friction and reaction between ThO_2 and tooling. The die was placed inside an analytical balance for filling with the powder. Once the powder was filled the punch was inserted into the die with a grafoil disk in between the punch and the powder. The filled die was then placed inside the SPS chamber with a carbon sleeve around it. The carbon sleeve was used to reduce radiation heat loss at high temperatures. The entire die assembly was set up inside the chamber, and the chamber was evacuated and then filled with the Argon, and the sintering process was initiated. The temperature during the experiment was monitored using an optical pyrometer. The applied uniaxial pressure, temperature, chamber pressure, current, and voltage were continually recorded as a function of time. The sintering process was controlled by a built-in Eurotherm controller, which was programmed using iTools software.

Initially, the temperature was ramped from room temperature to 600 ^{o}C at a heating rate of 30 ^{o}C/min. The pressure is maintained at 5 MPa, and this condition is maintained for 15 seconds. This step was intended to allow the pyrometer to respond since it has a low-temperature cut-off of 464 ^{o}C. Beyond this temperature, the heating rate was increased to 100 °C/min to a desired maximum sintering temperature of 1800 ℃. Further, the pressure was ramped to the desired sintering pressure of 60 MPa. The pressure ramp rate was coupled to the heating rate to reach the peak temperature and pressure at the same time. The hold time was maintained at 30sec. Three different heating and cooling rate of 50 ^{o}C/min 75 ^{o}C/min and 100 ^{o}C/min were used. Once at room temperature, the die was removed from the chamber, and the pellet was ejected. After

sintering, the chamber is allowed to cool, and the graphite die with sintered compact was taken out of the SPS chamber, and the pellets were subjected to different characterization techniques.

8.4.3 Characterization methods

The sintered pellets were ground using 500-grit sandpaper to remove the residual graphite foil. The cleaned specimens are characterized using techniques such as X-ray Diffraction (XRD), Raman spectroscopy, Scanning Electron Microscopy (SEM), Electron Back Scattered Diffraction (EBSD) and Laser Flash Apparatus (LFA). The XRD patterns were recorded using Bruker D8 Discover with chromium K-alpha radiation at a temperature of 25 ^{o}C. The 2θ angle was scanned from 20^{o} to 110^{o} with a step size of 0.01^{o} and a scanning time of 600s per step. The software X'pert High Score Plus was used to fit the peak profile. The Archimedes' method (Torbal density measurement kit) was used to determine the density of each pellet by immersing the pellets into the distilled water. Five reading were recorded for each specimen, and the average data with the error bar is reported. The samples were polished to mirror finish by grinding the pellets with silicon carbide (SiC) papers starting with a grain size of 46 μm and gradually bringing down to 5 μm. After polishing with the SiC paper, the samples were polished using 3 μm MD mol cloth with 3 μm MD mol suspension, and 1 μm MD nap cloth with 1 μm MD nap suspension. The microstructural studies using SEM and EBSD on the polished specimens were carried out with a SU 6600 field emission-scanning electron microscopy.

Thermal diffusivity measurements of samples were carried out using the LFA (TA instruments-DLF-1/EM-1300). In this technique, a high-power laser pulse (450 μs pulse width) from a solid-state Nd: glass laser pulse source is used to illuminate the front face of the sample while the resulting temperature rise is recorded on the rear face with a liquid nitrogen cooled InSb infrared detector. The samples used in this study were disc-shaped and measured about 12.7 mm in diameter and had the thickness in the range of 2 mm to 3 mm. The sample thickness was determined by averaging 5 values measured using a calibrated micrometer. The standard deviation of the average thickness was less than 0.02 mm. The samples are coated with the graphite spray for better absorption and emissivity of the laser flash. The measurements were conducted in the argon atmosphere starting from room temperature to 900 K. By measuring the time taken for the temperature rise in the rear face; laser flash technique records the thermal diffusivity (α) of the specimens using the Parkers relations [111] given as shown in equation (2.28). From the measured

α, the thermal conductivity as a function of temperature ($k(T)$) can be measured using the relation (2.29). In this work the Cp changes as a function of temperature was determined by comparing the maximum value of the temperature rise with that of a reference pellet, using the relation $Cp = Q/(dT.m)$, where Q represents the energy of the pulsed laser beam, m mass of the specimen, and dT is the maximum value of the temperature rise. The reference pellet used was certified stainless steel. However, the density changes as a function of temperature have been kept constant. The thermal conductivity measurements were made on cylindrical pellets of diameter 12.7 mm and thickness 2-3 mm.

8.5 Results and Discussions

8.5.1 Structural characterization using X-ray Diffraction

XRD was performed on all the sintered samples to determine the reaction products formed. Since the amount of SiC in the composites specimens were within the detection limits of XRD, a sample with higher weight percent (15 wt%) of SiC was fabricated by keeping the conditions similar to the ThO_2-5vol% SiC pellets.

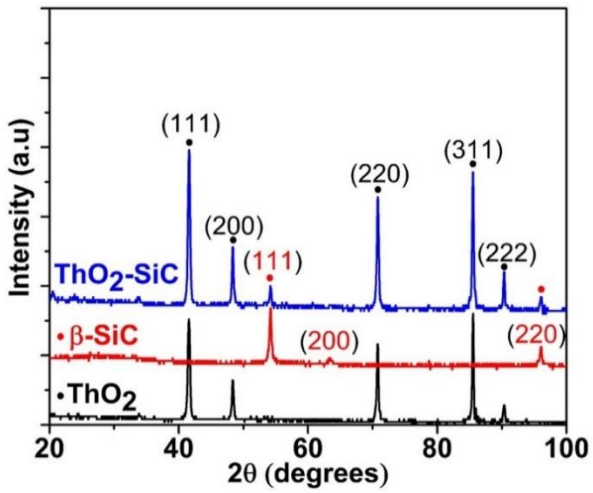

Fig. 8.2. XRD analysis of the precursors (ThO_2 and SiC) and the ThO_2-15 wt% SiC sintered pellet.

Fig. 8.2 compares the XRD patterns of the as-received ThO_2 and SiC powder with the sintered composite pellets with the higher SiC concentration. The comparison of XRD pattern clearly shows that no additional peaks other than ThO_2 and SiC were detected in the SPS sintered composite samples, indicating that no reaction products or intermetallic have been formed. For

brevity, the XRD analysis of all other samples considered in this work is provided as supplementary information (S.I).

8.5.2 Density measurement

The density of fuel pellets plays a significant role in nuclear fuel performance [283]. A fully dense fuel pellet is expected to have higher thermal conductivity than the porous pellets and therefore, fabricating a high density ThO_2-SiC pellets are crucial for obtaining enhanced thermal conductivity. However, some porosity in the fuel pellets are required to accommodate the fission gas and hence, achieving a density of ~96% TD is desired in the nuclear industry. The measured relative density (RD) of the ThO_2 and its composite pellets considered in this study, along with the sintering conditions used for fabricating each pellet is provided in table 8.1. The measured relative density of the composites indicates that the desired density of ~96% can be achieved using the sintering temperature of 1800 ^oC, the pressure of 60 MPa, and the hold time of 30 sec. The heating and cooling rate did not show any particular trend in the relative density value. However, it is interesting to note that under the same sintering conditions, the ThO_2-SiC composite had a higher density than the pure ThO_2. A similar trend of improvement in the density of Ni-Zn-Al alloy with the addition of SiC has been previously observed [295]. This increase in relative density might be due to the enhancement of thermal conductivity caused by SiC addition. Similar observations have been made in YSZ-CNT composites due to the addition of CNTs, with higher thermal conductivity [296].

Table 8.1. The density of the composite fuel. Sample A, B, C are ThO_2 with 10 vol% SiC, and sample D carresponds to 15 vol% SiC.

Sample name	Temp. (^oC)	Press. (MPa)	Time (s)	Heating rate (^oC/min)	Cooling rate (^oC/min)	Composite RD (% TD)	Pure ThO_2 RD (% TD)
A	1800	60	30	50	50	96.53±0.08	94.40±0.07
B	1800	60	30	75	75	98.66±0.04	95.50±0.07
C	1800	60	30	100	100	96.83±0.06	94.50±0.08
D	1800	60	30	75	75	97.76±0.07	95.50±0.07

8.5.3 Microstructure of the composite pellet

Fig. 8.2.a and b show the SEM micrographs of sample A and B, respectively. The microstructure of ThO_2-10 vol% SiC composite pellets reveals a uniform distribution of SiC particles in the

composite pellets. The particles were uniformly distributed without any agglomeration because of both ball milling and the dispersing agent ethanol. For the composites to have the desired property of enhanced thermal conductivity, ThO_2 and SiC need to have good interfacial contact. Fig. 8.2.c shows a magnified image of an individual SiC particle in ThO_2 matrix, the Fig. 8.2.c shows no evidence of crack and a good coherence between the additive and matrix. A similar observation was made by Yeo *et al.* [27] in the case of UO_2-SiC composite fabricated by SPS.

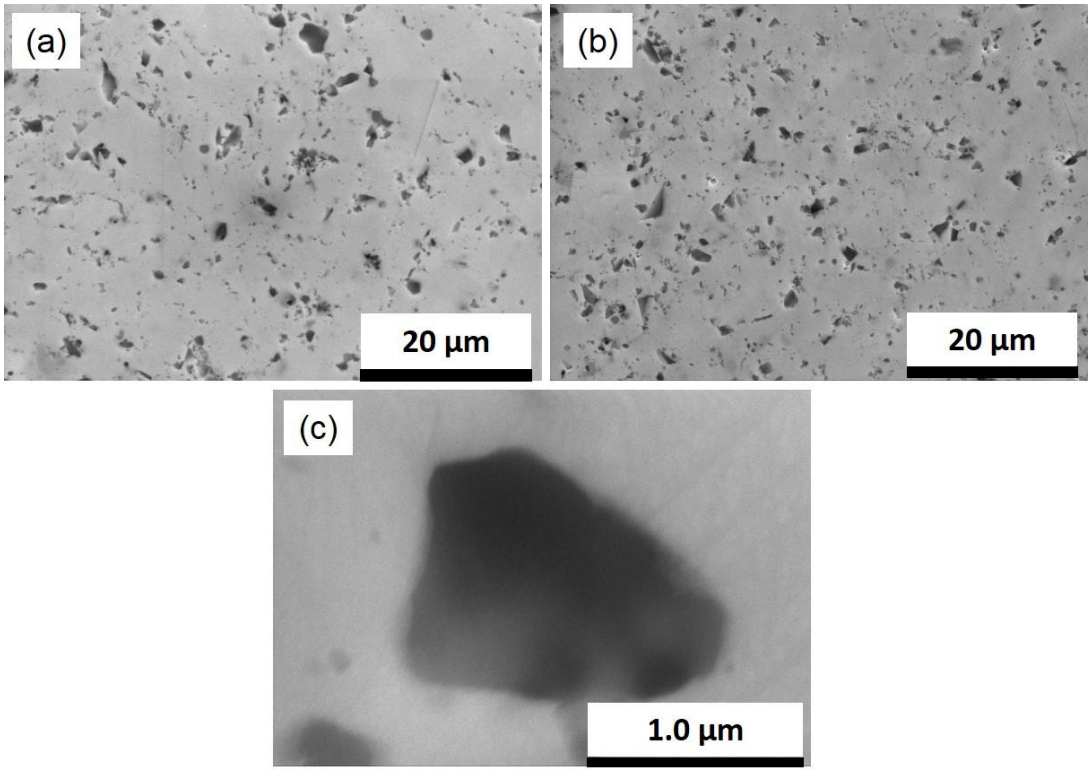

Fig. 8.3.(a) SEM micrograph of sample A, (b) SEM micrograph of sample B, (c) SEM micrograph indicating a good interfacial contact in sample A.

The EDX micrograph and distribution maps of the corresponding elements of sample A such as Th, O, and Si are acquired using the characteristic X-ray from the K-line, as shown in Fig. 8.4. From the analysis of the EDX mapping/imaging of the material, it was further confirmed that SiC was uniformly distributed in the ThO_2 matrix. Also, no other impurity elements were found in the sample as observed by EDX spectrum in Fig. 8.4.b. The carbon atom is not shown in the EDX plot because C in SiC represents a high-absorption situation because the Si L-shell absorption edges are located below the energy of the C K characteristic X-ray. The self-absorption of the C in SiC reduces its intensity relative to the Si peak such that the height of the Si peak limits the vertical

display range. Therefore, the C K peak is not visible as a distinct peak [297]. The role of SiC addition on the grain size of the composite pellets was studied using EBSD analysis. The EBSD micrograph and the grain size distribution of the pellets with and without the addition of SiC under the similar sintering conditions (conditions applied for the sample B) are shown in Fig.8.5. The average grain size of the composite fuels were 3 μm compared to the 6 μm of the pure ThO_2 fuel. The reduction of the grain size of the composite fuels is attributed to the pinning effects. Similar observations were made in the case of UO_2-SiC composite fuels [27]. The addition of the second phase particles increases the pinning effects resulting in the smaller grain size of a composite.

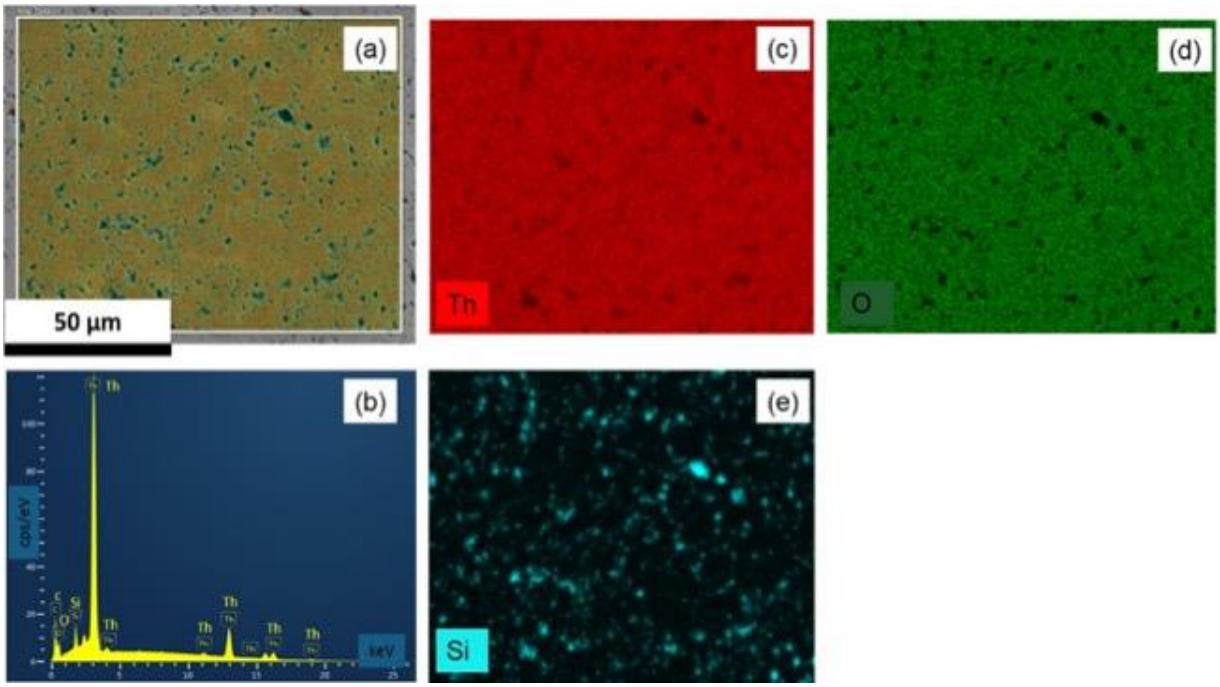

Fig. 8.4. (a), (b) SEM-EDX micrograph of sample A with the carresponding EDX analysis and distribution maps of the whole elemental composition (c) Th (d) O and (e) Si.

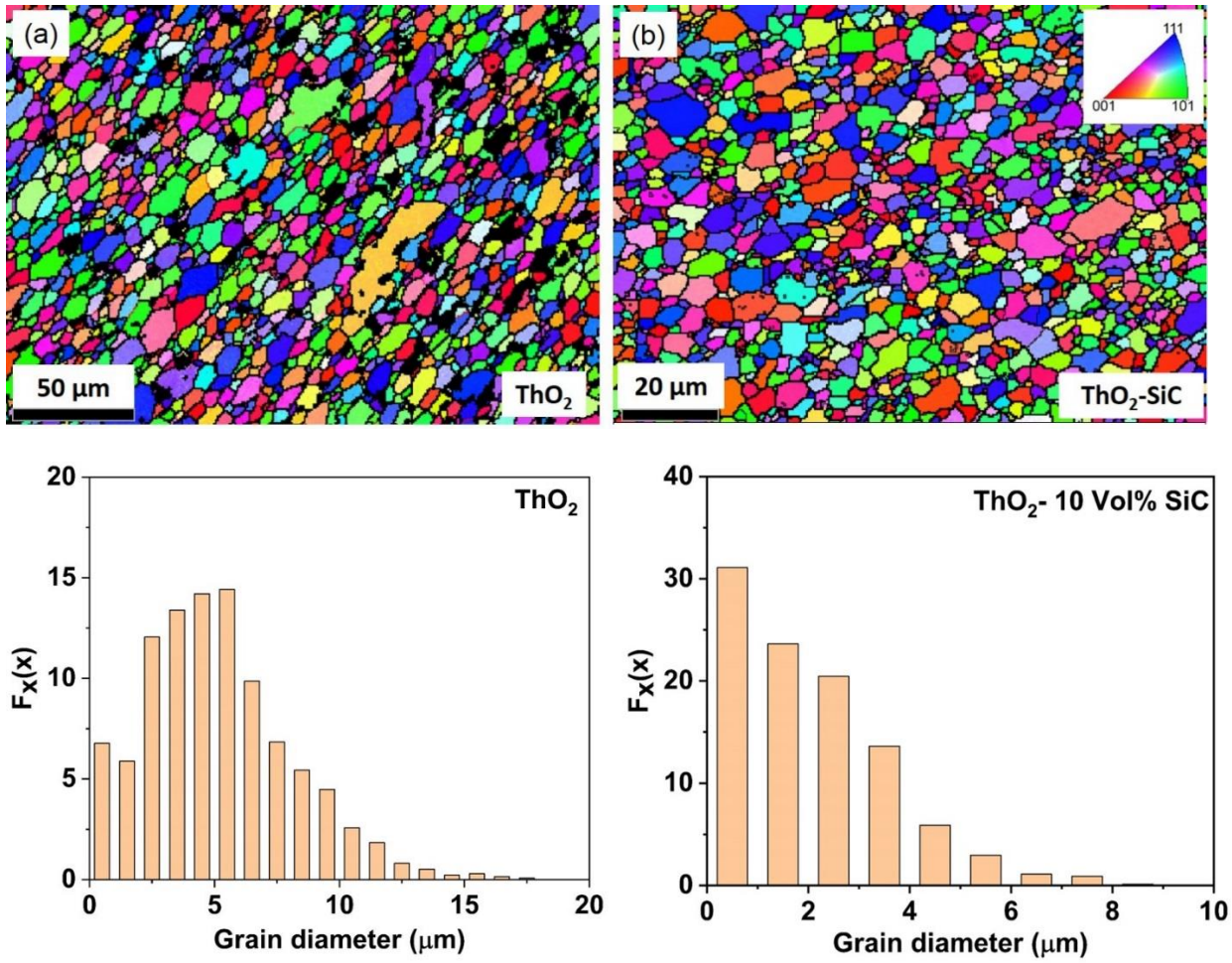

Fig. 8.5. Grain size comparison of the ThO_2 pellets with and without the addtion of SiC.

8.5.4 Thermal conductivity

The thermal conductivity and thermal diffusivity of the pellets of ThO_2 prepared with and without the addition of SiC via SPS are presented in Fig. 8.6. Three measurements were conducted from room temperature to 900 ^oC at an interval of 100 ^oC, and the average values were plotted. For thermal conductivity using laser flash apparatus, the estimated relative error for the whole temperature range is about 10% by considering the relative uncertainties on the thermal diffusivity (4.5%), specific heat (2%) and density (3%) [122,126,287]. The average thermal conductivity values of UO_2 and UO_2-10vol% SiC from the literature [27] at various temperatures are also shown in Fig.8.b. The SPS sintered ThO_2-SiC composite pellets have higher thermal conductivity than ThO_2 pellets. The composite pellet with a density of 96% TD had an increase in thermal conductivity of 46%, 56%, 49% at 100 °C, 500 °C and 800 °C, respectively, compared to the ThO_2

pellet at similar density. The reduction of thermal conductivity as a function of temperature is attributed to the phonon-phonon scattering phenomena in the ceramic material. Comparing to the UO_2-SiC composite, ThO_2-SiC composite fuels have significant improvement in the thermal conductivity, as shown in Fig.8.6.b.

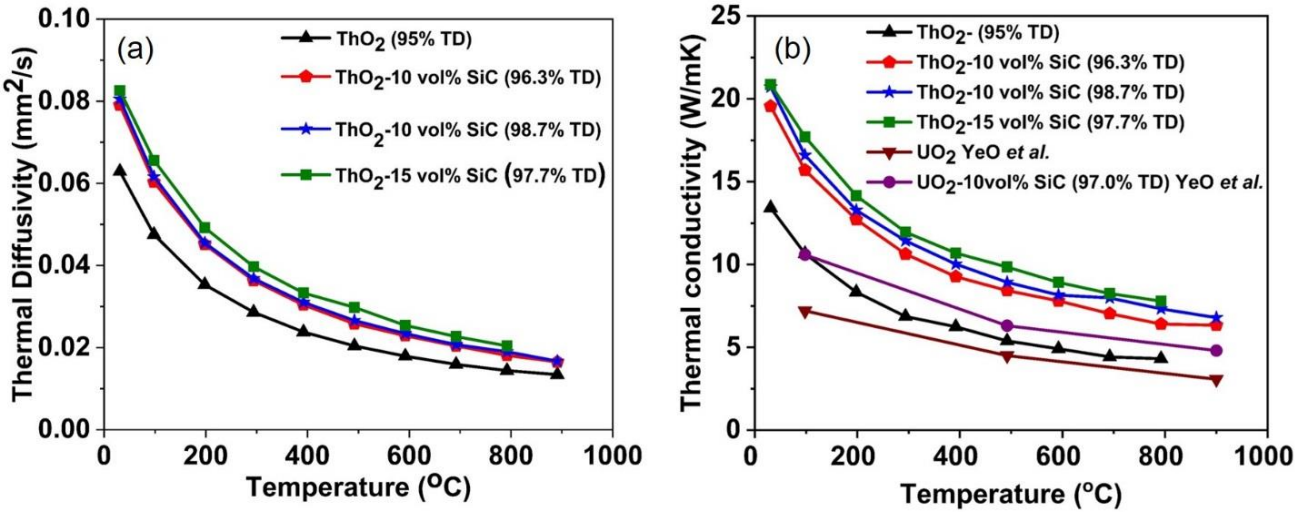

Fig. 8.6. (a) Thermal diffusivity, (b) thermal conductivity values of ThO_2 and ThO_2–SiC composite pellets sintered by SPS.

8.6 Conclusion

In this work, we have successfully manufactured high density ThO_2-SiC composite fuels via SPS technique. The XRD analysis of the fabricated composite pellets indicates that SPS could produce the composite pellets without the formation of any intermetallics or reaction products. The density measurement of the fuel pellets sintered at similar sintering conditions has revealed that the composite pellets had a higher density than the pellets of ThO_2 without the addition of SiC. The SEM micrograph and the EDX analysis of the sintered pellets have suggested that the using of ball milling and the process control agent to mix the powders has resulted in the uniform distribution of SiC in the ThO_2 matrix. Additionally, the SEM micrograph has also shown superior interfacial contact between SiC and ThO_2. The grain size measurement from the EBSD analysis has indicated that the addition of SiC to ThO_2 has marginally reduced the grain size. Finally, the study reveals that the SiC addition to ThO_2 has enhanced the thermal conductivity up to 56% compared to ThO_2 pellets. The results presented here suggest that SPS can offer a suitable method for manufacturing

composites with enhanced thermal conductivity provided the issues about the industrial scalability of the SPS is solved.

8.7 Supplementary Information

S.I.8.1 XRD Analysis of the samples

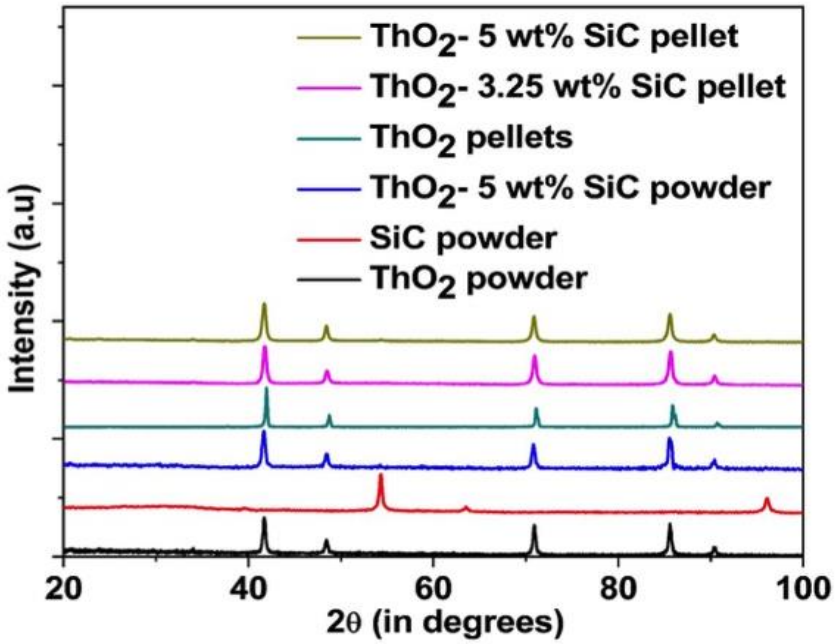

Fig. 8.7**.** XRD images for ThO_2 and ThO_2-SiC composites.

Chapter 9 : Conclusion and Future Work

9.0 Overview

The simulation and experimental results presented in this thesis can contribute to the development of the accident tolerant fuel. In this chapter, a conclusion of the key findings of each chapter is presented. Following that, the original contribution and some of the future work will be highlighted in details.

9.1 Conclusion

9.1.1 Atomisitc and experimental determination of the thermal conductivity of bulk and porous ThO_2 and surrogate CeO_2 fuels

Though the understanding of the fundamental principles of thermal transport of UO_2 is fairly established, the knowledge of the thermophysical and thermomechanical properties of ThO_2 and the surrogate CeO_2 is limited. Also, the available literature data on the thermal conductivity of these materials are scattered. Therefore, a first principle prediction of the thermal conductivity of ThO_2 and CeO_2 as a function of temperature was necessary. Understanding of the fundamental processes of thermal transport in these materials is vital for understanding various experimental findings. Chapter 3 presents, to the best of our knowledge, the most accurate DFT prediction of the k_L of ThO_2 as a function of temperature. This work also provides the details on the available three phonon scattering phase space, mode Grüneisen parameter, and the mode-wise thermal conductivity of ThO_2. Using the MD simulations, the effect of porosity on the k_L of ThO_2 was simulated, and the presented results showed that large supercell is required for such studies. The theoretical predictions of thermal conductivities were validated by experimental measurements made on the pellets with different porosity. To conclude, the complete analysis of the k_L of ThO_2 using the DFT has not only enabled to clarify the existing ambiguity in the thermal conductivity measurements and calculations but also provides the inputs required for the study of the mixed oxide fuels. A similar analysis of the thermal properties of CeO_2 is described in Chapter 4.

9.1.2 Role of nicrostructure in the thermophysical properties of the additives to thoria fuel

Since SiC and BeO are the potential additives in composite nuclear fuels, it is crucial to understand the thermophysical properties of these materials. Therefore, chapter 5 and 6 respectively describe the thermal and thermodynamic properties of SiC and BeO across a range of temperatures typical

for a nuclear reactor. SiC in its particles and the whisker forms are considered for the nuclear applications. In this work, we have provided the DFT predictions of the thermal conductivity of the cubic SiC in it's bulk and nanowire forms. This study demonstrated the dependence of thermal conductivity of SiC nanowires on the wire diameter and crystal orientation. To conclude, this study provides a new understanding of the thermal conductivity of SiC nanowires in comparison to the bulk form. Furthermore, this work may help in the selection of the diameter and the orientation of the nanofibers for various nuclear applications.

The dependence of structure on the structural, mechanical, phonons, phonon-assisted thermal properties and thermal conductivity of BeO was examined by considering its wurtzite and the cubic phase. Using the *ab-initio* approach, it was demonstrated that the cubic phase has better thermal conductivity than the common wurtzite phase of BeO. Since the understanding of the anisotropic thermal conductivity is essential in the evaluation of the fuel performance, this study predicted the anisotropy of the thermal conductivity of the BeO as a function of temperature and the results obtained show that the anisotropy is small. All these predictions are essential in evaluating the performance of the composite fuels in the normal operating conditions and the accident scenarios. These results obtained can also serve as the inputs for the phase-field modelling of fuel.

9.1.3 Effect of SPS parameters on the densification, microstructure and the thermal conductivity of ThO_2

One of the significant issue in the front end of the thorium fuel cycle has been the difficulty in fabricating the dense pellets using the conventional sintering techniques. The traditional sintering of the ThO_2 fuels required a maximum sintering temperature higher than 2000 ℃, longer sintering time, and also the help of various sintering aids. Therefore, the possibility of using SPS a non-conventional sintering method for fabricating the nuclear grade thoria pellets was explored. Chapter 7 provides a systematic investigation of the influence of the processing parameter on the densification process, microstructure, grain size and thermal conductivity of thoria. The range of sintering temperature, pressure, and hold time has been systematically varied between 1500–1800 ℃, 50–70 MPa and 5–15 m, respectively. Our study has established that SPS is capable of producing high density pellet of ThO_2 from the commercial powder at a temperature as low as 1600 ℃, while the sintering pressure and time were maintained at 50 MPa and 10 min, respectively.

Also, this study demonstrated that the density, microstructure, grain size and thermal conductivity could be controlled by the choice of the sintering parameters.

9.1.4 Effect of SiC addiction on the densification, microstructure and the thermal conductivity of ThO_2

The fabrication of ThO_2-SiC composite fuels by SPS can enhance the thermal conductivity of ThO_2 fuels by 56%. The enhanced thermal conductivity can reduce the temperature in the center of the fuel pellet during the regular operation and allow to withstand the loss of coolant for an extended time. Moreover, adding SiC can improve the sinterability of the ThO_2, which is evident from the improvement in the density of the composite pellets.

9.2 Original contribution

The following are original contributions that can be drawn from the research findings obtained in this study:

I. The thermophysical properties of ThO_2 and CeO_2 were calculated using atomistic-scale methods to complement the experimental findings. Our prediction of thermal conductivity of the ThO_2 with the recently developed pseudopotential is the most accurate compared to the experimental values. For the first time, a fully *ab initio* prediction of thermal conductivity of CeO_2 was made. It was established that like UO_2 the optical mode phonons also contribute to the thermal conductivity of ThO_2 and CeO_2 and can serve as an input for various mesoscale modelling.

II. For the first time, the thermal conductivity of the nanowires of SiC was predicted using the *ab-initio* technique. The dependence on diameter and crystal orientation of SiC nanowire has implications in the selection of SiC nanowires for nuclear applications. The structural, mechanical, phonons, phonon-assisted thermal properties and thermal conductivity of BeO in the WZ and ZB phase using *ab-initio* approach has been calculated. The predicted anisotropic variation *kc/ka* ratio in the temperature range of nuclear application was in agreement with the experimental results. Moreover, we have observed that the z-BeO is a better thermal conductor than the WZ phase, which may find exciting applications.

III. SPS was used to fabricate high density ThO_2 pellets at a low sintering temperature in a short time, without the addition of any sintering aid. A detailed analysis of the influence of sintering parameters on the densification of the ThO_2 pellets has been presented. ThO_2

pellet with the desired density of 95% TD was obtained at a temperature as low as 1600 ℃, potentially overcoming one of the major issues in the front end of the fuel cycle provided the problems with the industrial scalability of the SPS techniques are solved. The understanding of the influence of the sintering parameters on the density, intergranular pores, grain size and thermal conductivity enables to tailor the sintering parameter to fabricate a highly customized fuel with desired properties.

IV. High density ThO_2-SiC composite fuels were successfully manufactured via SPS technique for the first time. SiC addition to ThO_2 has enhanced the thermal conductivity up to 56% compared to ThO_2 pellets. The results presented here suggest that SPS can offer a suitable method for manufacturing composites with enhanced thermal conductivity.

9.3 Recommendation for future work

9.3.1 DFT determination of the thermal conductivity of mixed oxide

Since mixed oxide fuels are considered as a potential fuel in the SCWR of the CANDU reactors, it is essential to widen the database on the thermal properties of the mixed oxides. Though MD simulations are performed to determine the thermal properties of the mixed oxide fuels, an *ab-initio* prediction of these properties is still lacking. Therefore, it is recommended to perform a DFT calculation for predicting the thermal properties of the mixed oxides. The DFT predictions of the thermal conductivity of ThO_2 and CeO_2 presented in this thesis can serve for the prediction of the thermal conductivity of the mixed oxides fuels.

9.3.2 Irradiation behaviour of the composite pellets

A series of irradiation tests need to be conducted to evaluate the performance of the proposed ThO_2-SiC composite under reactor operating conditions. The knowledge of the difference in the thermal conductivity of the unirradiated and the irradiated composite pellet is essential in the pursuit of this evolutionary fuel concept. Also, the availability of data regarding the irradiation damage and the fission gas release in these composite fuels is essential for commercial application.

9.3.3 Thermal conductivity and the oxidation mechanism of the thorium nitride fuels

Among the fuels based on thorium, information about the compounds such as nitrides and silicides of Th is very limited. Recently, investigations on thorium nitride (ThN) have attracted the attention of the researchers due to its substantially higher actinide density (11.17 g Th/cm^3 vs 8.80 g Th/cm^3

for ThN and ThO_2, respectively), high melting point and higher thermal conductivity (ranging between 35-50 W/mK) [298]. However, the thermal conductivity prediction of ThN using DFT simulations were not made so far. Moreover, one of the major concerns in using metallic fuel such as ThN is the problem of oxidation in the oxygen-containing atmosphere during the fabrication, transportation, storage and in the worst-case accident scenario. Therefore, we recommend performing calculations to predict the phonon and electron contribution to the thermal conductivity of ThN and also the DFT calculation to understand the mechanism of the initial stages of ThN oxidation. Such calculations might help in finding a solution for improvement of oxidation resistance.

References

[1] IAEA, Energy, Electricity and Nuclear Power Estimates for the Period up to 2050, edition 2017.

[2] IAEA, Nuclear Energy Development in the 21st century: Global Scenarios and Regional Trends, IAEA Nucl. Energy Ser. No.NP-T-1.8. (2010) 1–5.

[3] M.E. Ricotti, Nuclear Energy: Basics, Present, Future, EPJ Web Conf. 54 (2013) 01005.

[4] W. Peiman, I. Pioro, K. Gabriel, Thermal Aspects of Conventional and Alternative Fuels in SuperCritical Water-Cooled Reactor (SCWR) Applications, Nucl. React. (2012).

[5] A. Albania, Accident Tolerant Fuel Concepts for Light Water Reactors, IAEA Tecdoc Ser. 1797 (2014) 13–16.

[6] S.J. Zinkle, K.A. Terrani, J.C. Gehin, L.J. Ott, L.L. Snead, Accident Tolerant Fuels for LWRs : A perspective, J. Nucl. Mater. 448 (2014) 374–379.

[7] J. Arborelius, K. Backman, L. Hallstadius, M. Limbäck, J. Nilsson, B. Rebensdorff, G. Zhou, K. Kitano, R. Löfström, G. Rönnberg, Advanced Doped UO_2 Pellets in LWR Applications, J. Nucl. Sci. Technol. 43 (2006) 967–976.

[8] T. Cardinaels, K. Govers, B. Vos, S. Van Den Berghe, M. Verwerft, L. De Tollenaere, G. Maier, C. Delafoy, Chromia Doped UO_2 Fuel: Investigation of the Lattice Parameter, J. Nucl. Mater. 424 (2012) 252–260.

[9] L. Bourgeois, P. Dehaudt, C. Lemaignan, A. Hammou, Factors Governing Microstructure Development of Cr_2O_3-Doped UO_2 During Sintering, J. Nucl. Mater. 297 (2001) 313–326.

[10] C. Riglet-Martial, P. Martin, D. Testemale, C. Sabathier-Devals, G. Carlot, P. Matheron, X. Iltis, U. Pasquet, C. Valot, C. Delafoy, R. Largenton, Thermodynamics of Chromium in UO_2 Fuel: A Solubility Model, J. Nucl. Mater. 447 (2014) 63–72.

[11] C. Delafoy, J. Bischoff, Benefits of Framatome's E-ATF Evolutionary Solution: Cr-Coated Cladding with Cr_2O_3-Doped Fuel, Topfuel. (2018) 1–11.

[12] T. Fujino, S. Nakama, N. Sato, K. Yamada, Solubility of Magnesium in UO_2, J. Nucl. Mater. 246 (1997) 150–157.

[13] H. Assmann, W. Dörr, G. Gradel, G. Maier, M. Peehs, Doping UO_2 with Niobia - Beneficial Or Not?, J. Nucl. Mater. 98 (1981) 216–220.

[14] K. Une, I. Tanabi, Masaomi Oguma, Effects of Addictives and the Oxygen Potential on the Fission Gas Diffusion in UO_2 Fuel, J. Nucl. Mater. 150 (1987) 93–99.

[15] Proceedings of the 2006 International Meeting on LWR fuel performance 'Nuclear Fuel: Addressing the future' - TopFuel 2006 Transactions. European Commission (EC) European Nuclear Society, Rue Belliard 65, 1040 Brussels (Belgium) (2006).

[16] H.G. Kim, J.H. Yang, W.J. Kim, Y.H. Koo, Development Status of Accident-Tolerant Fuel for Light Water Reactors in Korea, Nucl. Eng. Technol. 48 (2016) 1–15.

[17] Y.H. Koo, J.H. Yang, J.Y. Park, K.S. Kim, H.G. Kim, D.J. Kim, Y.I. Jung, K.W. Song, KAERI's Development of LWR Accident-Tolerant Fuel, Nucl. Technol. 186 (2014) 295–304.

[18] C. Haertling, R.J. Hanrahan, Literature Review of Thermal And Radiation Performance Parameters for High-Temperature, UO_2 Fueled Cermet Materials, J. Nucl. Mater. 366 (2007) 317–335.

[19] D.S. Tucker, M.W. Barnes, L. Hone, S. Cook, High Density, Uniformly Distributed W/UO_2 for Use in Nuclear Thermal Propulsion, J. Nucl. Mater. 486 (2017) 246–249.

[20] R.C. O'Brien, N.D. Jerred, Spark Plasma Sintering of W-UO_2 Cermets, J. Nucl. Mater. 433 (2013) 50–54.

[21] A.Vatulin, I.Konovalov, A.Savchenco, Y. Stetsky, Y. Trifonov, A.A. Bochvar Powder Metallurgy and Fabricating Processes of Cermet and Metmet Fuel in Russia, Powder Metall. Assoc. India, 26, (1999) 32-39.

[22] S. Ishimoto, M. Hirai, K. Ito, Y. Korei, Thermal Conductivity of UO_2-BeO Pellet, J. Nucl. Sci. Technol. 33 (1996) 134–140.

[23] W. Zhou, R. Liu, S.T. Revankar, Fabrication Methods and Thermal Hydraulics Analysis of Enhanced Thermal Conductivity UO_2-BeO Fuel in Light Water Reactors, Ann. Nucl. Energy. 81 (2015) 240–248.

[24] B. Li, Z. Yang, J. Jia, Y. Zhong, X. Liu, P. Zhang, R. Gao, T. Liu, R. Li, H. Huang, M. Sun, D. Mazhao, High Temperature Thermal Physical Performance of BeO/UO_2 Composites Prepared by Spark Plasma Sintering (SPS), Scr. Mater. 142 (2018) 70–73.

[25] S.K. Kim, W.I. Ko, H.D. Kim, S.T. Revankar, W. Zhou, D. Jo, Cost-Benefit Analysis of BeO-UO_2 Nuclear Fuel, Prog. Nucl. Energy. 52 (2010) 813–821.

[26] J.A. Khan, T.W. Knight, S.B. Pakala, W. Jiang, R. Fang, J.S. Tulenko, Enhanced Thermal Conductivity for LWR Fuel, Nucl. Technol. 169 (2017) 61–72.

[27] S. Yeo, E. McKenna, R. Baney, G. Subhash, J. Tulenko, Enhanced Thermal Conductivity

of Uranium Dioxide-Silicon Carbide Composite Fuel Pellets Prepared by Spark Plasma Sintering (SPS), J. Nucl. Mater. 433 (2013) 66–73.

[28] S. Yeo, R. Baney, G. Subhash, J. Tulenko, The Influence of SiC Particle Size and Volume Fraction on the Thermal Conductivity of Spark Plasma Sintered UO_2-SiC Composites, J. Nucl. Mater. 442 (2013) 245–252.

[29] Z. Chen, G. Subhash, J.S. Tulenko, Spark Plasma Sintering of Diamond-Reinforced Uranium Dioxide Composite Fuel Pellets, Nucl. Eng. Des. 294 (2015) 52–59.

[30] A. Cartas, H. Wang, G. Subhash, R. Baney, J. Tulenko, Influence of Carbon Nanotube Dispersion in UO_2-Carbon Nanotube Ceramic Matrix Composites Utilizing Spark Plasma Sintering, Nucl. Technol. 189 (2015) 258–267.

[31] T. Yao, G. Xin, S.M. Scott, B. Gong, J. Lian, Thermally-Conductive and Mechanically-Robust Graphene Nanoplatelet Reinforced UO_2 Composite Nuclear Fuels, Sci. Rep. 8 (2018) 2–10.

[32] B. Li, Z. Yang, M. Chu, Q. Huang, Z. Wang, R. Gao, Y. Zhong, X. Liu, L. Duan, P. Zhang, Ti_3SiC_2/UO_2 Composite Pellets with Superior High-Temperature Thermal Conductivity, Ceram. Int. 44 (2018) 19846–19850.

[33] C. Ekberg, D. Ribeiro Costa, M. Hedberg, M. Jolkkonen, Nitride Fuel for Gen IV Nuclear Power Systems, J. Radioanal. Nucl. Chem. 318 (2018) 1713–1725.

[34] K.D. Johnson, D. Adorno, Grain Growth in Uranium Nitride Prepared by Spark Plasma Sintering, J. Nucl. Mater. 503 (2018) 75–80.

[35] N.R. Brown, A. Aronson, M. Todosow, R. Brito, K.J. McClellan, Neutronic Performance of Uranium Nitride Composite Fuels In A PWR, Nucl. Eng. Des. 275 (2014) 393–407.

[36] M. Jolkkonen, P. Malkki, K. Johnson, J. Wallenius, Uranium Nitride Fuels in Superheated Steam, J. Nucl. Sci. Technol. 54 (2017) 513–519.

[37] J.W. Harrison, The Irradiation-Induced Swelling of Uranium Carbide, Atomic Energy Research Establishment UKAEA, Metallurgy Division, Harwell, Didcot, Berks., UK 30 (1969) 319–323.

[38] J.T. White, A.T. Nelson, J.T. Dunwoody, D.D. Byler, D.J. Safarik, K.J. McClellan, Thermophysical Properties of U_3Si_2, J. Nucl. Mater. 464 (2015) 275–280.

[39] A.T. Nelson, A. Migdisov, E.S. Wood, C.J. Grote, U_3Si_2 Behavior in H_2O Environments: Part II, Pressurized Water with Controlled Redox Chemistry, J. Nucl. Mater. 500 (2018)

81–91.

[40] K.D. Johnson, A.M. Raftery, D.A. Lopes, J. Wallenius, Fabrication and Microstructural Analysis of UN-U_3Si_2 Composites for Accident Tolerant Fuel Applications, J. Nucl. Mater. 477 (2016) 18–23.

[41] J.T. White, A.W. Travis, J.T. Dunwoody, A.T. Nelson, Fabrication and Thermophysical Property Characterization of UN/U_3Si_2 Composite Fuel Forms, J. Nucl. Mater. 495 (2017) 463–474.

[42] Development of LWR Fuels with Enhanced Accident Tolerance Final Technical Report, Westinghouse, (2015).

[43] K.A. Terrani, J.O. Kiggans, Y. Katoh, K. Shimoda, F.C. Montgomery, B.L. Armstrong, C.M. Parish, T. Hinoki, J.D. Hunn, L.L. Snead, Fabrication and Characterization of Fully Ceramic Microencapsulated Fuels, J. Nucl. Mater. 426 (2012) 268–276.

[44] K.A. Terrani, J.O. Kiggans, C.M. Silva, C. Shih, Y. Katoh, L.L. Snead, Progress on Matrix Sic Processing and Properties for Fully Ceramic Microencapsulated Fuel Form, J. Nucl. Mater. 457 (2015) 9–17.

[45] K.A. Terrani, L.L. Snead, J.C. Gehin, Microencapsulated Fuel Technology for Commercial Light Water and Advanced Reactor Application, J. Nucl. Mater. 427 (2012) 209–224.

[46] L.L. Snead, K.A. Terrani, Y. Katoh, C. Silva, K.J. Leonard, A.G. Perez-Bergquist, Stability of SiC-Matrix Microencapsulated Fuel Constituents at Relevant LWR Conditions, J. Nucl. Mater. 448 (2014) 389–398.

[47] M. Baker, Abundant Thorium as an Alternative Nuclear Fuel Important Waste Disposal and Weapon Proliferation Advantages, Energy Policy. 60 (2013) 4–12.

[48] V. Hall, A Review of the Benefits and Applications of the Thorium Fuel Cycle, Chemical Engineering Undergraduate Honors Theses. 25. (2010).

[49] K. Anantharaman, V. Shivakumar, D. Saha, Utilisation of Thorium in Reactors, J. Nucl. Mater. 383 (2008) 119–121.

[50] N. Science, Introduction of Thorium in The Nuclear Fuel Cycle, NEA No. 7224, OECD (2015).

[51] IAEA, Thorium Fuel Cycle—Potential Benefits and Challenges, IAEA TECDOC-1450, Int. At. Energy, (2005) 113.

[52] M. Floyd, B. Bromley, J. Pencer, A Canadian Perspective on Propgress in Thoria Fuel

Science and Technology, Canadian Nuclear Laboratories, (2016) 1–17.

[53] K. Furukawa, K. Arakawa, L.B. Erbay, Y. Ito, Y. Kato, H. Kiyavitskaya, A. Lecocq, K. Mitachi, R. Moir, H. Numata, J.P. Pleasant, Y. Sato, Y. Shimazu, V.A. Simonenco, D.D. Sood, C. Urban, R. Yoshioka, A Road Map for the Realization of Global-Scale Thorium Breeding Fuel Cycle by Single Molten-Fluoride Flow, 13th Int. Conf. Emerg. Nucl. Energy Syst. 2007, ICENES 2007. 1 (2007) 5–32.

[54] P. Trinuruk, T. Obara, Particle-Type Burnable Poisons for Thorium-Based Fuel in HTGR, Energy Procedia. 71 (2015) 22–32.

[55] A. Radkowsky, A. Galperin, The Nonproliferative Light Water Thorium Reactor: A New Approach to Light Water Reactor Core Technology, Nucl. Technol. 124 (1998) 215–222.

[56] H.K. Joo, J.M. Noh, J.W. Yoo, J.Y. Cho, S.Y. Park, M.H. Chang, Alternative Applications of Homogeneous Thoria-Urania Fuel in Light Water Reactors to Enhance the Economics of the Thorium Fuel Cycle, Nucl. Technol. 147 (2004) 37–52.

[57] G. Martin, R. Girieud, Middle-Term Thorium Strategy for PWR Fleets, Energy Policy. 99 (2016) 147–153.

[58] A. Talamo, W. Gudowski, Adapting the Deep Burn in-Core Fuel Management Strategy for the Gas Turbine - Modular Helium Reactor to a Uranium-Thorium Fuel, Ann. Nucl. Energy. 32 (2005) 1750–1781.

[59] S. Şahin, H.M. Şahin, A. Acir, T.A. Al-Kusayer, Criticality Investigations for the Fixed Bed Nuclear Reactor using Thorium Fuel Mixed with Plutonium or Minor Actinides, Ann. Nucl. Energy. 36 (2009) 1032–1038.

[60] J. Wallenius, Transmutation Of Nuclear Waste in Accelerator Driven Reactors, VTT Symp. (Valtion Tek. Tutkimuskeskus). (2003) 147–154.

[61] K. Insulander Björk, L. Kekkonen, Thermal-Mechanical Performance Modeling of Thorium-Plutonium Oxide Fuel and Comparison with on-Line Irradiation Data, J. Nucl. Mater. 467 (2015) 876–885.

[62] P.K. Vijayan, V. Shivakumar, S. Basu, R.K. Sinha, Role of Thorium in the Indian Nuclear Power Programme, Prog. Nucl. Energy. 101 (2017) 43–52.

[63] E. Schrödinger, An Undulatory Theory of the Mechanics of Atoms and Molecules, Phys. Rev. 28 (1926) 1049–1070.

[64] P. Hohenberg, W. Kohn, Inhomogeneous Electron Gas, Phys. Rev. B. 136 (1964) B864.

[65] W. Kohn, L.J. Sham, Self-Consistent Equations Including Exchange and Correlation Effects, Phys. Rev. 140 (1965) A1133-A1138.

[66] W. Kohn, L.J. Sham, Self Consistent Equations Including Exchange and Correlation Effects, Phys. Rev. 140 (1965) A1133–A1138.

[67] V. Sahni, K.P. Bohnen, M.K. Harbola, Analysis of the Local-Density Approximation of Density-Functional Theory, Phys. Rev. A. 37 (1988) 1895–1907.

[68] J.P. Perdew, K. Burke, M. Ernzerhof, Generalized Gradient Approximation Made Simple, Phys. Rev. Lett. 77 (1996) 3865–3868.

[69] A.D. Becke, A New Mixing of Hartree-Fock and Local Density-Functional Theories, J. Chem. Phys. 98 (1993) 1372–1377.

[70] A.D. Becke, Density-Fnnctional Exchange-Energy Approximation with Correct Asymptotic Behavior, P. Review A, 38 (1988) 3098-3100.

[71] G. Kresse, J. Furthmiiller, Efficiency of Ab-Initio Total Energy Calculations for Metals and Semiconductors Using A Plane-Wave Basis Set, 6 Computational Materials Science (1996) 15–50.

[72] S.J. Clark, M.D. Segall , C.J. Pickard, P.J. Hasnip, M.I.J. Probert, K. Refson, M.C. Payne, First Principles Methods Using CASTEP, Z. Kristallogr. 220 (2005) 567–570.

[73] P. Giannozzi, S. Baroni, N. Bonini, M. Calandra, R. Car, C. Cavazzoni, D. Ceresoli, G.L. Chiarotti, M. Cococcioni, I. Dabo, A.D. Corso, S. De Gironcoli, U. Gerstmann, C. Gougoussis, A. Kokalj, M. Lazzeri, L. Martin-samos, N. Marzari, F. Mauri, R. Mazzarello, S. Paolini, A. Pasquarello, L. Paulatto, C. Sbraccia, QUANTUM ESPRESSO: A Modular and Open-Source Software Project for Quantum Simulations of Materials, Int. J. Comp. Mater. (2009).

[74] L. Malakkal, B. Szpunar, J.C. Zuniga, R.K. Siripurapu, J.A. Szpunar, An Interface to Quantum ESPRESSO, in: Proc. 3rd World Congr. Integr. Comput. Mater. Eng. (ICME 2015), John Wiley & Sons, Inc., (2015) 155–162.

[75] M.W.D. Cooper, M.J.D. Rushton, R.W. Grimes, A Many-Body Potential Approach to Modelling the Thermomechanical Properties of Actinide Oxides, J. Phys. Condens. Matter. 26 (2014) 105401.

[76] L. Verlet, Computer Experiments on Classical Fluids. I. Thermodynamical Properties of Lennard-Jones Molecules, J. Phys. Rev. B, 159 (1967), 98-103.

[77] W.C. Swope, H.C. Andersen, P.H. Berens, K.R. Wilson, W.C. Swope, H.C. Andersen, P.H. Berens, K.R. Wilson, A Computer Simulation Method for the Calculation of Equilibrium Constants for the Formation of Physical Clusters of Molecules : Application to Small Water Clusters, J.Chem.Phys. 76 (1982), 637-649.

[78] G.A. Slack, S.B. Austerman, Thermal Conductivity of BeO Single Crystals, J. Appl. Phys. 42 (1971) 4713–4717.

[79] J. Callaway, Model for Lattice Thermal Conductivity at Low Temperatures, Phys. Rev. 113 (1959) 1046–1051.

[80] H. Gzyl, Integration of the Boltzmann Equation in the Relaxation Time Approximation, J. Stat. Phys. 29 (1982) 617–622.

[81] K. Hess, Boltzmann Transport Equation, Phys. Submicron Semicond. Devices. In: Grubin H.L., Ferry D.K., Jacoboni C. (eds) The Physics of Submicron Semiconductor Devices. NATO ASI Series (Series B: Physics), vol 180. Springer, Boston, MA (1988) 33–43.

[82] M. Toda, R. Kubo, N. Saitō, N. Hashitsume, Statistical Physics: Nonequilibrium Statistical Mechanics, publisher Springer-Verlag Berlin Heidelberg 31 (1991).

[83] W. Li, J. Carrete, N. A. Katcho, N. Mingo, Shengbte: A Solver of the Boltzmann Transport Equation For Phonons, Comput. Phys. Commun. 185 (2014) 1747–1758.

[84] J. Carrete, B. Vermeersch, A. Katre, A. van Roekeghem, T. Wang, G.K.H. Madsen, N. Mingo, AlmaBTE : A Solver of the Space–Time Dependent Boltzmann Transport Equation for Phonons in Structured Materials, Comput. Phys. Commun. 220 (2017) 351–362.

[85] G.P. Srivastava, Length-Scale Dependent Phonon Interactions, publisher Springer-Verlag New York 128 (2014).

[86] S. Baroni, P. Giannozzi, A. Testa, Green-Function Approach to Linear Response in Solids, Phys. Rev. Lett. 58 (1987) 1861–1864.

[87] K. Parlinski, Z.Q. Li, Y. Kawazoe, First-Principles Determination of the Soft Mode in Cubic ZrO_2, Phys. Rev. Lett. 78 (1997) 4063–4066.

[88] A. Togo, I. Tanaka, First Principles Phonon Calculations in Materials Science, Scr. Mater. 108 (2015) 1–5.

[89] F. Müller-plathe, A Simple Nonequilibrium Molecular Dynamics Method for Calculating the Thermal Conductivity, J. Chem. Phys. 106 (1997) 6082.

[90] R. Kubo, M. Toda, N. Hashitsume, Statistical Physics II, publisher Springer-Verlag Berlin

Heidelberg, 31 (1985).

[91] P. Cavaliere, Spark Plasma Sintering of Materials, publisher Springer, Cham (2019).

[92] A.M. Locci, A. Cincotti, S. Todde, R. Orrù, G. Cao, A Methodology to Investigate the Intrinsic Effect of the Pulsed Electric Current During the Spark Plasma Sintering of Electrically Conductive Powders, Sci. Technol. Adv. Mater. 11 (2010) 045005.

[93] S. Grasso, Y. Sakka, G. Maizza, Electric Current Activated/Assisted Sintering (ECAS): A Review of Patents 1906-2008, Sci. Technol. Adv. Mater. 10 (2009).

[94] S. Muñoz, U. Anselmi-Tamburini, Temperature and Stress Fields Evolution During Spark Plasma Sintering Processes, J. Mater. Sci. 45 (2010) 6528–6539.

[95] T. Hungría, J. Galy, A. Castro, Spark Plasma Sintering as a Useful Technique to the Nanostructuration of Piezo-Ferroelectric Materials, Adv. Eng. Mater. 11 (2009) 615–631.

[96] D. Jiang, D.M. Hulbert, U. Anselmi-Tamburini, T. Ng, D. Land, A.K. Mukherjee, Optically Transparent Polycrystalline Al_2O_3 Produced by Spark Plasma Sintering, J. Am. Ceram. Soc. 91 (2008) 151–154.

[97] J.R. Groza, A. Zavaliangos, Nanostructured Bulk Solids by Field Activated Sintering, Rev. Adv. Mater. Sci. 5 (2003) 24–33.

[98] J. Wan, R.G. Duan, A.K. Mukherjee, Spark Plasma Sintering of Silicon Nitride/Silicon Carbide Nanocomposites With Reduced Additive Amounts, Scr. Mater. 53 (2005) 663–667.

[99] H. Zhang, B.N. Kim, K. Morita, H.Y. Keijiro Hiraga, Y. Sakka, Effect of Sintering Temperature On Optical Properties And Microstructure of Translucent Zirconia Prepared by High-Pressure Spark Plasma Sintering, Sci. Technol. Adv. Mater. 12 (2011) 055003.

[100] M. Nygren, Z. Shen, On the Preparation of Bio, Nano and Structural Ceramics and Composites by Spark Plasma Sintering, Solid State Sci. 5 (2003) 125–131.

[101] D.H. Shim, S.S. Jung, H.S. Kim, H. Cho, J.K. Kim, T.G. Kim, S.J. Yoon, Effect of Carbon Nanotubes on the Properties of Spark Plasma Sintered ZrO_2 CNT Composites, Arch. Metall. Mater. 60 (2015) 1315–1318.

[102] C. Plapcianu, C. Valsangiacom, J.E. Schaffer, A. Wieg, J. Garay, L. Stanciu, Spark Plasma Sintering Studies of Nanosize Lanthanidedoped Ceria Obtained by Sol-Gel Method, J. Optoelectron. Adv. Mater. 13 (2011) 1101–1108.

[103] R.S. Dobedoe, G.D. West, M.H. Lewis, Spark Plasma Sintering of Ceramics: Understanding Temperature Distribution Enables More Realistic Comparison with

Conventional Processing, Adv. Appl. Ceram. 104 (2005) 110–116.

[104] D.M. Hulbert, A. Anders, D. V. Dudina, J. Andersson, D. Jiang, C. Unuvar, U. Anselmi-Tamburini, E.J. Lavernia, A.K. Mukherjee, The Absence of Plasma in "Spark Plasma Sintering," J. Appl. Phys. 104 (2008) 033305.

[105] M. Tokita, Trends in Advanced SPS Spark Plasma Sintering Systems and Technology, Soc. Powder Tech. Jpn. 30 (1993) 790.

[106] G.D. Zhan, J. Kuntz, J. Wan, J. Garay, A.K. Mukherjee, A Novel Processing Route to Develop a Dense Nanocrystalline Alumina Matrix (<100 nm) Nanocomposite Material, J. Am. Ceram. Soc. 86 (2002) 200–202.

[107] M. Omori, Sintering, Consolidation, Reaction and Crystal Growth by the Spark Plasma System, Mater. Sci. Eng. A. 287 (2000) 183–188.

[108] W. Chen, U.A. Tamburini, J.E. Garay, J.R. Groza, Z.A. Munir, Fundamental Investigations on the Spark Plasma Sintering/Synthesis Process: I. Effect of DC Pulsing on Reactivity, Mater. Sci. Eng. A. 394 (2005) 132–138.

[109] N. Chawake, L.D. Pinto, A.K. Srivastav, K. Akkiraju, B.S. Murty, R.S. Kottada, On Joule Heating During Spark Plasma Sintering of Metal Powders, Scr. Mater. 93 (2014) 52–55.

[110] J.B. Nelson, D.P. Riley, An Experimental Investigation of Extrapolation Methods in the Derivation of Accurate Unit-Cell Dimensions of Crystals, Proc. Phys. Soc. 57 (1945) 160–177.

[111] W.J. Parker, R.J. Jenkins, C.P. Butler, G.L. Abbott, Flash Method of Determining Thermal Diffusivity, Heat Capacity, and Thermal Conductivity, J. Appl. Phys. 32 (1961) 1679.

[112] A.J. Breslin, W.B. Harris, Use Of Thoriated Tungsten Electrodes In Inert Gas Shielded Arc Welding-Investigation of Potential Hazard, Am. Ind. Hyg. Assoc. Q. 13 (1952) 191–195.

[113] S.L. Sources, G. Smart, Solid-State Light Sources Getting Smart, Science 308 (2005) 1274–1278.

[114] K. Bakker, E.H.P. Cordfunke, R.J.M. Konings, R.P.C. Schram, Critical Evaluation of the Thermal Properties Of ThO_2 And $Th_{1-y}U_yO_2$ and a Survey of the Literature Data On $Th_{1-y}Pu_yO_2$, J. Nucl. Mater. 250 (1997) 1–12.

[115] M. Murabayashi, Y. Takahashi, T. Mukaibo, Effect of Porosity on the Thermal Conductivity of ThO_2, J. Nucl. Sci. Technol. 6 (1969) 657–662.

[116] D.L. McElroy, J.P. Moore, P.H. Spindler, Status and Progress Report for Thorium Fuel

Cycle Development for 1967 and 1968, Report ORNL-4429 1968.

[117] J.H. Koenig, Progress Report No.2, Ceramics Research Station Progress Report, (1953).

[118] J.R. Springer, E.A. Eldridge, M.U. Goodyear, T.R. Wright, J.F. Langedrost, Fabrication, Characterization and Thermal Property Measurements of ThO_2-UO_2 Fuel Materials, Battelle Memorial institute Report BMI-X10210, (1967).

[119] P.S. Murti, C.K. Mathews, Thermal Diffusivity and Thermal Conductivity Studies on Thorium- Lanthanum Mixed Oxide Solid Solutions, J. Phys. D. Appl. Phys. 24 (1991) 2202–2209.

[120] R.A. Laskiwicz, G.F. Melde, S.K. Evans, P.E. Bohaboy, Thermal Conductivity of Uranium-Plutonium Oxide, USAEC Report GEAP-13733, General Electric Company, September (1971).

[121] C.G.S. Pillai, P. Raj, Thermal Conductivity of ThO_2 and $Th_{0.98}U_{0.02}O_2$, J. Nucl. Mater. 277 (2000) 116–119.

[122] M. Saoudi, D. Staicu, J. Mouris, A. Bergeron, H. Hamilton, M. Naji, D. Freis, M. Cologna, Thermal Diffusivity and Conductivity of Thorium- Uranium Mixed Oxides, J. Nucl. Mater. 500 (2018) 381–388.

[123] J.H. Yang, K.W. Kang, K.W. Song, C.B. Lee, Y.H. Jung, Fabrication and Thermal Conductivity of (Th,U)O_2 Pellets , Nucl. Technol. 147 (2017) 113–119.

[124] P.S. Ghosh, P.S. Somayajulu, A. Arya, G.K. Dey, B.K. Dutta, Thermal Expansion and Thermal Conductivity of (Th,Ce)O_2 Mixed Oxides : A Molecular Dynamics and Experimental Study, J. Alloys Compd. 638 (2015) 172–181.

[125] P.S. Ghosh, P.S. Somayajulu, K. Krishnan, N. Pathak, A. Arya, G.K. Dey, Thermal Expansion And Thermal Conductivity of (Th,U)O_2 Mixed Oxides: A Molecular Dynamics and Experimental Study, J. Alloys Compd. 650 (2015) 165–177.

[126] C. Cozzo, D. Staicu, J. Somers, A. Fernandez, R.J.M. Konings, Thermal Diffusivity And Conductivity of Thorium–Plutonium Mixed Oxides, J. Nucl. Mater. 416 (2011) 135–141.

[127] T.R.G. Kutty, R.V. Kulkarni, P. Sengupta, K.B. Khan, K. Bhanumurthy, A.K. Sengupta, J.P. Panakkal, A. Kumar, H.S. Kamath, Development of CAP Process for Fabrication of ThO_2-UO_2 Fuels Part II: Characterization and Property Evaluation, J. Nucl. Mater. 373 (2008) 309–318.

[128] D.T. Morelli, G. A. Slack, High Lattice Thermal Conductivity Solids, High Therm.

Conduct. Mater. (2006) 37–68.

[129] H.Y. Xiao, Y. Zhang, W.J. Weber, Thermodynamic Properties of $Ce_xTh_{1-x}O_2$ Solid Solution from First-Principles Calculations, Acta Mater. 61 (2012) 467–476.

[130] Y. Lu, Y. Yang, P. Zhang, Thermodynamic Properties and Structural Stability of Thorium Dioxide, J. Phys. Condens. Matter. 24 (2012) 225801.

[131] B. Szpunar, J.Szpunar, Thoria Ehancement of Nuclear Reactor Safety, Phys. Int. 4 (2013) 110–119.

[132] J.J. Ma, J.G. Du, M.J. Wan, G. Jiang, Molecular dynamics study on thermal properties of ThO_2 doped with U and Pu in high temperature range, J. Alloys Compd. 627 (2015) 476–482.

[133] R.K. Behera, C.S. Deo, Atomistic Models to Investigate Thorium Dioxide (ThO_2), J. Phys. Condens. Matter. 24 (2012).

[134] M.W.D. Cooper, S.C. Middleburgh, R.W. Grimes, Modelling the Thermal Conductivity of $(U_x\ Th_{1-x})O_2$ And $(U_x\ Pu_{1-x})O_2$, J. Nucl. Mater. 466 (2015) 29–35.

[135] M.J. Rahman, B. Szpunar, J.A. Szpunar, The Induced Anisotropy in Thermal Conductivity of Thorium Dioxide And Cerium Dioxide, Mater. Res. Express. 4 (2017) 075512.

[136] J. Liu, Z. Dai, X. Yang, Y. Zhao, S. Meng, Lattice Thermodynamic Behavior in Nuclear Fuel ThO_2 from First Principles, J. Nucl. Mater. 511 (2018) 11–17.

[137] T. Arima, K. Yoshida, T. Matsumoto, Y. Inagaki, K. Idemitsu, Thermal Conductivities of ThO_2, NpO_2 and Their Related Oxides: Molecular Dynamics Study, J. Nucl. Mater. 445 (2014) 175–180.

[138] J. Park, E.B. Farfán, K. Mitchell, A. Resnick, C. Enriquez, T. Yee, Sensitivity of Thermal Transport in Thorium Dioxide to Defects, J. Nucl. Mater. 504 (2018) 198–205.

[139] J.P. Perdew, A. Ruzsinszky, G.I. Csonka, O. A. Vydrov, G.E. Scuseria, L. A. Constantin, X. Zhou, K. Burke, Generalized Gradient Approximation for Solids and their Surfaces, Phys.Rev.Lett. 100 (2008) 136406.

[140] D. Pérez Daroca, A.M. Llois, H.O. Mosca, Point Defects in Thorium Nitride: A First-Principles Study, J. Nucl. Mater. 480 (2016) 1–6.

[141] Y. Wang, S.L. Shang, H. Fang, Z.-K. Liu, L.Q. Chen, First-Principles Calculations of Lattice Dynamics and Thermal Properties Of Polar Solids, J. Comput. Mater. 2 (2016) 16006.

[142] S. Plimpton, Fast Parallel Algorithms for Short-Range Molecular Dynamics, J. Comput. Phys. 117 (1995) 1–19.

[143] D.P. Sellan, E.S. Landry, J.E. Turney, A.J.H. Mcgaughey, C.H. Amon, Size Effects in Molecular Dynamics Thermal Conductivity Predictions, Phys. Rev. B 81 (2010) 214305.

[144] A. Nakajima, A. Yoshihara, M. Ishigame, Defect-Induced Raman Spectra in Doped CeO_2, Phys. Rev. B. 50 (1994) 13297–13307.

[145] L. Malakkal, B. Szpunar, J.C. Zuniga, R.K. Siripurapu, J.A. Szpunar, First Principles Calculation of Thermo-Mechanical Properties of Thoria Using Quantum ESPRESSO, Int. J. Comput. Mater. Sci. Eng. 05 (2016) 1650008.

[146] H. Shao, X. Tan, J. Jiang, H. Jiang, First Principles Study on the Elastic Properties of Cu_2GeSe_3, EPL Europhysics Lett. 113 (2016) 26001.

[147] Max Born, K. Huang, Dynamical Theory of Crystal Lattices publisher Oxford University Press (1954).

[148] P.M. Macedo, W. Capps, J.B.Watchman, Elastic Constants of Single Crystal ThO_2 at 25 °C, J. Am. Ceram. Soc. (1964) 651.

[149] B. Szpunar, J. A. Szpunar, Theoretical Investigation of Structural and Thermo-Mechanical Properties of Thoria up to 3300 K Temperature, Solid State Sci. 36 (2014) 35–40.

[150] B.T. Wang, H. Shi, W.D. Li, P. Zhang, First-Principles Study of Ground-State Properties and High Pressure Behavior of ThO_2, J. Nucl. Mater. 399 (2010) 181–188.

[151] V. Kanchana, G. Vaitheeswaran, A. Svane, A. Delin, First-Principles Study of Elastic Properties of CeO_2, ThO_2 and PuO_2, J. Phys. Condens. Matter. 18 (2006) 9615–9624.

[152] C. Sevik, T. ÇağIn, Mechanical And Electronic Properties of CeO_2, ThO_2, and $(Ce,Th)O_2$ alloys, Phys. Rev. B, 80 (2009) 014108.

[153] M. Idiri, T. L. Bihan, S. Heathman, J. Rebizant, Behavior of Actinide Dioxides Under Pressure: UO_2 and ThO_2, Phys. Rev. B, 70 (2004) 014113.

[154] J.S. Olsen, L. Gerward, V. Kanchana, G. Vaitheeswaram, The Bulk Modulus of ThO_2-An Experimental and Theoretical Study, J. Alloys Compd. (2004) 37–40.

[155] K. Clausen, W. Hayes, J.E. Macdonald, R. Osborn, P.G. Schnabel, M.T. Hutchings, A. Magerl, Inelastic Neutron Scattering Investigation of the Lattice Dynamics of ThO_2 and CeO_2 , J. Chem. Soc. Faraday Trans. 2. 83 (1987) 1109.

[156] K.K. Phani, D. Sanyal, Elastic Properties of Porous Polycrystalline Thoria-A Relook, J. Eur.

Ceram. Soc. 29 (2009) 385–390.

[157] K. Phani, S. Niyogi, Porosity Dependance of Ultrasonic Velocity and Elastic Modulus in Sintered Uranium Dioxide-A Discussion, J. Mater. Sci. Lett. 5 (1986) 427–430.

[158] L. Lindsay, D.A. Broido, Three-Phonon Phase Space and Lattice Thermal Conductivity in Semiconductors, J. Phys. Condens. Matter. 20 (2008) 165209.

[159] S. Baroni, D. Gironcoli, D.C. Andrea, P. Giannozzi, Phonons and Related Crystal Properties from Density Functional Perturbation Theory, Rev. Mod. Phys. 73 (2001) 515–562.

[160] S. Wang, W. Wang, G. Zhao, Thermal Transport Properties of Antimonene : An *Ab Initio* Study, Phys. Chem. Chem. Phys. 18 (2016) 31217–31222.

[161] L. Malakkal, B. Szpunar, R.K. Siripurapu, J.A. Szpunar, Thermal Conductivity of Bulk and Nanowire of Cubic-Sic from *Ab Initio* Calculations, Comput. Mater. Sci. 128 (2017) 249–256.

[162] J. Szpunar, B. Szpunar, Thermal Conductivity in Improvement of Safety of Nuclear Fuel, J. Int. Sci. Publ. Mater. Methods Technol., 2014: 741–750.

[163] J.W.L. Pang, W.J.L. Buyers, A. Chernatynskiy, M.D. Lumsden, B.C. Larson, S.R. Phillpot, Phonon Lifetime Investigation of Anharmonicity and Thermal Conductivity of UO_2 By Neutron Scattering and Theory, Phys. Rev. Lett. 110 (2013) 157401.

[164] M.S. Dresselhaus, I.L. Thomas, Alternative Energy Technologies, Nature. 414 (2001) 332–337.

[165] H. Inaba, Ceria-Based Solid Electrolytes, Solid State Ionics. 83 (1996) 1–16.

[166] S. Ershov, M.E. Druart, M. Poelman, D. Cossement, R. Snyders, M.G. Olivier, Deposition of Cerium Oxide Thin Films By Reactive Magnetron Sputtering for the Development of Corrosion Protective Coatings, Corros. Sci. 75 (2013) 158–168.

[167] C.E. Castano, M.J. O'Keefe, W.G. Fahrenholtz, Cerium-Based Oxide Coatings, Curr. Opin. Solid State Mater. Sci. 19 (2015) 69–76.

[168] X. Wang, J.A. Szpunar, Effect of CeO_2 Coating On The Isothermal Oxidation Behaviour Of Ni-Based Alloy 230, Oxid. Met. 88 (2017) 565-582.

[169] J.A. Katalenich, M.R. Hartman, R.C.O. Brien, S.D. Howe, Fabrication of Cerium Oxide and Uranium Oxide Microspheres for Space Nuclear Power Applications, Proceedings of Nuclear and Emerging Technologies for space (2013) 6762.

[170] A.T. Nelson, D.R. Rittman, J.T. White, J.T. Dunwoody, M. Kato, K.J. Mcclellan, An

Evaluation of the Thermophysical Properties of Stoichiometric CeO_2 in Comparison to UO_2 and PuO_2, J. Am. Ceram. Soc. 97 (2014) 3652–3659.

[171] M. Khafizov, I.W. Park, A. Chernatynskiy, L. He, J. Lin, J.J. Moore, D. Swank, T. Lillo, S.R. Phillpot, A. El-Azab, D.H. Hurley, Thermal Conductivity in Nanocrystalline Ceria Thin Films, J. Am. Ceram. Soc. 97 (2014) 562–569.

[172] G.A. Slack, Thermal Conductivity of Pure and Impure Silicon, Silicon Carbide, and Diamond, J. Appl. Phys. 35 (1964) 3460–3466.

[173] X. Wu, J. Lee, V. Varshney, J.L. Wohlwend, A.K. Roy, T. Luo, Thermal Conductivity of Wurtzite Zinc-Oxide from First-Principles Lattice Dynamics-A Comparative Study with Gallium Nitride, Sci. Rep. 6 (2016) 22504.

[174] H. Shao, X. Tan, G. Liu, J. Jiang, H. Jiang, OPEN A First-Principles Study on the Phonon Transport in Layered BiCuOSe, Nat. Publ. Gr. (2016) 1–9.

[175] L.D. Zhao, S.H. Lo, Y. Zhang, H. Sun, G. Tan, C. Uher, C. Wolverton, V.P. Dravid, M.G. Kanatzidis, Ultralow Thermal Conductivity and High Thermoelectric Figure of Merit in SnSe Crystals., Nature. 508 (2014) 373.

[176] L. Malakkal, B. Szpunar, R.K. Siripurapu, J.A. Szpunar, Thermal Conductivity of Bulk and Nanowire of Cubic-Sic from *Ab Initio* Calculations, Comput. Mater. Sci. 128 (2017) 249–256.

[177] L. Malakkal, B. Szpunar, R.K. Siripurapu, J.C. Zuniga, J.A. Szpunar, Thermal Conductivity of Wurtzite and Zinc Blende Cubic Phases of Beo from *Ab Initio* Calculations, Solid State Sci. 65 (2017) 79–87.

[178] S. Mukhopadhyay, L. Lindsay, D.J. Singh, Optic Phonons and Anisotropic Thermal Conductivity in Hexagonal $Ge_2Sb_2Te_5$, Sci. Rep. 6 (2016) 37076.

[179] N. Mingo, Scattering Rates Cross-Plane Heat Conduction in Thin Films with *Ab-Initio* Phonon Dispersions and Scattering Rates, Appl. Phys. Lett. 108, (2016) 193104.

[180] L.L. Sun, Y. Cheng, G.F. Ji, Elastic and Optical Properties of CeO_2 via First-Principles Calculations, J. At. Mol. Sci. 1 (2010) 143–151.

[181] B. Szpunar, J. Szpunar, Density Functional Studies of Selected Metal Dioxides, J. Phys. Chem. Solids. 74 (2013) 1632–1639.

[182] T. Gürel, R. Eryiğit, *Ab Initio* Pressure-Dependent Vibrational and Dielectric Properties of CeO_2, Phys. Rev. B. 74 (2006) 014302.

[183] Z. Yang, T.K. Woo, M. Baudin, K. Hermansson, Atomic and Electronic Structure of Unreduced and Reduced CeO_2 Surfaces: A First-Principles Study, J. Chem. Phys. 120 (2004) 7741–7749.

[184] L.D. Landau, E.M. Lifshitz, A.M. Kosevich, L.P. Pitaevskii, J.B. Sykes, W.H. Reid, Theory of Elasticity, (1986) 187.

[185] P.T. Jochym, K. Parlinski, Ab Initio Lattice Dynamics and Elastic Constants of ZrC, Eur. Phys. J. B. 15 (2000) 265–268.

[186] A. Reuss, Berechnung Der Fließgrenze Von Mischkristallen Auf Grund Der Plastizitätsbedingung Für Einkristalle, ZAMM - J. Appl. Math. Mech. / Zeitschrift Für Angew. Math. Und Mech. 9 (1929) 49–58.

[187] W.Voigt, Lehrb. Der Kriystallphysik. (1928) 962.

[188] R. Hill, The Elastic Behaviour of a Crystalline Aggregate, Proc. Phys. Soc. Sect. A. 65 (2002) 349–354.

[189] A. Togo, F. Oba, I. Tanaka, First-Principles Calculations of the Ferroelastic Transition Between Rutile-Type and $CaCl_2$ -Type SiO_2 at High Pressures, Phys. Rev. B - Condens. Matter Mater. Phys. (2008) 1–9.

[190] S. Mochizuki, Infrared Optical Properties of Cerium Dioxide, Phys. Stat. Sol. B. 114 (1982) 189.

[191] J. Roleček, Š. Foral, K. Katovský, D. Salamon, K. Katovský, A Feasibility Study of Using CeO_2 as a Surrogate Material During the Investigation of UO_2 Thermal Conductivity Enhancement, Advances in Applied Ceramics. 116 (2017) 123-131.

[192] D.T. Morelli, G.A. Slack, High Lattice Thermal Conductivity Solids, High Therm. Conduct. Mater. (2006) 37–68.

[193] S. Nichenko, D. Staicu, Thermal Conductivity of Porous UO_2 : Molecular Dynamics Study, J. Nucl. Mater. 454 (2014) 315–322.

[194] A. Prasad, L. Bichler, Effect of Spark Plasma Sintering Process Parameters on Density and Microstructure of Cerium (IV) Oxide, Ceramic Transactions. 261 (2018) 217–224.

[195] D. Marrocchelli, N.H. Perry, S.R. Bishop, Understanding Chemical Expansion in Perovskite-Structured Oxides, Phys. Chem. Chem. Phys. 17 (2015) 10028–10039.

[196] C. Balaji Gopal, M. García-Melchor, S.C. Lee, Y. Shi, A. Shavorskiy, M. Monti, Z. Guan, R. Sinclair, H. Bluhm, A. Vojvodic, W.C. Chueh, Equilibrium Oxygen Storage Capacity of

Ultrathin $CeO_{2-\delta}$ Depends Non-Monotonically on Large Biaxial Strain, Nat. Commun. 8 (2017) 15360.

[197] L. Hallstadius, S. Johnson, E. Lahoda, Cladding for High Performance Fuel, Prog. Nucl. Energy. 57 (2012) 71–76.

[198] C.P. Deck, H.E. Khalifa, B. Sammuli, T. Hilsabeck, C.A. Back, Fabrication of SiC-SiC Composites for Fuel Cladding in Advanced Reactor Designs, Prog. Nucl. Energy. 57 (2012) 38–45.

[199] G.L. Harris, Properties Of Silicon Carbide, publisher Inspec (1995).

[200] L.M. Ivanova, P.A. Aleksandrov, K.D. Demakov, Thermoelectric Properties of Vapor-Grown Polycrystalline Cubic SiC, Inorg. Mater. 42 (2006) 1205–1209.

[201] D. Strauch, K. Karch., P.Pavone, W. Windl, *Ab Initio* Calculation of Structural , Lattice Dynamical , and Thermal Properties of Cubic Silicon Carbide, Int. J. Quantum Chem. 56 (1995) 801–817.

[202] K. Karch, P. Pavone, W. Windl, O. Schütt, D. Strauch, *Ab Initio* Calculation of Structural and Lattice-Dynamical Properties of Silicon Carbide, Phys. Rev. B. 50 (1994) 17054–17063.

[203] W.H. Lee, X.H. Yao, First Principle Investigation of Phase Transition and Thermodynamic Properties of SiC, Comput. Mater. Sci. 106 (2015) 76–82.

[204] Y.P. Lu, D.W. He, J. Zhu, X.D. Yang, First-Principles Study of Pressure-Induced Phase Transition in Silicon Carbide, Phys. B Condens. Matter. 403 (2008) 3543–3546.

[205] M. Methfessel, Calculated Elastic Constants and Deformation Potentials of Cubic SiC, Phys. Rev. B. 43 (1991) 6500–6509.

[206] S. Nowak, Crystal Lattice Dynamics of Various Silicon-Carbide Polytypes, Proc. SPIE. 4412 (2001) 181–186.

[207] J.F. Vetelino, S.S. Mitra, Lattice Dynamics of Cubic SiC, Phys. Rev. 178 (1969) 1349–1352.

[208] L.L. Snead, T. Nozawa, Y. Katoh, T.S. Byun, S. Kondo, D. A. Petti, Handbook of SiC Properties for Fuel Performance Modeling, J. Nucl. Mater. 371 (2007) 329–377.

[209] W. Lu, C.M. Lieber, Nanoelectronics from the Bottom Up, Nat. Mater. 6 (2007) 841–50.

[210] W. Xie, G. Moebus, S.W. Zhang, Carbon Nanotube to SiC Nanorod Conversion in Molten Salt Studied by EELS And Aberration Corrected HRTEM, Electron Microsc. Anal. Gr.

Conf. 241 (2010).

[211] M.A. Blanco, E. Francisco, V. Luaña, GIBBS: Isothermal-Isobaric Thermodynamics of Solids From Energy Curves Using a Quasi-Harmonic Debye Model, Comput. Phys. Commun. 158 (2004) 57–72.

[212] F.D. Murnaghan, The Compressibility of Media Under Extreme Pressures, Proc. Natl. Acad. Sci. U.S.A. 30 (1944) 244–247.

[213] R.E. Peierls, Quantum Theory of Solids, Oxford University Press, London, (1955).

[214] W. Li, N. Mingo, L. Lindsay, D.A. Broido, D.A. Stewart, N.A. Katcho, Thermal Conductivity of Diamond Nanowires from First Principles, Phys. Rev. B 85 (2012) 195436.

[215] J. Carrete, N. Mingo, S. Curtarolo, Low Thermal Conductivity and Triaxial Phononic Anisotropy Of SnSe, Appl. Phys. Lett. 105 (2014) 101907.

[216] X. Sha, R.E. Cohen, First-Principles Thermoelasticity of BCC Iron Under Pressure, Phys. Rev. B 74 (2006) 214111.

[217] J. Serrano, J. Strempfer, M. Cardona, M. Schwoerer-Böhning, H. Requardt, M. Lorenzen, B. Stojetz, P. Pavone, W.J. Choyke, Determination of the Phonon Dispersion of Zinc Blende (3C) Silicon Carbide by Inelastic X-Ray Scattering, Appl. Phys. Lett. 80 (2002) 4360–4362.

[218] D. Olego, M. Cardona, P. Vogl, Pressure Dependence of the Optical Phonons and Transverse Effective Charge in 3C-SiC, Phys. Rev. B. 25 (1982) 3878.

[219] L.B.O. Madelung, ed., Physics of Group-IV And III-V Compounds, Vol 17, Springer-Verlag, (1982).

[220] G.P.Srivastava, Lattice Thermal Conduction Mechanism in Solids, Therm. Conduct. Mater., Springer Science & Business Media, (2006) 1–10.

[221] I. Barin, Thermochemical Data of Pure Substances, Third Edit, Newyork:VCH, (1995).

[222] R.E.Taylor, H.Groot J, Thermophysical Properties Research Laboratory Report No. TRPL 1336, Unpublished. (1993).

[223] A. Sparavigna, Lattice Thermal Conductivity in Cubic Silicon Carbide, Phys. Rev. B. 66 (2002) 174301.

[224] L. Lindsay, D.A. Broido, T.L. Reinecke, *Ab Initio* Thermal Transport in Compound Semiconductors, Phys. Rev. B. 87 (2013) 165201.

[225] D.R. Clarke, Materials Selection Guidelines for Low Thermal Conductivity Thermal Barrier Coatings, Surf. Coatings Technol. 163–164 (2003) 67–74.

[226] W. Li, N. Mingo, Thermal Conductivity of Bulk And Nanowire InAs, AlN, and BeO Polymorphs From First Principles, J. Appl. Phys. 114 (2013) 183505.

[227] Z. Wang, X. Zu, F. Gao, W.J. Weber, J.P. Crocombette, Atomistic Simulation of the Size and Orientation Dependences of Thermal Conductivity in GaN Nanowires, Appl. Phys. Lett. 90 (2007) 161923.

[228] R.M. Hazen, L.W. Finger, High-Pressure and High-Temperature Crystal Chemistry of Beryllium Oxide, J. Appl. Phys. 59 (1986) 3728–3733.

[229] E. Loh, Optical Phonons in BeO Crystals, Phys. Rev. 166 (1968) 673–678.

[230] V.A. Sashin, M.A. Bolorizadeh, A.S. Kheifets, M.J. Ford, Electronic Band Structure of Beryllium Oxide, J. Phys. Condens. Matter. 15 (2003) 3567–3581.

[231] A. Victor, T. Douglas, Thermodynamic Properties of Magnesium Oxide and Beryllium Oxide from 298 to 1200 K, J. Res. Natl. Bur. Stand, 67 (1963) 325–329.

[232] G.P. Akishin, S.K. Turnaev, V.Y. Vaispapir, M.A. Gorbunova, Y.N. Makurin, V.S. Kiiko, A.L. Ivanovskii, Thermal Conductivity of Beryllium Oxide Ceramic, Refract. Ind. Ceram. 50 (2009) 465–468.

[233] Y. Takahashi, M. Murabayashi, Measurement of Thermal Properties of Nuclear Materials by Laser Flash Method, J. Nucl. Sci. Technol. 12 (1975) 133–144.

[234] S. Duman, A. Sütlü, S. Bağc, H.M. Tütüncü, G.P. Srivastava, Structural, Elastic, Electronic, and Phonon Properties of Zinc-Blende and Wurtzite BeO, J. Appl. Phys. 105 (2009) 033719.

[235] W. Li, N. Mingo, Thermal Conductivity of Bulk and Nanowire InAs, AlN, and BeO Polymorphs From First Principles, J. Appl. Phys. 114 (2013) 183505.

[236] S. Goumri-Said, M.B. Kanoun, Ab-Initio Investigations of the Electronic Properties of Bulk Wurtzite Beryllia and its Derived Nanofilms, Solid State Phys. 374 (2010) 3977–3981.

[237] D. Groh, R. Pandey, M.B. Sahariah, E. Amzallag, I. Baraille, M. Rérat, First-Principles Study of the Optical Properties of BeO in its Ambient and High-Pressure Phases, J. Phys. Chem. Solids. 70 (2009) 789–795.

[238] A.J. Cinthia, G.S. Priyanga, R. Rajeswarapalanichamy, K. Iyakutti, Structural, Electronic and Mechanical Properties of Alkaline Earth Metal Oxides MO (M=Be, Mg, Ca, Sr, Ba), J. Phys. Chem. Solids. 79 (2015) 23–42.

[239] M.B. Sahariah, S. Ghosh, Ab Initio Calculation of Lattice Dynamics in BeO, J. Phys.

Condens. Matter. 20 (2008) 395201.

[240] U.D. Wdowik, Structural Stability and Thermal Properties of BeO from the Quasiharmonic Approximation., J. Phys. Condens. Matter. 22 (2010) 045404.

[241] F. Luo, Y. Cheng, L.C. Cai, X.R. Chen, Structure and Thermodynamic Properties of BeO: Empirical Corrections in the Quasiharmonic Approximation, J. Appl. Phys. 113 (2013) 033517.

[242] H. Song, H.F. Liu, E. Tian, Structural and Thermodynamic Properties of Hexagonal BeO at High Pressures and Temperatures, J. Phys. Cond. Matt. 19 (2007) 456209.

[243] Y.N. Makurin, I.R. Shein, M.A. Gorbunova, V.S. Kiiko, A.L. Ivanovskii, First-Principle Quantum-Chemical Calculations of Several Thermomechanical Parameters of Beryllium Ceramics, Refract. Ind. Ceram. 47 (2006) 310–313.

[244] H. Iwanaga, A. Kunishige, S. Takeuchi, Anisotropic Thermal Expansion in Wurtzite-Type Crystals, J. Mater. Sci. 35 (2000) 2451–2454.

[245] D. Vanderbilt, Soft Self-Consistent Pseudopotentials in a Generalized Eigenvalue Formalism, Phys. Rev. B. 41 (1990) 7892–7895.

[246] V. Milman, M.C. Warren, Elasticity of Hexagonal BeO, J. Phys. Condens. Matter. 13 (2001) 241–251.

[247] G.G. Bentle, Elastic Constants of Single-Crystal BeO at Room Temperature, J. Am. Ceram. Soc. 49 (1966) 125–128.

[248] C.F. Cline, H.L. Dunegan, G.W. Henderson, Elastic Constants of Hexagonal BeO, ZnS and CdSc J. Appl. Phys. 38 (1967) 1944–1948.

[249] P.E. Van Camp, V.E. Van Doren, Ground-State Properties And Structural Phase of Beryllium Oxide, J. Phys. Cond. Matter (1996) 3385–3390.

[250] A. Bosak, K. Schmalzl, M. Krisch, W. Van Beek, V. Kolobanov, Lattice Dynamics of Beryllium Oxide: Inelastic X-Ray Scattering and *Ab Initio* Calculations, Phys. Rev. B. 77 (2008) 224303.

[251] M. Posternak, A. Baldereschi, A. Catellani, R. Resta, *Ab Initio* Study of the Spontaneous Polarization of Pyroelectric BeO, Phys. Rev. Lett. 64 (1990) 1777.

[252] O. Schutt, P. Pavone, W. Windl, K. Karch, D. Strauch, *Ab Initio* Lattice Dynamics and Charge Fluctuations in Alkaline-Like Earth Oxides, Phys. Rev. B. 50 (1994) 3746-3753.

[253] F. Luo, Z.C. Guo, X.L. Zhang, C.Y. Yuan, C.A. Liu, L.C. Cai, Pressure Effects on Structural

and Elastic Properties of BeO from First-Principles Calculations, Phys. Stat. Sol. B. 252 (2015) 212–218.

[254] T. Yao, S.K. Hong, Oxide and Nitride Semiconductors. Processing, Properties, and Applications, Springer Science & Business Media, 2012.

[255] D.L. Anderson, Equations of State of Solids for Geophysics and Ceramic Science, Oxford Monogr. Geol. Geophys. 31 (1995) 405.

[256] J. Francl, W.D. Kingery, Thermal Conductivity: IV, Apparatus for Determining Thermal Conductivity by a Comparative Method, J. Am. Ceram. Soc. 37 (1954) 80–84.

[257] G.A. Slack, S.F. Bartram, Thermal Expansion of Some Diamond like Crystals, J. Appl. Phys. 46 (1975) 89–98.

[258] R.M. Berman, J. Belle, Thorium Dioxide: Properties and Nulear Application, Report DOE 16 (1984).

[259] C. Ronchi, J.P. Hiernaut, Experimental Measurement of Pre-Melting and Melting of Thorium Dioxide, J. Alloys Compd. 240 (1996) 179–185.

[260] M.G. Adamson, E.A. Aitken, R.W. Caputi, Experimental and Thermodynamic Evaluation of the Melting Behavior of Irradiated Oxide Fuels, J. Nucl. Mater. 130 (1985) 349–365.

[261] C.E. Curtis, J.R. Johnson, Interim Report Properties of Thorium Oxide Ceramics, ORNL (1954), 1809.

[262] M.S. Nair, U. Basak, R. Ramachandran, S. Majumdar, Sintering of ThO_2, ThO_2-UO_2, ThO_2-PuO_2 Fuel Pellets with Additives, Trans Powder Met. Assoc India. (1999) 26-53.

[263] K.W. Kang, J.H. Yang, K.S. Kim, K.W. Song, C.H. Lee, Y.H. Jung, (Th,U)O_2 Pellets: Fabrication and Thermal Properties, J Kor Nucl Soc. 35 (2003) 299–308.

[264] T. Shiratori, K. Fukuda, Fabrication of Very High Density Fuel Pellets of Thorium Dioxide, J. Nucl. Mater. 202 (1993) 98–103.

[265] I. Amato, R.L. Colombo, A.M.P. Balzari, Hot-Pressing of Uranium Dioxide, J. Nucl. Mater. 20 (1966) 210–214.

[266] J.H. Yang, K.W. Song, Y.W. Lee, J.H. Kim, K.W. Kang, K.S. Kim, Y.H. Jung, Microwave Process for Sintering of Uranium Dioxide, J. Nucl. Mater. 325 (2004) 210–216.

[267] J.H. Yang, Y.W. Kim, J.H. Kim, D.J. Kim, K.W. Kang, Y.W. Rhee, K.S. Kim, K.W. Song, Pressureless Rapid Sintering of UO_2 Assisted by High-Frequency Induction Heating Process, J. Am. Ceram. Soc. 91 (2008) 3202–3206.

[268] D.J. Sprouster, E. Kardoulaki, R. Weidner, A.M. Raftery, M. Elbakhshwan, R. Pokharel, H.M. Reiche, D.D. Byler, S.K. Ghose, E. Dooryhee, K.J. McClellan, L.E. Ecker, In Situ X-Ray Characterization of Uranium Dioxide during Flash Sintering, Materialia. (2018) 176–182.

[269] L. Ge, G. Subhash, R.H. Baney, J.S. Tulenko, E. McKenna, Densification of Uranium Dioxide Fuel Pellets Prepared by Spark Plasma Sintering (SPS), J. Nucl. Mater. 435 (2013) 1–9.

[270] T. Ironman, J. Tulenko, G. Subhash, T. Ironman, Exploration of Viability of Spark Plasma Sintering for Commercial Fabrication of Nuclear Fuel Pellets, Nucl. Technol. 200 (2017) 144–158.

[271] E.K. Papynov, O.O. Shichalin, A.Yu. Mironeko, I.G. Tananaev, V.A. Avramenko, V.I. Sergienko, UO_2 Fuel Pellets Fabrication via Spark Plasma Sintering using Non-Standard Molybdenum Die, IOP Conf. Ser. Mater. Sci. Eng. 307 (2018) 0–5.

[272] E.A. Olevsky, W.L. Bradbury, C.D. Haines, D.G. Martin, D. Kapoor, Fundamental Aspects of Spark Plasma Sintering : I. Experimental Analysis of Scalability, J.Amer.Cera.Soc.2413 (2012) 2406–2413.

[273] H. Muta, Y. Murakami, M. Uno, K. Kurosaki, S. Yamanaka, Thermophysical Properties of $Th_{1-x}U_xO_2$ Pellets Prepared by Spark Plasma Sintering Technique, J. Nucl. Sci. Technol. 50 (2013) 181–187.

[274] H. Muta, H. Kado, Y. Ohishi, K. Kurosaki, S. Yamanaka, Effect of Oxygen Defects on Thermal Conductivity of Thorium-Cerium Dioxide Solid Solutions, J. Nucl. Mater. 483 (2017) 192–198.

[275] T. Yao, W. Zhu, G. Xin, F. Lu, J. Lian, S.M. Scott, Fabrication of Lanthanum-Doped Thorium Dioxide by High-Energy Ball Milling and Spark Plasma Sintering, J. Nucl. Mater. 485 (2017) 207–215.

[276] A. Cambriani, K. Popa, C. Kübel, L. Balice, G.D. Sorarù, J.F. Vigier, M. Cologna, E. De Bona, O. Walter, D. Bouëxière, Nano and Micro $U_{1-x}Th_xO_2$ Solid Solutions: from Powders to Pellets, J. Nucl. Mater. 498 (2017) 307–313.

[277] V. Tyrpekl, M. Cologna, D. Robba, J. Somers, Sintering Behaviour of Nanocrystalline ThO_2 Powder using Spark Plasma Sintering, Journal of the European Ceramic Society 36 (2016) 767–772.

[278] M. Ishigame, M. Kojima, Second Order Raman Spectera of Thorium Dioxide, J. Phys. Soc. Jpn. 41 (1976) 202-210.

[279] B. Palanki, Fabrication of Thorium and Thorium Dioxide, Nat. Sci. 07 (2015) 10–17.

[280] R.J. Ackermann, E.G. Rauh, A Thermodynamic Study of the Tungsten-Oxygen System at High Temperatures, J. Phys. Chem. 67 (2007) 2596–2601.

[281] A. Baena, T. Cardinaels, J. Van Eyken, J.L. Puzzolante, K. Binnemans, M. Verwerft, Effect of Sintering Atmosphere on the Hardness of ThO_2, J. Nucl. Mater. 477 (2016) 222–227.

[282] U. Anselmi Tamburini, S. Gennari, J.E. Garay, Z.A. Munir, Fundamental Investigations on the Spark Plasma Sintering/Synthesis Process: II. Modeling of Current and Temperature Distributions, Mater. Sci. Eng. A. 394 (2005) 139–148.

[283] R.O. Meyer, The Analysis of Fuel Densification, Office of Nuclear Reactor Regulation 8 (1976).

[284] J.A. Turnbull, The Effect of Grain Size on the Swelling and Gas Release Properties of UO_2 During Irradiation, J. Nucl. Mater. 50 (1974) 62–68.

[285] B. Burton, G.L. Reynolds, J.P. Barnes, The Influence of Grain Size on the Creep of Uranium Dioxide, J. Mater. Sci. 8 (1973) 1690–1694.

[286] M. Paggi, P. Wriggers, Numerical Modelling of Intergranular Fracture in Polycrystalline Materials and Grain Size Effects, Frat. Ed Integrità Strutt. Ed Integrità Strutt. 5 (2011) 5–14.

[287] L. Malakkal, A. Prasad, E. Jossou, J. Ranasinghe, B. Szpunar, L. Bichler, J. Szpunar, Thermal Conductivity of Bulk and Porous ThO_2: Atomistic and Experimental Study, J. Alloys Compd. 798 (2019) 507–516.

[288] IAEA, Advanced Fuel Pellet Materials and Fuel Rod Design for Water Cooled Reactors, Tech. Comm. Meet. Held Villigen. 1654 (2010) 241.

[289] Y.W. Rhee, D.J. Kim, J.H. Kim, J.H. Yang, K.S. Kim, K.W. Kang, K.W. Song, Fabrication of Sintered Annular Fuel Pellet for HANARO Irradiation Test, J. Nucl. Sci. Technol. 47 (2010) 345–350.

[290] Y.H. Koo, J.H. Yang, J.Y. Park, Y.S. Yang, H.K. Kim, K.W. Song, Status of Dual Cooled Annular Fuel Development in KAERI, Enlarg. Halden Program. Gr. Meet. (2013) 1–6.

[291] Z. Chen, G. Subhash, J.S. Tulenko, Master Sintering Curves for UO_2 and UO_2-SiC Composite Processed by Spark Plasma Sintering, J. Nucl. Mater. 454 (2014) 427–433.

[292] R. Liu, W. Zhou, P. Shen, A. Prudil, P.K. Chan, Fully Coupled Multiphysics Modeling of Enhanced Thermal Conductivity UO_2-BeO Fuel Performance in a Light Water Reactor, Nucl. Eng. Des. 295 (2015) 511–523.

[293] D. Chandramouli, S.T. Revankar, Development of Thermal Models and Analysis of UO_2 - BeO Fuel During a Loss of Coolant Accident , Int. J. Nucl. Energy. 2014 (2014) 1–9.

[294] J. Buckley, J.D. Turner, T.J. Abram, Uranium Dioxide-Molybdenum Composite Fuel Pellets with Enhanced Thermal Conductivity Manufactured via Spark Plasma Sintering, J. Nucl. Mater. 523 (2019) 360–368.

[295] K.M. Mampuru, E. Ajenifuja, A.P.I. Popoola, O. Popoola, Effect of Silicon Carbide Addition on the Microstructure, Hardness and Densification Properties of Spark Plasma Sintered Ni-Zn-Al Alloy, J. King Saud Univ. Sci. (2019) 0–4.

[296] A. Karanam, L. Bichler, R. Fong, on the Densification Behavior of (0.2, 0.5, and 1 wt Pct) CNT-YSZ Ceramic Composites Processed via Spark Plasma Sintering, Metall. Mater. Trans. B Process Metall. Mater. Process. Sci. 46 (2015) 1666–1673.

[297] D.E.Newbury, N.W.M.Ritchie, Is Scanning Electron Microscopy/Energy Dispersive X-Ray Spectrometry (SEM/EDS) Quantitative?, J. Scanning. Microscopy 35 (2013) 141–168.

[298] A.J. Parkison, S.S. Parker, A.T. Nelson, Fabrication of ThN Using a Carbothermic Reduction to Nitridation Process, J. Am. Ceram. Soc. 99 (2016) 3909–3914.

APPENDIX A

AN INTERFACE TO QUANTUM ESPRESSO

Linu Malakkal[1], Barbara Szpunar[2], Juan Carlos Zuniga[3], Ravi Kiran Siripurapu[1], Jerzy A. Szpunar[1]
[1]Department of Mechanical Engineering, University of Saskatchewan
[2]Department of Physics and Engineering Physics, University of Saskatchewan
[3]Information and communications technology, research computing, University of Saskatchewan

Abstract

Our project aims at providing the materials engineering fraternity with a simple and effective interface using ipython to operate Quantum ESPRESSO (QE), an open source code for materials simulation. QE is a first principles code using density functional theory, plane waves and pseudo potentials; it has ability to predict material properties. Ipython notebook interface uses the scope of the following libraries; Atomic Simulation Environment, matplotlib, scipy, numpy, pyspglib, elastic and newly developed library: QE-nipy-advanced to predict the properties. QE-nipy-advanced is the latest version of QE-nipy. The latest version incorporates features that can take care of all the input parameters supported by PWscf and PHonon packages of Quantum ESPRESSO. Thermo-mechanical properties of some nuclear materials with different magnetic and metallic behavior has been studied using the QE-nipy-advanced, but in here we demonstrate the thermo-mechanical properties of non-magnetic insulator like silicon carbide and thoria, which are materials for future nuclear reactor applications.

Further Details to this work can be found in the following reference.

L. Malakkal, B. Szpunar, R. K. Siripurapu, J. C. Zuniga, J. A. Szpunar; "An Interface to Quantum ESPRESSO" published as proceedings of 3rd World Congress on Integrated Computational Materials Engineering (ICME 2015) Pennsylvania USA, published by Wiley publications.

APPENDIX B

Copyright permission of Manuscript #1, chapter 3 of the thesis

ELSEVIER LICENSE
TERMS AND CONDITIONS

Aug 13, 2019

This Agreement between Mr. Linu Malakkal ("You") and Elsevier ("Elsevier") consists of your license details and the terms and conditions provided by Elsevier and Copyright Clearance Center.

License Number	4647281165559
License date	Aug 13, 2019
Licensed Content Publisher	Elsevier
Licensed Content Publication	Journal of Alloys and Compounds
Licensed Content Title	Thermal conductivity of bulk and porous ThO2: Atomistic and experimental study
Licensed Content Author	Linu Malakkal, Anil Prasad, Ericmoore Jossou, Jayangani Ranasinghe, Barbara Szpunar, Lukas Bichler, Jerzy Szpunar
Licensed Content Date	Aug 25, 2019
Licensed Content Volume	798
Licensed Content Issue	n/a
Licensed Content Pages	10
Start Page	507
End Page	516
Type of Use	reuse in a thesis/dissertation
Intended publisher of new work	other
Portion	full article
Circulation	1
Format	both print and electronic
Are you the author of this Elsevier article?	No
Will you be translating?	No
Title of your thesis/dissertation	Thermal conductivity a road towards accident tolerant fuel
Expected completion date	Nov 2019
Estimated size (number of pages)	200

Requestor Location	Mr. Linu Malakkal Department of Mechanical Engineering 57 Campus drive Saskatoon, SK S7N 5A9 Canada Attn: Mr. Linu Malakkal
Publisher Tax ID	GB 494 6272 12
Total	0.00 USD

Terms and Conditions

INTRODUCTION

1. The publisher for this copyrighted material is Elsevier. By clicking "accept" in connection with completing this licensing transaction, you agree that the following terms and conditions apply to this transaction (along with the Billing and Payment terms and conditions established by Copyright Clearance Center, Inc. ("CCC"), at the time that you opened your Rightslink account and that are available at any time at http://myaccount.copyright.com).

GENERAL TERMS

2. Elsevier hereby grants you permission to reproduce the aforementioned material subject to the terms and conditions indicated.

3. Acknowledgement: If any part of the material to be used (for example, figures) has appeared in our publication with credit or acknowledgement to another source, permission must also be sought from that source. If such permission is not obtained then that material may not be included in your publication/copies. Suitable acknowledgement to the source must be made, either as a footnote or in a reference list at the end of your publication, as follows:

"Reprinted from Publication title, Vol /edition number, Author(s), Title of article / title of chapter, Pages No., Copyright (Year), with permission from Elsevier [OR APPLICABLE SOCIETY COPYRIGHT OWNER]." Also Lancet special credit - "Reprinted from The Lancet, Vol. number, Author(s), Title of article, Pages No., Copyright (Year), with permission from Elsevier."

4. Reproduction of this material is confined to the purpose and/or media for which permission is hereby given.

5. Altering/Modifying Material: Not Permitted. However figures and illustrations may be altered/adapted minimally to serve your work. Any other abbreviations, additions, deletions and/or any other alterations shall be made only with prior written authorization of Elsevier Ltd. (Please contact Elsevier at permissions@elsevier.com). No modifications can be made to any Lancet figures/tables and they must be reproduced in full.

6. If the permission fee for the requested use of our material is waived in this instance, please be advised that your future requests for Elsevier materials may attract a fee.

7. Reservation of Rights: Publisher reserves all rights not specifically granted in the combination of (i) the license details provided by you and accepted in the course of this licensing transaction, (ii) these terms and conditions and (iii) CCC's Billing and Payment terms and conditions.

8. License Contingent Upon Payment: While you may exercise the rights licensed immediately upon issuance of the license at the end of the licensing process for the transaction, provided that you have disclosed complete and accurate details of your proposed use, no license is finally effective unless and until full payment is received from you (either by publisher or by CCC) as provided in CCC's Billing and Payment terms and conditions. If full payment is not received on a timely basis, then any license preliminarily granted shall be deemed automatically revoked and shall be void as if never granted. Further, in the event that you breach any of these terms and conditions or any of CCC's Billing and Payment terms and conditions, the license is automatically revoked and shall be void as if never granted. Use of materials as described in a revoked license, as well as any use of the materials beyond the scope of an unrevoked license, may constitute copyright infringement and publisher reserves the right to take any and all action to protect its copyright in the materials.

9. Warranties: Publisher makes no representations or warranties with respect to the licensed material.

10. Indemnity: You hereby indemnify and agree to hold harmless publisher and CCC, and their respective officers, directors, employees and agents, from and against any and all claims arising out of your use of the licensed material other than as specifically authorized pursuant to this license.

11. No Transfer of License: This license is personal to you and may not be sublicensed, assigned, or transferred by you to any other person without publisher's written permission.

12. No Amendment Except in Writing: This license may not be amended except in a writing signed by both parties (or, in the case of publisher, by CCC on publisher's behalf).

13. Objection to Contrary Terms: Publisher hereby objects to any terms contained in any purchase order, acknowledgment, check endorsement or other writing prepared by you, which terms are inconsistent with these terms and conditions or CCC's Billing and Payment terms and conditions. These terms and conditions, together with CCC's Billing and Payment terms and conditions (which are incorporated herein), comprise the entire agreement between you and publisher (and CCC) concerning this licensing transaction. In the event of any conflict between your obligations established by these terms and conditions and those established by CCC's Billing and Payment terms and conditions, these terms and conditions shall control.

14. Revocation: Elsevier or Copyright Clearance Center may deny the permissions described in this License at their sole discretion, for any reason or no reason, with a full refund payable to you. Notice of such denial will be made using the contact information provided by you. Failure to receive such notice will not alter or invalidate the denial. In no event will Elsevier or Copyright Clearance Center be responsible or liable for any costs, expenses or damage incurred by you as a result of a denial of your permission request, other than a refund of the amount(s) paid by you to Elsevier and/or Copyright Clearance Center for denied permissions.

LIMITED LICENSE

The following terms and conditions apply only to specific license types:

15. **Translation**: This permission is granted for non-exclusive world English rights only unless your license was granted for translation rights. If you licensed translation rights you may only translate this content into the languages you requested. A professional translator must perform all translations and reproduce the content word for word preserving the integrity of the article.

16. **Posting licensed content on any Website**: The following terms and conditions apply as follows: Licensing material from an Elsevier journal: All content posted to the web site must maintain the copyright information line on the bottom of each image; A hyper-text must be included to the Homepage of the journal from which you are licensing at http://www.sciencedirect.com/science/journal/xxxxx or the Elsevier homepage for books at http://www.elsevier.com; Central Storage: This license does not include permission for a

scanned version of the material to be stored in a central repository such as that provided by Heron/XanEdu.

Licensing material from an Elsevier book: A hyper-text link must be included to the Elsevier homepage at http://www.elsevier.com . All content posted to the web site must maintain the copyright information line on the bottom of each image.

Posting licensed content on Electronic reserve: In addition to the above the following clauses are applicable: The web site must be password-protected and made available only to bona fide students registered on a relevant course. This permission is granted for 1 year only. You may obtain a new license for future website posting.

17. **For journal authors:** the following clauses are applicable in addition to the above:

Preprints:

A preprint is an author's own write-up of research results and analysis, it has not been peer-reviewed, nor has it had any other value added to it by a publisher (such as formatting, copyright, technical enhancement etc.).

Authors can share their preprints anywhere at any time. Preprints should not be added to or enhanced in any way in order to appear more like, or to substitute for, the final versions of articles however authors can update their preprints on arXiv or RePEc with their Accepted Author Manuscript (see below).

If accepted for publication, we encourage authors to link from the preprint to their formal publication via its DOI. Millions of researchers have access to the formal publications on ScienceDirect, and so links will help users to find, access, cite and use the best available version. Please note that Cell Press, The Lancet and some society-owned have different preprint policies. Information on these policies is available on the journal homepage.

Accepted Author Manuscripts: An accepted author manuscript is the manuscript of an article that has been accepted for publication and which typically includes author-incorporated changes suggested during submission, peer review and editor-author communications.

Authors can share their accepted author manuscript: immediately via their non-commercial person homepage or blog by updating a preprint in arXiv or RePEc with the accepted manuscript via their research institute or institutional repository for internal institutional uses

or as part of an invitation-only research collaboration work-group directly by providing copies to their students or to research collaborators for their personal use for private scholarly sharing as part of an invitation-only work group on commercial sites with which Elsevier has an agreement.

After the embargo period via non-commercial hosting platforms such as their institutional repository via commercial sites with which Elsevier has an agreement. In all cases accepted manuscripts should: link to the formal publication via its DOI bear a CC-BY-NC-ND license - this is easy to do if aggregated with other manuscripts, for example in a repository or other site, be shared in alignment with our hosting policy not be added to or enhanced in any way to appear more like, or to substitute for, the published journal article.

Published journal article (JPA): A published journal article (PJA) is the definitive final record of published research that appears or will appear in the journal and embodies all value-adding publishing activities including peer review co-ordination, copy-editing, formatting, (if relevant) pagination and online enrichment.

Policies for sharing publishing journal articles differ for subscription and gold open access articles:

Subscription Articles: If you are an author, please share a link to your article rather than the full-text. Millions of researchers have access to the formal publications on ScienceDirect, and so links will help your users to find, access, cite, and use the best available version.

Theses and dissertations which contain embedded PJAs as part of the formal submission can be posted publicly by the awarding institution with DOI links back to the formal publications on ScienceDirect.

If you are affiliated with a library that subscribes to ScienceDirect you have additional private sharing rights for others' research accessed under that agreement. This includes use for classroom teaching and internal training at the institution (including use in course packs and courseware programs), and inclusion of the article for grant funding purposes.

Gold Open Access Articles: May be shared according to the author-selected end-user license and should contain a CrossMark logo, the end user license, and a DOI link to the formal publication on ScienceDirect.

Please refer to Elsevier's posting policy for further information.

18. **For book authors** the following clauses are applicable in addition to the above: Authors are permitted to place a brief summary of their work online only. You are not allowed to download and post the published electronic version of your chapter, nor may you scan the printed edition to create an electronic version. **Posting to a repository:** Authors are permitted to post a summary of their chapter only in their institution's repository.

19. **Thesis/Dissertation**: If your license is for use in a thesis/dissertation your thesis may be submitted to your institution in either print or electronic form. Should your thesis be published commercially, please reapply for permission. These requirements include permission for the Library and Archives of Canada to supply single copies, on demand, of the complete thesis and include permission for Proquest/UMI to supply single copies, on demand, of the complete thesis. Should your thesis be published commercially, please reapply for permission. Theses and dissertations which contain embedded PJAs as part of the formal submission can be posted publicly by the awarding institution with DOI links back to the formal publications on ScienceDirect.

Elsevier Open Access Terms and Conditions

You can publish open access with Elsevier in hundreds of open access journals or in nearly 2000 established subscription journals that support open access publishing. Permitted third party re-use of these open access articles is defined by the author's choice of Creative Commons user license. See our open access license policy for more information.

Terms & Conditions applicable to all Open Access articles published with Elsevier:

Any reuse of the article must not represent the author as endorsing the adaptation of the article nor should the article be modified in such a way as to damage the author's honour or reputation. If any changes have been made, such changes must be clearly indicated.

The author(s) must be appropriately credited and we ask that you include the end user license and a DOI link to the formal publication on ScienceDirect.

If any part of the material to be used (for example, figures) has appeared in our publication with credit or acknowledgement to another source it is the responsibility of the user to ensure their reuse complies with the terms and conditions determined by the rights holder.

Additional Terms & Conditions applicable to each Creative Commons user license:

CC BY: The CC-BY license allows users to copy, to create extracts, abstracts and new works from the Article, to alter and revise the Article and to make commercial use of the Article

APPENDIX C

Copyright permission of Manuscript #2, chapter 4 of the thesis

Creative Commons Licenses

Scientific Reports articles are published open access under a CC BY license (Creative Commons Attribution 4.0 International License). The CC BY license allows for maximum dissemination and re-use of open access materials and is preferred by many research funding bodies. Under this license users are free to share (copy, distribute and transmit) and remix (adapt) the contribution including for commercial purposes, providing they attribute the contribution in the manner specified by the author or licensor (read full legal code).

Under Creative Commons, authors retain copyright in their articles.

Visit our open research site for more information about Creative Commons licensing.

Compliance with funder mandates

Nature Research's services and policies ensure that authors can fully comply with the public access requirements of major funding bodies worldwide. For information and advice about compliance, consult our open access policy information, or contact us.

Further information

Further information about Nature Research’s open access policies and publishing options can be found on our open research site.

APPENDIX D

Copyright permission of Manuscript #3, chapter 5 of this thesis

ELSEVIER LICENSE
TERMS AND CONDITIONS

Aug 13, 2019

This Agreement between Mr. Linu Malakkal ("You") and Elsevier ("Elsevier") consists of your license details and the terms and conditions provided by Elsevier and Copyright Clearance Center.

License Number	4647250952146
License date	Aug 13, 2019
Licensed Content Publisher	Elsevier
Licensed Content Publication	Computational Materials Science
Licensed Content Title	Thermal conductivity of bulk and nanowire of cubic-SiC from ab initio calculations
Licensed Content Author	Linu Malakkal, Barbara Szpunar, Ravi Kiran Siripurapu, Jerzy A. Szpunar
Licensed Content Date	Feb 15, 2017
Licensed Content Volume	128
Licensed Content Issue	n/a
Licensed Content Pages	8
Start Page	249
End Page	256
Type of Use	reuse in a thesis/dissertation
Portion	full article
Circulation	1
Format	both print and electronic

Are you the author of this Elsevier article?	No
Will you be translating?	No
Title of your thesis/dissertation	Thermal conductivity a road towards accident tolerant fuel
Expected completion date	Nov 2019
Estimated size (number of pages)	200
Requestor Location	Mr. Linu Malakkal Department of Mechanical Engineering 57 Campus drive Saskatoon, SK S7N 5A9 Canada Attn: Mr. Linu Malakkal
Publisher Tax ID	GB 494 6272 12
Total	0.00 CAD

Terms and Conditions

INTRODUCTION

1. The publisher for this copyrighted material is Elsevier. By clicking "accept" in connection with completing this licensing transaction, you agree that the following terms and conditions apply to this transaction (along with the Billing and Payment terms and conditions established by Copyright Clearance Center, Inc. ("CCC"), at the time that you opened your Rightslink account and that are available at any time at http://myaccount.copyright.com).

GENERAL TERMS

2. Elsevier hereby grants you permission to reproduce the aforementioned material subject to the terms and conditions indicated.

3. Acknowledgement: If any part of the material to be used (for example, figures) has appeared in our publication with credit or acknowledgement to another source, permission must also be sought from that source. If such permission is not obtained then that material may not be included in your publication/copies. Suitable acknowledgement to the source

must be made, either as a footnote or in a reference list at the end of your publication, as follows:

"Reprinted from Publication title, Vol /edition number, Author(s), Title of article / title of chapter, Pages No., Copyright (Year), with permission from Elsevier [OR APPLICABLE SOCIETY COPYRIGHT OWNER]." Also Lancet special credit - "Reprinted from The Lancet, Vol. number, Author(s), Title of article, Pages No., Copyright (Year), with permission from Elsevier."

4. Reproduction of this material is confined to the purpose and/or media for which permission is hereby given.

5. Altering/Modifying Material: Not Permitted. However figures and illustrations may be altered/adapted minimally to serve your work. Any other abbreviations, additions, deletions and/or any other alterations shall be made only with prior written authorization of Elsevier Ltd. (Please contact Elsevier at permissions@elsevier.com). No modifications can be made to any Lancet figures/tables and they must be reproduced in full.

6. If the permission fee for the requested use of our material is waived in this instance, please be advised that your future requests for Elsevier materials may attract a fee.

7. Reservation of Rights: Publisher reserves all rights not specifically granted in the combination of (i) the license details provided by you and accepted in the course of this licensing transaction, (ii) these terms and conditions and (iii) CCC's Billing and Payment terms and conditions.

8. License Contingent Upon Payment: While you may exercise the rights licensed immediately upon issuance of the license at the end of the licensing process for the transaction, provided that you have disclosed complete and accurate details of your proposed use, no license is finally effective unless and until full payment is received from you (either by publisher or by CCC) as provided in CCC's Billing and Payment terms and conditions. If full payment is not received on a timely basis, then any license preliminarily granted shall be deemed automatically revoked and shall be void as if never granted. Further, in the event that you breach any of these terms and conditions or any of CCC's Billing and Payment terms and conditions, the license is automatically revoked and shall be void as if never granted. Use of materials as described in a revoked license, as well as any use of the materials beyond the scope of an unrevoked license, may constitute copyright infringement

and publisher reserves the right to take any and all action to protect its copyright in the materials.

9. Warranties: Publisher makes no representations or warranties with respect to the licensed material.

10. Indemnity: You hereby indemnify and agree to hold harmless publisher and CCC, and their respective officers, directors, employees and agents, from and against any and all claims arising out of your use of the licensed material other than as specifically authorized pursuant to this license.

11. No Transfer of License: This license is personal to you and may not be sublicensed, assigned, or transferred by you to any other person without publisher's written permission.

12. No Amendment Except in Writing: This license may not be amended except in a writing signed by both parties (or, in the case of publisher, by CCC on publisher's behalf).

13. Objection to Contrary Terms: Publisher hereby objects to any terms contained in any purchase order, acknowledgment, check endorsement or other writing prepared by you, which terms are inconsistent with these terms and conditions or CCC's Billing and Payment terms and conditions. These terms and conditions, together with CCC's Billing and Payment terms and conditions (which are incorporated herein), comprise the entire agreement between you and publisher (and CCC) concerning this licensing transaction. In the event of any conflict between your obligations established by these terms and conditions and those established by CCC's Billing and Payment terms and conditions, these terms and conditions shall control.

14. Revocation: Elsevier or Copyright Clearance Center may deny the permissions described in this License at their sole discretion, for any reason or no reason, with a full refund payable to you. Notice of such denial will be made using the contact information provided by you. Failure to receive such notice will not alter or invalidate the denial. In no event will Elsevier or Copyright Clearance Center be responsible or liable for any costs, expenses or damage incurred by you as a result of a denial of your permission request, other than a refund of the amount(s) paid by you to Elsevier and/or Copyright Clearance Center for denied permissions.

LIMITED LICENSE

The following terms and conditions apply only to specific license types:

15. **Translation**: This permission is granted for non-exclusive world **English** rights only unless your license was granted for translation rights. If you licensed translation rights you may only translate this content into the languages you requested. A professional translator must perform all translations and reproduce the content word for word preserving the integrity of the article.

16. **Posting licensed content on any Website**: The following terms and conditions apply as follows: Licensing material from an Elsevier journal: All content posted to the web site must maintain the copyright information line on the bottom of each image; A hyper-text must be included to the Homepage of the journal from which you are licensing at http://www.sciencedirect.com/science/journal/xxxxx or the Elsevier homepage for books at http://www.elsevier.com; Central Storage: This license does not include permission for a scanned version of the material to be stored in a central repository such as that provided by Heron/XanEdu.

Licensing material from an Elsevier book: A hyper-text link must be included to the Elsevier homepage at http://www.elsevier.com . All content posted to the web site must maintain the copyright information line on the bottom of each image.

Posting licensed content on Electronic reserve: In addition to the above the following clauses are applicable: The web site must be password-protected and made available only to bona fide students registered on a relevant course. This permission is granted for 1 year only. You may obtain a new license for future website posting.

17. **For journal authors:** the following clauses are applicable in addition to the above:

Preprints:

A preprint is an author's own write-up of research results and analysis, it has not been peer-reviewed, nor has it had any other value added to it by a publisher (such as formatting, copyright, technical enhancement etc.).

Authors can share their preprints anywhere at any time. Preprints should not be added to or enhanced in any way in order to appear more like, or to substitute for, the final versions of articles however authors can update their preprints on arXiv or RePEc with their Accepted Author Manuscript (see below).

If accepted for publication, we encourage authors to link from the preprint to their formal publication via its DOI. Millions of researchers have access to the formal publications on

ScienceDirect, and so links will help users to find, access, cite and use the best available version. Please note that Cell Press, The Lancet and some society-owned have different preprint policies. Information on these policies is available on the journal homepage.

Accepted Author Manuscripts: An accepted author manuscript is the manuscript of an article that has been accepted for publication and which typically includes author-incorporated changes suggested during submission, peer review and editor-author communications.

Authors can share their accepted author manuscript:

1. immediately
    1. via their non-commercial person homepage or blog
    2. by updating a preprint in arXiv or RePEc with the accepted manuscript
    3. via their research institute or institutional repository for internal institutional uses or as part of an invitation-only research collaboration work-group
    4. directly by providing copies to their students or to research collaborators for their personal use
    5. for private scholarly sharing as part of an invitation-only work group on commercial sites with which Elsevier has an agreement
2. After the embargo period
    1. via non-commercial hosting platforms such as their institutional repository
    2. via commercial sites with which Elsevier has an agreement

In all cases accepted manuscripts should:

1. link to the formal publication via its DOI
2. bear a CC-BY-NC-ND license - this is easy to do
3. if aggregated with other manuscripts, for example in a repository or other site, be shared in alignment with our hosting policy not be added to or enhanced in any way to appear more like, or to substitute for, the published journal article.

Published journal article (JPA): A published journal article (PJA) is the definitive final record of published research that appears or will appear in the journal and embodies all value-adding publishing activities including peer review co-ordination, copy-editing, formatting, (if relevant) pagination and online enrichment.

Policies for sharing publishing journal articles differ for subscription and gold open access articles:

Subscription Articles: If you are an author, please share a link to your article rather than the full-text. Millions of researchers have access to the formal publications on ScienceDirect, and so links will help your users to find, access, cite, and use the best available version.

Theses and dissertations which contain embedded PJAs as part of the formal submission can be posted publicly by the awarding institution with DOI links back to the formal publications on ScienceDirect.

If you are affiliated with a library that subscribes to ScienceDirect you have additional private sharing rights for others' research accessed under that agreement. This includes use for classroom teaching and internal training at the institution (including use in course packs and courseware programs), and inclusion of the article for grant funding purposes.

Gold Open Access Articles: May be shared according to the author-selected end-user license and should contain a CrossMark logo, the end user license, and a DOI link to the formal publication on ScienceDirect.

Please refer to Elsevier's posting policy for further information.

18. **For book authors** the following clauses are applicable in addition to the above: Authors are permitted to place a brief summary of their work online only. You are not allowed to download and post the published electronic version of your chapter, nor may you scan the printed edition to create an electronic version. **Posting to a repository:** Authors are permitted to post a summary of their chapter only in their institution's repository.

19. **Thesis/Dissertation**: If your license is for use in a thesis/dissertation your thesis may be submitted to your institution in either print or electronic form. Should your thesis be published commercially, please reapply for permission. These requirements include permission for the Library and Archives of Canada to supply single copies, on demand, of the complete thesis and include permission for Proquest/UMI to supply single copies, on demand, of the complete thesis. Should your thesis be published commercially, please reapply for permission. Theses and dissertations which contain embedded PJAs as part of the formal submission can be posted publicly by the awarding institution with DOI links back to the formal publications on ScienceDirect.

Elsevier Open Access Terms and Conditions

APPENDIX E

Copyright permission of Manuscript #4, provided in Chapter 6 of this thesis

The copyright permission given when contacted the journal.

As an author of an Elsevier journal, you retain certain rights detailed in this webpage:https://www.elsevier.com/about/our-business/policies/copyright, provided that you properly acknowledge the original source of the material as follows: "Reproduced from *Authors name. Article title. Journal title year; volume number(issue number):first page-last page.* Copyright © *year [if applicable: name of learned society,* published by*]* Elsevier Masson SAS. All rights reserved."

If any part of the material to be used (for example, figures) has appeared in our publication with credit or acknowledgement to another source, permission must also be sought from that source (if such permission is not obtained then that material may not be included in your publication/copies). Should the reuse you intend to make of your material be not included in such retained rights, please contact me directly with more details.

APPENDIX F

Copyright permission of Manuscript #5, provided in Chapter 7 of this thesis

Title: The effect of SPS processing parameters on the microstructure and thermal conductivity of ThO2

Author: Linu Malakkal,Anil Prasad,Jayangani Ranasinghe,Ericmoore Jossou,Dotun Oladimeji,Barbara Szpunar,Lukas Bichler,Jerzy Szpunar

Publication: Journal of Nuclear Materials

Publisher: Elsevier

Date: 15 December 2019

Logged in as:
Linu Malakkal
Account #:
3001500901
LOGOUT

Please note that, as the author of this Elsevier article, you retain the right to include it in a thesis or dissertation, provided it is not published commercially. Permission is not required, but please ensure that you reference the journal as the original source. For more information on this and on your other retained rights, please visit: https://www.elsevier.com/about/our-business/policies/copyright#Author-rights

BACK CLOSE WINDOW